Development of soft magnetic alloy by nanomaterials

Amar Jabar Albaaji

A thesis submitted to the Cardiff University in Candidature for the degree of Doctor of Philosophy

Wolfson Centre for Magnetics
Cardiff School of Engineering
Cardiff University
Wales, United Kingdom

June, 2017

Declaration

This work has not been submitted in substance for any other degree or award at this or any other university or place of learning, nor is being submitted concurrently in candidature for any degree or another award.

Signed …… (Amar Albaaji) Date ……

STATEMENT 1

This thesis is being submitted in partial fulfilment of the requirements for the degree of PhD.

Signed …… (Amar Albaaji) Date ……

STATEMENT 2

This thesis is the result of my own independent work/investigation, except where otherwise stated, and the thesis has not been edited by a third party beyond what is permitted by Cardiff University Policy on the Use of Third Party Editors by Research Degree Student. Other sources are acknowledged by explicit references. The views expressed are my own.

Signed ……. (Amar Albaaji) Date ……

STATEMENT 3

I hereby give consent for my thesis, if accepted, to be available online in the University's Open Access repository and for inter-library loan, and for the title and summary to be made available to outside organisations.

Signed …… (Amar Albaaji) Date ……

Table of Contents

List of figures

Symbols and abbreviations

σ_y ……yield strength
σ_i ……intrinsic lattice resistance
k_y…… Hall-Petch parameters
d ……. grain size
A……exchange stiffness constant
δ_W……wall thickness
μ_0…… permeability of vacuum
$\bar{r}$…… average radius of particles
V_f ……volume fraction of particles
l…… stress wavelength
$\Delta\sigma$ …… internal stress
M_s…… magnetisation saturation
K_1……magnetocrystalline anisotropy
T_c …… curie temperature
a ……lattice constant
B ……broadening in radians
λ ……wavelength
t…… thickness
w……lateral
l……length
OD……outer diameter
ID…… inner diameter
L_{ex} ……exchange length
dp ……particle diameter
Vp …… volume fraction of reinforcement
b……Burgers vector
r……radius of the particle
G…… shear modulus
l_c…… critical length
CNT…… carbon nanotube
MWCNT……multi walled carbon nanotube
SWNT…… single walled carbon nanotube
GNP……graphene nanoplatelet
SiC_p……silicon carbide particles
SPS……spark plasma sintering
MEA……More electric aircraft
LCD……local disorder
NSD…… nanoscale dispersion
MA…… mechanical alloying
PCA…… process control agent
PBA……polyester binder assistant
PVA……polyvinyl alcohol
RBM……radial breathing mode
BPR……ball to powder ratio
FWHM……full width half maximum
APDS……antiphase domain size
DMF…… dimethylformamide
LVDT……linear variable differential transformer

Acknowledgement

I am in debt to my parents, wife, and children, for their patient and supporting during my PhD. study. The Iraqi government sponsored my scholarship; I would like to offer my special thanks to the Iraqi government and Cardiff University for supporting this study.

I am extremely appreciative to my academic supervisors, Dr J. P Hall and Prof S.L Evans for their supporting, comprehensive discussions and beneficial suggestions during the period of my doctoral study, without their continuous support and guidance, it would be impossible for this achievement. I am greatly grateful to Prof M.J. Reece and Dr Elinor G. Castle from the Queen Mary University of London for their allowance and teaching to use the spark plasma sintering facility at Nanoforce Technology Ltd., London to prepare the samples. In addition to the constructive comments provided by them during my PhD. study. I want to thank Dr Greg Shaw in Cardiff School of Chemistry for helping me to use the Raman spectroscopy during my research work. I appreciate the help offered by Dr Duncan Muir to use the EDS and SEM facilities in Earth Science. I would like to express my sincere thanks to Dr Fiona Robinson for her help in doing heat treatment in Cogent Power Ltd. I would like to thank Dr P.I Anderson and Dr Christopher Harrison in Wolfson centre for magnetics for their help in magnetic property measurement. I pass my thanks to Dr M. Harbottle in Cardiff School of Engineering for allowing me to use the optical microscope. I extend my thanks also to Dr Georgi Lalev in Cardiff School of Optometry for assisting me in using TEM. I am also grateful to mechanical and civil workshop staff for aiding me in getting the samples and test them as early as possible. I am thankful to my colleagues in Wolfson centre, Dr Vishu Goel Dr Mahesh Kumar Mani, Dr Tomasz Kutrowski, Mr Hamid, for their help and motivation provided during my research. I extend my thanks to my friends Maasi Al-Mayali, Nabeel Almuramady and Hayder Miri Hamzah.

Abstract

Equiatomic FeCo alloy which has the highest saturation magnetisation of any soft magnetic material is limited in application due to it being very brittle. The development of composite carbon nano-particulate filled alloys has achieved little or no overall benefit due to difficulties with agglomeration in the mixing process.

In this research, improvement in mechanical and magnetic properties has been achieved in FeCo alloy composite with a very low fraction carbon nanotube (CNT) reinforcement prepared only by low energy ball milling, with notable improvement as compared to composites prepared previously by pre-mixing in dimethylformamide, followed by low energy ball milling.

Significant improvement in hardness and magnetic properties have been obtained in FeCo alloy by reinforcement with a small addition of graphene nanoplatelet (GNP) alone and prepared by low energy ball milling. However, significant overlapping between the nanoplatelets deteriorated the strength and elongation. Inserting CNT among nanoplatelets was found to reduce the overlapping and enabled refinement of the microstructure, however, at the expense of some increase in porosity in the spark plasma sintered materials.

The spark plasma sintering conditions have been optimised at relatively low sintering pressure by use of high temperature and controlling the heating rate and dwelling time to enable near-full densification in base FeCo alloy. By careful selection of sintering parameters, it was found to be possible to increase yield strength, elongation and suppress the intergranular fracture in FeCo alloy, combined with good magnetic properties. This optimised SPS process was developed following the above-described solvent dispersion studies and applied subsequently to following alloy-composite developments.

The ultimate strength, yield strength and elongation were significantly improved by embedding GNP in flaked FeCo powder, which enabled uniform dispersion up to 6 vol. % in contrast to very poor dispersion in spherical powder.

The increased coercivity from dispersion in flaked FeCo powder was reduced by quenching the composites from the disordered region, which led to further improvement in elongation. However, the highest tensile strength of the heat treated samples was obtained after quenching from the ordered region.

Interface bonding was improved in CNT- and GNP- filled FeCo alloy composites by high energy ball milling, which increased the properties of the composites. However, significant damage to the structure was imparted by ball milling of carbonaceous nanomaterial when the time of ball milling was extended. By nature of their two-dimensional form, dispersion of GNPs was found to be far more challenging in FeCo alloy compared with the CNTs. However, the mechanical properties of the GNP composite exceeded those of their counterpart CNT composite even at a lower volume fraction.

Chapter 1: General introduction

FeCo alloys have a unique combination of high saturation magnetisation, high Curie temperature and good strength. There is emerging need for using FeCo alloy in a stringent operation conditions, the applications in modern power generation system, magnetic bearing in transporting system, actuator and energy storage system like flywheel applications are required not only good magnetic properties but also high mechanical properties, such as high yield strength and good thermal stability up to 600 ºC [1]. The equiatomic FeCo alloy at a temperature lower than 720 ºC is thermodynamically stable in long-range ordered structure, which causes extreme brittleness in the alloy. Most efforts are made to improve the mechanical properties of FeCo alloys rely on alloying with a ternary element, heat treatment and deformation [2].

The gap in the knowledge from the literature review is identified as there are very limited to no attempts were used composite strategy to improve the properties of FeCo alloy by nanomaterials. This method offers unique advantages over the aforementioned methods such as improvement in creep resistance, less deteriorate in magnetic properties. Recently, FeCo alloy was reinforced by micrometre reinforcement silicon carbide particles SiCp and whisker SiCw, and nanometre reinforcement carbon nanotube CNT. The improvement in bending strength was not significant and limited to 1 vol. % CNT due to poor dispersion [3]. Therefore, the current work takes the challenge on using carbonaceous nano-reinforcement to improve the properties of FeCo alloy through different strategies, to achieve a better dispersion for reinforcement, and the best combination of mechanical and magnetic properties.

Spark plasma sintering (SPS) is relatively new sintering technique with advantages of fast densification combined with insignificant grain growth and short time for sintering. This process is used to synthesise high-performance materials which are extremely difficult to obtain by conventional route like hipping sintering process [4]. During the SPS process, a uniaxial pressure is used, along with a pulsed high DC current (>1000 A) at a relatively low voltage (~ 10 V) through graphite die to consolidate the powdered materials. A heating rate as high as 1000 ºC/min can be achieved in SPS. This process enables clean grain boundaries with reduced impurity segregation at grain boundaries, improved bonding quality and magnetic properties [5, 6]. The SPS process which is used for sintering ceramic, metal, and composite, shows advantages in sintering nanocomposite and

nanostructure over conventional sintering methods due to its ability to preserve nanostructure features and to obtain fully dense material [6, 7].

The aim of the research was to improve the mechanical properties of FeCo alloy with less deterioration in magnetic properties by spark plasma sintering parameters, and through reinforcing FeCo alloy by different carbonaceous nanomaterials. The interfacial bonding can improve by coating reinforcement [8], high energy ball milling [9] and short sintering time like spark plasma sintering, which reduces the thickness of interface layer [10]. Away from the coating, these approaches were used. The methods and materials prepared in this study are summarised below:

- Spark plasma sintering conditions of equiatomic FeCo alloy were optimised at low sintering pressure of 50 MPa, to avoid frequent breakage of the graphite die during high sintering pressure of 80 MPa. Near fully densification with improved mechanical and magnetic properties was achieved at sintering pressure of 50 MPa.
- Using solvent for mixing CNTs with ceramic or polymer matrix enables homogenous dispersion. Therefore, the influence of per-mixing of CNTs with FeCo alloy powder in dimethylformamide on dispersion was tested. The improvement in properties was very limited due to poor dispersion
- A mixture of CNT in ethanol was used to disperse GNPs in FeCo alloy with aim of reducing the overlapping between GNPs. Despite the reduction in GNPs overlapping and refining the structure, the porosities were included from inserting CNTs, which decreased the properties of FeCo alloy composites.
- The influence of the FeCo alloy powder morphology on dispersion GNP was studied. The homogeneous dispersion of GNP in flaked powder improves the mechanical properties significantly as a compared to spherical powder.
- Heat treatment was done on 4 vol. % GNPs composite of flaked powder, the disordered structure showed an improvement in elongation and a reduction in coercivity.
- High energy ball milling was used to dispersion 1.5 vol. % CNT in FeCo alloy over different periods, to optimise the best time for improved interface bonding with less damage to CNT. The best combination between mechanical and magnetic properties can be obtained with a short ball milling time of 1 h.
- High energy ball milling was also used to dispersion 1 vol. % GNPs in FeCo alloy with the same aim to CNT-composites, the best mechanical properties were achieved after 4 h.

Chapter 2: Literature review

2.1. Introduction

New electric driven systems are required for modern aircraft that are used in both civil and military applications. Many advantages are offered from pushing electric systems in More Electric Aircraft (MEA) over traditional hydraulic, pneumatic, and mechanical driven systems. This includes substantial benefits in maintainability, reliability, environment, performance, survivability, and cost [11-13]. In the transport industry, a reduction in weight is a priority and, therefore, materials with high power density are needed. FeCo alloys with high saturation induction can meet this requirement. MEA requires the use of soft magnetic material in stringent operation conditions because these materials are exposed to high temperatures and stresses in the operating environment. Although the high Curie temperature of FeCo alloy retains good magnetic properties at high temperature [1], the mechanical properties of equiatomic FeCo alloy means that it is unfit due to extreme brittleness from favourable ordered structure B2 at room temperature. With the emergence of MEA applications, efforts are now being made to improve the mechanical rather than the magnetic properties of FeCo alloy to meet the requirements of these harsh applications [14]. However, unsurprisingly, the study of equiatomic binary FeCo alloy is discontinued in the literature, with focus given instead to the ternary FeCo-V alloy because its properties are easier to manipulate. Recently, an alternative to the ternary alloy, FeCo alloy composite materials have been developed to improve the mechanical properties with less deterioration of the magnetic properties, as well as providing more stable mechanical properties at high temperatures.

2.2. Binary FeCo alloy

2.2.1. Phase equilibrium diagram of FeCo alloy

The phase equilibrium diagram of FeCo alloy is shown in Figure 2.1 a. Near equiatomic FeCo alloys are favourable for ordered B2 structure (α') or (α_2) phase at room temperature at cobalt content variation of 29-70 at.-% Co. The ordered structure is described as two interpenetrated simple cubic sub-lattices, in which one of sub-lattice is occupied by an Fe atom and the other is occupied by a Co atom, as seen in Figure 2.1 b. The B2 structure is disordering to b.c.c. (α) phase at a temperature above ~ 730 ºC, which transfers to f.c.c. (γ) phase at a temperature above ~ 983 ºC. The Curie temperature corresponds to

transformation from (α) to (γ) in FeCo alloy, giving a maximum value of Curie temperature of 985 ºC in the alloy with 46 at.-% Co [1].

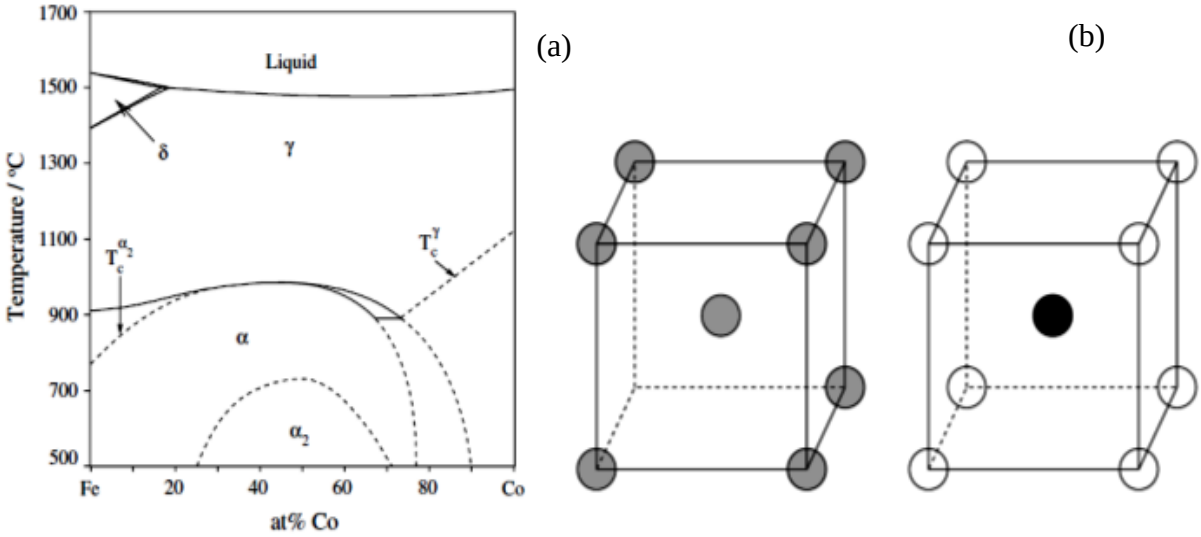

Figure 2.1. (a) The binary diagram of Fe-Co alloy exhibiting ordered bcc (α2), disordered bcc(α), and fcc(γ) phases and Curie temperature (Tc)[15], (b) b.c.c and ordered B2 structure [2].

2.2.2. Mechanical properties

2.2.2.1. General introduction

The discontinuity in yielding in (Figure 2.2) is observed in a carbon-iron alloy, and also in the ordered intermetallic alloys, which is formed due to: pinning dislocation motion; the density of mobile dislocation is low; and the stress has a slight effect on dislocation velocity [17, 18]. The lower yield point is more reliable for purpose of strength comparison than the upper yield point because it follows the Hall-Petch equation, which is related the change in yield strength to grain size, and due to affect the sample geometry, alignment, and strain rate on the upper yield strength value [19].

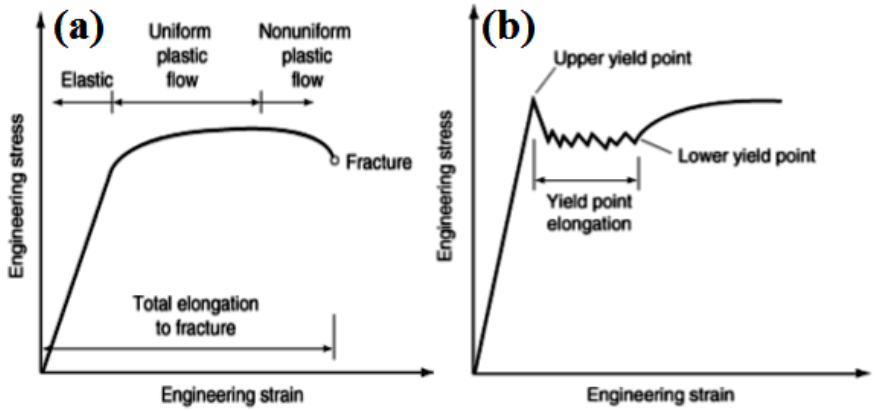

Figure 2.2. (a) Typical engineering stress-strain curve, (b) abrupt in yielding curve [16].

2.2.2.2. Mechanical properties of equiatomic FeCo alloy

Equiatomic FeCo alloys are extremely brittle due to their thermodynamical stabilisation in the ordered structure B2 at room temperature [1]. Therefore, almost all of the available data that is used to study the deformation behaviour of equiatomic FeCo alloys is obtained from compression tests. There have been very few studies on tensile deformation of the binary FeCo alloy which exhibit that the yield strength and the elongation of alloy depend on the cobalt content. Both the yield strength and elongation of equiatomic FeCo alloys are increased in ordered structure of Co-rich alloys. However, the ductility of the ordered equiatomic FeCo alloy and Fe rich alloy is virtually zero and these alloys fail before achieving yield strength, showing only fracture strength, as shown in Figure 2.3 [20].

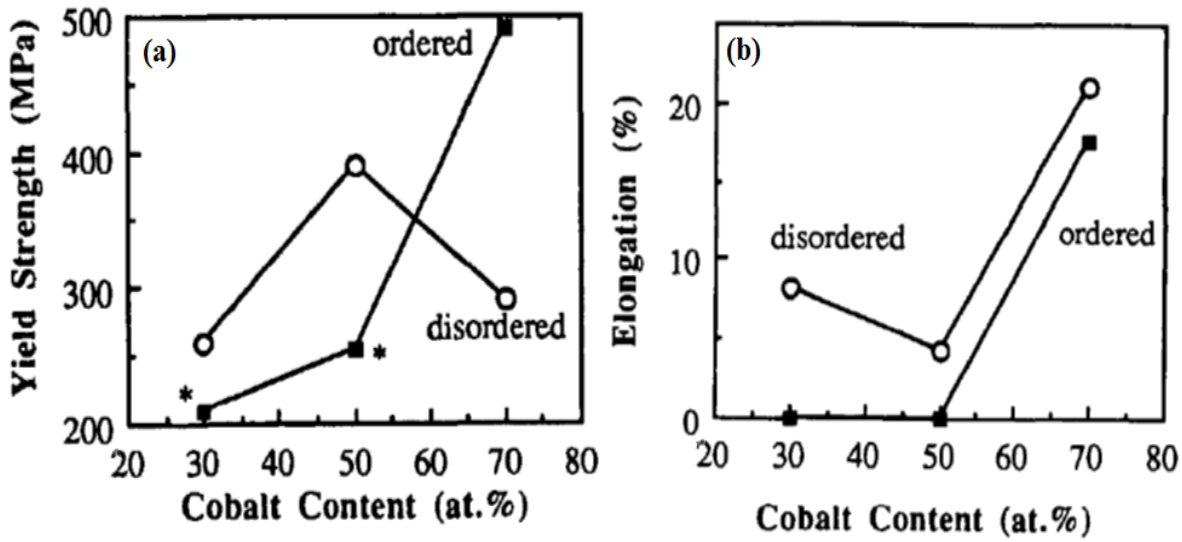

Figure 2.3. Effect of cobalt content on (a) yield strength and (b) elongation, * Indicate to facture strength [20].

The dislocation mobility in the ordered structure is very difficult because the dominant deformation mechanism is the planar slip while all of the disordered FeCo alloys exhibit wavy slip, as seen in Figure 2.4. The consequence of this is the extreme brittleness in the ordered FeCo alloys, while the disordered structure shows more ductility in binary FeCo alloy [21]. Therefore, it is suggested that even partial disordering at grain boundaries improves the ductility of FeCo alloy through allowing wavy slip in these regions [22].

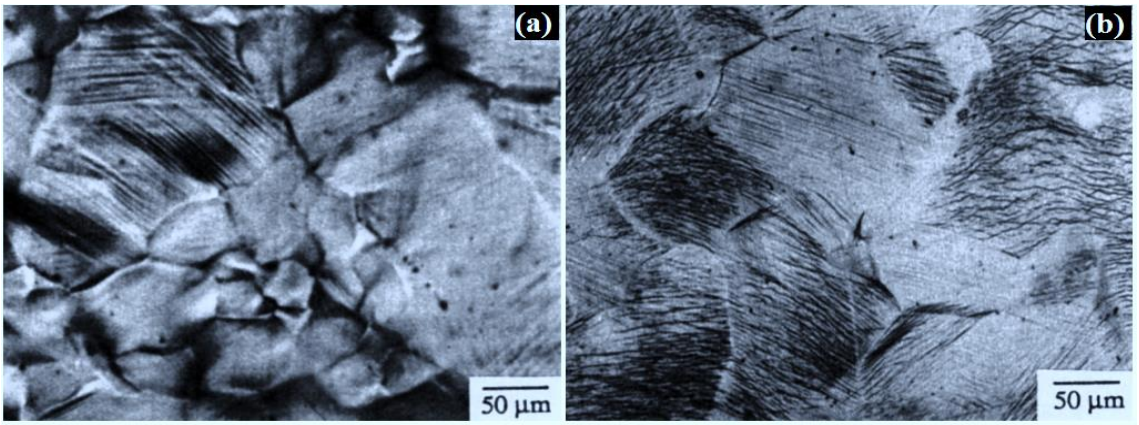

Figure 2.4. (a) Planar slip in ordered state of the binary FeCo alloy; (b) wavy slip in disordered state [21].

Brittle fracture mode is observed in both ordered structure with zero elongation and disordered structure with only 4 % elongation in equiatomic FeCo alloy, showing almost an intergranular fracture that combines with a small amount of transgranular cleavage, as seen in Figure 2.5. Deviation from the equiatomic composition by increasing cobalt content improves the ductility in FeCo alloy; therefore, both the ordered and disordered state fail by ductile fracture with dimples on fracture surface [20].

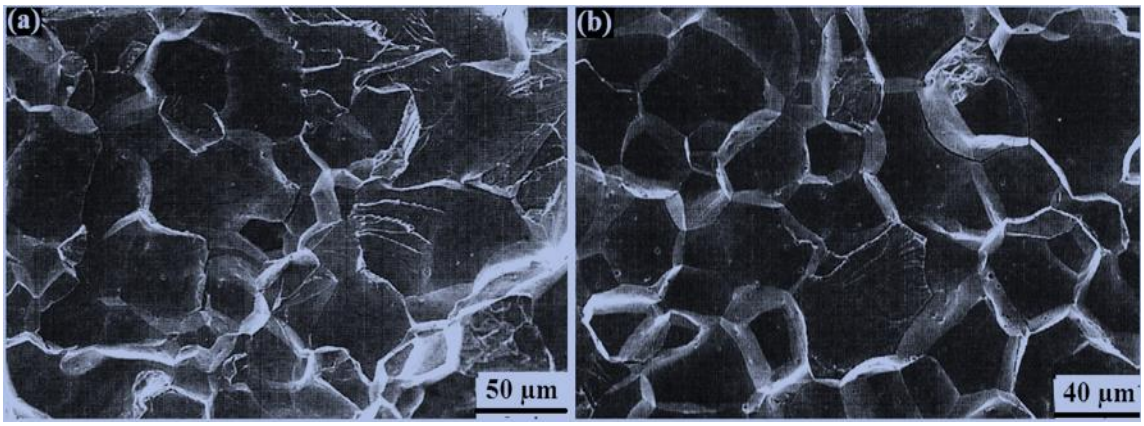

Figure 2.5. SEM of fracture surface of equiatomic FeCo alloy: (a) ordered structure, (b) disordered structure [20].

2.3. Adopted procedures to improve the mechanical properties of FeCo alloy

2.3.1. Addition vanadium to FeCo alloy

Despite the innovation of high induction combined with higher permeability in equiatomic FeCo alloys and lower coercivity than the Fe rich alloy by Elmen in 1929, the extreme brittleness of the equiatomic alloys and their high cost prevent their industrial applications

[2]. In 1932, White and Wahl [23] found that the addition of vanadium to equiatomic FeCo alloy relieved the poor ductility and enabled hot rolling in the disordered state by up to 90 %. Similar to other alloying elements, adding vanadium to FeCo alloy deteriorates its magnetic properties [24-26]. The saturation magnetisation of FeCo alloy was decreased about 4 % when about 2 % vanadium was added and, therefore, to retain good softness the added vanadium must be below 3 wt.-%. However, the resistivity, which is important to reduce the losses in FeCo alloy, was significantly increased from 1.95 to 46.4 μΩ.cm [24, 27]. It is suggested that the addition of vanadium to FeCo alloy may slow ordering, which leads to improvement in ductility [28]. Stoloff and Davies [29] studied the influence of an ordered structure on the yield strength and ductility of FeCo-2 % V alloy, the samples were quenched from a high temperature within the range of 500–900 ºC. A peak in yield strength is observed at a critical degree of order (*S=0.2*), at a temperature of T_p (~710 ºC), which is just below the critical transformation temperature of the order-disorder structure, as shown in Figure 2.6. This peak was shifted to the disordered region when the vanadium content increased to 3 wt.-% because of increased precipitation [30]. Thornburg [31] studied the annealing effect of cold worked FeCo-2%V alloy within the range of 640-760 ºC on the final properties, discontinuous variation in strength and coercivity with annealing temperature, and the peak value for ductility was achieved in the partially recrystallised structure. Hailer's [32] study of FeCo-2V-0.3Nb supports the same behaviour and the mechanism behind it. Sourmail [33] criticised both cases and attributed the discontinuity in the strength and coercivity property versus annealing temperature to the sharp grain growth rate around the critical temperature *Tc*≈ 720 ºC. However, a partially recrystallised structure with the lowest degree of ordering was recently suggested for a better combination between mechanical and magnetic properties in FeCo-2V alloy [34].

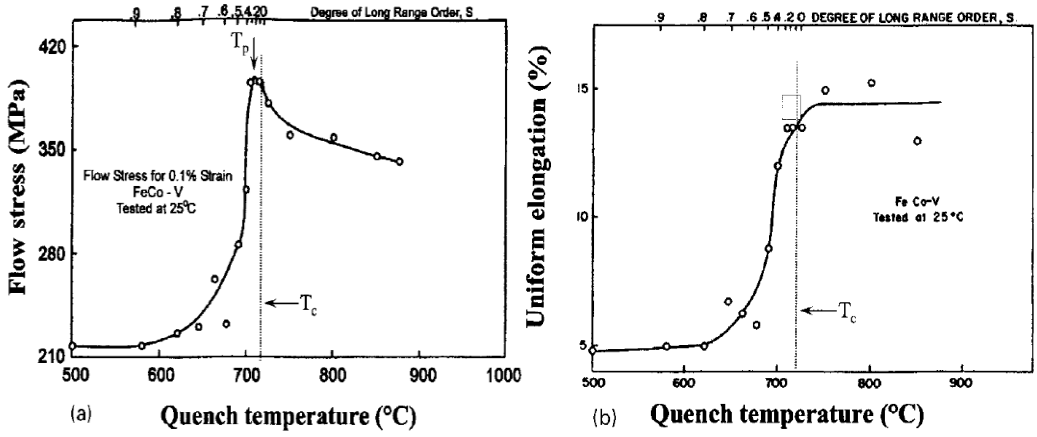

Figure 2.6. Variation of (a) flow stress and (b) elongation with quenching temperature

Glezer et al. [35] studied the grain boundary chemistry of FeCo and FeCo-2%V. They suggested that the ductility of ordered FeCo-2%V was improved because of partial disordering at the grain boundaries by segregated impurity. Because of the need to use FeCo alloy at a temperature greater than 500 ºC, the oxidation behaviour of FeCo-2V alloy was studied by [36]. Two layers were formed during oxidation, the outer layer involved $(Fe, Co)_3O_4$ and Fe_2O_3, while the inner layer consisted of cobalt oxides.

2.3.2. The effect of other alloying elements beyond vanadium

Although the improvement in the mechanical properties of FeCo-V alloys is significant in disordered structures, there are very few studies that have reported advances in the ductility of an ordered structure in FeCo alloy. This structure showed ductile behaviour after alloying with specific elements such as W, Nb, Ta, M_o, C and Ni and intensive cold working [25, 37]. The precipitates that are formed caused deviation in the chemical composition of the matrix, producing local concentration disorder regions (LCD) around precipitates, which were refined and uniformly distributed after intensive cold working, leading to a ductile ordered structure [38]. High plastic deformation has a considerable potential to deteriorate the magnetic properties if there is no subsequent annealing treatment. George et al. [39] compared boron and carbon addition to FeCo-V and FeCo alloys. They found that the ductility was significantly enhanced in the ordered structure of the ternary alloy, in the range of 2.1-2.5 wt.-% vanadium, because of the refining slip by fine boride or carbide precipitates. Unfortunately, neither boron nor carbon have improved ductility or suppressed grain boundary fracture of equiatomic FeCo. An intergranular fracture before yield strength was observed in equiatomic FeCo alloy doped with boron or carbon. Whether or not the fine precipitates formed by carbon or boron have a significant influence on the magnetic properties is still not established.

2.3.3. The effect of grain size on mechanical properties

The mechanical properties of equiatomic FeCo alloys are highly correlated with the grain size, following the Hall-Petch relationship in both the ordered and the disordered state [40]:

$$\sigma_y = \sigma_i + k_y d^{-1/2} \qquad (2\text{-}1)$$

where σ_y is the yield strength σ_i and k_y are the intrinsic lattice resistance and Hall-Petch parameters, respectively and d is the grain size.

Sunder [41] reported that the stress concentration at grain boundaries due to planar slip of dislocations in ordered state can be reduced by refining grain size, which improves ductility in the ordered state. The ductility of FeCo alloy is inversely varied with the square root of the grain or subgrain size [42]. However, attention must be paid to select the most suitable temperature of heat treatment because the kinetic of grain growth at an annealing temperature higher than the critical temperature of ordering is reasonably faster than at an annealing temperature below the critical temperature of ordering, see Table 2.1 [43].

Table 2.1 Effect of annealing temperature for 1 h on the rate of grain growth FeCo-2V alloy.

Annealing temperature (°C)	**675**	**688**	**700**	**711**	**725**	**750**	**Extrapolate to 775**
Grain size (μm)	0.6	0.8	1.4	3.0	7.9	12.0	17.1

2.4. Magnetic properties

2.4.1. General introduction

The basic magnetic properties of materials are explained on the hysteresis curve in Figure 2.7. Broadly, magnetic materials can be categorised into two main groups depending on how easy they are to magnetise, they can be either soft magnetic or hard magnetic. Soft magnetic materials can be magnetised easily by a relatively low magnetic field, and they retain relatively low remanence after the applied field is removed.

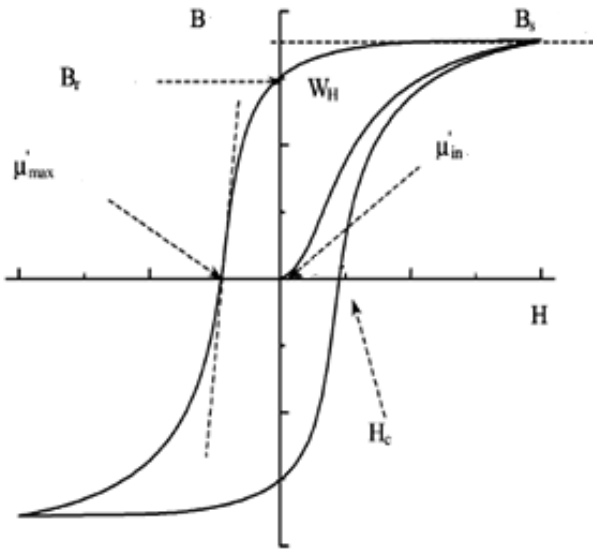

Figure 2.7. Magnetic properties of materials as defined on the flux density B versus magnetic field H. Coercivity H_c, remanence B_R, hysteresis loss WH, initial permeability μ_{in}, maximum differential permeability and saturation flux density [44].

In general, soft magnetic materials are characterised by a high initial permeability of 1.1-1,000,000 and low coercivity of 0.16-1000 A.m^{-1} [44]. Soft magnetic materials are broadly classified into metallic alloys, intermetallics and ceramics, as seen in Figure 2.8 [1, 45]. Soft magnetic materials are needed in different applications, such as power generation and distribution, actuator, magnetic shielding, data storage, and microwave communication. Iron-(30-50) cobalt alloys exhibit the highest saturation magnetisation among the soft magnetic material for value (2.45 T) combined with high Curie temperature (920-985 ºC), making them an attractive material for high temperature and light weight, power dense applications. The magnetic properties and the current applications of equiatomic FeCo alloy are summarised in Tables 2.2 and 2.3, respectively [1].

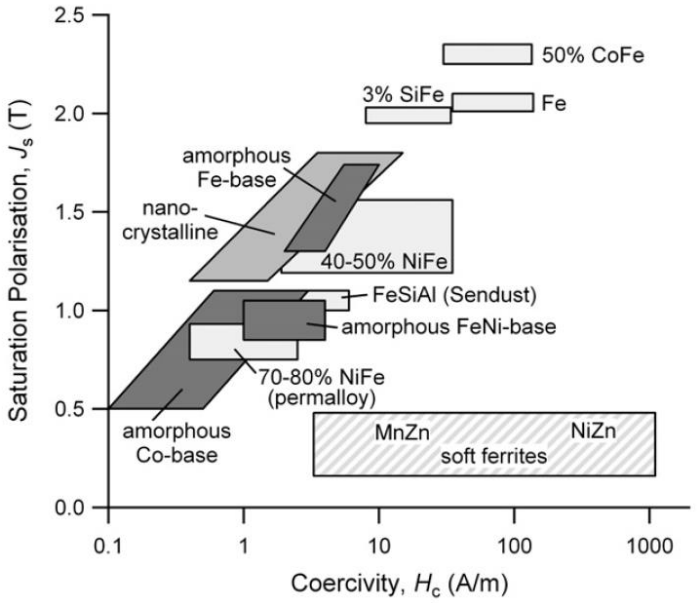

Figure 2.8. Comparison of the saturation magnetic polarisations (=$\mu_\circ$ MS) and coercivities of different soft magnetic materials [45].

Table 2.2 Magnetic properties of equiatomic FeCo alloy [1].

Magnetic properties	**Value**
Saturation magnetisation (T)	2.4
Coercivity (A m^{-1})	150
Curie temperature (ºC)	980
Initial permeability	800
Maximum permeability	5000-8000
Saturation magnetostriction (ordered condition)	
$\lambda_{100}=150\times10^{-6}$, $\lambda_{111}=25\times10^{-6}$, $\lambda_{polycrystal}=60\times10^{-6}$	
Magnetocrystalline anisotropy constant (J m^{-3})	0

Table 2.3 The current applications of equiatomic FeCo alloy [1].

High performance transformers, Pole tips for high field magnets
Magnetically driven actuators in impact printers, Diaphragm in telephone handsets
Solenoid valves, Magnetostrictive transducers
Flux guiding parts in inductive speed counters, Electromagnetically controlled nozzles
Internal starter/generator in aircraft

2.4.2. Saturation magnetisation

The saturation magnetisation, in general, is insensitive to the microstructure and strongly relies on the chemical composition [27]. Pure iron, which is one of the best known soft magnetic materials, cannot be used directly in industry because of its high softness and low resistivity. Efforts to improve the strength and resistivity of iron were made through alloying. Although saturation magnetisation is only increased when the iron is alloyed with cobalt, the high cost of cobalt and the extreme brittleness of the binary FeCo alloy are limiting factors. Adding vanadium or other alloying elements to improve the strength of FeCo alloy has a detrimental effect on the saturation induction of the alloy, which is also found to be affected by the degree of ordering [27, 46]. Variation of saturation moment of FeCo alloy with the degree of order is shown in Figure 2.9 a [28]. Hug et al. studied the effect of tensile strengthening (ε=1.5-3.5 % strain) on the magnetisation of the ordered FeCo-2V alloy, see Figure 2.9 b [47]. Plastic deformation decreases magnetisation, especially along the rolling direction. The same has also been observed in the soft magnetic Fe-Si alloy in non-oriented grain. This behaviour links in Fe-Si alloy to the modification in the magnetoelastic energy during deformation [48]. Nevertheless, the higher saturation magnetostriction of FeCo-V alloys ($\lambda_s \approx 60\times10^{-6}$) as compared to Fe-Si alloy makes FeCo-V alloys more sensitive to mechanical strengthening.

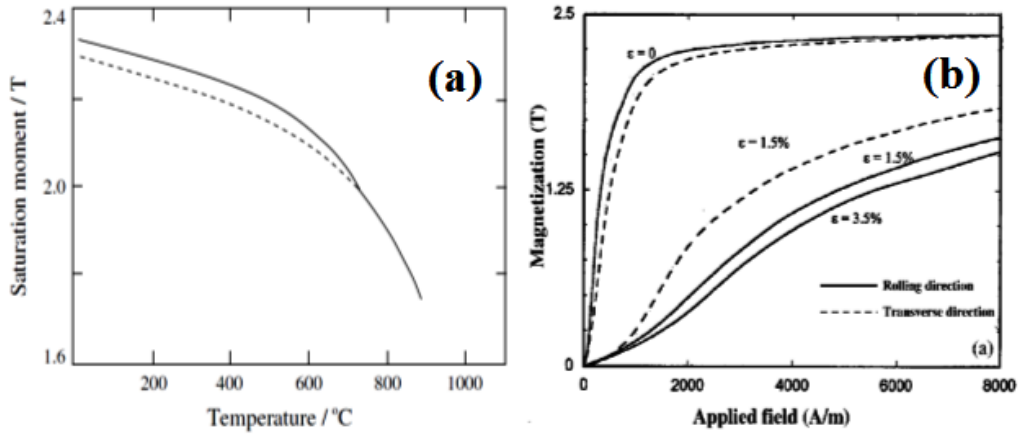

Figure 2.9 (a) Change of saturation moment with temperature, the disordered alloys below the critical temperature represents by broken line [28]; (b) effect of strain on magnetisation [47].

Fingers and Kozlowski [49] reported a variation in saturation induction as the grain size changed for the FeCo-2V-0.3Nb alloy at different annealing conditions (as shown in Table 2.4); however, this change may be related to experience error (5%).

Table 2.4 Saturation magnetisation of FeCo-2V-0.3Nb at different annealing temperatures.

Temperature (°C)	Time (h)	Grain size (μm)	Saturation induction (T)
704	1	1.13	2.37
720	1	1.68	2.40
720	2	2.80	2.43
732	1	2.33	2.40

2.4.3. Coercivity

Coercivity (H_c) is defined as the strength of the applied reverse magnetic field that causes a reduction in magnetic induction to zero. Coercivity is microstructure sensitive and, therefore, it is affected by heat treatment or deformation [50, 51].

The effect of grain size on coercivity is shown in Figure 2.10. Herzer [52] suggested that in large grains (larger than 150 nm) the domains can form within the grains because it follows the easy magnetic direction. Thus, the magnetisation process is governed by the magneto-crystalline anisotropy K_1 of the crystallites, here the coercivity and grain size (D) are inversely proportion, see Table 2.5. However, for very small grains (up to 50 nm) the alignment parallel to easy direction is impeded because there is higher ferromagnetic exchange interaction and more magnetic moments forces are needed for alignment. Therefore, the effective anisotropy is averaged over several grains in reduced

magnitude and coercivity follows the power-law D^6 (Table 2.5). However, in a recent study, neither D^6 nor 1/D dependence is observed to correlate the coercivity with grain size in FeCo nano-particles produced by ball-milling [53]. Lee et al. [54] used mechanical alloying (MA) and mechanochemical alloying (MCA) to produce nanocrystalline structure FeCo alloy. MA led to a disordered structure, while ordered state and less strained structure were produced in MCA and this improved the magnetic properties [55].

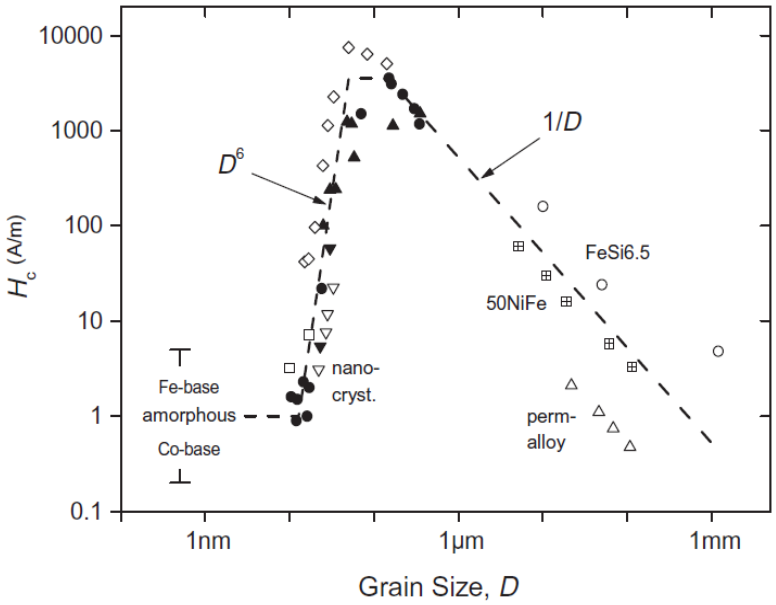

Figure 2.10. Coercivity Hc versus grain size D for different soft magnetic alloys [45].

The residual stresses cause magnetostriction effective anisotropies, which are related to H_C by Equation 3 in Table 2.5. Magnetic inclusions are generally separated regions with magnetic properties that are different to the matrix material, which could be: voids, cracks, insoluble second phase materials and oxide or carbide [50]. The relationship between the volume fractions of inclusions with coercivity is given by Equation 4 in Table 2.6. However, to apply this equation, the wall thickness must not be greater than the size of the particle. Dijkstra et al. [56] reported that the volume fraction and state of dispersion of the inclusion have an effect on the coercivity. The maximum effect occurs when the diameter of the inclusion is in the order of the thickness of the domain wall (in FeCo ~ 260 nm) [57].

Table 2.5 The effect of different parameters and their functions on coercivity.

Parameter	Coercivity function	
1-Micrometre grain size	$H_c \approx 3\sqrt{\frac{k_B T_c K_1}{a M_s}}\frac{1}{D}$	[57]
2-Nanometre grain size	$H_C = \frac{P_c K_1^4 D^6}{\mu_0 M_s A^3}$	[51]
3-Stress effect	$H_c \approx -\frac{3}{2}\pi\frac{\lambda_S \Delta\sigma}{\mu_0 M_s}\frac{\delta_W}{l}$	[53]
4-Inclusion (Kersten model)	$H_c = 2.4\frac{\delta_W K_1}{M_s \mu_0 \bar{r}} V_f^{2/3}$	[57]

where A is the exchange stiffness constant, Pc is ≈ 1, δ_W is wall thickness, μ_0 the permeability of vacuum, $\bar{r}$ the average radius of particles, V_f volume fraction of particles. δ_W is the wall thickness, l is the stress wavelength, $\Delta\sigma$ is the internal stress, D the grain size, M_s the magnetisation saturation, K_1 the magnetocrystalline anisotropy, T_c the curie temperature and a lattice constant.

2.5. X-ray diffraction of FeCo alloy

Heat treatment and ball milling processes have both been used to change the degree of ordering in FeCo alloys [58]. Detecting superlattice lines is very difficult by X-ray due to the very small difference between the atomic factors of Fe and Co in *Cu Kα* radiation. However, the intensity ratio (R) of superlattice lines to fundamental lines was found to be stronger in *Co Kα* radiation, which opens the possibility for observing superlattice peaks within ($30^o < 2\theta < 130^o$) [59]. The induced strains during ball milling for powder can be classified into uniform strain and non-uniform strain. The former causes shifting in peaks of X-ray reflection to lower angles, while the latter leads to a broadening and reduction of the intensity. Moreover, nanostructures can be formed during the ball milling processes, which has an influence on the material's properties. Apart from the use of TEM imagining to determine the crystallite size, the Scherrer method that relies on X-ray profile analysis is still the dominant averaged method to measure the size of crystallites less than about 0.1 μm [60]. The Scherrer equation for measuring crystallite size in nanometers is:

$$t = \frac{0.9\,\lambda}{B\cos\theta}$$

Where: t is crystallite size B is the broadening in radians and λ is the wavelength of *Co Kα* radiation (1.78896 Å).

2.6. Powder metallurgy and sintering

2.6.1. Introduction to powder metallurgy

Powder metallurgy (PM) is defined as processes which mix the individual powdered components to the desired form. The blended powders are then charged to the appropriate die for pressing, and then sintered at suitable pressures and temperatures [61]. Mechanical alloying (MA) is a complementary PM process, which is frequently used to obtain uniform dispersion of nanosized particles in metal powder. The metal powder's size and shape differs depending on the processes that are used to prepare the powder, including: one dimensional (acicular, irregular rod like), two dimensional (dendrite, flake), and three dimensional (spherical, rounded, irregular, porous, angular) [62]. PM offers a number of advantages over other fabrication processes including: absence melting during processes; precise control of dimensional tolerance with excellent surface finishing; an exceptional combination of two materials with different features; mass production of components; control on operation atmosphere enables to reduce oxidation during processes; environmental friendly process can save time and energy; useful in manufacturing huge and complex shaped components; homogeneity and high strength; and, toughness and ductility can be achieved in PM parts. Adopting a PM route enables bulk geometries to be obtained from brittle raw materials; therefore, it is the most suitable process to develop inherent brittle equiatomic FeCo alloys. Spark plasma sintering (SPS) enables sintering materials with minimum defects, which will be described in the next subsection.

2.6.2. Spark plasma sintering (SPS)

SPS is a relatively new sintering technique that uses a pulsed direct current to heat the graphite pressure die, allowing very quick heating and cooling rates, short soaking time, and high pressures to attain completely dense samples. The SPS technique has been successfully used to sinter nanocomposites with fully dense and conserved nanostructure features [6, 7]. Nanostructure intermetallic, ceramic, metal, and composite materials have been successfully fabricated by high energy ball milling with the aid of SPS, which allows less grain growth and maintains nanostructures [63–66].

SPS differs from other sintering routes because of the heating rate, applied pressure and pulsed current. One of the significant differences that characterises SPS over conventional sintering process is the high heating rate of 1000 $^{o}C.min^{-1}$. Most investigations using the SPS route have reported high-density concomitant with sintered

materials with a smaller grain size, which are likely to be related to the superior properties of sintered materials created by the SPS method [6]. Not only have a clean grain boundary and improved microstructure been achieved but also magnetic materials with high oxidation and corrosion resistance have been produced in SPS [67-69]. Furthermore, SPS is a binder-free process that does not need a pre-compact process because the powder is directly filled into a graphite die, through which the pressure is applied and the current is passed, leading to a completely dense material with superior mechanical properties [7, 70]. Typically, a graphite die and punches are used in SPS processes (Figure 2.11a), allowing the DC current to pass through them and sample (if the sample is conducting) to be used as a source of Joule heating during consolidation: the flow of the electric current is shown in Figure 2.11b.

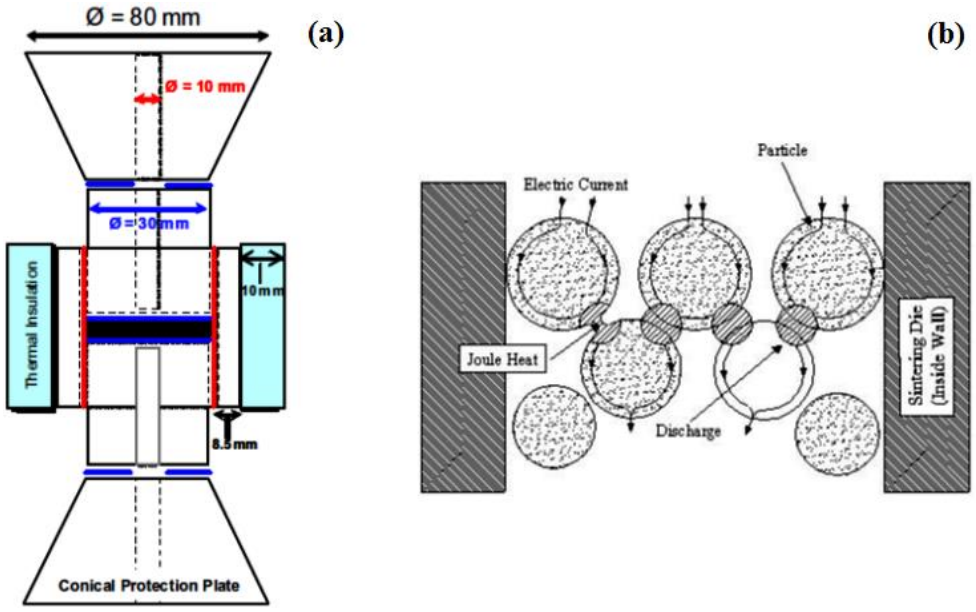

Figure 2.11. (a) Scheme of the parts and dimensions of SPS die and punch assembly [64], (b) the DC pulse flow through powder particles [71].

The graphite assembly of the die and punch limits the applied pressure during sintering processes to values lower than 100 MPa. A connection of the spark plasma furnace to a chamber of vacuum or inert atmosphere allows sintering in a lower oxidation atmosphere. To measure the heat generated by ON-OFF DC pulse current, a thermocouple is inserted through a die-hole for a distance about 1-2 mm away from the powdered sample to measure the temperature during sintering. The basic sequences of stages during powder sintering are: particle rearrangement, activation and powder refining, formation and growth of the sintering neck, and finally localised plastic deformation and densification [72, 73]. The exact mechanism during SPS processes is still debated and unclear [6]. During SPS processes, the highest temperature may be achieved in the contact area between particles,

which exceeds the melting temperature of the material. Therefore, the local melting that occurred improves the inter-particles bonding [74]. To avoid further grain growth, the sintering temperature needs to be selected in the range to obtain almost full densification with less grain growth [75] because the grain growth rate is faster than densification at high sintering temperature [76]. Shen et al. [75] reported that above certain critical temperatures during SPS, the grain growth can also occur very fast with essentially thermal activated mechanisms. Therefore, to achieve fully densified compact material with less grain growth, the sintering temperature must not be too high and the sintering time must be short.

2.6.3. Soft magnetic sintered by SPS

SPS has been employed extensively over the past decade with the aim to improve mechanical and magnetic properties of materials. Cha et al. [71] improved the strength of soft magnetic composite (SMC) by using SPS process, an increase in fracture strength around 1.3 to 1.7 times with reduction in magnetic loss from 192 W/kg to 21 W/kg were achieved in iron base composite prepared by SPS in comparison to conventional method. Zhang et al. [55] used SPS to consolidate bulk nanocrystalline of FeC alloy prepared by mechanical milling. A high compression yield strength of 1900 MPa and fracture strength 3500 MPa combine with 40 % plastic strain were obtained. FeCo alloy nano powder has also been produced by ball milling [77, 78]. However, deterioration in magnetic properties can happen after ball milling due to oxidation, contamination, and strains in the structure. Therefore, a pre-annealing process for powder was used to obtain full densification in conventional sintering method [79–82]. While it is found that using SPS in sintering is most effective for removing oxide and to improve the material's properties. Full densification is crucial to achieving the full potential in nanostructure soft magnetic alloy, which can be achieved by SPS [53, 83]. Mani et al. [84] examined the influence of Spark plasma parameters on near equiatomic FeCo alloy. Different parameters (700-950 ºC, 40-100 MPa, 2-10 min) were tested to specify the optimum sintering conditions. It was found that the best parameters for sintering were 900 ºC, 80 MPa and 2-5min because maximum density and optimum magnetic properties were achieved at these conditions.

2.7. Composite material

2.7.1. Introduction

A composite material is a material that is produced from the mixing of two or more constituent materials that differ in their physical or chemical properties. The properties of the composite are superior over the matrix alone. The role of the matrix material is not only to hold the reinforcement within a composite but also to transfer the load to the reinforcement, which can be classified as metal, ceramic, or polymer matrix. In general, the reinforcement phase can be classified as particles, fibres, or laminates [85]. The type and size of the reinforcement have an influence on the properties. A significant improve in tensile strength can be achieved by reducing the size of the reinforcement [86, 87]. Typically, carbonaceous reinforcements have advantages over other ceramic reinforcements, such as low coefficient of thermal expansion, high damping capacity, good self-lubricant and dimensional stability [88-90].

2.7.2. Metal matrix composite

A metal alloy is frequently used as a matrix material in this type of composite rather than metal alone. This composite is widely used to obtain superior properties, such high creep resistance with weight saving for aerospace applications [91]. The nanosized carbon-based fillers are introduced into a metallic matrix to improve the very wide properties [92] and is normally followed by secondary processes such as hot extrusion, rolling and forging to improve dispersion, density, alignment of reinforcement in composites, and the interface bonding [85, 93-95].

2.7.3. Carbonaceous reinforcement

2.7.3.1. Carbon nanotube

Since the discovery of carbon nanotubes (CNT) by Iijima in 1991 [96], a vast range of research has been performed to evaluate and explore advanced applications for CNT. The types and dimensions of CNT are seen in Figure 2.12. The structures of CNT can be classified depending on chiral vector into zigzag, armchair, and chiral, the structure and bonding types of CNT are shown in Figure 2.13 [99]. The armchair structure exhibits metallic behaviour, while the zigzag structure is a semiconductor and the chiral carbon nanotube is characterised by electrical properties. Carbon nanotubes are very interesting material and they can be used in many different applications, such as reinforcement for metal, ceramic, polymer matrix composite [101-103], an effective hydrogen storage

material [104], field emission source [105], chemical sensors [106], scanning probe microscopy tips [107] and they also have applications in drug delivery [108].

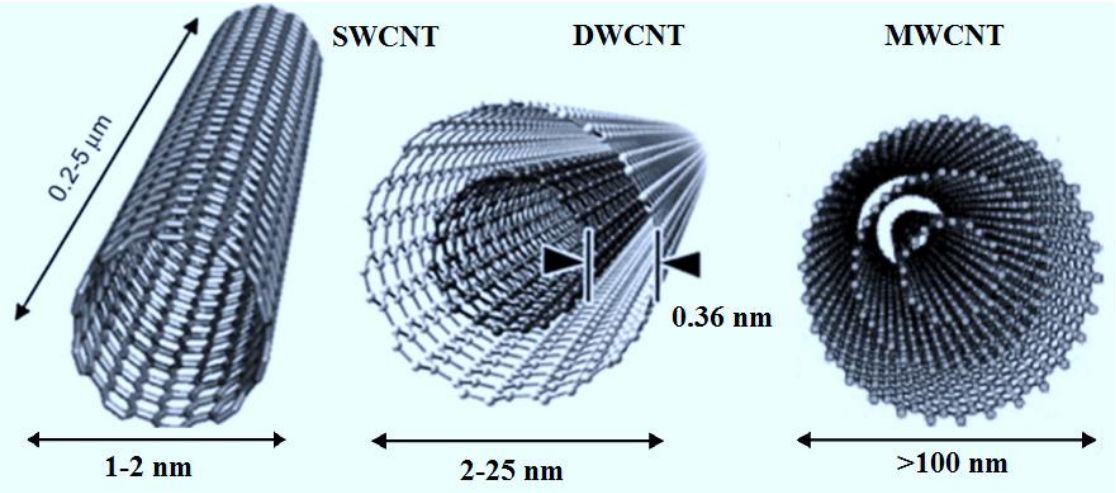

Figure 2.12. Dimensions and number of layers of single walled carbon nanotube SWCNT, double walled carbon nanotube DWCNT, and multiwalled carbon nanotube MWCNT [97, 98].

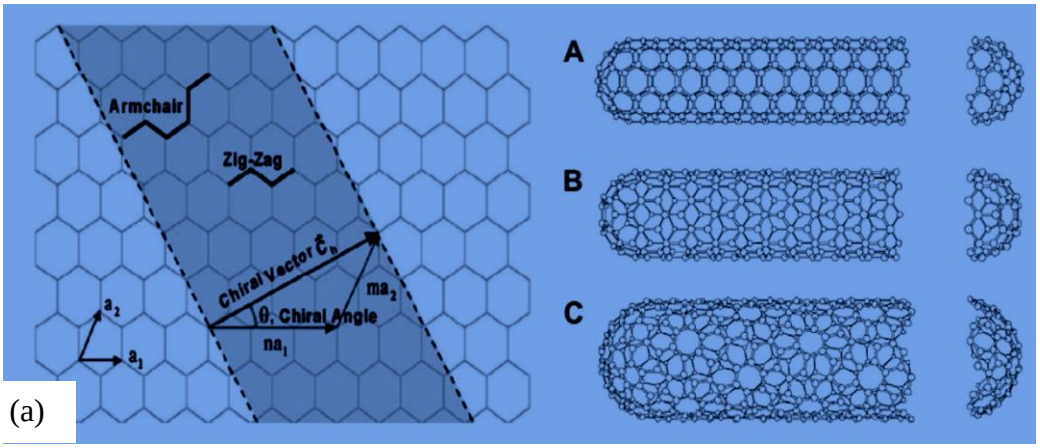

(b)

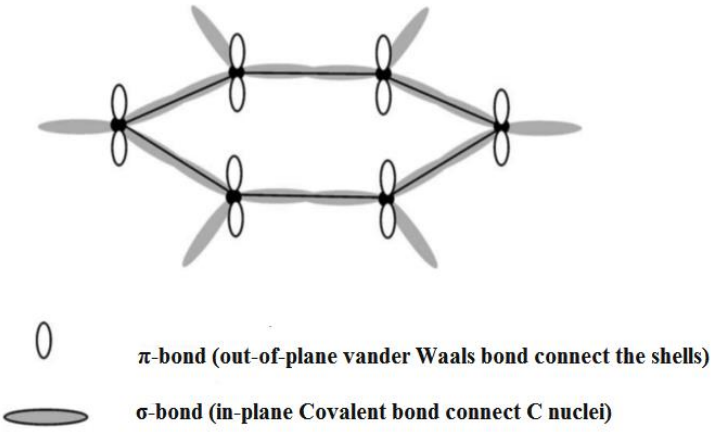

Figure 2.13. (a) Schematic diagram shows different chiralities of a CNT (A: archair; B:zigzag; C:chiral), (b) basic hexagonal bonding structure for graphene sheet [99, 100].

2.7.3.2. Graphene

Until 2004, it was believed that the exfoliation of graphite would lead to a thermodynamically unstable graphite atomic layer [109]. However, in 2004, Geim et al. used adhesive tape to exfoliate graphite crystals [110]. Graphene is a very thin material with a thickness of around one atom and it is composed of sp^2 carbon atoms arranged in a two-dimensional honeycomb structure. The carbon allotropic structural changes are shown in Figure 2.14 [111]. Graphene can be divided depending on the thickness to single layer graphene, graphene nanosheet (GNS) for thicknesses in a range 2–30 nm and graphene nanoplatelets (GNP) for thicknesses within 30–80 nm or even up to 100 nm in some reports [112]. Due to its unique electrical, thermal, and mechanical properties [113, 114], which are compared with the properties of CNT in Table 2.6, graphene has attracted considerable interest in a wide range of potential applications, such as a second phase for reinforcing metal, ceramic, polymer matrix composite [115-117], energy storage/generation applications [118], bio-applications [119], cellular imaging and the drug delivery [120] films of transparent electrodes [121,122].

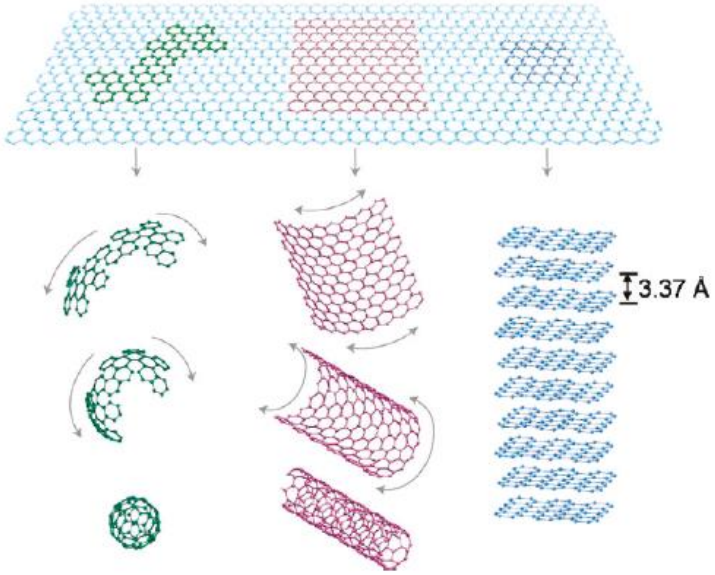

Figure 2.14. Graphene can be wrapped to form the 0-D buckyballs, rolled to form the 1-D nanotubes, and stacked to form the 3-D graphite [111].

Table 2.6 Dimensions and properties of carbon nanotube and graphene [100, 111, 123–128].

Fibres	Density ($g\ cm^{-3}$)	Average dimension (nm)	Young's modulus (GPa)	Tensile strength (GPa)	Electrical conductivity ($S\ cm^{-1}$)	Thermal conductivity ($W\ mK^{-1}$)
Graphene	2.2	(Depending on production process) w = 100′ s nm up to cm t =single layer-multi layers	1000	130	Up to 6000	4840-5300
MWCNT	1.4-1.8	OD = 5.6-24.8 ID =1-6.6 $l = 0.66\text{-}5.81\times10^{3}$	270- 950	11-63	10^{3}-10^{5}	>3000

Where: t is the thickness, w is the lateral, l is the length, OD is the outer diameter and ID is the inner diameter.

2.7.3.3. Modification treatment of carbon nanostructures

The van der Waals attraction between CNTs promotes the agglomeration of nanotubes, making the synthesis of components from CNTs extremely challenging. Therefore, significant efforts have been directed to modify the surface properties of carbon nanostructures, which can be chemical or physical based method. The physical method is characterised by less damage to the carbon nanostructure, less opportunity for re-agglomeration of carbon nanostructure in the matrix and it is easier to use [100].

Chemical functionalisation depends on linking the functional entities onto the carbon nanostructure by covalent bonding. This occurs by chemical reaction of fluorine, amino, alkyl or hydroxyl with carbon nanostructure, leading to sidewall functionalisation. Defects such as open ends and/or holes in the sidewalls, pentagon or heptagon irregularities and oxide can be used as another method for chemical functionalisation. Defects can be made by using strong acids or oxidant such as HNO_3, H_2SO_4 and $KMnO_4$ [129, 130] or by plasma treatment [131].

The physical functionalisation process relies on non-covalent bond for altering the interfacial properties [100]. The free π-electrons are responsible for electrical conductivity in carbon nanotubes and graphene. These electrons could also be used to improve adsorption of polymer or surfactant on the surface of carbon nanostructure through π-π stacking interaction during functionalisation [132, 133]. In the physical functionalisation process, the surface is enriched by a polymer such as a ply(phenylenevinylene) or by surfactants such as sodium dodecylesulfate (SDS) which are bonded by van der Waals and π-π stacking processes [134-136]. This leads to enrichment of the surface with a hydroxyl group and overcome on van der Waals forces between carbon nanostructures.

An alternative to surface modification to improve the dispersion of carbonaceous materials can be found in the mechanical dispersion methods, which include ultrasonic, shear mixing and ball milling. However, fragmentation and a decrease in aspect ratio can occur in carbonaceous materials created by mechanical dispersion [137,138].

2.7.3.4. Interface bonding

Interface bonding between reinforcement and matrix has a significant influence on the properties of composite materials. Interface bonding is more influential on the properties of nanosized filler composite because of the considerable increase in surface area. An appropriate interface design must be guaranteed to achieve good mechanical bonding with low thermal contact between reinforcement and matrix, which is of great interest in carbon nanomaterial reinforcement [92]. Bonding at the interface can be strong which increases the strength of the composite but reduces the ductility or weak which causes pull-out of fibre at low load, leading to lower strength [10]. It is essential for the interfacial bonding to be strong enough for the load to transfer from the matrix to the reinforcement. Therefore, control of the interface chemical reactions is necessary to obtain the desired interfacial bonding. This can be performed by SPS, which minimises the interfacial reaction during sintering because it allows densification at short time, which works together with the functionalisation groups on the surface of carbonaceous to improve the interface bonding in composite materials [85, 139]. The excessive reactions at the interface produce a large amount of intermetallic compound, which deteriorates the mechanical properties [140-143].

2.7.3.5. Dispersion methods for the preparation of nanocomposite materials

Novel composite materials with superior properties are developed from embedding nano-reinforcement in metal matrix [144]. Ma et al. compared the tensile strength and creep resistance of Al-1 vol. % Si_3N_4 (15 nm) nanocomposite and Al-15 vol. % SiCp (3.5 μm). The tensile strength was comparable and creep strength was nearly double in the nanocomposite, despite the lower fraction of reinforcement [87, 145]. Metal matrix nanocomposites are synthesised by several different methods, as shown in Figure 2.15.

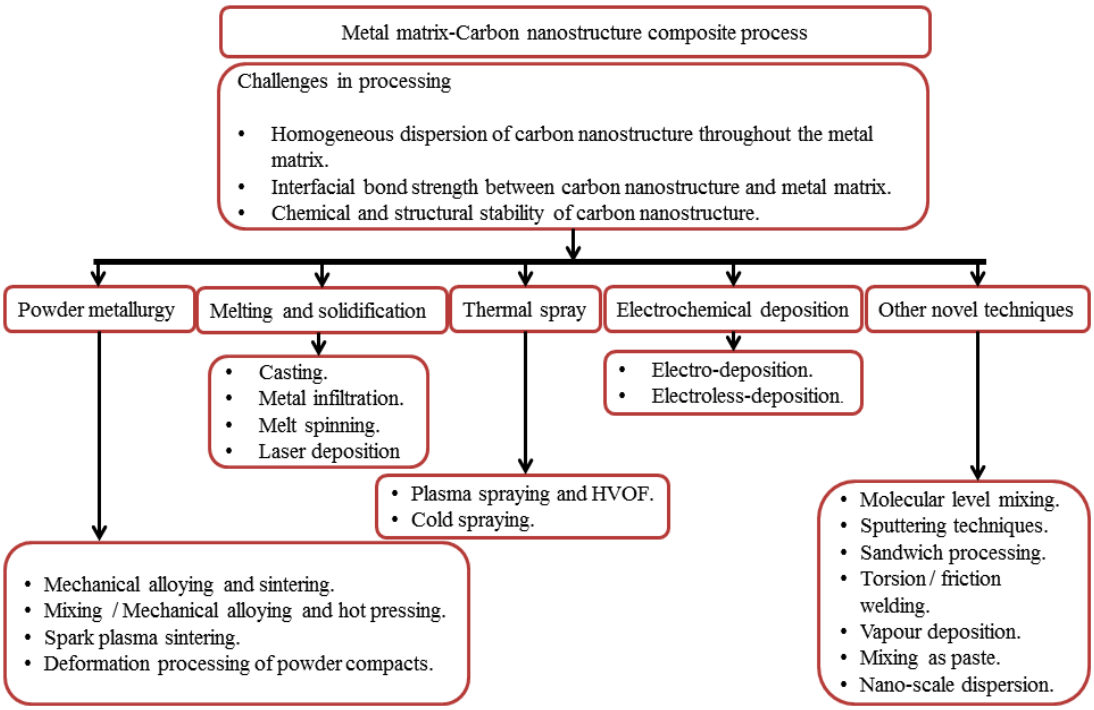

Figure 2.15. Synthesis processes of carbonaceous metal matrix nano composite [10].

2.7.3.6. Strengthening efficiency of dispersion method

Bakshi and Agarwal [85] have compared the efficiency of different dispersion methods used in Al-CNTs composite, as shown in Figure 2.16. Three regions were suggested for strengthening, which are: (i) low fraction (1-2 vol. % CNT) the strength is increased as the content of reinforcement increased; (ii) intermediate fraction (2-5 vol. % CNT), where the strength is decreased in comparison to low fraction composites; and, (iii) high fraction (above 5 vol. % CNT), where the strength is more decreased with increased fraction of reinforcement. The ball milling process is still a competitive procedure of dispersion carbonaceous material in comparison to the novel processes of dispersion. However, the broad variation in ball-milling parameters has a significant influence on the final properties of composite materials.

From the different models that can be used to predict theoretical strength in the nanocomposite, a close matching between the experimental data and the predicted value by Halpin-Tsai was observed up to 2 vol. % CNT. However, deviation occurs at higher volume fractions, due to poor dispersion [10, 85, 146].

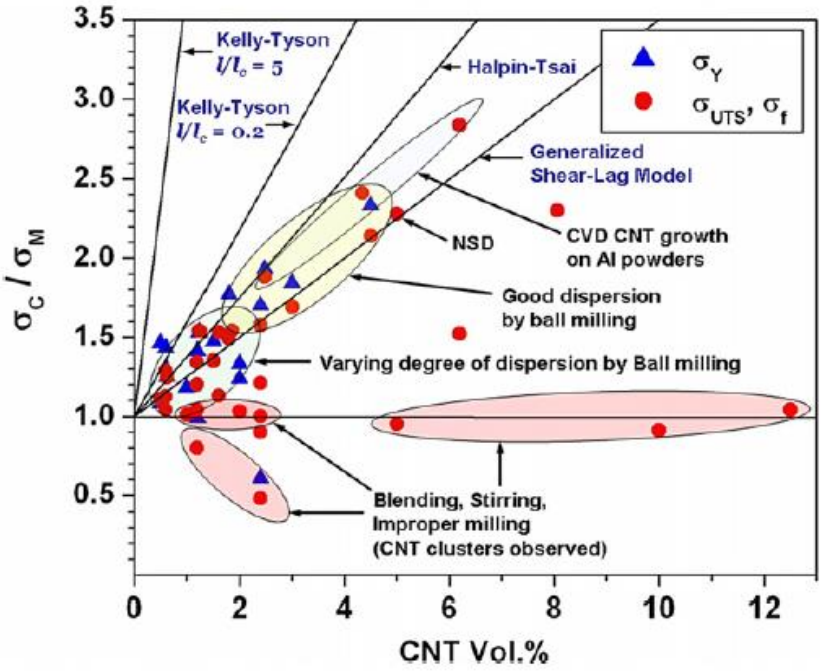

Figure 2.16. Effect of processing route and volume fraction of CNT on tensile strength in Al/CNT composite [85].

2.8. Carbon nanotube-metal matrix composite

Almost all of the published papers on using CNTs or GNPs in metal matrix composite for structural applications employ Al, Cu and Mg as a matrix alloy. There are very few studies on using iron base alloy as a matrix. Because of the complication of achieving uniform dispersion in CNT or GNP composites, the true strengthening effect of CNT or GNP has never been realised. Therefore, several different dispersion methods have been adopted to tackle the challenge of achieving uniform dispersion, as presented in the following sections.

2.8.1. Methods for dispersion CNT in metal matrix

Tremendous improvement in polymer properties has been achieved by dispersion CNT [103] because of the ease of dissolving polymer and the dispersion of functionalised CNT in the solvents, which enable uniform dispersion of CNT in the polymer matrix. However, the situation is more complicated in a metal matrix and, therefore, different methods have been investigated to improve the dispersion of CNT in the metal matrix. The first work on CNT reinforced metal matrix composite was performed by [101], here the CNTs and aluminium powder were mixed by stirring in ethanol. The tensile strength of the unreinforced and composites material with 5 vol. % and 10 vol. % were nearly identical. This happened because of poor dispersion and the clustering of CNTs. Laha et al. [147]

used plasma spray to sintering CNT-Al powder after blending in ball milling machine without a milling medium. The CNT was stable without oxide formation with the base alloy, even though an extremely high temperature of (10,000-15,000 K) can be generated during plasma spray. This was attributed to CNT agglomeration and uneven flow through the plasma. Noguchi et al. [148] developed a nanoscale dispersion method (NSD) that initially depends on the homogenous dispersion of CNTs in an elastomer matrix. The elastomer matrix was then displaced by Al by putting plates of Al on a slab of elastomer composite in a furnace at a temperature of 800 ºC for one hour. The influence of capillary action caused the replacement process to take place. Although the compressive mechanical properties of the composites were widely enhanced, it is believed that contamination might occur during elastomer decomposition. Nanoscale dispersion with SPS was used by Kwon et al. [70] and a nearly threefold increase in the strength of the metal matrix was attributed to the uniform dispersion of CNT and to the strong interfacial bonding by carbide phase. This is the main advantage of the SPS process, which allows high interface bonding through formation limited thin layers of carbide at the interface [85]. Jiang et al. [149] claim that enriching flaky metal powder with a hydrophilic can trigger the uniform dispersion of carbon nanostructures. In their work, a high volume fraction was uniformly dispersed relying on this approach. However, anisotropy in properties might result from changing powder morphology from spherical to flake shape. Paying particular attention to in situ synthesis of composites, He et al. [150] suggest an approach in which Ni particles (1 wt. %) were precipitated on Al by calcination and reduced to provide active nanoparticles for subsequent growth of CNT by chemical vapour deposition (CVD). Their results showed a high quality dispersion. Cha et al. [151] used the molecular mixing method to disperse carbon nanotubes in copper. The dispersion procedure involves suspending the functionalised CNT in ethanol and mixing the suspension with copper ions. The solution was then vaporised, dried, calcinated and reduced. The composite powder was next consolidated by spark plasma. Uniform dispersion of CNTs within the Cu-powder enables a compressive yield strength of 10 vol. % CNTs-composite that is three times higher than that of the alone Cu. However, the oxygen content was increased by increasing the volume fraction of reinforcement during molecular mixing; therefore, the ductility was decreased accordingly [152]. Furthermore, the oxides deteriorate the magnetic properties by forming obstacles to domain wall movement. Normally, the increase in strength of the carbonaceous composite leads to a decrease in ductility [94, 153] thanks to the smaller ductility of the fibre [85]. To the best of author knowledge, only one study shows an

improvement in strength combined with increased ductility [154], which might be due to formation the precipitate from reaction with carbon.

2.8.2. Using ball milling for dispersion

2.8.2.1. General introduction to ball milling

Mechanical alloying (MA) is a powder metallurgy technique that involves a repeated welding, fracturing and re-welding of powder particles during solid-state processes in a high-energy ball mill [155]. This process was firstly employed in the 1960s by Benjamin as an alternative method to the reinforcement coating processes, which could not produce uniform dispersion for reinforcement in the metal matrix. MA was originally used to develop the properties of nickel- and iron-based superalloys by fine oxide particles [156, 157]. The energy of ball milling can be changed by varying the time, temperature, atmosphere, ball to powder ratio, speed and design of the ball milling machine. Lubricants are used during ball milling processes to reduce the intensive cold-welding between powders, which is known as a process control agent (PCA). Stearic acid is commonly used as a solid organic PCA. However, organic solvents (methanol, ethanol, isopropanol alcohol, etc.) as a PCA are useful to reduce the agglomeration of carbonaceous nanomaterials, which positively affects dispersion. This process is commonly known as a wet powder mixing process, in which after mechanical alloying the composite mixture is dried in an oven [158]. A schematic for the deformation in powder and dispersion during high energy ball milling is shown in Figure 2.17.

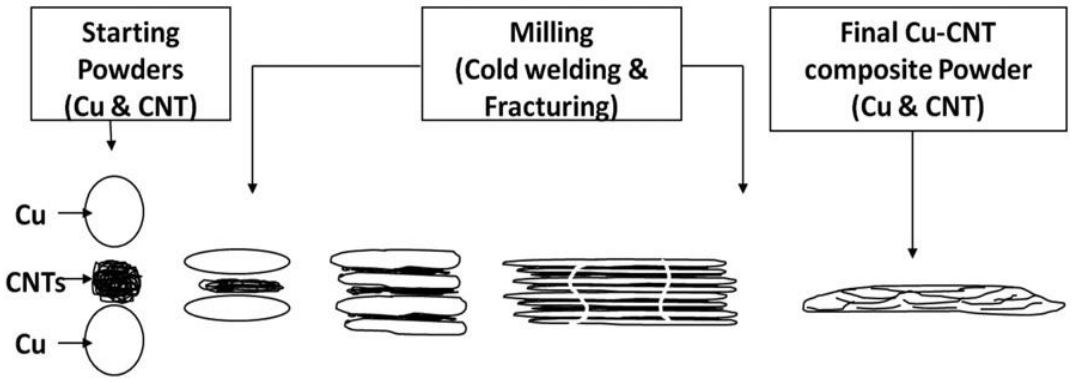

Figure 2.17. Schematic explains the morphological changes occurred during milling of copper-CNT powders [159].

Depending on the ball milling conditions, there are four possibilities for reinforcement distribution (see Figure 2.18). The reinforcement phase can be distributed along the grain boundaries of the matrix phase or inside the matrix grains, as shown in Figures 2.18 (a) and (b), respectively. The reinforcement phase is embedded inside the grains and along the

grain boundaries Figure 2.18 (c), while in Figure 2.18 (d) the homogenous distribution for both the matrix and reinforcement grains is shown [157].

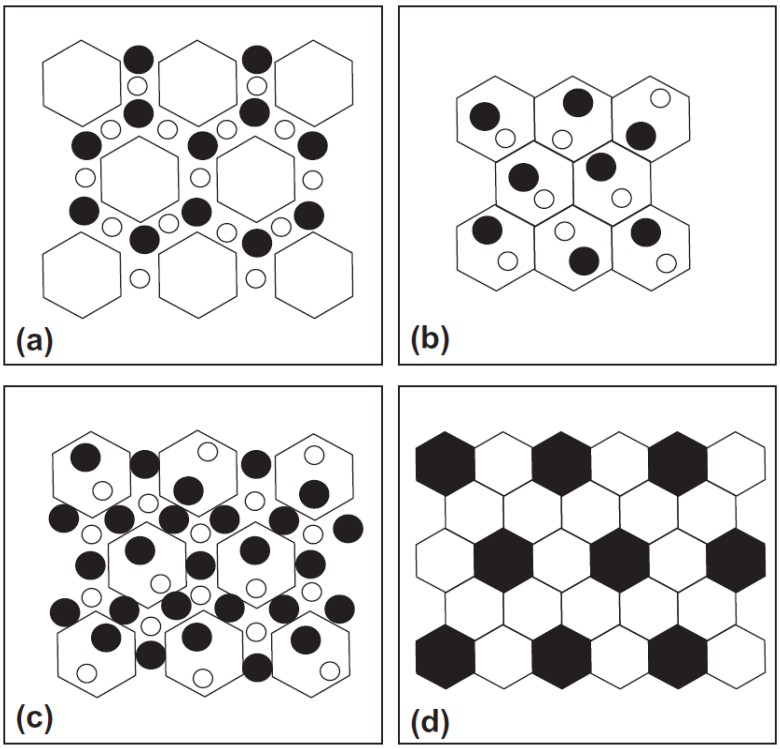

Figure 2.18. The possibility for distribution of the matrix and reinforcement phases in a nanocomposite. The open hexagons represent the matrix grains, while the open and filled circles represent the reinforcement phase(s) [157].

2.8.2.2. Ball milling of a CNT composite

It is found that acidic purification of CNTs from the synthesis impurities like catalyst particles, and amorphous carbon and using wet ball milling can significantly improve the dispersion of CNT, especially at high rotation speed [160]. However, using harsh ball milling conditions for the dispersion of CNTs could cause serious damage to the structure of CNTs, depending on the quality of the CNTs that are used. The length of the tube is also affected by ball milling a reduction in length can occur during ball milling. However, for aspect ratio 30, the short tubes have the same reinforcing function as the long tubes [138, 160, 161]. Esawi and Morsi [162] used high energy ball milling to disperse CNTs. Their results showed that the CNTs were uniformly dispersed in metal powder and the structure was intact even after intensive ball milling. Singhal et al. [163] functionalised carbon nanotube with ammonium bicarbonate during ball milling process and reported superior mechanical properties as compared to non-functionalised or acid functionalised carbon nanotubes, due to uniform dispersion and strong interfacial bonding. Liao and Tan [164] compared high energy and low energy ball milling with novel polyester binder-assisted (PBA) mixing method. In the PBA process, CNTs were mixed with polyethylene glycol

(PEG). The mixture was then heated to the viscous temperature, where the Al powder was fed and blended. The mixture was then cooled cured and the PEG was decomposed by heating to 400 ºC. The highest value for tensile strength and hardness was achieved by high energy ball milling process due to better dispersion. Dispersion of CNTs in soft magnetic alloy Ni-Fe alloys has been studied by [165]. However, a high pressure of 300 MPa was used in cold compaction process and long dwelling for one hour at 1040 ºC was used during the sintering processes, consequently the fraction of porosity in consolidated materials was considerably high. In a pre-mixing method, ultrasonic agitation was used to mix a Fe_3Al powder with 5 vol. % CNTs in methanol, the subsequent slurries were then ball milled for 12 h, dried and sintered by spark plasma. An enhancement in compressive yield strength and micro-hardness were achieved [166]. Recently, CNTs were agitated by ultrasonic in Dimethylformamide (DMF) with FeCo alloy powder for different volume fraction up to 4 %, then dried and dry ball milling. For comparison, other samples were prepared by only dry ball milling. Then, spark plasma was used to densify the samples. Only minor improvements in mechanical and magnetic properties were achieved due to poor dispersion [167]. To improve dispersion of CNTs in FeCo alloy, electroless plating was used to coat CNTs with Ni-P layer. Unfortunately, intensive agglomeration for CNTs was observed not only after plating process but also even after 1 h ball mill in the consolidated FeCo alloy composite [168]. Therefore, CNT-FeCo alloy composites prepared by reinforcement coating and ball milling were found to exhibit lower strength than the coated micrometre SiC whisker reinforcing FeCo alloy, which was only dispersed by ultrasonic agitation [169]. In spite of the advantages in improving the interfacial bonding by coating the reinforcement, chemical impurities and oxides can be included in the final compact during processing [92]. Furthermore, the influence of the coating metal on the properties needs to be considered during the comparison because FeCo alloy is very sensitive to the alloying element.

2.9. Graphene nanoplatelets-metal matrix composite

The dispersion of graphene nanoplatelets (GNPs) in the base matrix is rather complicated when compared to carbon nanotube (CNTs) because the exfoliated sheets are gathered to form sheets close in dimension to graphite structure during dispersion and drying, leading to the advantages of the nanostructure being easily missed. Furthermore, due to the two-dimensional form of GNPs, the interfacial contact area is increased. This makes the dispersion of graphene more complicated when compared to nanoparticles or nanotubes

[170]. Therefore, depending on the quality of dispersion, both a considerable decrease and a remarkable increase in mechanical properties have been reported in GNP metal matrix composite [171, 172]. However, the improvement in properties is superior by embedding GNP in material when compared to CNT. Rafiee et al. [173] reported higher mechanical properties in GNPs composite over CNTs composite, which was attributed to the higher specific surface area and two-dimensional geometry of GNPs, as well as to the wrinkled surface which enhanced the interface bonding of GNPs.

2.9.1. Different methods for the dispersion of GNP in a metal matrix

Several dispersion methods have been used to obtain the homogeneous dispersion of carbon nanostructures in a matrix material. These methods are mainly classified as mechanical mixing, chemical mixing and electrode deposition [133, 174]. Kim et al. [175] used graphene oxide as a dispersion agent for both multiwall and single-wall carbon nanotubes in water. The graphene oxide strongly interacted with the surface of CNTs throughout π-π attractions, leading to homogenous dispersion. Graphene was also used as a dispersion tool to decrease the agglomeration in SiC nanoparticle [176]. Wimalasiri et al. [177] used single-walled carbon nanotubes (SWCNTs) to prevent re-stacking between graphene sheets for fabrication electrodes from carbon nanotube and graphene composite. The increased space between graphene sheets caused by CNTs improved the transport of electrolyte ions within the electrode. The dispersibility of graphene was enhanced by increasing the functionalisation group on MWCNTs by acidic treatment [178]. This strategy has been previously tested to improve dispersion of GNP in matrix from polymer [179], ceramic [180, 181], and light weight metal alloy [182]. The mechanical properties were enhanced due to the improvement in the dispersion.

Graphene oxide (GO) has attracted researchers to use it as a starting material for graphene. The main difference between graphene and GO is the many groups of hydroxyl, carbonyl, carboxylic and epoxy on the surface of GO, making the dispersion of GO much easier in solution and more stable than graphene [183]. Wang et al. [115] modified the surface of flaked powder through coating by polyvinyl alcohol (PVA), and Al powder was then mixed with GO. The slurry was then mechanically stirred, filtered and rinsed with deionised water. A reduction process and decomposition of PVA was performed in Ar at 550 ºC for 2 h, which was followed by consolidation and extrusion. Around 62 % improvement in tensile strength was achieved when compared to unreinforced matrix. GO was also mixed with unmodified flaked powder of metal matrix in ethanol by [183] and

uniform dispersion for reduced GO was obtained. However, it is reported that GNs are better for reinforcement than the reduced GO [184]. This might be due to less damage on GNs. Hwang et al. [185] used molecular-level mixing to synthesise graphene-copper composite by a reduction of graphene and copper oxides. SPS process was used for consolidation. The yield strength was increased by about 80 % for only 2.5 vol. %; however, the elongation was significantly decreased to about 60 %, which might be due to oxide contamination. The stability of GNPs at high SPS condition of 1850 ºC and a pressure of 80 MPa was studied by [186]. The results indicated that the structure of GNPs is feasible to maintain at high sintering temperature with very slight damage in the structure. The SPS process helps to maintain the structure integrity of GNPs, even at sintering temperature higher than the other sintering methods [171, 186]. This provides an opportunity for sintering composite materials at a relatively high sintering temperature.

2.9.2. Ball milling of GNP composite

In situ exfoliation of graphite during processing of the composite has been used to disperse graphene nanosheets (GNs) in alumina by ball milling, which was then sintered by spark plasma. Although the dispersion of GNs in the composite was considerably improved, the size of dispersed GNs was inhomogeneous and defects were introduced to GNs during ball milling [187]. A liquid lubricant can be used during graphite exfoliation to reduce the violent shocks during ball milling and the agglomeration of the nanoparticles [188]. High energy ball milling enabled a dispersion of very high volume fraction of GNP. Chu and Jia [172] dispersed 12 vol. % GNP in a copper matrix. A Spex mixer was used for ball milling and a very high speed of 1200 rpm was used for 3 h under argon atmosphere for a ball to powder ratio 10:1. It was noticed that the addition of GNPs reduces welding between powder and aids grinding during ball milling. A uniform dispersion up to 8 vol. % GNP led to about 114 % increase in yield strength. Rashad et al. [189] compared the effect of dispersion GNP and CNTs by ball milling on tensile and compression properties of magnesium alloy. Improvement in tension and compression strength was observed in CNT composite when compare to GNPs composite thanks to the difficulty in achieving uniform dispersed in GNPs composite. However, it is interesting to notice that a high tensile extension was obtained in GNPs composite. Increasing elongation by introducing a greater volume fraction of graphene nano-flakes was also observed by [190]. In a study by Shin et al. [191], the mixture of Al and few-layer graphene (FLG) was ball milled in argon and stearic acid was used as a process control agent. Then, the composite powder was charged

and compacted in 1.5 mm copper tube. The compact was hot rolled at 500 ºC for 12 % reduction per pass to achieve a sample with 1 mm thickness. The tensile strength was doubled. From a comparison with the tensile strength of MWCNT composite in the literature, the authors reported that the FLG is about 3.5 times more effective in strengthening.

2.10. Raman spectroscopy

Raman spectroscopy is a powerful tool that can be used to determine the degree of structural ordering or the presence of contaminants in carbonaceous materials. The characteristic bands in all the graphite based materials can be classified into first-order (1100-1700 cm^{-1}) and second-order (above 2300 cm^{-1}) Raman spectra [192]. Figure 2.19 shows the Raman spectrum of MWCNT and single layer graphene. The main peaks are seen at 1583 cm^{-1} (commonly referred to as G), the D peak is at 1350 cm^{-1} and the shoulder D′ is at around 1620 cm^{-1}. In addition to the overtone peak, 2D or G′ appears at 2680 cm^{-1}, the D+G peak appears at around 2950 cm^{-1}, the 2D′ peak appears at 3245 cm^{-1}, and finally the 2D+G peak occurs at 4290 cm^{-1} [193]. A split in the G band was observed in CNT, the main reason for this is due to the stronger tube morphology of the CNTs in contrast to the flat morphology of graphene sheets [194]. The relative intensities between the D-band, relating to structural defects, and G-band, relating to the order of the graphite structure ($R=I_D/I_G$), is widely used to evaluate the defect density of carbonaceous materials [70, 195]. The strain in graphite can be detected from the shifting and splitting of the Raman modes [196, 197]. The G-band peak position is very sensitive to strain in the graphene structure; hence, the shift in wave number will change according to alteration in the vibration frequency of the G band due to the included strains.

Up shifting is also observed in the 2D peak. Although it has been reported that the Raman spectra could also be utilised to determine the number of layers in graphene by the shape, width, and position of the 2D peak, this can only be used for limited n-layer graphene (for n up to 5). The intensity of a sharp 2D peak in a single graphene is roughly 4 times more intense than the G peak. Meanwhile, in graphite the 2D involves two components, $2D_1$ and $2D_2$, which are roughly about 1=4 and 1=2 the height of the G peak, respectively. The increase in the layer number causes a broadening and up-shift in the 2D band as compared to between one and two layers [198]. The structure of carbonaceous materials is very sensitive to dispersion, sintering and matrix material [199]. Therefore,

monitoring the structural change in carbonaceous materials during the process is very crucial to achieve high quality dispersion with less damage.

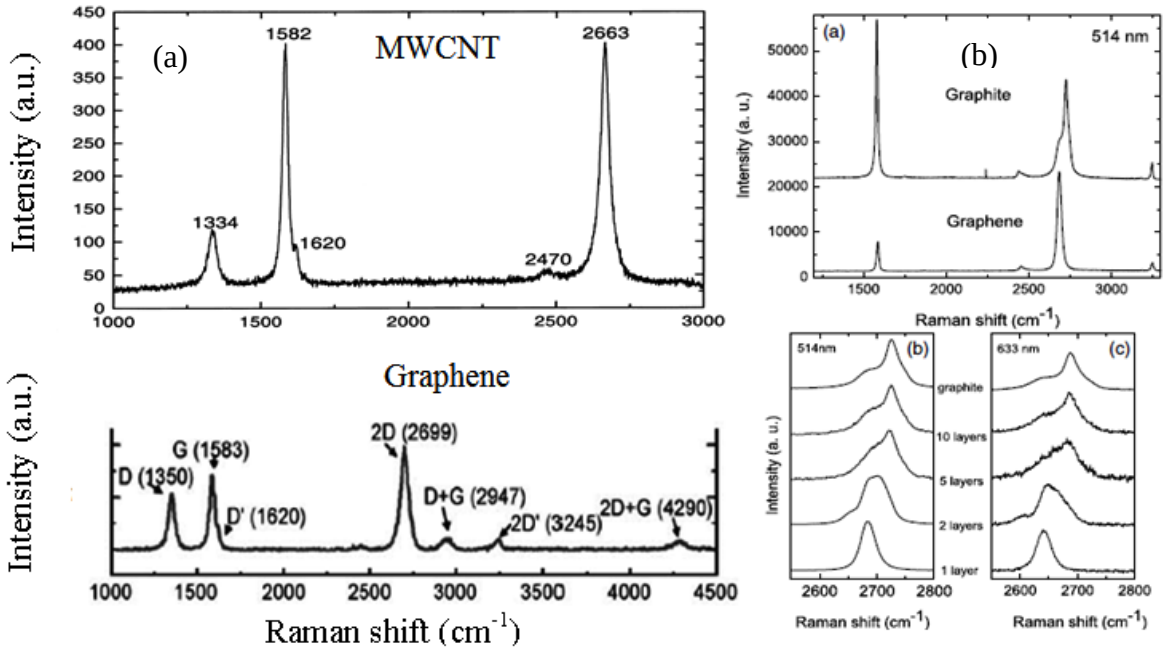

Figure 2.19. (a) Typical Raman spectrum of MWCNT and single-layer graphene, (b) comparison of Raman spectra between bulk graphite and graphene at 514 nm, evolution of spectra with the number of layers at 514 nm and 633 nm respectively [193, 198, 200].

Chapter 3: Experimental work

3.1. Introduction

This chapter outlines the methodologies, which were followed to prepare FeCo alloys without reinforcement and with different types of nano-reinforcement. Multi-walled carbon nanotubes (CNTs), Graphene nanoplatelets (GNPs) and hybrid reinforcement (CNTs + GNPs) were dispersed at different volume fractions through different dispersion methods. The sintered materials by spark plasma sintering were structural, mechanically, and magnetically evaluated, in addition to X-ray diffraction and Raman spectra analyses.

3.2. Starting materials

Gas atomised Fe-50% Co-0.2% Si powder (as analysed by the supplier) was supplied by Sandvik Osprey Powder Group. Multi-walled carbon nanotubes (CNTs) and Graphene nanoplatelets (GNPs) were provided by Haydale Ltd, which were functionalized by plasma treatment to incorporate covalently bonded oxide group on their surfaces, to improve the dispersibility of the carbonaceous nanomaterial [201, 202].

3.3. Particle size of FeCo Powder

The distribution of particle size of the FeCo alloy powder was analysed using "Malvern Mastersizer 3000" with laser scattering. Hydro EV dispersion unit was used to disperse FeCo alloy powder, the unit is a semi-automated wet dispersion of size 600 ml, having immersed centrifugal pump and stirrer. The fundamental of working the Mastersizer is illustrated in Figure 3.1. The programme of Mastersizer analyser was supplied with the particle reflective index and absorption index of FeCo powder for values 1.740 and 1.000 respectively. The scattering pattern result from the laser beam that passed through the dispersed powder was used to calculate the particle size by Mastersizer 3000 software.

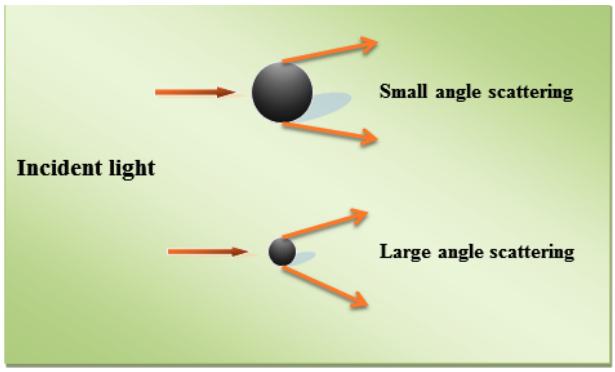

Figure 3.1. Operational principle of Malvern Mastersizer analyser (Schematic).

3.4. Spark plasma sintering (SPS)

Spark plasma sintering is a relatively new sintering method with main advantage of maintaining the nanostructure after sintering [10]. The materials were densified using the spark plasma sintering facility (HPD 25/1 FCT, Germany) at Queen Mary, University of London, as seen in Figure 3.2. The FeCo alloy powders or FeCo alloy composite powders were located in a 30 mm graphite die, which was fitted with the punches and was lined with graphite paper. Specac manual hydraulic pressing system, which allows variation of the load within a range of 0-15 tonnes, was used for initial pressing of powder before handling the die set to SPS furnace. A protection layer of graphite wool plate was wrapped around die assembly for thermal insulation. The sintering temperature was measured by an optical pyrometer, which was inserted in the upper half of the die set through a 10 mm diameter hole. The sintering temperature was generated by DC pulse current cycle of 15 ms on and 5 ms off. A hydraulic press was used to apply uniaxial pressure by steel ram, which was maintained at a constant value or changed during the process.

Figure 3.2. SPS furnace (image) in Nanoforce Technology, Queen Mary University, London.

3.5. CNT-FeCo alloy composite

3.5.1. Powder Mixing

Two different methods were used to mix FeCo alloy powder with functionalised multi-walled carbon nanotubes. The first method (A) involved dry mixing of the reinforcement with 20 g of FeCo alloy powder for volume fractions of 0.5 to 4.5 vol. %, followed by ball milling the mixture in an air atmosphere for 1 h at ball to powder ratio (BPR) ~ (1:1) by a

Spectromill ball pestle impact grinder (Chemplex Industries Inc., Model 1100), which is shown in Figure 3.3.

The second method (B) involved wet mixing of multi-walled carbon nanotubes with FeCo alloy powder in dimethylformamide (DMF) for volume fractions of 0.5 to 3 vol. %. DMF has commonly used as a solvent for dispersing carbon nanotubes [203]. The suspension of carbon nanotubes in DMF was stirred under ultrasonic agitation for 60 min followed by the addition 20 g of the alloy to each suspension. The resulting slurry was sonicated for 30 min. The composite slurry was then dried on a hot plate at the evaporation temperature for DMF (150 ºC) overnight. Then, the dried mixture was milled in the ball pestle impact grinder at BPR ~ (1:1) for 1 h.

Figure 3.3. Spectro Mill ball pestle impact grinder used for ball milling.

3.5.2. Spark plasma sintering of materials

The FeCo alloy and composite powder mixtures were consolidated in a graphite die using a spark plasma sintering furnace (HPD 25/1 FCT, Germany). All the samples were heated to the sintering temperature at a constant rate of 50 ºC.min^{-1} under a vacuum of 5 hPa. An initial ram pressure of 7 MPa was applied from room temperature to 400 ºC; followed by an increase to 80 MPa pressure and simultaneous heating to 900 ºC for a 3 minute dwell [84]. Samples were left to cool in the furnace and extracted from the die using a manual hydraulic press.

3.6. (CNT/GNP)-FeCo alloy composite

3.6.1. Powder Mixing

GNP was dispersed in FeCo alloy powder by using Spectromill ball pestle impact grinder (Chemplex Industries Inc., Model 1100) in an air atmosphere with steel ball pestles at BPR of ~ (1:1) for 1h. Three different volume fractions (0.5, 1 & 2 vol. %) of GNP were dispersed in 20 g of FeCo alloy powders. The mixture of CNT and GNP, which is referred as GNT, was also used as reinforcement for soft magnetic FeCo alloy at same volume fraction. The aim of inserting CNT among GNPs is to reduce re-staking between GNP sheets. Therefore, the mixing ratio of CNT: GNP was low for a value of (1:10). In order to reduce the effect of ultrasonic on the quality of nanomaterial, GNT was magnetically stirred in 100 ml of ethanol for 0.5 h, followed by ultrasonication for 0.5 h. GNT was then mixed with 20 g of FeCo alloy powder to form a composite slurry. The composite mixture was sonicated for 1 h in 150 ml ethanol, and then the samples were dried on a hot plate at 80 ºC overnight. After drying, the powder was then ball milled using the same conditions described for the GNP dispersions.

3.6.2. SPS process

Twenty gram of FeCo alloy powders and composite powder mixtures were consolidated in a graphite die lined with graphite foil using a spark plasma sintering furnace (HPD 25/1 FCT, Germany). All the samples were heated to the sintering temperature at a constant rate of 50 ºC min^{-1} under a vacuum of 5 hPa. The initial 7 MPa pressure was applied from room temperature up to 400 ºC; followed by an increase to 80 MPa, and simultaneous heating to 900 ºC where the samples sintered for a 3 min dwelling time. After rapid cooling in contact with the water cooled pistons of the spark plasma sintering furnace, the samples were manually extracted from the die using a hydraulic press.

3.7. Effect SPS parameters on properties of FeCo alloy

In this part, the effects of spark plasma sintering on structural, mechanical, and magnetic properties were studied. For each sample, a 30 mm graphite die, lined with graphite foil, was charged with 20 g of pre-alloyed equiatomic FeCo powder. After pre-compacting the powder in the die using a Specac manual cold press, the prepared die was then transferred to the SPS furnace and subjected to a pre-programmed sintering procedure. All sintering was performed under vacuum (5 hPa), under a constant 50 MPa uniaxial pressure. The SPS logs all key processing data, including temperature, pressure, current and voltage outputs;

and also monitors sample shrinkage rate via the relative movement of the upper piston (measured by inbuilt LVDT). A total of three different heating rates (50, 100 and 300 ^{o}C/min) were investigated. For each heating rate, the 'optimum' sintering temperature was chosen based on the point at which maximum shrinkage occurred (+ 50 ^{o}C to ensure good densification). Following this, the second batch of samples was sintered at that 'optimum' temperature for 15 min in order to assess the time taken before shrinkage is complete (i.e. when shrinkage rate measurements fall to 0); to give the 'optimum' sintering time. In the third round, then, the samples were sintered under the 'optimised' sintering conditions (temperature and time) for each heating rate. The resulting sintering conditions for all samples are summarised in tables in following results chapter and given alphabetical identities which will be referred to hereafter for simplicity.

3.8. GNPs-spherical and flaked FeCo alloy powders composites

3.8.1. Dispersion and sintering GNP-spherical FeCo alloy powder (procedure A):

GNPs were dispersed in spherical FeCo alloy powder by using Spectromill ball pestle impact grinder (Chemplex Industries Inc., Model 1100) in an air atmosphere with steel ball pestles for the ball to powder ratio BPR of ~ (1:1) for 1 h without process control agent (PCA) up to 4 vol.%. Then, the powdered samples were sintered at a constant rate of 50 ºC min^{-1} under a vacuum of 5 hPa. The initial 7 MPa pressure was applied from room temperature up to 400 ºC; followed by an increase to 80 MPa pressure and simultaneous heating to the sintering temperature of 900 ºC for a dwell time of 3 min.

3.8.2. Dispersion and sintering GNP-Flaked FeCo alloy powder (procedure B):

Planetary ball milling machine (Fritsch pulverisette 5 Germany) was used for dispersion, which was supplied with 80 ml tungsten carbide jar and hardened steel balls of 10 mm, the machine and the procedure of filling the jar with inert gas and the jar locking system are shown in Figure 3.4. In order to prepare the flaky FeCo alloy powder, 50 g of spherical FeCo alloy powder was ball milled at BPR of ~ (2:1) for 6 h using 8 ml of isopropanol alcohol as PCA, the efficiency of isopropanol alcohol in dispersion GNPs has been reported in [204, 205]. Operation parameters were 300 r.p.m, 15 min work and 10 min pause to reduce temperature during milling. The jar was provided with a sealing lid that allows filling the jar with an inert gas, high purity argon was used as inert gas to avoid

oxidation during the process. After filling the jar with argon gas, especial locking system was used during operation which helps to maintain the jar in an inert atmosphere. The gases were released after ball milling using the valve to drop jar pressure to atmosphere pressure. The aforementioned procedure was repeated to end with 100 g of flaky powder, which was used for subsequent processes to prepare composite materials.

The same machine was used to mix 20 g of flaky FeCo alloy powders with GNPs in the argon atmosphere. GNP was dispersed in flaky FeCo alloy powder using 6 ml of isopropanol alcohol as PCA. The BPR of (~1:1) was used for 1 h during dispersion processes, which are similar to the parameters of dispersion in procedure A. The operation conditions were 400 r. p. m. for 30 min work and 15 min pause to reduce the temperature in powder. Hotplate was used for drying composite slurries at 120 ºC for 5 h. During sintering, the high sintering pressure of 50 MPa was instantaneously applied at room temperature under a vacuum of 5 hPa. Hereafter, the heating rate of 50 ºC min^{-1} was used to increase temperature to 1100 ºC, where the sintering was performed without dwelling. For both procedures, after fast cooling in contact with the water cooled pistons of the spark plasma sintering furnace, the compacts were manually extracted from the die by a hydraulic press.

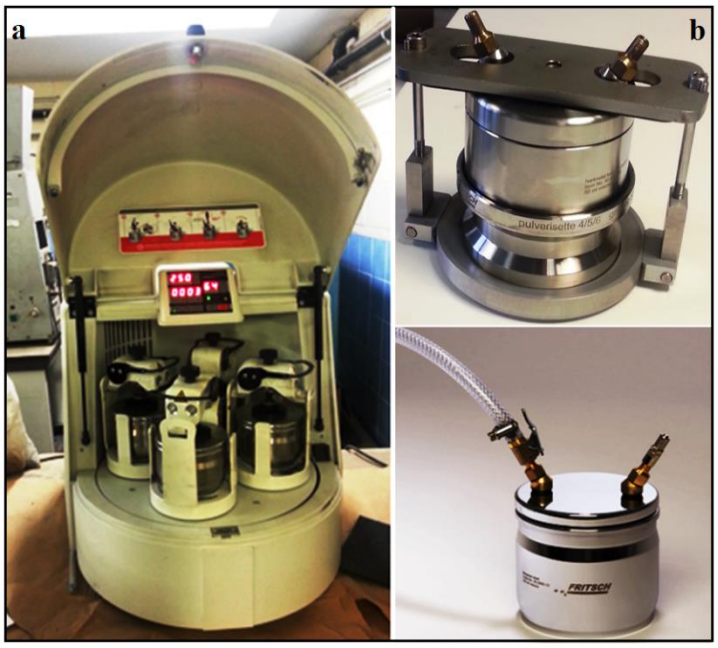

Figure 3.4. (a) Planetary ball mill machine (Fritsch pulverisette 5) used for ball milling and (b) process to fill the jar with inert gas.

3.9. Heat treatment of wet ball milled 4 vol. % GNP-FeCo alloy composites

The 4 vol. % GNP composites were prepared following the aforementioned procedure B. Then, the samples were heat treated in "Cogent company". A shallow tray was used during heat treatment to enable safe and quick handling for the sample from the furnace at the end of the soak time. Samples were heated up to specified soak temperatures, which are 600, 710, 750, 800 and 900 ºC from ambient temperature in an N_2 (3 % H_2) atmosphere, for soaking time of 1 h. The samples were then quenched as fast as possible after removal from the furnace. Despite using inert atmosphere and less exposure to air there was slight oxidation on the samples, therefore, before testing all the samples were ground carefully to remove the oxide layer or any sites for crack initiation due to heat treatment.

3.10. High energy Ball milling of 1.5 vol. % CNT and 1 vol. % GNP-FeCo alloy composites

High energy ball milling processes were performed on planetary ball milling machine (Fritsch pulverisette 5 Germany), in order to improve dispersion and interface bonding of nanomaterials. Fixed amount from CNT and GNP of loading 1.5 vol. % CNT and 1 vol. % GNPs were dispersed separately in 20 g of FeCo alloy powder, which was filled with inert gas. To improve dispersion and reduce the violent effect of ball milling, 6 ml from isopropanol alcohol was used as process control agent (PCA). The ball milling processes were performed for different periods of time, which are (0.5, 1, 2, 4, 6 h) for a ball to powder ratio BPR of ~ (6:1). The operation conditions were; 250 r. p. m of rotation speed, 30 min milling and 15 min pause to reduce the temperature in powder. The resulting slurries were dried on a hot plate by heating at 120 ºC for 5 h.

The all different trails were adopted to develop FeCo alloy in this work, are summarised in following chart Figure 3.5.

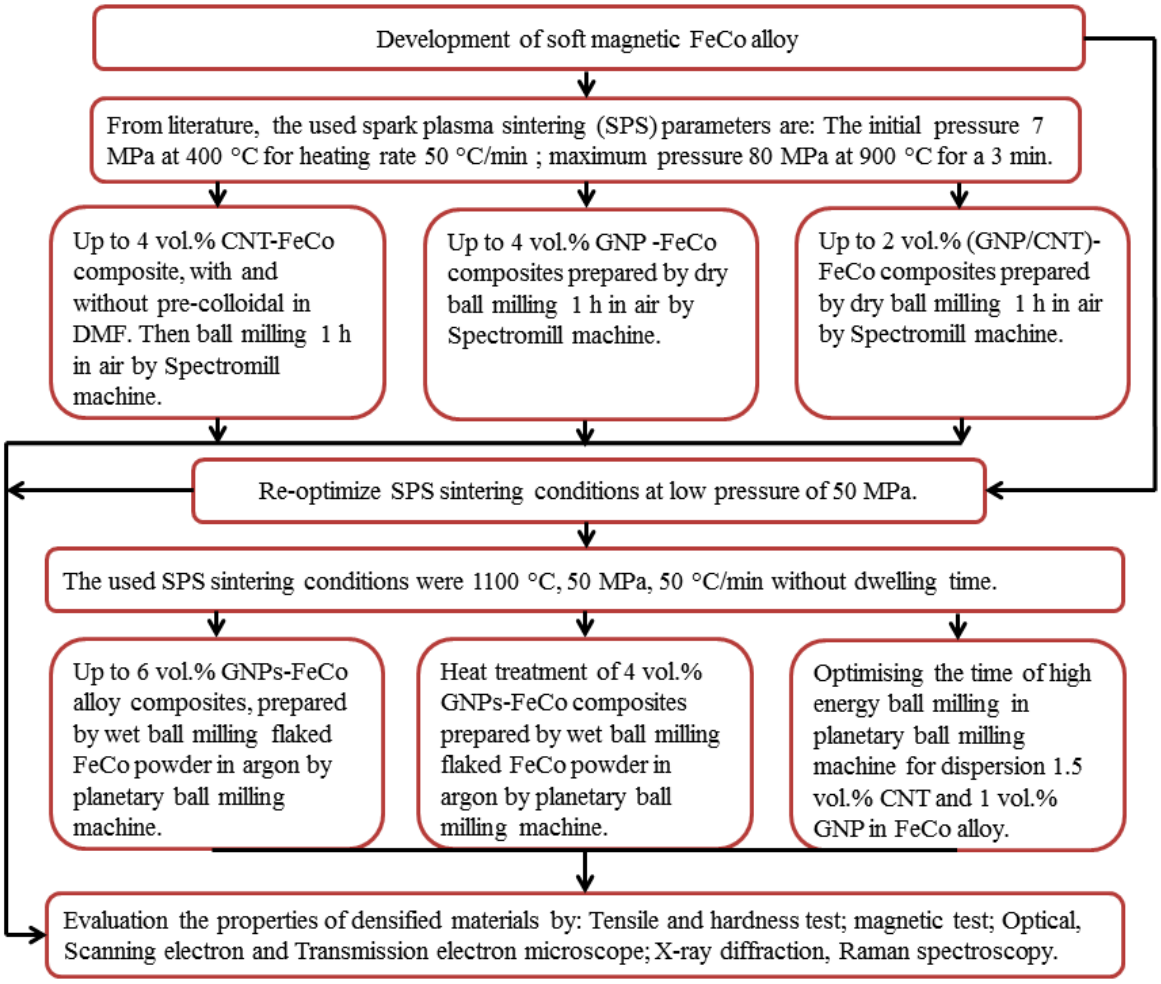

Figure 3.5. Flow chart of key steps for fabrication during development FeCo alloy.

3.11. Characteristics of materials

3.11.1. Density measurements:

All the sintered samples were ground using Emery paper to remove the graphite layer. The bulk density of sintered materials was measured by water buoyancy method. A Sartorius kit, which determines the density depending on Archimedes' immersion principle, was used to measure the real density of the sintered samples firstly in air. Then, the submerging density was measured in distilled water. The actual densities of sintered materials were then recorded directly from the kit and were divided on theoretical densities, taking the theoretical densities for CNT, GNP and FeCo powders as; 1.4 g cm^{-3}, 2.2 g cm^{-3} and 8.174 g cm^{-3} respectively and using the rule of mixture, to report the relative densities values.

3.11.2. Microstructural characterisation

The section of arc segment was mounted using Bakelite thermosetting (Resin-6) powder, which was pressed by Struers Primo Press Mounting Press at 185 ºC for 5 min heating and 4 min cooling. The cross section of arc segment was then ground with different grade of silicon paper started with 320 µm to 4000 µm. Polishing processes were performed using different discs contained abrasives for sizes 9, 3 and 1 µm. Then, the samples were etched using 10 % Nital (10 % HNO_3 + 90 % ethanol) for 30 sec. Optical microscopy study was performed using (Nikon ECLIPSE LV 100). Different magnification images from Scanning Electron Microscopy (SEM) (Oxford instrument) were carefully used to analyse the fracture behaviour of tensile samples. Transmission Electron Microscope (TEM) (JEM-2100 LaB6) of high resolution was used to study the structure of raw GNPs and CNTs.

3.11.3. X-Ray Diffraction test

X-ray diffraction (XRD) of Philips PW 3830 Automated Powder Diffraction supplied with Co tube was used for inspection the crystallographic phases. The tests were carried out with a wavelength of Kα radiation (λ_{Co} =1.78896 Å) using (PANalytical, XPERT Pro); to analysis the crystallographic phases and variation in the ordered structure of FeCo alloys and their composites. The scanning angles were ranged between 10 and 110 º2θ at a scan speed of 8×10^{-3} º2θ sec^{-1} at operation conditions 35 kV and 40 mA. While the operation conditions were 42 kV and 40 mA at a very slow scan speed of 25×10^{-5} º2θ sec^{-1} in the expected º2θ range of the ordered structure. JCPDS (Joint Committee on Powder Diffraction Standards) database was used to compare with the obtained diffractograms to determine the crystallographic phases present in materials.

3.11.4. Raman Spectroscopy

Raman spectroscopy (Renishaw in Via Raman microscope) was used to qualify GNP and CNT powders as a raw, and after embedding in FeCo alloy. The test was performed on tensile samples, the excitation wavelength of laser line was maintained at 514 nm for all samples with a power of 25 mW and spot size of 5 µm. Raman spectra scans between 1000 and 3200 cm^{-1} were obtained after 15 accumulations.

3.12. Mechanical and Magnetic Properties

3.12.1. Mechanical properties

3.12.1.1. Tensile and hardness measurements

Tensile samples were cut from 30 mm diameter monolithic FeCo alloy and composites discs using electron discharge machining (EDM) of dimensions 11 mm × 3 mm × 1.25 mm [17]. The specimen surface was subjected to grinding with fine grit emery papers to eliminate scratches if any were included during EDM cutting processes. In each case, three samples were tested, and then the average values and standard deviation were recorded. The tensile test experiments were conducted at room temperature in air using a Shimadzu testing machine at a crosshead speed of 2 $mm.min^{-1}$ of a 20 kN load cell. The schematic of disc and image of cut magnetic and tensile samples are shown in Figure 3.6.

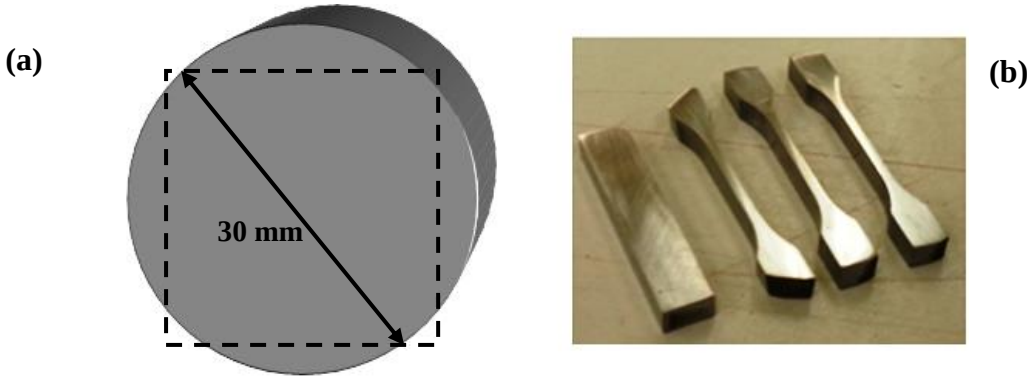

Figure 3.6. (a) Schematic showing the disc which the sample was cut (b) image of tensile and magnetic sample cut by EDM.

3.12.1.2. Hardness:

Hardness measurements for both FeCo alloys and their composites were performed at five different locations using a Vickers hardness tester (HTM 5027, Vickers Ltd., Crayford, Kent, England) with an applied load of 30 g for 4 sec. A square-based diamond pyramid indenter was used in this measurement.

3.12.2. DC Magnetic test

The DC magnetic experiments for the sintered materials were conducted using a DC permeameter developed at the Wolfson Centre for Magnetics, Cardiff University, as seen in Figure 3.7 [206]. Rectangular samples of dimensions (24 mm ×3 mm ×5 mm) were cut from 30 mm diameter sintered discs using an EDM cutting machine and were ground using silicon carbide papers to remove the scratches from cutting. The samples were closely wound with a search coil for fixed number of turns at 15, a thin wire (around 0.01 mm) of copper coated with enamel was used to wind the pickup coil. The DC magnetic response

for samples was evaluated by changing the magnetic field up to 25 kA/m. The adjustable pole pieces were used to place the sample, forming a closed magnetic circuit. To measure the magnetic flux density, the enamel coating was removed from the ends of search coil and was then connected to integrating fluxmeter. A Gaussmeter with Hall probe was used to measure the magnetic field strength. A computer was connected to both the fluxmeter and Gaussmeter via a GPIB programmable input card. The samples were demagnetized by reducing the magnetic field from the highest value to zero. Input parameters must be included through a LabView interface before start testing. These involve; demagnetization time, amplitude and number of cycles, loop period cross-section area of the sample, the applied peak field and magnetic path length. The budget for uncertainty in measurements is shown in the appendix.

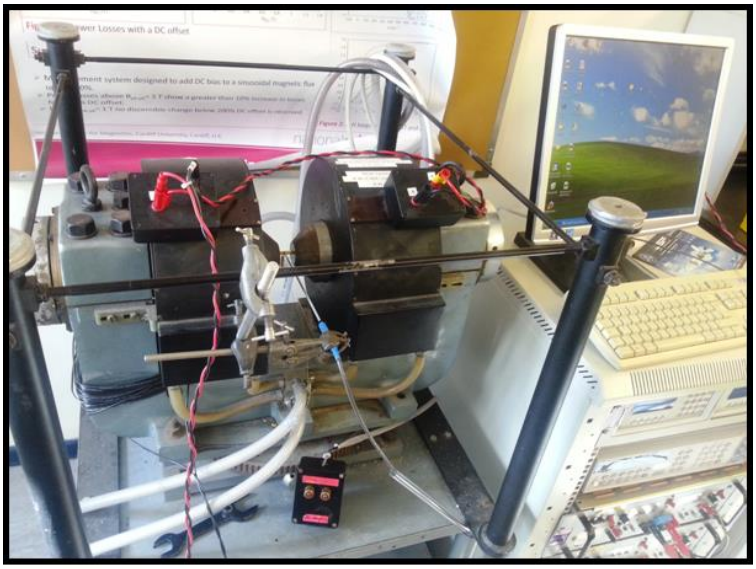

Figure 3.7. Quasi DC magnetic property measurement of a consolidated sample (image).

Chapter 4: Results and discussion of Carbon nanotube composites

4.1. Introduction

Uniform dispersion for CNT in polymer and ceramic matrix can be achieved by mixing CNT with the matrix material in a solvent such as DMF. The aim of the current work is to test the effect of pre-mixing in DMF on dispersion of carbon nanotube in FeCo alloy powder.

4.2. Characterisation of as-received CNTs

4.2.1. As received FeCo powder

As received FeCo alloy powder shows a spherical morphology of wide range variety in size, as shown in Figure 4.1, the Dv (10), Dv (50) and Dv (90) were found to be 9.79 µm, 23.4 µm and 54.0 µm, respectively from Mastersizer analyser, see Figure 4.2.

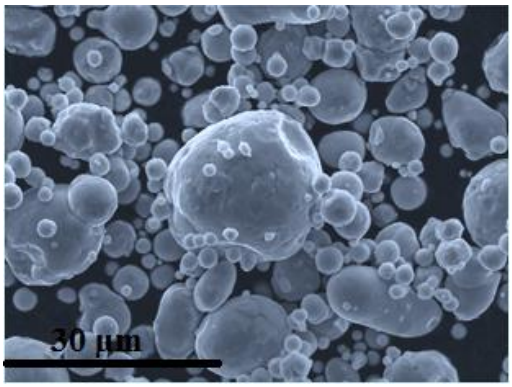

Figure 4.1. SEM of as received FeCo alloy powder.

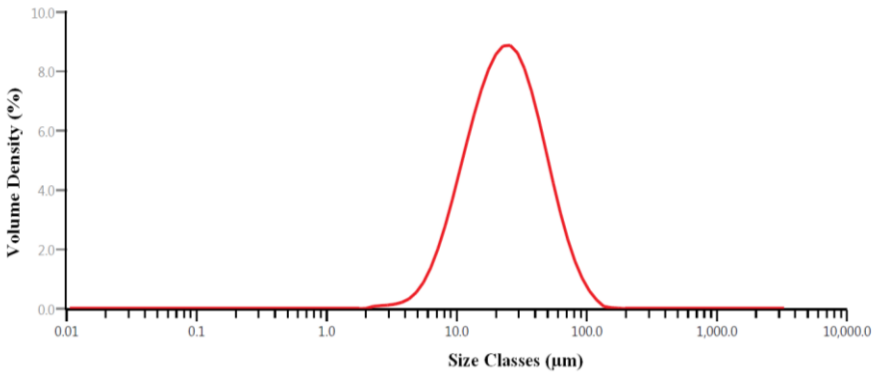

Figure 4.2. Mastersizer curve of particles distribution.

4.2.2. Transmission electron microscopy (TEM)

TEM was used to evaluate as-received CNTs, the arrows in Figure 4.3 identify defects which may be subdivided into dimensional and structural defects.

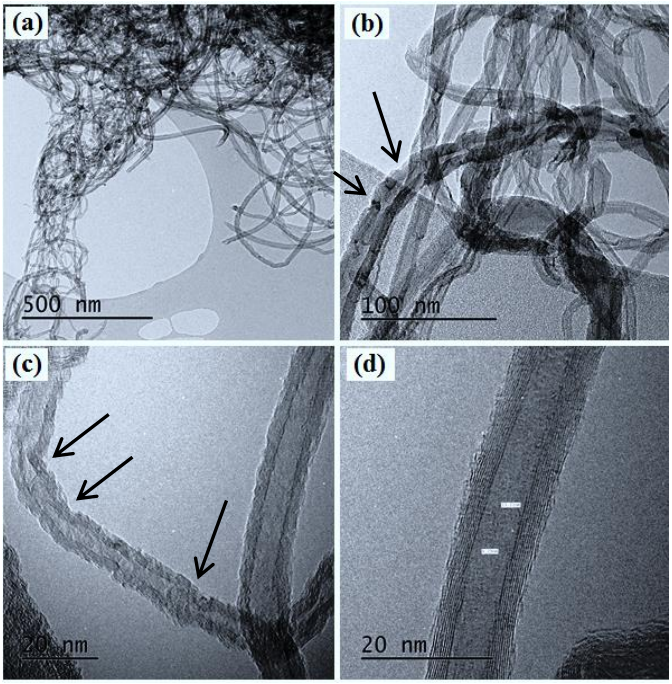

Figure 4.3. Transmission electron micrographs of plasma treated CNTs; the arrows highlight defects.

Most of the CNTs are tangled with each other, which impedes their dispersion. The non-uniformity in the graphene layers, discontinuity on the inside of the fibres and defects on the outer surfaces suggest that the defects may not only be produced during fabrication but also by the functionalization processes. The amorphous carbon was observed on the surface of the fibres. These imperfections are preferred sites for chemical reaction. Some dark areas were observed on the CNTs, which are probably metal inclusions, occurring from the reaction with the metallic catalyst used during their fabrication [211]. The measured dimensions of the CNTs exhibit a mean outer diameter of around 10.45 nm, while the inner diameter is around 4.29 nm. This corresponds to 34 concentric shells of carbon sheets in some cases, but for most CNTs, it was typically about 10. Caps were observed at the ends of some of the CNTs, while some tubes showed open ends. This opening of the hemispherical cap is due to oxidation during the functionalization step.

4.2.3. X-ray characteristics

An XRD pattern of the as-received CNTs, generated using a copper anode, is shown in Figure 4.4. The main peaks for carbon nanotubes were observed at 2θ values of ~ 26º and ~ 43º and are in good agreement with the pattern previously reported in [168]. The d_{002}

calculated using the Bragg equation ($\lambda = 2d\sin\theta$) is 0.3445 nm, which is consistent with spacing for graphite of 0.3348 - 0.3360 nm (5 % experimental error). A broadening of the peak at ~ 26º could be observed, and is likely due to the presence of oxides introduced to the CNTs during functionalization process; with the variation in *d* spacing due to the incorporation of oxygen between the lattice planes. Broadening could also be due to contributions from the amorphous regions of the CNTs.

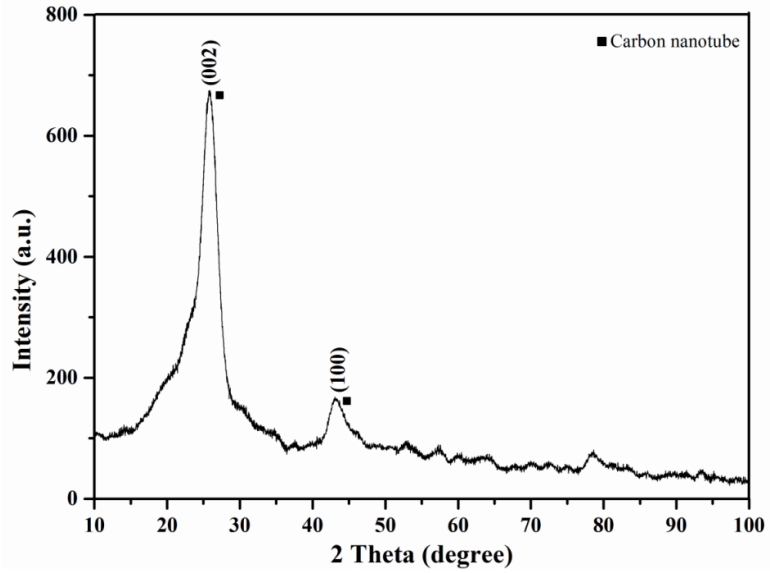

Figure 4.4. XRD pattern of as received CNTs, the main diffraction planes are labelled.

4.2.4. Raman spectrum of Carbon nanotube

Raman spectrum test was performed for as received and plasma treated CNTs, the defects density for nanotube is detected by D band. The intensity of this band was increased after plasma treatment (Figure 4.5), which means functionalization processes to introduce O_2 group on CNT outer layer effect on the quality of CNTs.

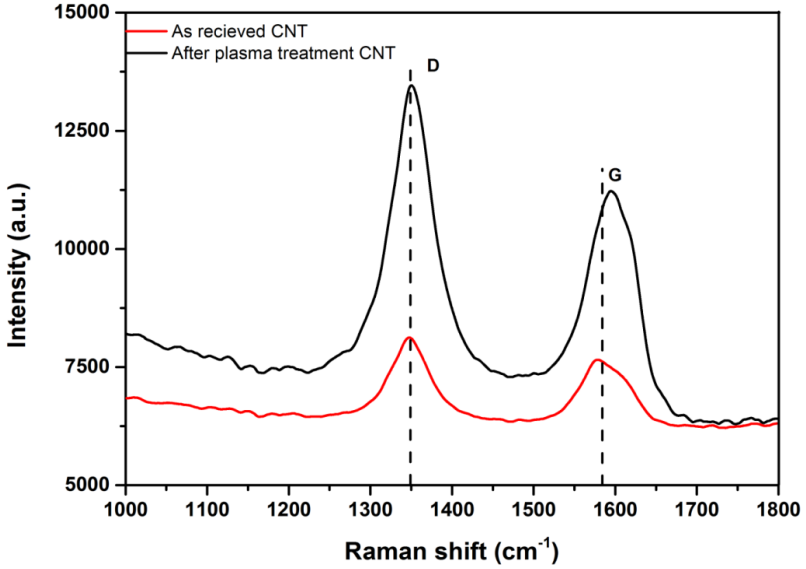

Figure 4.5. Raman spectrum of as received and plasma treated CNTs.

4.3. Effect of ball milling and CNT on composite

4.3.1. Densification and density

The densification behaviour of as received monolithic FeCo alloy and CNTs composite were different as shown in Figure 4.6. The volume fraction of reinforcement affected the densification behaviour. The composite materials densified at lower temperatures compared to as received alloy, which could be due to the influence of CNTs on the densification mechanism. In addition, the ball milling step decreased the particle size in the composite which increased the surface area between reactants; leading to faster densification kinetics through improved mass transport by diffusion [194, 212].

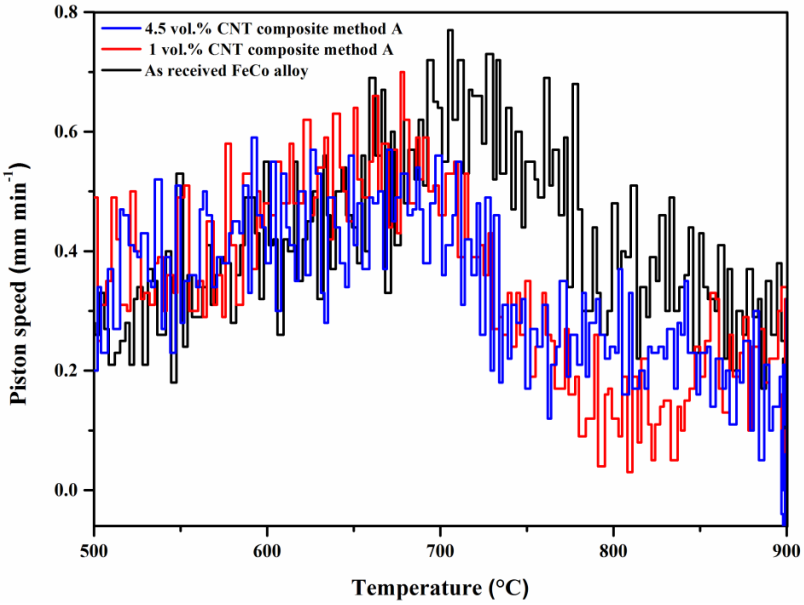

Figure 4.6. Shrinkage sintering curve, for the as received FeCo alloy in comparison to the 1 and 4.5 vol.% CNT composite materials prepared using method A.

The density was higher in the composites containing up to 1.5 vol. % CNT as compared to the monolithic equiatomic FeCo alloy Figure 4.7. The highest value for density was achieved for the 0.5 vol. % CNTs composites; while the density dropped sharply at higher volume fractions. This behaviour was attributed to the increased agglomeration of the CNTs, which led to induce porosity in the structure of composite material, more agglomeration was introduced at high volume fraction for reinforcement leading to more drop in density.

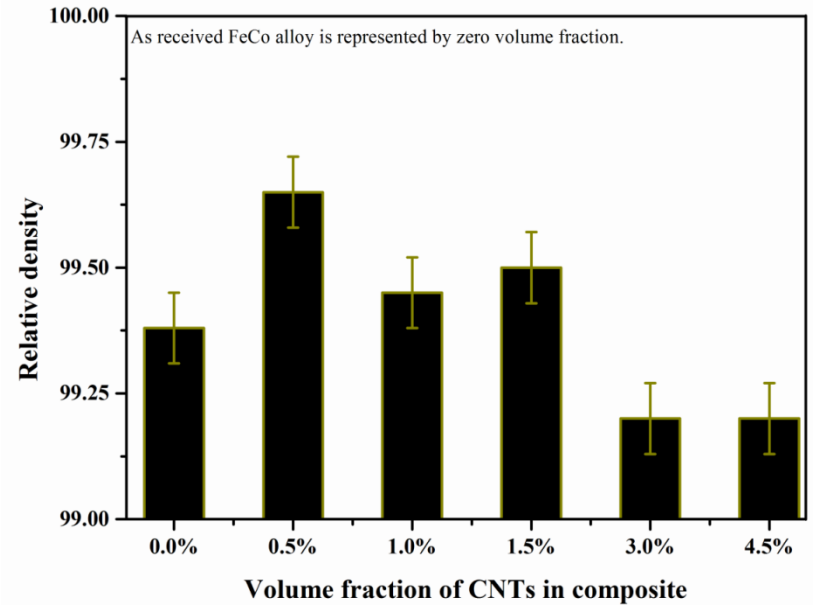

Figure 4.7. Relative density of SPS sintered composite materials fabricated using method A against volume fraction of CNTs (%) compared to monolithic FeCo alloy.

4.3.2. Oxidation of powder

Figure 4.8 shows a comparison between monolithic FeCo alloy powders before and after ball milling processes. The maghemite phase was formed in FeCo alloy powder after 1.5 h ball milling in the air atmosphere. The FeCo alloy powder is heated up during ball milling, leading to formation oxide layer, which deteriorates densification during sintering because it forms a diffusion barrier during sintering.

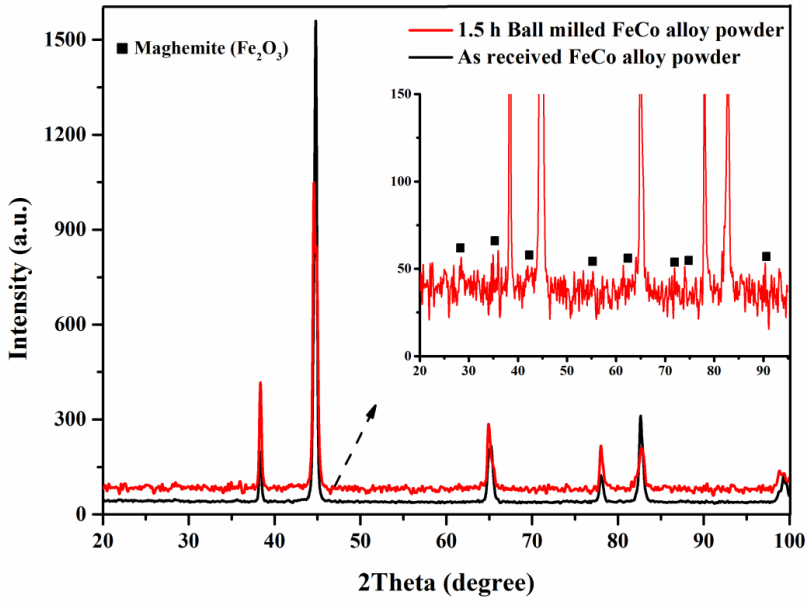

Figure 4.8. XRD shows oxidation of FeCo alloy due to ball milling in air atmosphere.

4.3.3. X-ray diffraction characterization

Figure 4.9 a and b show wide range and narrow slow scan range XRD patterns (Co Kα) for the sintered as received, ball milled FeCo alloy and CNT-FeCo alloy composites. The

enlarged pattern of the superlattice line (100) (Figure 4.9 b) was used to observe the ordering of the FeCo alloy, which was scanned in the range of the expected superlattice line according to [59]. The pattern shows that the addition of 1 vol. % CNTs with ball milling produced a reduction in the antiphase domain size for the ordered crystalline phase. The crystallite domain sizes were calculated using the Scherrer equation of the (100) peak (Figure 4.9 b) as 45.75 nm to 28.10 nm and 34.32 nm for as received Fe50Co alloy, 1 vol. % CNT and 4.5 vol. % CNT-FeCo alloy composites, respectively. The composite with a higher volume fraction of CNTs displayed an increase in crystallite size, yet a high intensity of order structure was observed in the XRD patterns. As such, it appears that an increase in the volume fraction of CNTs produces an increase in the volume fraction of ordering as compared to the monolithic alloy and low volume fraction composites.

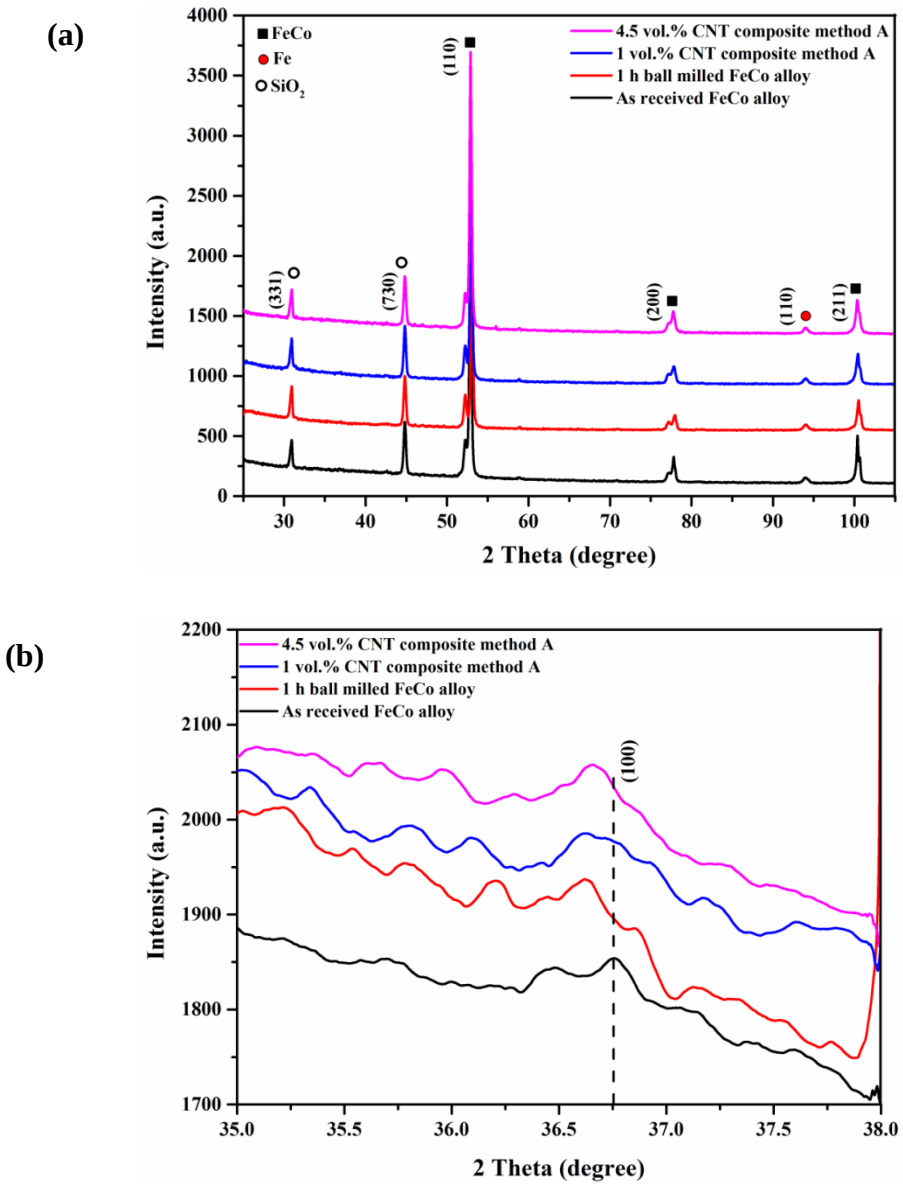

Figure 4.9. XRD patterns (a) slow scan for sintered FeCo as received alloy, 1 h ball milled FeCo alloy, 1 vol.% CNT composite and 4.5 vol.% CNT composite; (b) (100) Superlattice peak for displayed material.

Strains can be classified into uniform strain and non-uniform strain, the former shifting peaks of X-ray reflection to lower angles, while the latter lead to broadening and to reduce the intensity [60]. Ball milling processes can induce stresses in powder, however, the intensity of ball milling was very low, as the process was performed for BPR 1:1 for 1 h to disperse the reinforcement in the FeCo alloy. Residual stress may be released during sintering at high temperature. This suggests the effects of strain on broadening X-ray reflection are minimal, as the recovery reduces the magnitude of the residual stress and recrystallization eliminates the residual stress leading to the maximum sharpness in diffraction line [60].

4.3.4. Optical microstructure

Figure 4.10 shows the optical microstructure for both FeCo alloy and composites.

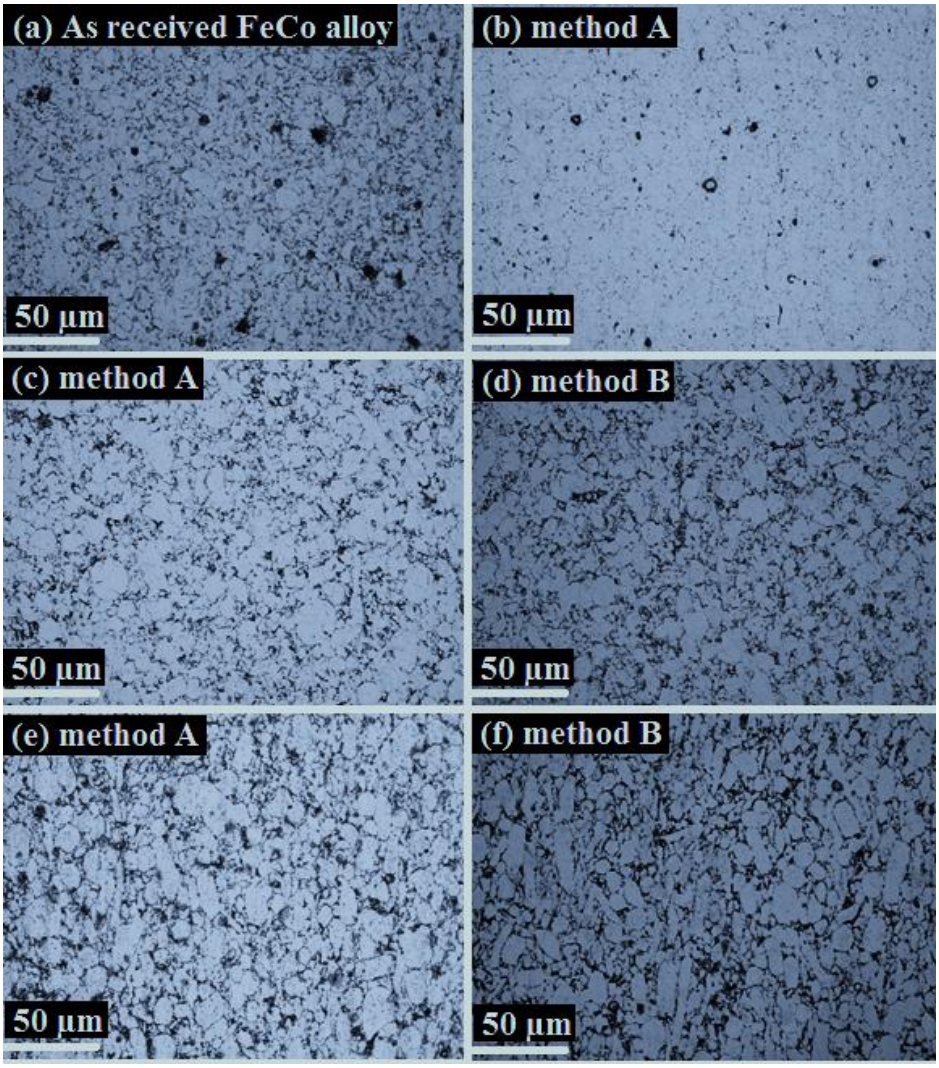

Figure 4.10. Optical microstructure of: (a) FeCo alloy; (b), (c) and (e) are 0.5 vol.%, 1 vol.% and 3 vol.% CNT composite, respectively prepared by method A. (d) and (f) are 1 vol.% and 3 vol.% CNT composite, respectively prepared by method B.

A very fine microstructure was observed for the 0.5 vol. % CNT composite, which reflects the role of CNTs in refining the microstructure. However, this behaviour is different at higher volume fractions of CNTs due to the segregation of CNTs to the grain boundaries. This agglomeration causes poor densification at higher volume fractions, therefore, pores and elongated particles were observed at high volume fractions. The ball milling process changes the shape of the powder particles; and thus, an elongated particulate structure is observed after sintering. This structure becomes more evident due to the increasing fraction of agglomeration and the poor densification at the high volume fraction of CNT. No difference can be observed in the microstructure between the two methods used to prepare the composites.

4.3.5. Magnetic properties of consolidated materials

The upper halves of hysteresis curves of monolithic FeCo alloy and composite materials are presented in Figure 4.11.

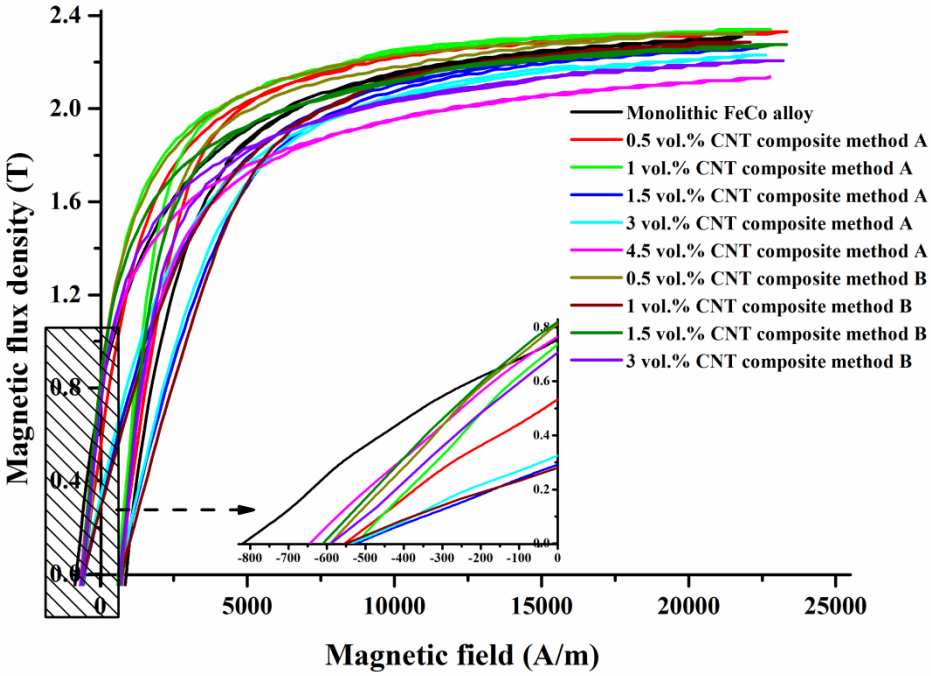

Figure 4.11. Upper halves of hysteresis curves for FeCo alloy and its composites.

The magnetic properties of the FeCo alloy and composite materials were fabricated following mixing methods A and B are summarised in Figure 4.12. The saturation induction is highly dependent on sample density; with the saturation induction trend closely following that of the density trend (Figure 4.7) with increasing volume fraction of CNTs. The highest saturation induction was achieved in the composite material at 1 vol. % CNTs, consistent with it having a high density. With an increased volume fraction of

CNTs, a drop in saturation is seen due to the agglomeration of the reinforcement as observed in (Figure 4.10) and the subsequent of that drops in density.

The coercivity was declined in the composites produced by both fabrication methods in comparison to the monolithic FeCo alloy. Coercivity is typically inversely proportional to the grain size; however, the results indicate a decrease in coercivity with decreasing grain size. Previous models in [52, 213] have explained this behaviour in terms of the anisotropy energy. For a very small grain size (D) < 100 nm the ferromagnetic exchange length will often be larger than the grain size (D). The exchange length in a soft magnetic alloy is calculated as follows:

$$L_{ex} = (A/K_1)^{1/2} \quad (4\text{-}1)$$

Using exchange constant A=1.7×10^{-11} J/m and magnetic anisotropic constant K_1=8 kJ/m^3 for calculation the exchange length in FeCo alloy [214], giving L_{ex}= 46 nm, which is in value higher than the measured ordered crystallite size as 45.75 nm to 28.10 nm and 34.32 nm for as received FeCo alloy, 1 vol. % CNT and 4.5 vol. % CNT, respectively. Meanwhile, the change in coercivity with crystallite size follows Néel's model. Therefore, the effective anisotropy energy is averaged over a number of grains and is thus reduced in magnitude. In this anomalous behaviour of nanocrystalline magnetic materials, the coercivity exhibits D^6 dependence, which contrasts with the conventional rule for polycrystalline magnetic materials, which exhibits 1/D dependence. As discussed previously, the Scherrer calculations show a crystallite size below 100 nm in the monolithic FeCo alloy, which decreases further for the composite samples. This may, therefore, account for some of the trends seen in coercivity. However, at the highest volume fraction of CNTs, the coercivity increased. Néel [215] suggested that the coercivity is directly proportional to the volume fraction of non-magnetic inclusions. Residual stresses produced due to the difference in the coefficient of thermal expansion between the CNTs and the monolithic equiatomic FeCo alloy may lead to domain wall pinning, thereby increasing coercivity and creating a trade-off between coercivity decrease due to grain size and increase due to domain wall pinning as the volume fraction of reinforcement is increased.

A high resistivity is crucial for producing low-loss components. Resistivity measurements of the monolithic FeCo alloy and CNT composites fabricated using method A are shown as an insert in Figure 4.12. A slight increase in resistivity is observed from 3.5

μΩ.cm for monolithic FeCo alloy to 5.6 μΩ.cm for the composite with the highest density up to 1.5 vol. % CNTs. Higher volume fractions of CNTs (3 and 4.5 vol. %) further increase the resistivity of composite materials, which may be also due to the increase in the level of porosity.

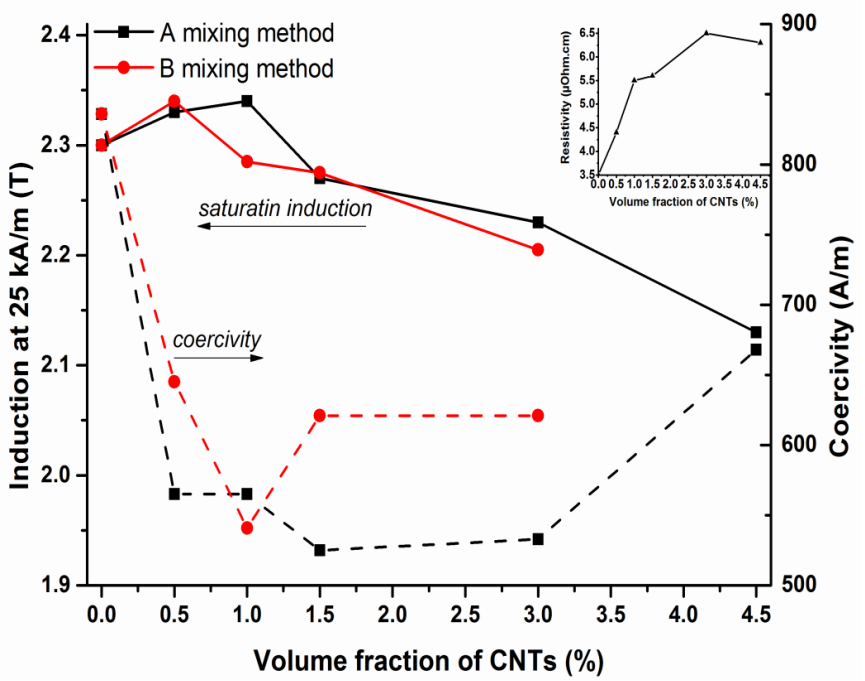

Figure 4.12. Effect of volume fraction of CNTs on: saturation induction; coercivity of FeCo-CNT composites, the monolithic alloy is represented as 0 vol. % CNT. The insert curve shows the change in resistivity with increasing volume fraction of CNTs for composites prepared using method A.

4.3.6. Mechanical properties of the sintered materials

Tensile stress-strain curves for monolithic FeCo alloy and CNT-FeCo alloy composite materials were prepared following two producers of dispersion for different volume fractions are presented in Figure 4.13. While summarise for the tensile properties and the mechanical hardness of the FeCo alloy and composite materials prepared using the two different methods of dispersion are presented in Figures 4.14 and 4.15 respectively. The addition of a small amount of CNTs up to 1 vol. % produces an improvement in tensile strength in comparison to the base alloy. The greatest improvement is observed with the addition of 0.5 vol. % CNTs. In this case, a tensile strength and Vickers hardness of 821 ±30.77 MPa and 352 ±15.15 VHN, respectively were measured.

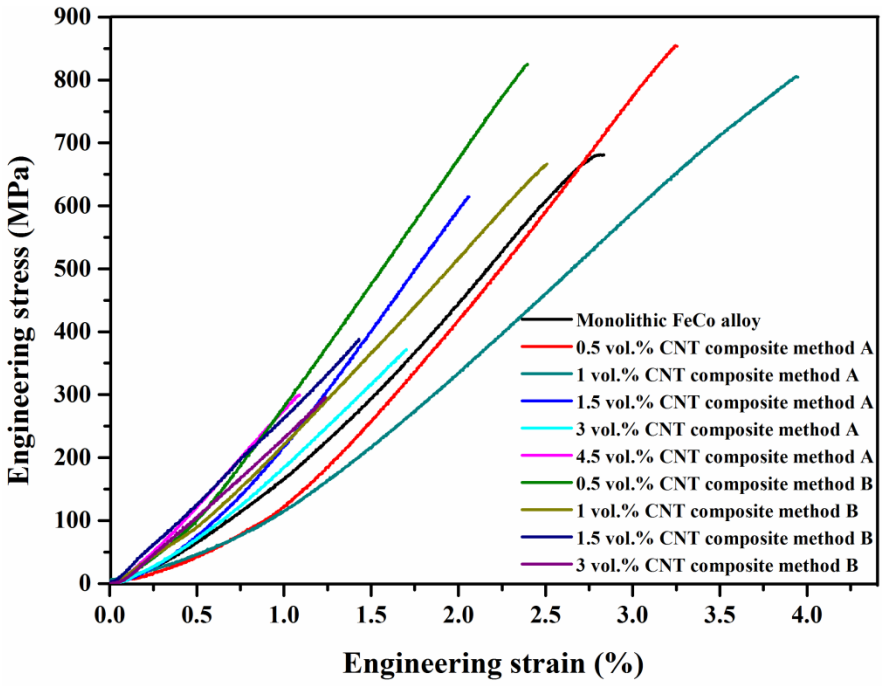

Figure 4.13. Tensile stress-strain curves of monolithic FeCo alloy and composite materials.

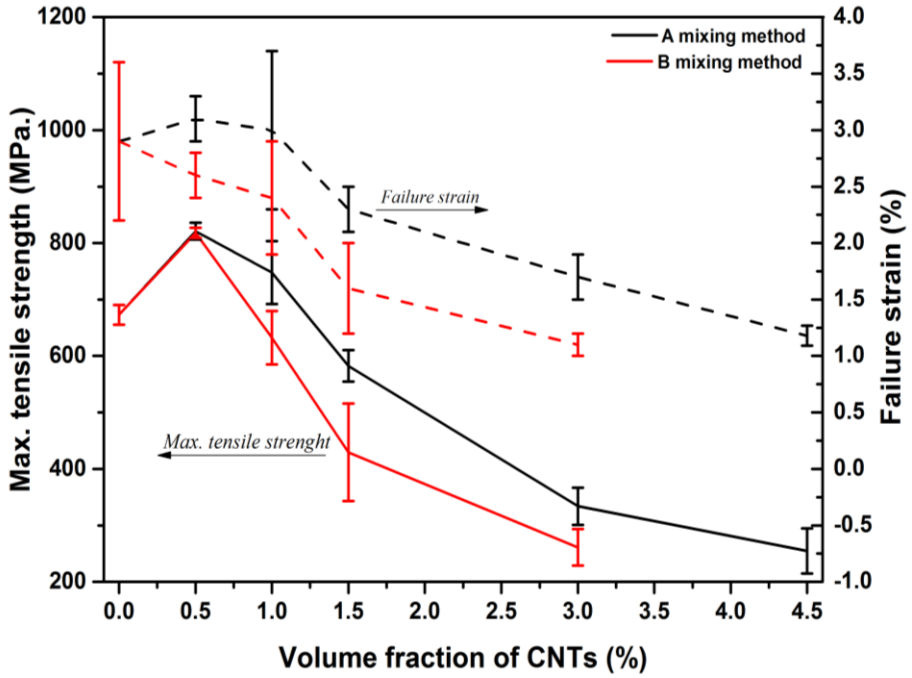

Figure 4.14. Effect of volume fraction of CNTs on: tensile strength (solid lines) and failure strain (dashed lines) of (Fe50Co)-CNT composites fabricated by two different dispersion methods and SPS; the monolithic alloy is represented as 0 vol. % CNT.

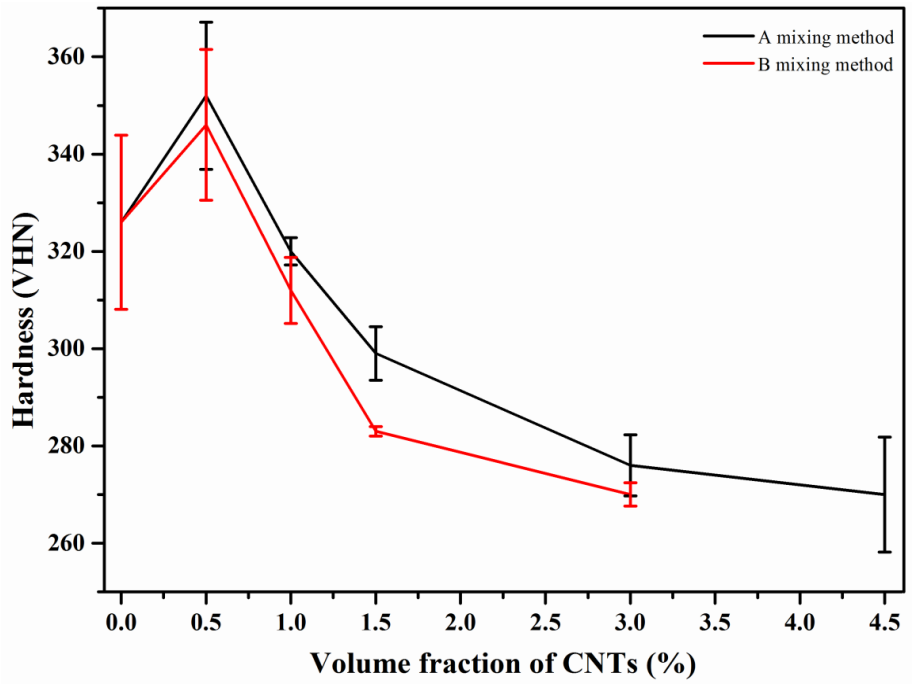

Figure 4.15. Effect of volume fraction of CNTs on: hardness of (Fe50Co)-CNT composites fabricated by two different dispersion methods and SPS; the monolithic alloy is represented as 0 vol. % CNT.

There are different mechanisms for improvement the mechanical properties of composite materials such as load transfer between the matrix and reinforcement, grain size refinement and dislocation strengthening mechanisms. It is reported that the mechanical properties are highly correlated with the grain size in FeCo alloys; following the Hall-Petch relationship in both the ordered and the disordered state [216].

$$\sigma_y = \sigma_i + k_y d^{-1/2} \qquad (4\text{-}2)$$

where σ_y is the yield strength, d is the average grain diameter, σ_i is materials constant describing the intrinsic resistance of the lattice to dislocation motion, and k_y is the strengthening coefficient.

The optical micrographs of the FeCo composites show that the addition of a low volume fraction of 0.5 vol. % CNTs refines the microstructure and improves densification. Thus, an increase in tensile strength and hardness at low volume fractions is achieved. However, the mechanical properties deteriorate at higher volume fractions of reinforcement using both fabrication processes. The decrease was higher for composites produced using mixing method B. It was experimentally observed that the CNTs tended to separate as a surface layer on the powder after drying using method B, leading to more agglomeration of the CNTs and subsequently poorer densification.

An increase in the failure strain was observed in the composites containing low volume fractions of reinforcement. EDS results (Figure 4.16) for monolithic FeCo alloy and its composites show a deviation in the chemical composition of the composite in

comparison to the alloy. This suggests that the CNTs lead to chemical deviations in the matrix surrounding them. It has been reported [20] that inclusion particles in FeCo alloy cause a chemical deviation in the matrix around them, which could lead to disorder around the inclusions and possible improvement in the ductility. Moreover, additions of small amounts of CNTs lead to the development of a very fine microstructure, and may form metal carbides because of the reaction with any amorphous carbon on the CNTs. This may not necessarily be detectable by XRD, since the amount of carbides produced would be lower than the sensitivity of the technique. These two parameters play an important role in the improvement of ductility, as has been reported previously [38].

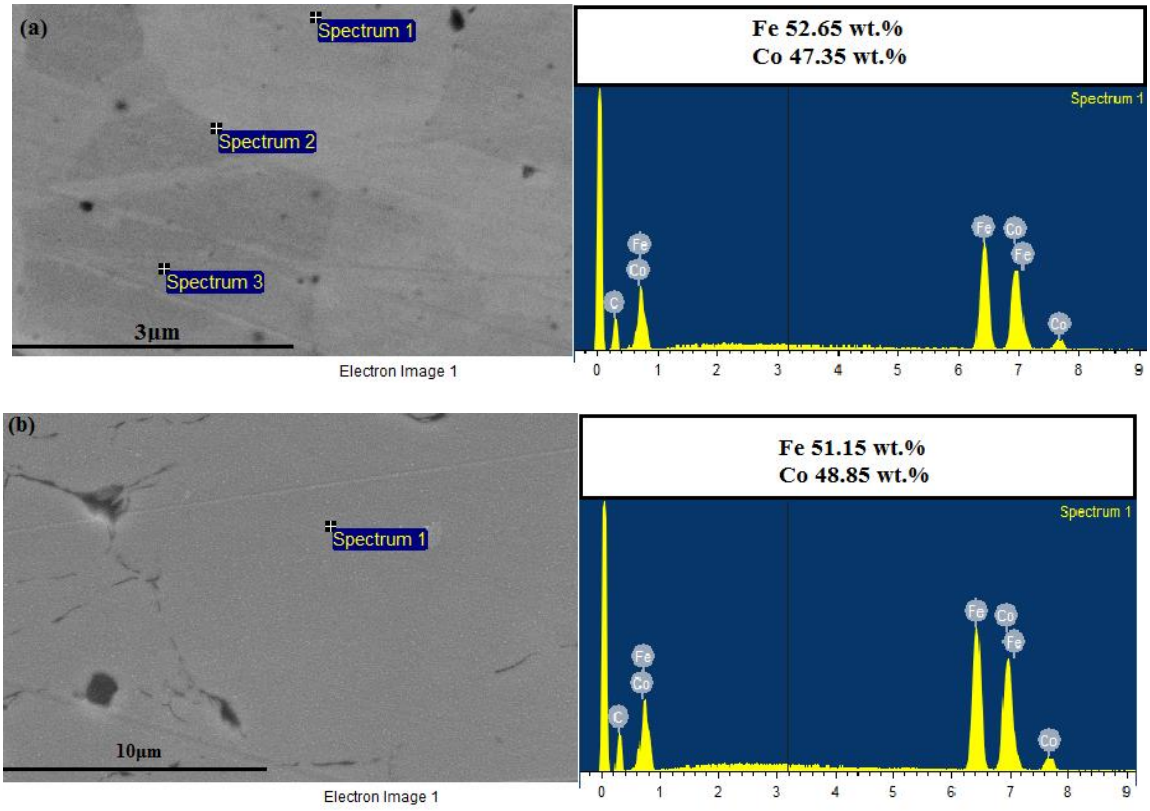

Figure 4.16. EDS spectra of (a) Monolithic FeCo alloy, (b) 3 vol. % CNTs composite method A.

4.3.7. Fractographic studies

Fractographic images of the monolithic FeCo alloy and composite materials with different volume fractions of CNTs are shown in Figure 4.17. Mixed modes of fracture between intergranular and transgranular were observed for both the monolithic FeCo alloy and the composite materials. Small tubular holes were observed on the fracture surface, as indicated by arrows in the image (c), which are likely to be the former locations of CNTs were extracted during fracture. Porosity can be seen to increase at high volume fractions of

CNTs, as shown in image (d), while images (e) and (f) show the agglomeration of CNTs between powder particles. The high magnification insert in (f) shows the presence of CNT bundles at the boundary. These bundles would have hampered densification in the composite.

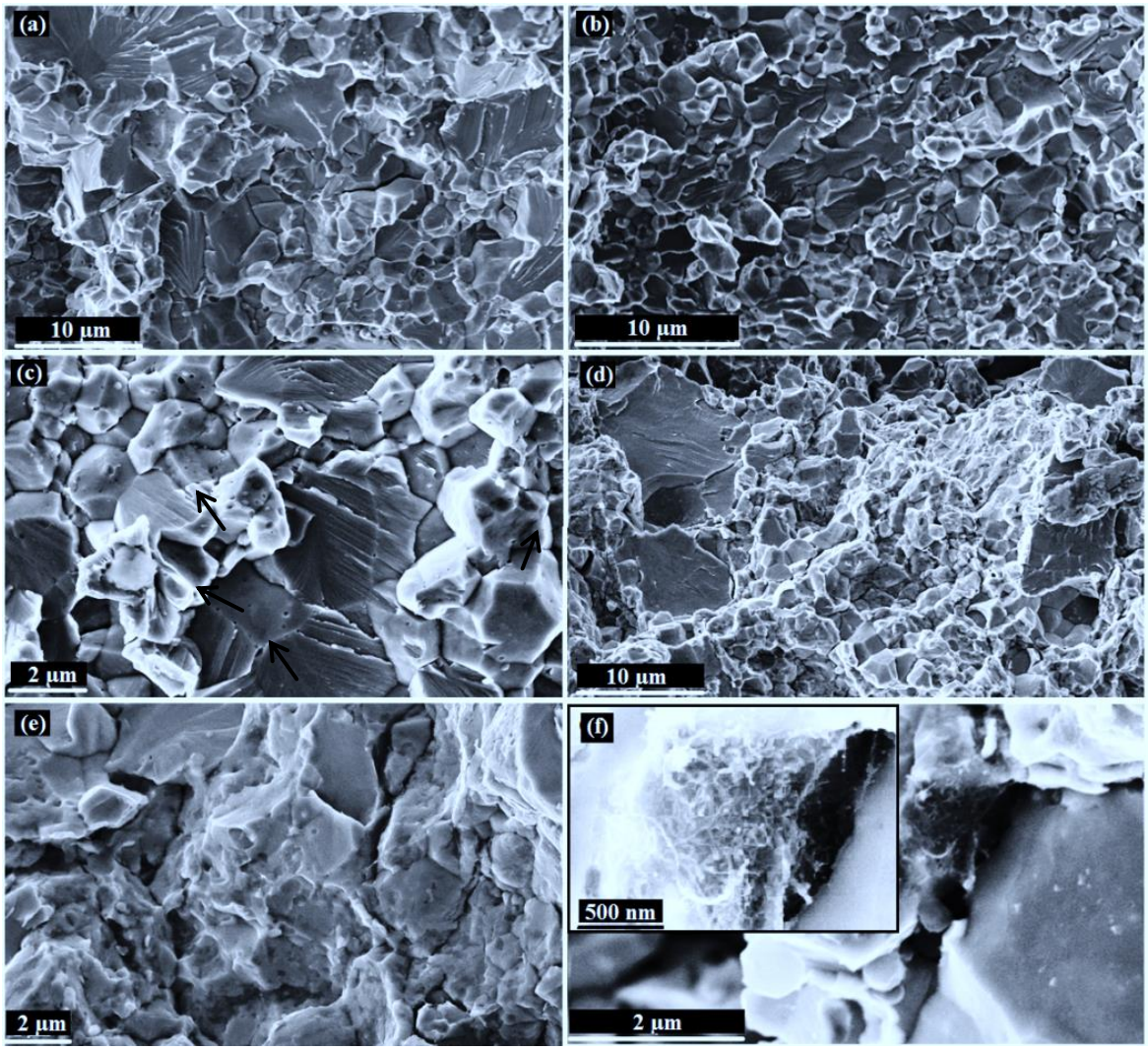

Figure 4.17. Fractographic images of materials prepared using rout A : (a) FeCo monolithic alloy; (b) 0.5 vol.% CNT composite; (c) 1 vol.% CNT composite; (d) 1.5 vol.% CNT composite; (e) 3 vol.% CNT composite; (f) 4.5 vol.% CNT composite. High magnification image inert in (f) shows CNTs bundle between powder particles boundaries.

4.3.8. Raman spectroscopy

In addition to the main characteristic bands in carbon nanotube, there is also an exceptional band, which can only be observed in SWNT, and is a radial breathing mode (RBM) in the range 100 cm^{-1} to 400 cm^{-1} [192, 217]. Figures 4.18 (a and b) show the Raman spectra results for the CNT-FeCo alloy composites and the change in *R* ratio with respect to the volume fraction of CNTs for plasma treated MWCNTs and the composites fabricated by

the two different methods. A split in the G band was observed, which demonstrates that the integrity of CNTs is maintained throughout the fabrication process, as reported in [194]. The main reason for this is due to the stronger tube morphology of the CNTs in contrast to the flat morphology of graphene sheets. However, the splitting in the G band is less pronounced in MWCNT and in large radius CNTs. This suggests that a thinning in the radius of the CNTs may occur during the fabrication process, reducing the number of layers; or that the radii of most the CNTs in the powder are in the range of band splitting, since DWCNTs were observed in TEM images. Mixing method B gives a high value of R at low volume fraction, which reflects the effect of the processing route on the quality of CNTs. The damage of the CNTs was reduced at higher volume fraction as compared to mixing method A. This could be due to the less effective ultrasonic dispersion processing of higher volume fractions of CNTs, due to a less effective transmission of the ultrasonic wave in solution, leading to a greater segregation of CNTs on the surface of the slurry. With dispersed 'pockets' of CNTs present in the powder, many of the CNTs were therefore shielded from damage during ball milling. Inam et al. [199] reported that the structural features of the CNTs in composites are very sensitive to the spark plasma sintering conditions and to the matrix material. This means that the improvement in the quality of CNTs could be due to the effective thermal annealing during cooling in SPS furnace following the sintering process. The stress on the surface of the CNTs introduced by the functionalization process may be released by removing defects and oxides from the CNTs.

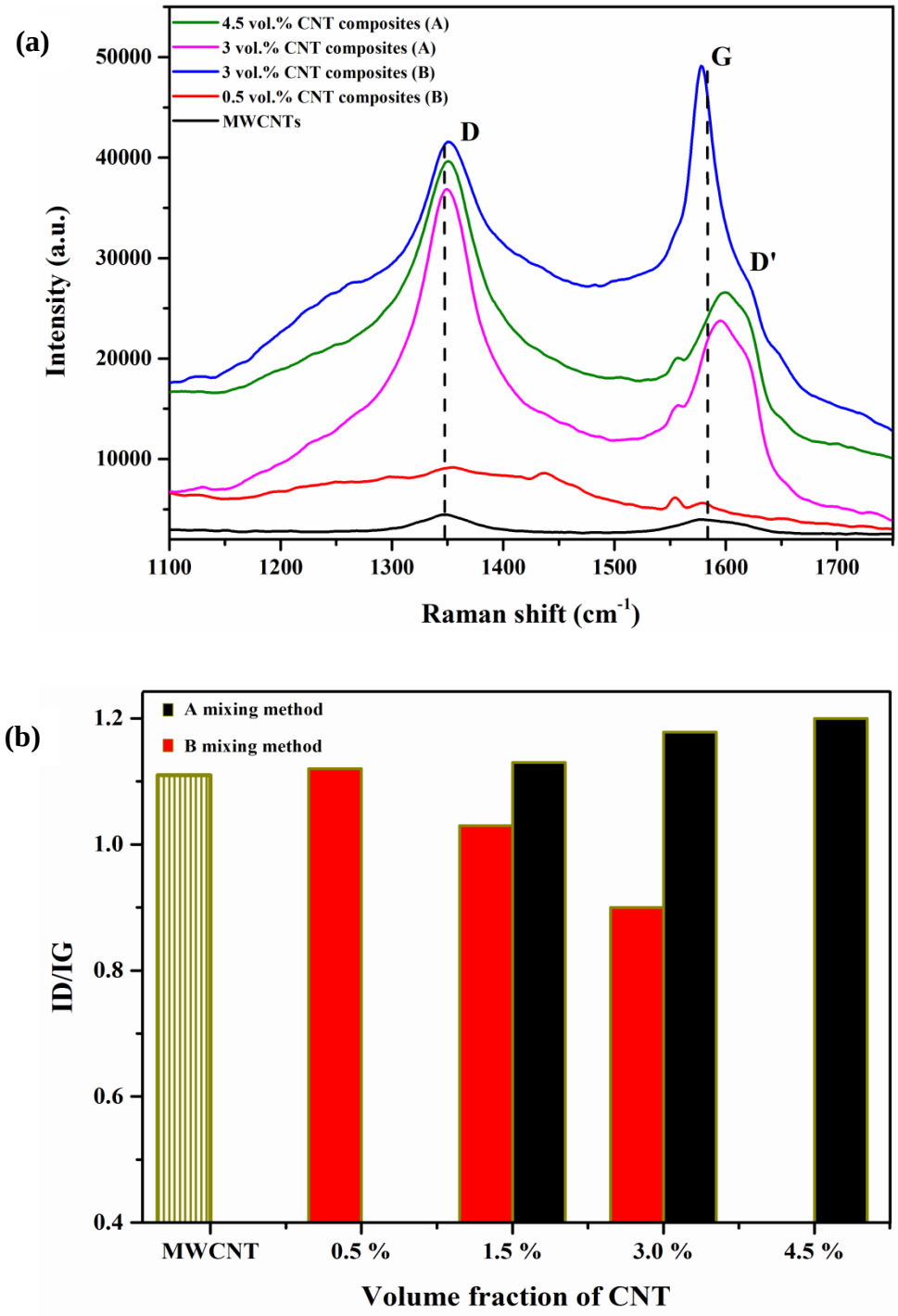

Figure 4.18. (a) Raman spectra of MWCNTs and FeCo alloy composites; (b) Intensity ratio (R =ID / IG) of composite fabricated by two methods.

Summary

CNT-FeCo alloy composites were prepared with and without pre-mixing in DMF followed by ball milling for different volume fraction for reinforcement. The samples were sintered at conditions of 900 °C, 80 MPa, 50 °C/min for 3 min as reported elsewhere. It is observed that the CNTs tended to separate as a surface layer on the FeCo alloy powder after drying the solvent, due to the wide different in the densities. The microstructure was refined after embedding CNT in FeCo alloy. Surface observations of as-received CNTs revealed a layer amorphous of carbon, which can be a source for carbides in the microstructure, however, their amount might beyond the sensitivity of XRD instrument. Dispersion of CNTs by only ball milling showed better properties than composites prepared with premixing in solvent, however, the properties were improved for amount of 1 vol.% CNTs followed by a significant decrease due to inhomogeneous dispersion at high volume fraction.

Chapter 5: Results and discussion of GNP and GNP/CNT composites

5.1. Introduction

Graphene nanoplatelet GNPs is promising reinforcement material, due to the unique properties for this reinforcement. However, the challenge here in addition to the much difficulty in obtaining uniform dispersion as a compared to CNTs, is the easily slipping between the overlapped GNPs under stresses, causing fast deterioration in properties. The main aim of this work was to reduce overlapping and to improve dispersion of GNPs by inserting CNTs among them, by the strong interact between GNPs with the surface of CNTs throughout π-π attractions.

5.2. TEM analysis of GNPs and CNTs

The graphene nanoplatelets and carbon nanotube morphologies are shown in Figure 5.1.

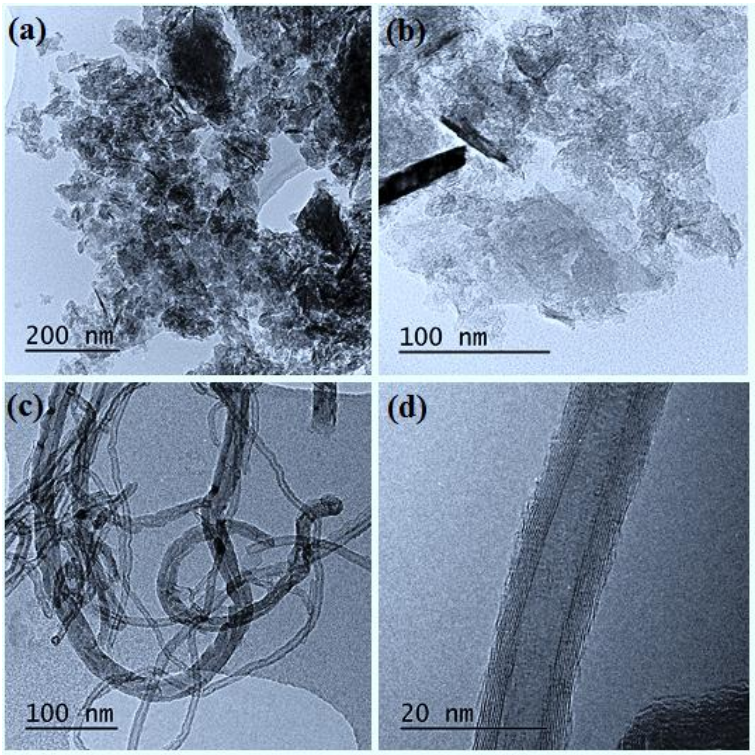

Figure 5.1. Transmission Electron Microscope (TEM) of; (a, b) GNP and (c, d) CNT.

A wrinkled morphology is observed for the GNPs, which may produce porosity in the composites. A variety of sizes were observed, and very small sheets were noticed to be stacked on larger sheets. The thickness of the GNP sheets ranges from ~ 4 to 42 nm. The

width of the sheets ranges from ~ 27 to 223 nm, while the length varies from ~ 85 to 487 nm. Most of the CNTs are tangled together, which impedes their dispersion. The measured dimensions of the CNTs exhibit a mean outer diameter of around 10.45 nm, while the inner diameter is around ~ 4 nm (corresponding to ~ 10 concentric shells of carbon sheets).

5.3. Characteristics of composites

5.3.1. Optical microstructure

The optical micrographs of the monolithic FeCo alloy and composite materials are shown in Figure 5.2. The uniform structure in as received monolithic FeCo alloy as shown in (Figure 5.2a) was converted to elongated grains structure in the sintered samples prepared with powders that had been ball milled, as shown in Figure 5.2b. The microstructure of the GNP composites was inhomogeneous (Figure 5.2c) with excessively growth grains surrounded by small grains.

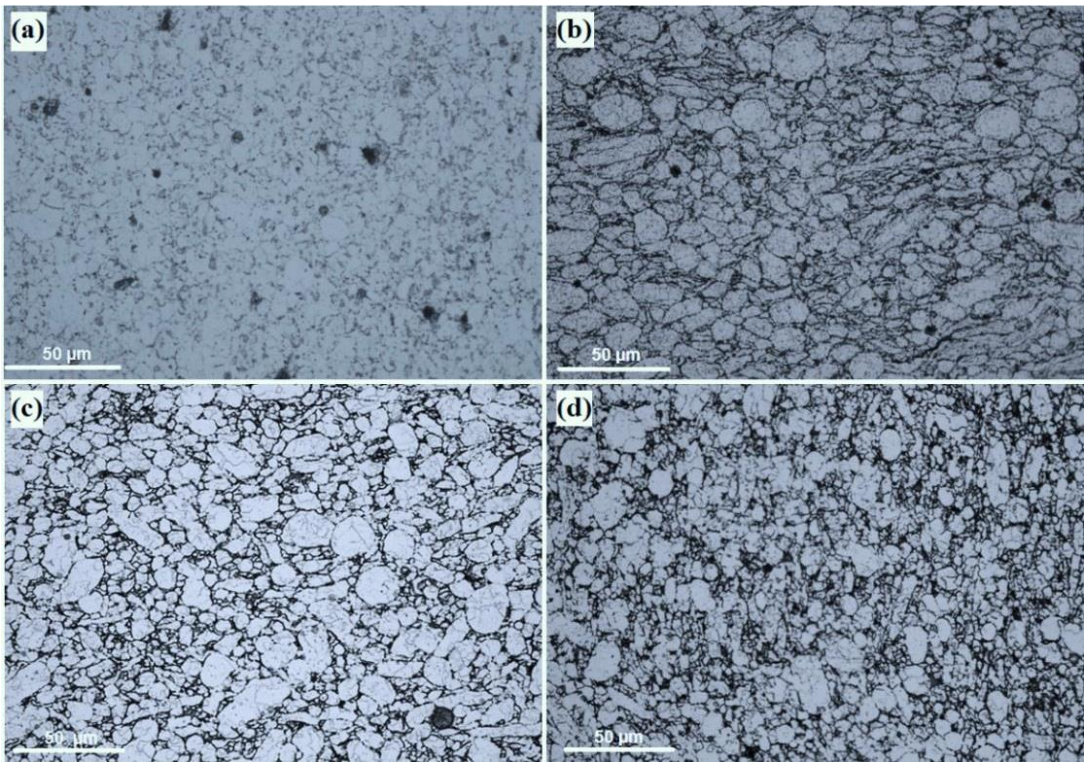

Figure 5.2. Optical microstructure of: (a) as received FeCo alloy; (b) 1 h ball milling FeCo compact (c) 2 vol.% GNP composite (d) 2 vol.% GNT composite.

Adding a small amount of CNTs (1:10) significantly change the microstructure. The homogenous microstructure observed may result from the uniform dispersion and prevent the stacking of the nanophases. Figure 5.2d shows refinement in the microstructure, which is occurred due to the addition CNTs to GNPs as compared to the GNP composite (Figure 5.2c). An increase in the volume fraction of reinforcement leads to more agglomeration for

reinforcement in the microstructure, which results in increased porosity. Impurity elements such as (O, N, H_2) may segregate at grain boundaries, grain boundaries were investigated using EDS spectra. The spectra were taken from the grain boundaries of sintered FeCo alloy and 1 vol. % GNP-FeCo alloy composite did not show any difference in chemical composition between the materials.

5.3.2. Densification of sintered FeCo alloy composites

The shrinkage curves of the consolidated monolithic FeCo alloys and composite materials are presented in Figure 5.3. The significant difference is observed between as received FeCo alloy with respect to ball milled FeCo alloy and FeCo alloy composites, meanwhile the influences of ball milling on structure through introducing stresses, dislocations, refining grain size, and contamination are the most important on densification rather than the reinforcement. The relative density of the spark plasma sintered GNP-FeCo alloy and GNT-FeCo alloy composites are shown in Figure 5.4. Almost full densification was achieved for the as received FeCo alloy, with a relative density higher than 99 %. In comparison, the final density of the FeCo alloy after 1 h ball milling was reduced to 98 %. The addition of reinforcements increased the final density in comparison to the ball milled FeCo alloy, yet it decreased overall with increasing volume fraction of reinforcement. The density of the GNT composites was lower as compared to the GNP composites, which might be attributed to the presence of carbon nanotubes in the GNT composites. The 2-D morphology of the GNPs leads to a higher surface area as compared to the 1-D carbon nanotubes. An increase in the contact area between the GNPs and the matrix alloy leads to a higher density; while, CNTs inserted between the GNPs may introduce porosity between the sheets and reduce the density.

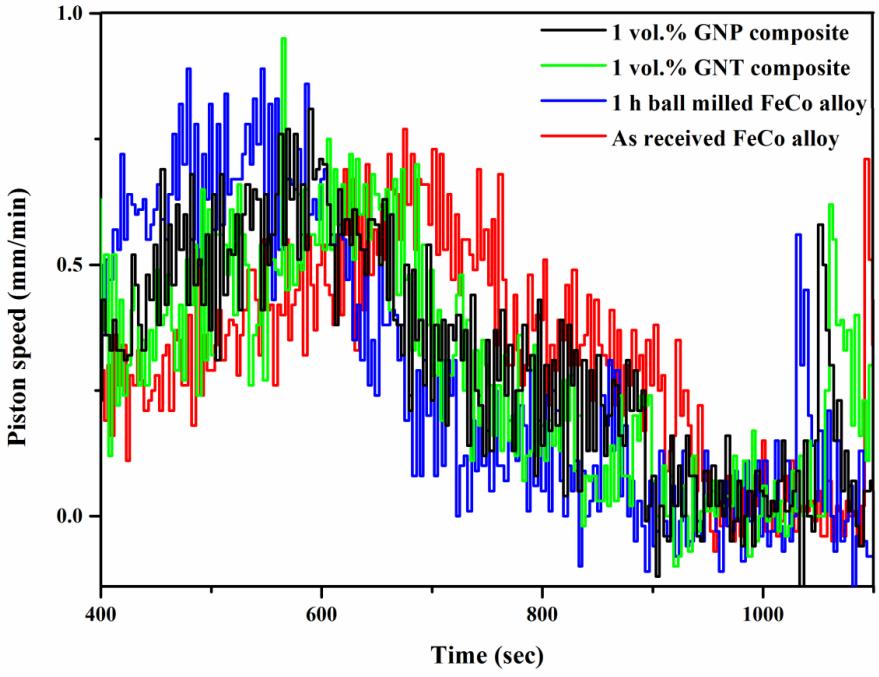

Figure 5.3. Shrinkage curves of the indicated materials.

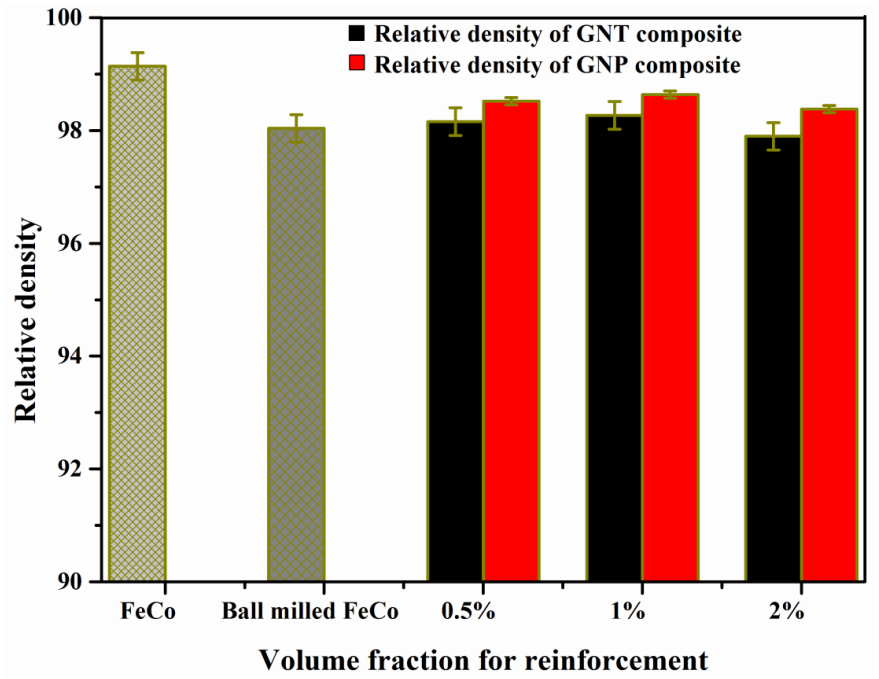

Figure 5.4. Variation of relative density of SPS sintered composite materials against volume fraction of GNP and GNT (vol. %) as compared to the monolithic FeCo alloy.

5.3.3. X-ray diffraction analysis of the consolidated materials

XRD patterns of the sintered FeCo alloy and its composites are presented in Figure 5.5. In spite of the slow X-ray scan rate used for all of the FeCo alloy composites, the distinctive 2θ =26.5º peak of the GNPs was not observed due to its relatively low volume fractions, which are beyond the sensitivity of the XRD technique. To clarify any shift in peaks position, the figure was enlarged, as shown in the insert (Figure 5.5). The fundamental peaks were shifted to lower angles in the composite materials as compared to the as

received FeCo alloy. This is due to the stresses introduced during ball milling. A broadening of the XRD peaks was also observed in the composite materials, due to microstructure refinement following ball milling. The volume fraction of the ordered state has an effect on both the magnetic and mechanical properties of FeCo alloys.

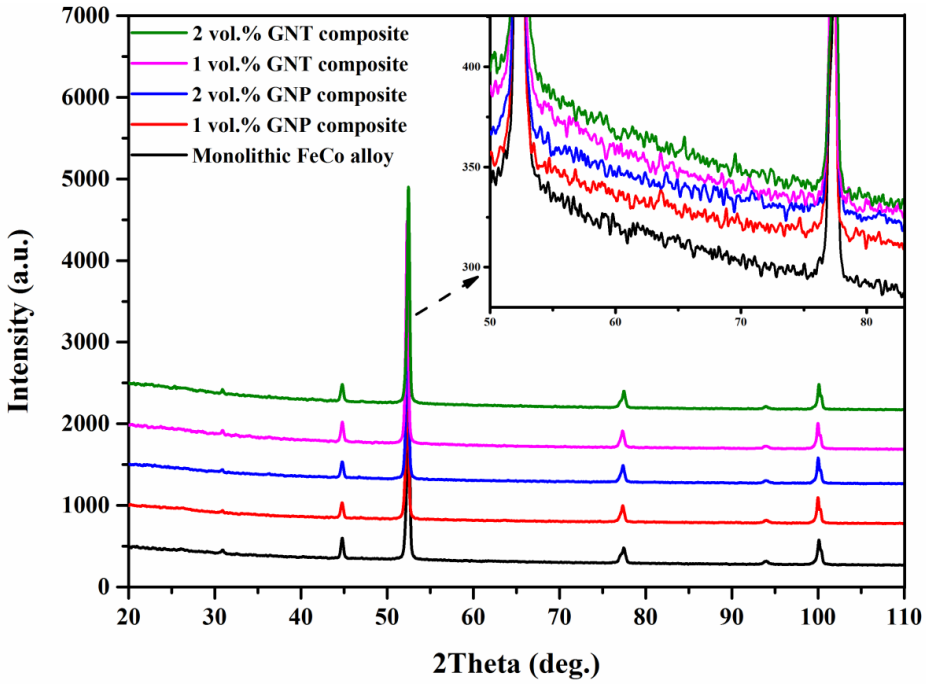

Figure 5.5. XRD patterns for FeCo as received; 1 vol. % GNP composite; 2 vol. % GNP composite; 1 vol. % GNT and 2 vol. % GNT composite.

Avery slow scan rate and high-intensity XRD (Co Kα) was employed in order to investigate the (100) superlattice line reflection of the sintered FeCo alloy, 1 h ball milled FeCo alloy, GNT and GNP composites as shown in Figure 5.6. The long-range ordering fraction in FeCo alloy has been shown to reduce following ball mill [167]. With 1 vol. % GNP dispersion in the FeCo alloy an increase in volume fraction of ordering was observed. However, the introduction of 2 vol. % GNP did not make any significant difference to the degree of ordering and crystallite size. The intensity of the superlattice reflection was found to be higher in the GNP composites as compared to the GNT composites; indicating a greater volume fraction of ordering in the GNP composite. This is confirmed by the shift of the peak to lower angles in the GNP composites due to the strains induced by the more ordering reaction as compared to the GNT composites. Clegg and Buckley [28] reported that the change in lattice parameter between the disordered and ordered phases is about 0.2 %; varying from 0.28550 to 0.28570 nm. The anti-phase domain sizes were estimated from the superlattice line in Figure 5.6 using the Scherrer equation. A significant reduction in the anti-phase domain sizes was observed in the 1 vol. % GNT composite, which reflects

the role of carbon nanotubes in refining the crystallite structure or due to improved dispersion, while GNP additions did not influence on the nanostructure.

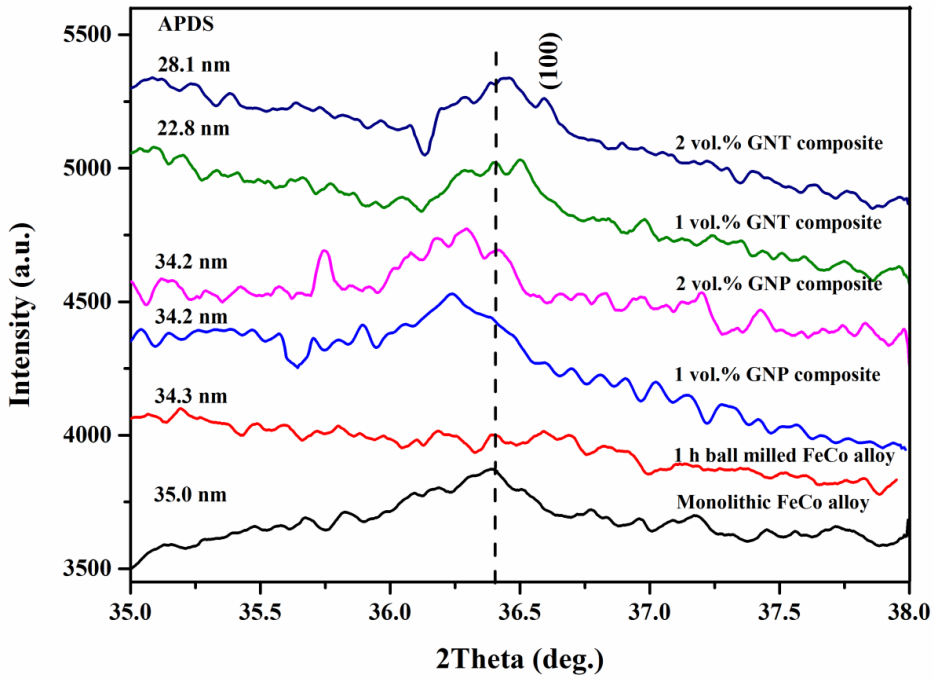

Figure 5.6. Slow scan XRD patterns show (100) superlattice line reflection with anti-phase domain size (APDS) of monolithic FeCo alloy, 1 h ball milled FeCo alloy and displayed composites.

5.3.4. Magnetic properties

The upper halves of the hysteresis curves of the consolidated material are shown in Figure 5.7, and a summary of the magnetic induction ($B_{sat.}$), coercivity (H_c) and remanence (B_r) of these materials is shown in Figure 5.8. An increase in saturation induction and reduction in coercivity is observed in the GNP composites compared to as-received FeCo alloy, for reinforcement additions up to 1 vol. %. In general, a higher remanence is observed in the GNT composite as compared to the GNP composites (Figure 5.8, inset). In order to separate the effects of ball milling from the effect of reinforcement on the magnetic properties, the 1 h ball milled FeCo alloy was also investigated. The saturation induction of 1 h ball milled FeCo alloy was reduced from 2.30 T to 2.23 T, while exhibiting a decline in coercivity from 836 to 763 A m^{-1}.

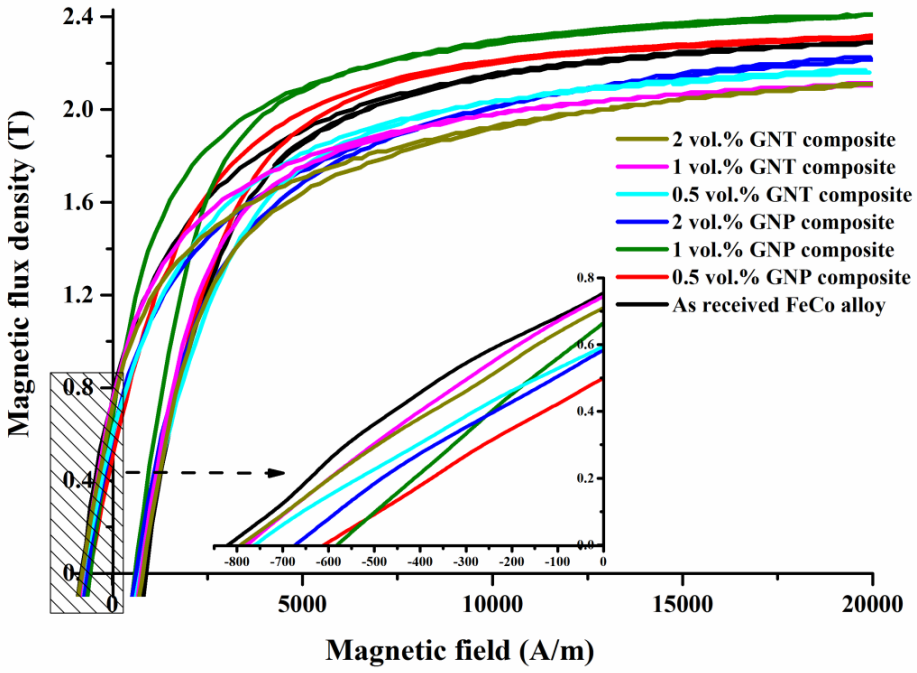

Figure 5.7. Upper halves of hysteresis curves of the indicated materials.

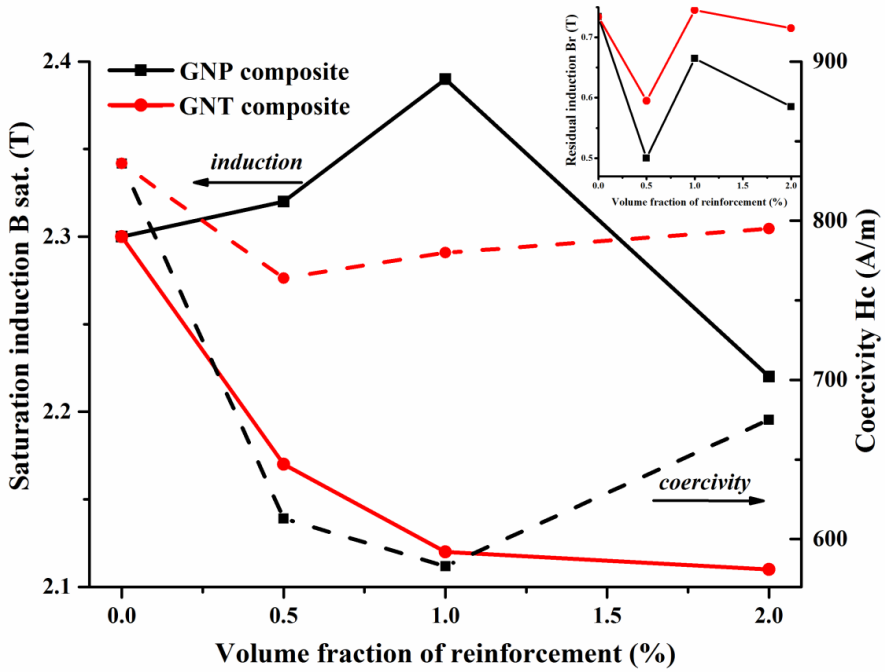

Figure 5.8. Effect of volume fraction of GNP and GNT on: saturation induction (solid lines); coercivity (dashed lines) and remanence (insert) of (equiatomic FeCo alloy) composites fabricated by spark plasma sintering at magnetic field of 25 kA/m.

It was shown in the previous section that the density after ball milling under air atmosphere dropped, which can account for the reduction in saturation induction due to oxide formation [167]. The 1 vol. % of GNPs composite exhibited a higher saturation induction value of 2.39 T than the 1 h ball milled FeCo alloy 2.23 T due to the increase in density produced by the addition GNPs to the ball milled FeCo alloy as confirmed in Figure 5.4. However, with the addition of 1 vol. % of GNTs the saturation induction

dropped to 2.12 T. The increased space between GNPs due to inserting CNTs leads to drop in density due to porosity (Figure 5.4). Further, the increased saturation in GNP composite can also be explained by the ferromagnetic behaviour of graphene and improved electrical conductivity of this composite [218, 219], which could affect the densification processes during SPS and subsequent magnetic properties. The 2-D form of the GNPs exhibits open edges, in contrast to the inserted CNTs which have closed π-electron systems. The nonbonding state also creates nanomagnetic properties at edges [220]. However, the inserted CNTs will influence magnetic properties primarily because of the residual metallic catalysts on their surface and secondary due to the introduction of porosity.

The coercivity is sensitive to the change in the microstructure, especially grain size. The plastic deformation has also a significant effect on coercivity, the increased dislocation density from deformation stresses may change the anisotropy constant K_1, which reflects on coercivity value [47]. The ball milling was used here with all samples for a limited time of 1 h and low BPR of ~ (1:1), as a result of that the effect of ball milling stresses was not significant on the coercivity or stresses were released during the cooling in SPS furnace. The coercivity after ball milling under air atmosphere dropped, which may have been caused by the formation of nanocrystalline structure. The slow scan rates XRD (Co Kα) patterns (Figure 5.6) revealed a (100) superlattice reflection with crystallite dimensions reduced to the nanoscale. It has been shown [52, 221] that at this scale the trend in coercivity would follow that of the average magneto-crystalline anisotropy when the crystallite size becomes less than the ferromagnetic exchange length, leading to a drop in coercivity. The composites with GNT displayed a higher coercivity than the GNP composites, which is due to the more refined grain size (Figure 5.2d) of GNT composite as a result of better dispersion, and also because of the decrease in density. The restacking of GNPs increased at higher volume fraction composites, leading to an increase in size GNPs to be closer to micron, therefore, the effectiveness of GNPs to reduce grain growth was decreased.

5.3.5. Mechanical properties

The tensile stress-strain curves of as received FeCo alloy, GNPs and GNT composites of different volume fractions are shown in Figure 5.9. In addition to that the influence of ball milling on properties was also considered by testing 1 h ball milled monolithic FeCo alloy. The ultimate tensile strength, the mechanical hardness and failure strain of the as a received monolithic FeCo alloy which is represented as (0 vol. % reinforcement) and the

composites with different volume fraction of GNPs and GNTs are summarised in Figures 5.10 and 5.11, respectively. The 1 h ball milled FeCo alloy was also examined and compared to alloy prepared with unmilled powder, exhibiting a decrease in ultimate tensile strength from 673 ±17.43 to 643 ±40 MPa; failure strain was also dropped from 2.9 ±0.70 to 2.4 %, while the hardness increased from 326.5 ±18 VHN to 355.7 ±5 VHN.

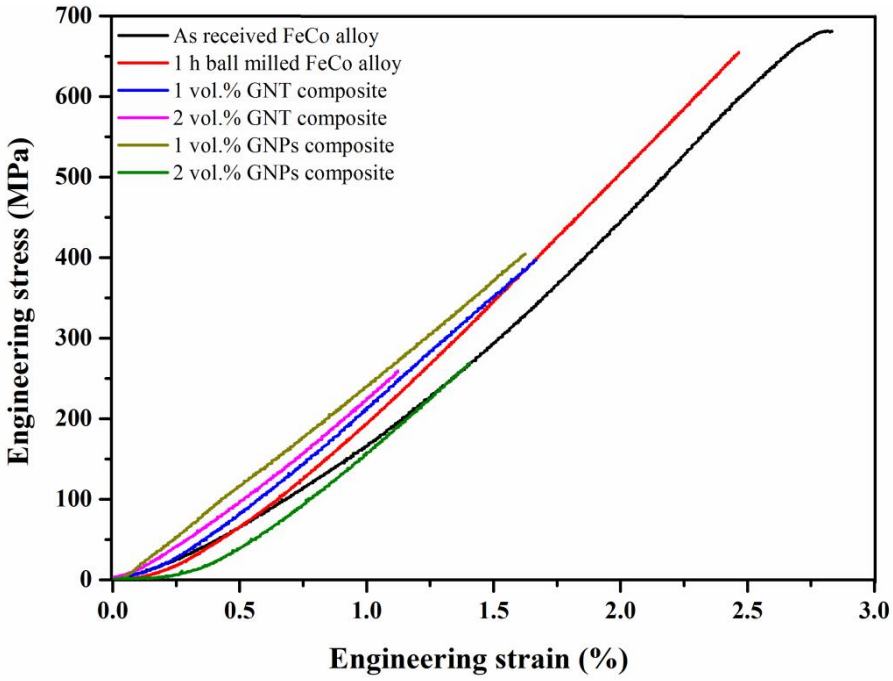

Figure 5.9. Tensile stress-strain curves of the indicated materials.

Hard oxides formed during ball milling lead to an increase in hardness, yet they hindered densification process and hence lower the tensile strength and failure strain. The addition of GNPs to the FeCo alloy led to a decrease in tensile strength. This was possibly due to the restacking of GNP sheets as shown in Figure 5.13c, which causes an easily slip in the agglomerated GNPs with respect to one another and a separation under stresses. Strength arising from nano-reinforcement mechanisms will deteriorate once the GNPs become agglomerated into a close to micro-sized clusters, reducing the tensile strength by acting as stress concentrators. An improvement in tensile strength was subsequently observed in the hybrid GNT composite, where the addition of CNTs prevents agglomeration of the GNPs. A marked increase in hardness to 385.3 ±35 VHN was observed in the 1 vol. % GNP-FeCo alloy composite, as shown in Figure5.10. This represents an 18 % increase in hardness in comparison to the as received FeCo alloy. The highest density value among the composite materials was achieved for the 1 vol. % GNP composite, leading to an increase in the hardness. The hardness decreased for the 2 vol. % GNP composite, because of the decrease in density produced by agglomeration of GNPs.

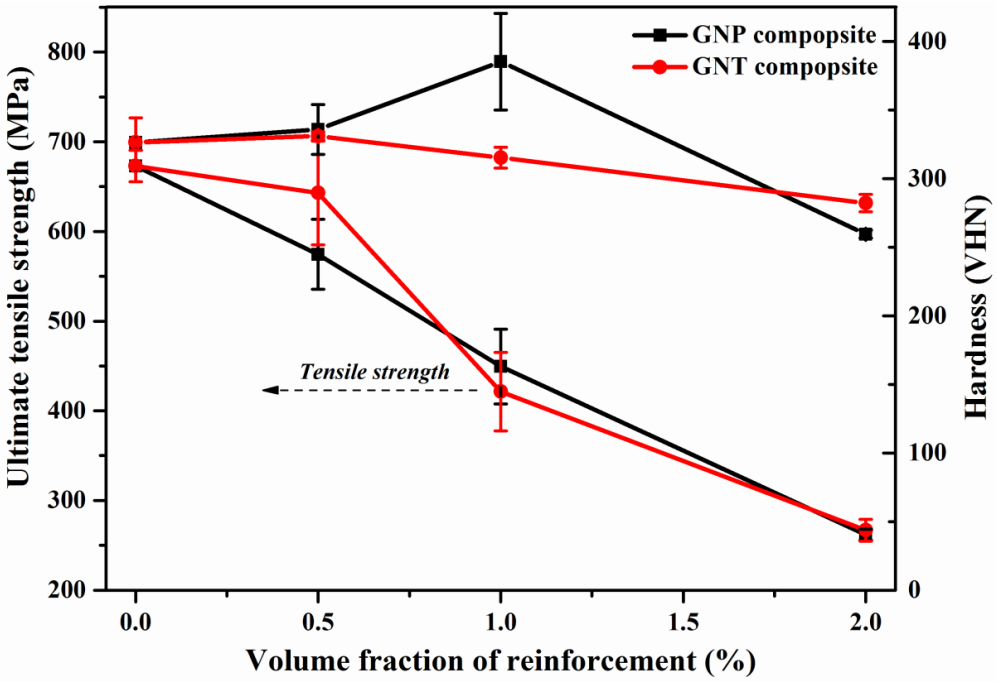

Figure 5.10. Effect of volume fraction of GNP and GNT on: tensile strength and hardness of FeCo alloy composites fabricated by spark plasma sintering.

The composite material exhibit decrease in failure strain especially at higher loading as compared to as received FeCo alloy (Figure 5.11), confirming increased brittleness in FeCo alloy from agglomeration.

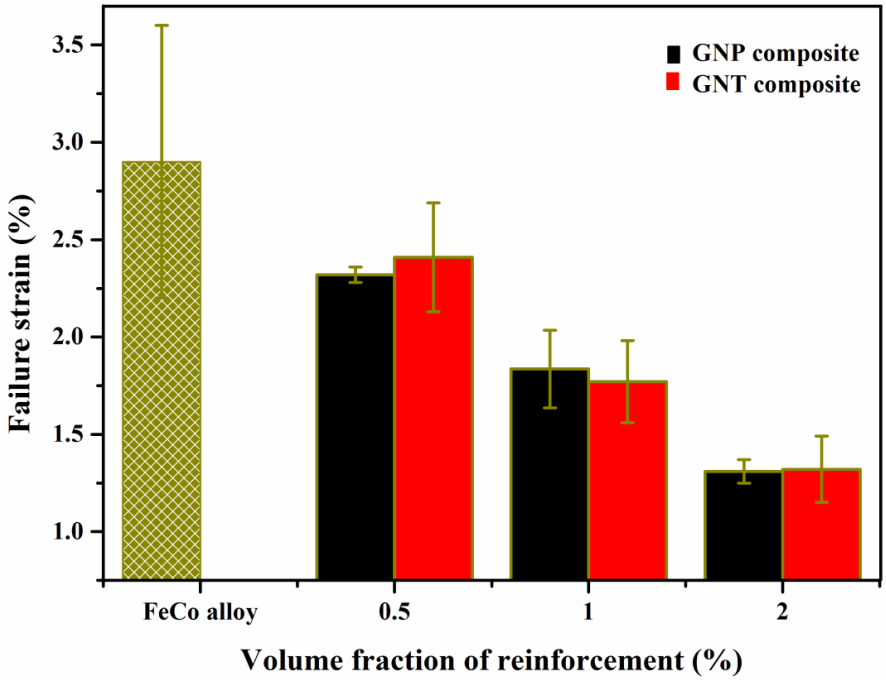

Figure 5.11. Effect of volume fraction of GNP and GNT on failure strain of FeCo alloy composites fabricated by spark plasma sintering.

Figure 5.12 shows the fracture surfaces of monolithic FeCo alloy, 1 vol. % GNP composite and 1 vol. % GNT composite. Mixed mode of intergranular and transgranular fracture predominate in all the sintered materials, indicating that the inherent weakness of grain boundaries cannot be avoided by poor dispersion of the nanophase.

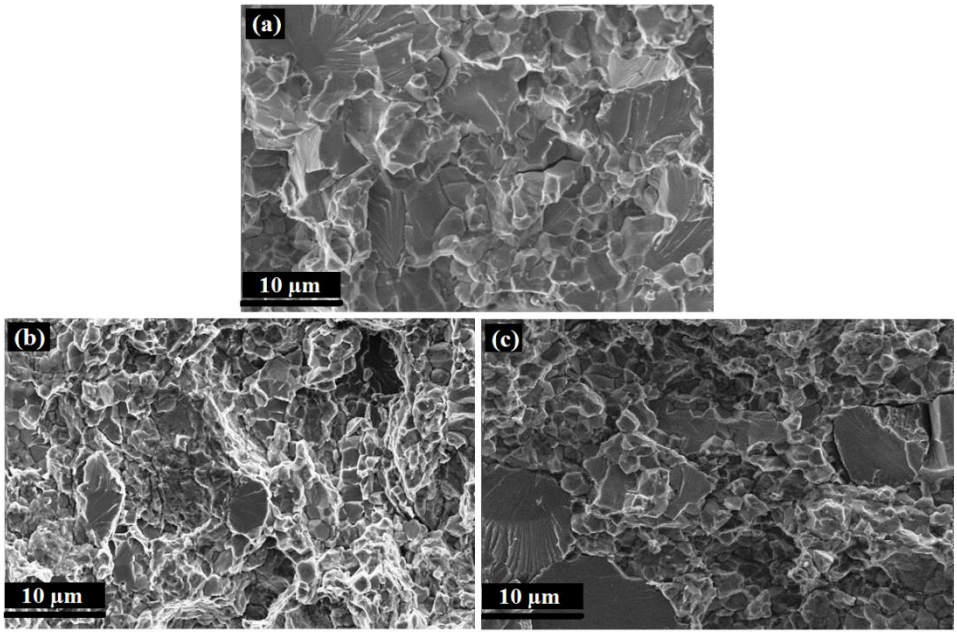

Figure 5.12. Fractographic images of: (a) as received FeCo alloy; (b) 1 vol. % GNP composites; and (c) 1 vol. % GNT composites fabricated by spark plasma sintering.

Evidence of toughening mechanisms, such as crack deflection and GNPs pull out, is observed in Figure 5.13a, c. A large GNP can be seen to warp around a grain. It is expected that the flexibility of GNPs allows them to bend around and become embedded between the grains during sintering. The large surface area of GNPs increases the contact area with the matrix, leading to an increased interfacial force, requiring more energy to pull out the GNP sheets as compared to the CNTs. However, overlapping between GNPs decreases the interface bonding efficiency. It is observed that thin GNP sheets are effective at inhabiting crack propagation as compared to thick overlapped GNP sheets, which are easily sheared and form pores, degrading the mechanical and physical properties. The CNTs are embedded between the GNPs as observed in Figure 5.13d; pull-out of the CNTs occurred during fracture. The high aspect ratio of the CNTs allows them to bridge the fracture surface, as shown in Figure 5.13b.

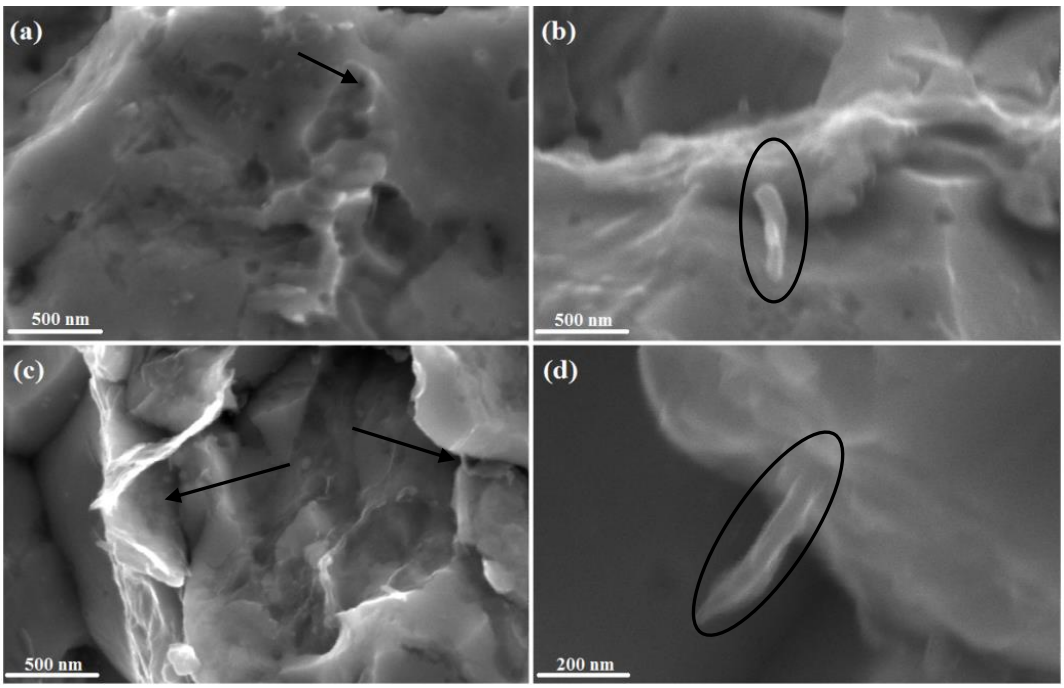

Figure 5.13. High magnification of fractographic images; (a, c) 0.5 and 1 vol. % GNP composites respectively; (b, d) 0.5 and 1 vol. % GNT composites respectively. The arrows show pull-out of GNP (a), thin and overlapped GNP(c). Ellipses exhibit CNTs bridging (b) and pull-out of GNPs (d).

5.3.6. Raman spectroscopy

Raman spectra of the as received GNP, FeCo alloy and the GNP and GNT-FeCo alloy composites are shown in Figure 5.14. The FeCo alloy does not produce any Raman signals. The structure of GNP was retained after all of the fabrication processes as evidenced from the shape of the single-peak shape of the 2D band in the Raman spectrum; indicating the presence of the graphene morphology as opposed to the graphite morphology, which would give rise to a split-peak [198].

Table 5.1 lists the peak intensity ratio *($R=I_D/I_G$)*, in addition to the G and 2D peak positions. The GNPs were observed to be of higher quality than the CNTs, as evidenced by the lower *R* ratio of the GNPs (1.00) compared to CNTs (1.11). An increase in *R* ratio was observed for all the composites. This was particularly notable for the GNP-FeCo alloy composites as compared to the as received GNPs. This may have resulted from an interfacial reaction of the matrix with the side wall of the GNPs, or could have induced by ball milling. However, this ratio decreased in the GNT composites as compared to the GNP composites, suggesting that the addition of CNT to GNP in ethanol may help to maintain the structure of the GNP. Furthermore, the oxidation for reinforcement was reduced due to using a good vacuum (5 hPa), helping to improve the quality of carbon nanostructure, as the high quality for vacuum during sintering process is crucial to preservation carbon

nanostructure in sintered composites materials [199]. Strains are induced in the GNPs by the fabrication processes and by mechanical testing of the composite material. Such strains will lead to alterations in the interatomic distance of the graphene. The G band peak position is very sensitive to strain in the graphene structure. Hence the shift in wave number will change according to alteration in the vibration frequency of the G band due to strain [196]. Up shifting was observed in the peak position of the G-band (ω_G) peak for the composites in comparison to the as received GNP. A shift of between 8.6 cm^{-1} to 22.8 cm^{-1} is observed in the GNP composites, and a 10.6 cm^{-1} to 13.6 cm^{-1} shift is observed for the GNT composites as compared to the as received GNP. This indicates that significant strains have been induced in the GNPs in the aforementioned composites. Up shifting is also observed in the 2D peak. Since the 2D band peak is very sensitive to the number of layers in graphene, a change in position, width and shape could occur in the 2D peak with an increasing number of layers [198]. The shifting was reduced in 1 and 2 vol. % GNT composite indicating that less overlapping had occurred between the GNP sheets as a result of the addition CNTs.

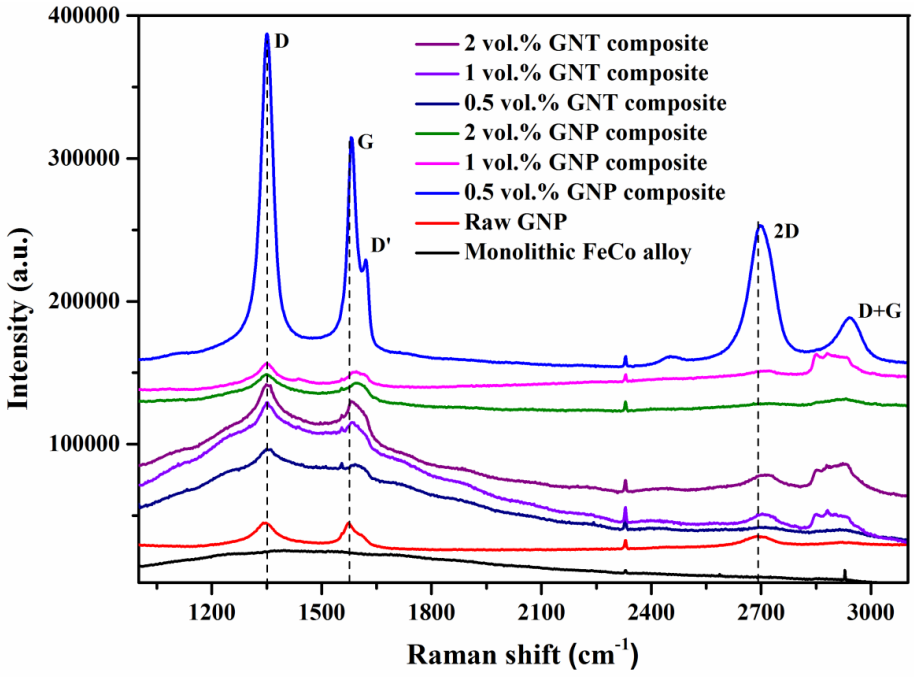

Figure 5.14. Raman spectra of GNP, GNT composites and as-received graphene.

Table 5.1: Raman spectra data of sintered materials.

State	$R=I_D/I_G$	ω_G (cm^{-1})	ω_{2D} (cm^{-1})
Raw GNP	1.00	1573.0	2691.0
Raw CNT	1.11	1578.0	2691.0
0.5 vol.% GNP composite	1.37	1581.6	2699.8
1 vol.% GNP composite	1.15	1595.0	2708.6
2 vol.% GNP composite	1.09	1595.8	2716.4
0.5 vol.% GNT composite	1.07	1586.6	2710.7
1 vol.% GNT composite	1.06	1583.2	2703.5
2 vol.% GNT composite	1.06	1585.5	2709.0

Summary

GNT composites were prepared by mixing in CNT ethanol solvent and followed by ball milling, which was compared with GNP composite prepared by only ball milling without addition for CNTs. The samples were sintered following sintering conditions reported in the literature, which are 900 °C, 80 MPa, 50 °C/min for 3 min. The overlapping between GNPs can be reduced by inserting CNTs among the nanoplatelets, despite the microstructure is more refined when CNTs included with the reinforcement, an increase in porosities were observed. The ordered structure was increased by reinforcing FeCo alloy with alone GNPs, which caused significant improvement in magnetic properties up to 1 vol. % GNPs. Overall, the mechanical properties were decreased as compared to base alloy, however, a slight improvement in properties was observed in composite contain a mixture of reinforcement (CNTs+GNPs) as a compare to alone GNPs composite.

Chapter 6: Results and discussion of optimisation sintering conditions at low pressure

6.1. Introduction

The previously reported work for optimising sintering conditions of FeCo alloy was based on using relatively high sintering pressure of 80 MPa to achieve full densification. Adopting the same sintering conditions does not show improvement in mechanical properties and caused a frequent breakage for the graphite die. Therefore, the sintering conditions at relatively lower sintering pressure were evaluated to optimise sintering parameters, aiming to improve the mechanical and magnetic properties of FeCo alloy.

6.2. Characteristics of sintered materials

6.2.1. Effect SPS parameters on densification

The shrinkage curves of FeCo alloys sintered at 1100 ºC for heating rates 50, 100 and 300 ºC.min^{-1} are shown in Figure 6.1.

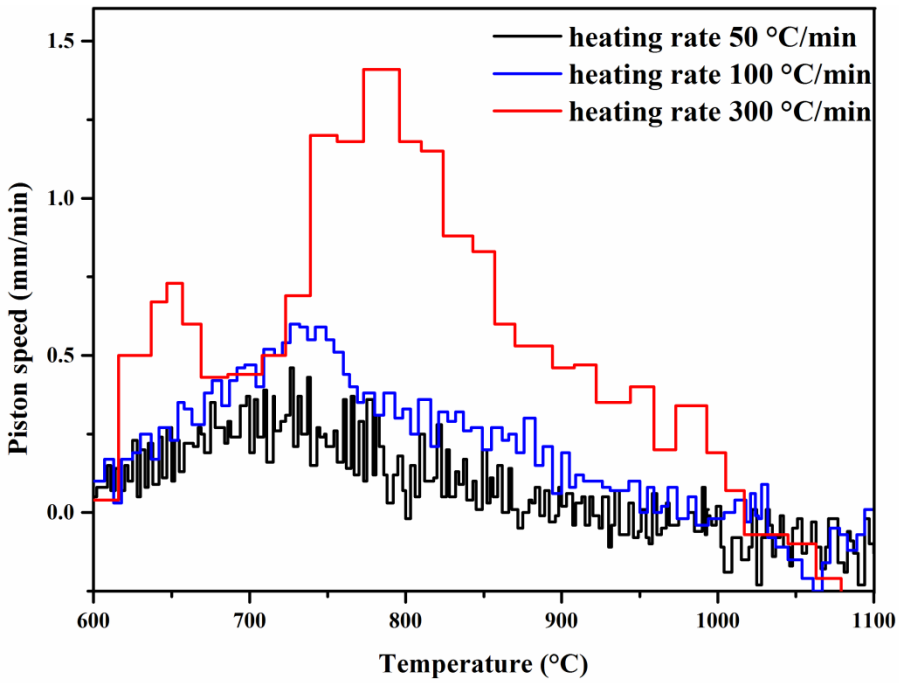

Figure 6.1. Shrinkage curves of FeCo alloy sintered at 1100 °C for indicated heating rates.

A wide difference is observed in shrinkage rate at the faster heating rate of 300 ºC.min^{-1} with respect to other heating rates. This is a consequence of the variation of sintering mechanism with faster heating rates, such behaviour is reported in [222]. The non-densifying surface diffusion mechanism which is active at low temperature is avoided by

the fast heating rate, instead to densifying mechanisms include grain boundary and volume diffusion [223]. However, a faster rate yielded porosity in sintered FeCo alloy.

6.2.2. Effect SPS parameters on density and microstructure

The samples identity, relative density and grain size with different sintering conditions are shown in Table 6.1.

Table 6.1. Identity, relative densities and grain size of sintered FeCo alloy.

FeCo alloy identity	Spark plasma sintering conditions	Relative density (%)	Grain size (μm)
A	**Sintering at 1100 °C without dwelling. Heating rate 50 ºC/min.**	**99.0 ± 0.4%**	**29.8**
B	**Sintering at 850 °C for 15 min. Heating rate 50 ºC/min.**	**99.8 ± 0.4%**	**6.7**
C	**Sintering at 850 °C for 5 min. Heating rate 50 ºC/min.**	**99 .0 ± 0.4%**	**6.4**
D	**Sintering at 1100 °C without dwelling. Heating rate 100 ºC/min.**	**99.5 ± 0.4%**	**23.2**
E	**Sintering at 800 °C for 15 min. Heating rate 100 ºC/min.**	**99.1 ± 0.4%**	**6.4**
F	**Sintering at 800 °C for 5 min. Heating rate 100 ºC/min.**	**97.7 ± 0.4%**	**6.1**
G	**Sintering at 1100 °C without dwelling. Heating rate 300 ºC/min.**	**99.2 ± 0.4%**	**22.6**
H	**Sintering at 800 °C for 15 min. Heating rate 300 ºC/min.**	**98.2 ± 0.4%**	**6.6**
I	**Sintering at 800 °C for 5 min. Heating rate 300 ºC/min.**	**96.4 ± 0.4%**	**5.9**

The density reduced with increasing heating rates, there is inconsistency in the literature about the effect heating rate on the density of materials sintered by SPS [6]. At heating rates greater than 100 ºC min^{-1}, the sintering mechanism tends to be dominated by diffusion via viscous flow, which allows the grains to slip and rotate with respect to neighbouring grains in order to minimise their grain boundary energy [224], the porosities may induce in the sintered materials when this process is incomplete due to short sintering time. During SPS, localised temperature gradients can occur across the thickness of the powder particles due to localised overheating at the particle surface, caused by the more resistive contacts between particles. This effect becomes more pronounced at higher heating rates, leading to reduced densification since the interior of the particles can remain relatively cool. The highest density value was achieved at sintering conditions 50 ºC.min^{-1}, 850 ºC and 15 min, suggesting that the slowest heating rate is more suitable than fast heating rates in sintering FeCo alloy. Increasing sintering pressure has been suggested to improve densification in sintered materials [6]. This parameter was considered by sintering sample at 80 MPa, showing relative density of 99.1 %. In the current study, a relative density of 99.8 % was

obtained at significant lower sintering pressure of 50 MPa, through careful selection of sintering temperature, heating rate and sintering time. The benefit of sintering at low pressure 50 MPa and high temperature is not only to obtain high density but also to reduce the risk of fracture of the graphite die at high pressure.

The grain size of the densified alloy is significantly affected by sintering temperature, as shown in (Figure 6.2).

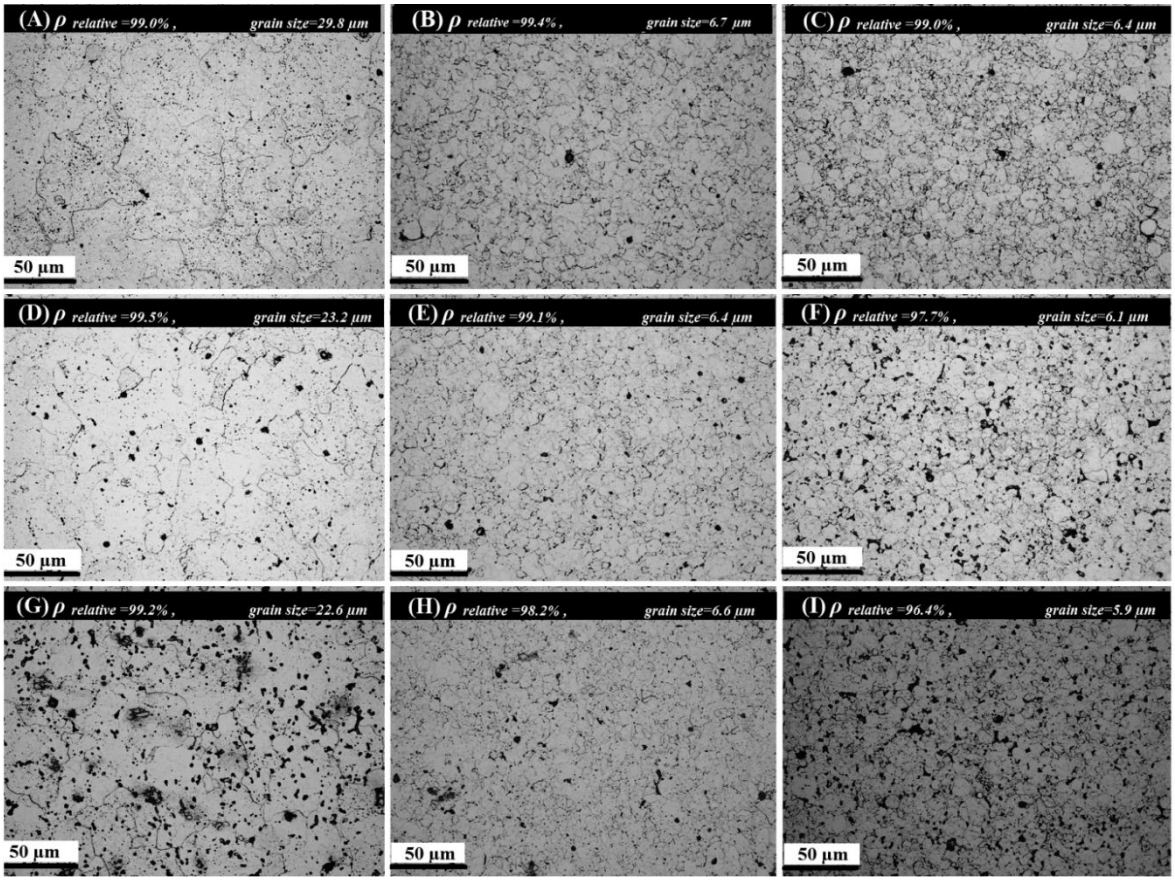

Figure 6.2 Optical microstructure of the FeCo alloys densified under the sintering conditions indicated in Table 1.

The grain size of the densified alloy is significantly affected by sintering temperature. The grain growth is fast for samples sintered at 1100 ºC with average grain size 29.8 μm. Decreasing sintering temperature to 850 ºC significantly refines grain size to average grain size of 6.7 μm. The heating rate also affects grain size, which was reduced with increasing heating rates, as shown in Table 6.1. High heating rates reduce the time of powder dwelling in nondensifying mechanisms at lower temperatures, where grain growth occurs due to dominant surface diffusion processes [5].

6.2.5. XRD characteristics of the consolidated materials

XRD results for sintered FeCo alloys at different SPS conditions are seen in (Figures 6.3 and 6.4).

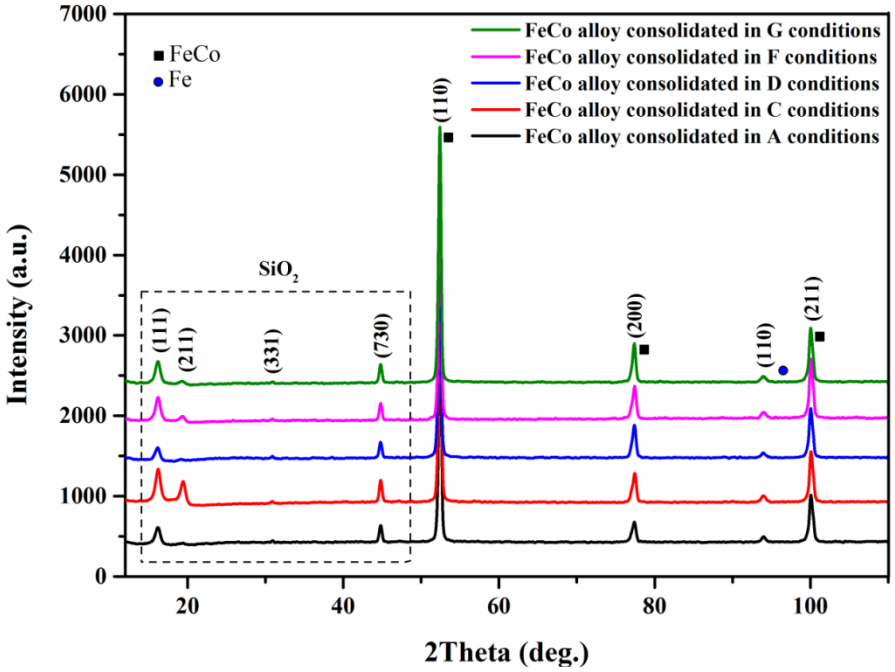

Figure 6.3. XRD for FeCo alloy compacts sintered at indicated sintering conditions.

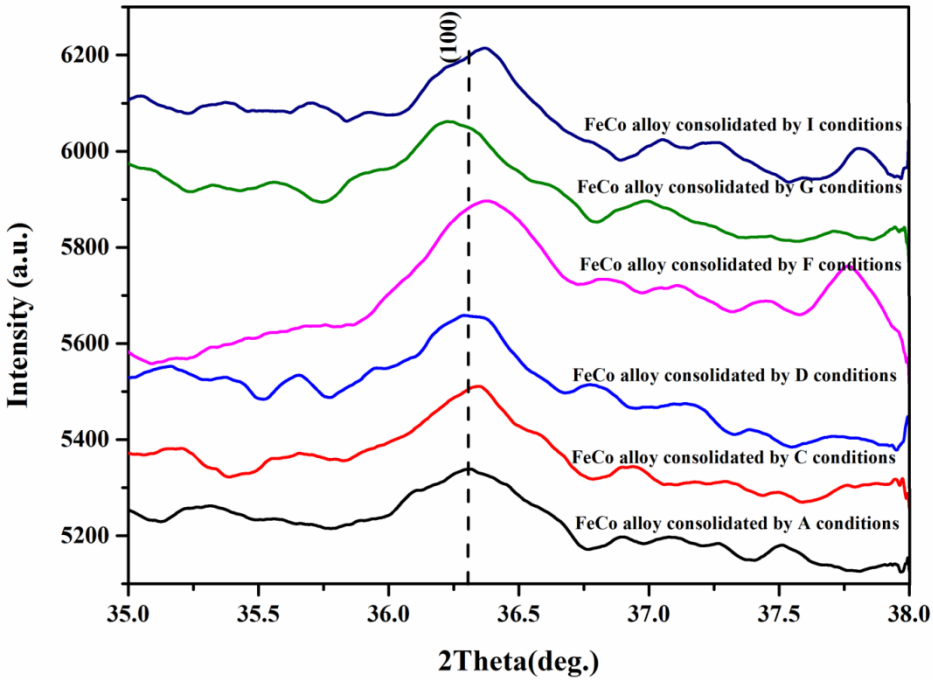

Figure 6.4. XRD for super lattice line for FeCo alloy compacts sintered at indicated sintering conditions.

The main peaks of FeCo alloy were observed, in addition to evidence for oxidation which is a result of exposure the powder to air Figure 6.3. In comparison between the formed ordered structure at various sintering conditions (Figure 6.4), it shows an increase in the

ordered state in FeCo alloys sintered at 850 ºC and 800 ºC as compare to 1100 ºC, especially at the heating rate of 100 ºC.m^{-1}. Increasing the dwell time from zero to 5 min and reducing the sintering temperature to close the ordered region allowed to a more ordered reaction, which caused an increase in the ordered structure in the final composition.

6.2.3. Magnetic properties

The upper halves of hysteresis curves of sintered FeCo alloys at different sintering conditions are presented in Figure 6.5. A comparison between the magnetic properties of the sintered FeCo alloys is shown in Figure 6.6. Regardless of the sintering time, the saturation induction shows linear relationship with sintering temperature for heating rate 50 ºC.min^{-1} Figure 6.6. Inconsistent behaviour is observed for the other heating rates.

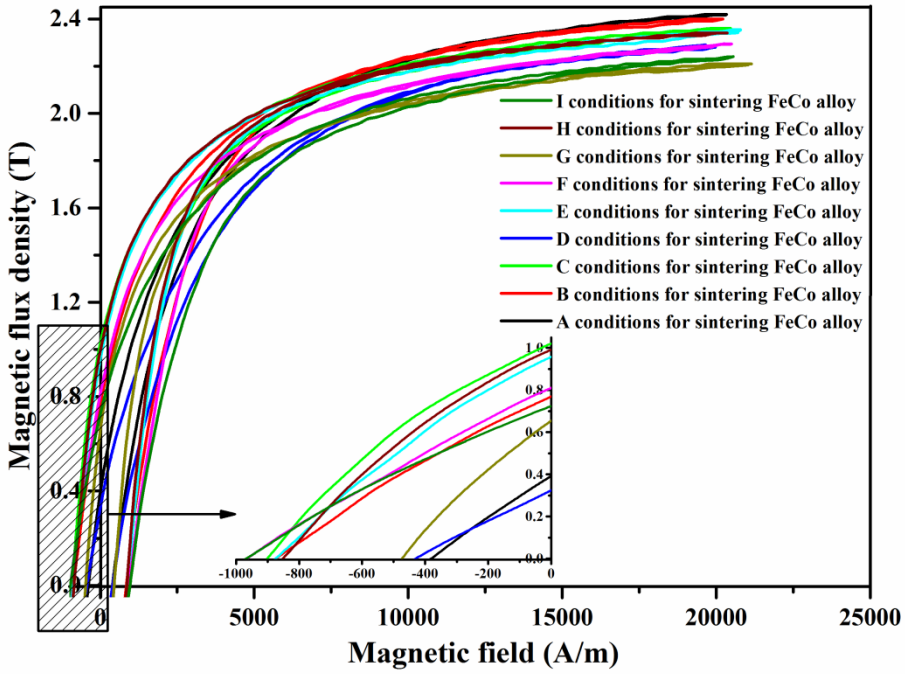

Figure 6.5. Upper hysteresis curves for sintered FeCo alloy at various conditions.

The highest value of saturation induction for all sintering temperature was achieved at heating rate 50 ºC.min^{-1}, due to improved densification at this rate. The magnetic properties of FeCo alloy fabricated by powder metallurgy are mainly affected by grain size and density of the component. The former has a significant influence on coercivity, while saturation magnetisation of powder metallurgy product is more sensitive to density [4, 225]. Increase the dwelling time at a sintering temperature of 850 ºC and 800 ºC was very effective in increasing the density of the sintered FeCo alloys, therefore a significant improvement in saturation induction was achieved at these sintering conditions Table 6.2. The improvement in saturation induction may also happen as a result of a change in the

fraction of ordered state, which rationalises that even reduction in density in some samples does not cause a reduction in saturation induction value since the saturation induction in fully ordered structure exceeds the disordered structure by 2-3% [1].

An increase in coercivity is observed for the samples sintered at 800 ºC of heating rates 300 ºC.min^{-1} compared with sample sintered at temperature 850 ºC for lower heating rate 50 ºC.min^{-1}. However, for all heating rates, the coercivity was lower at the highest sintering temperature of 1100 ºC than other sintering temperature as exhibited in Figure 6.6.

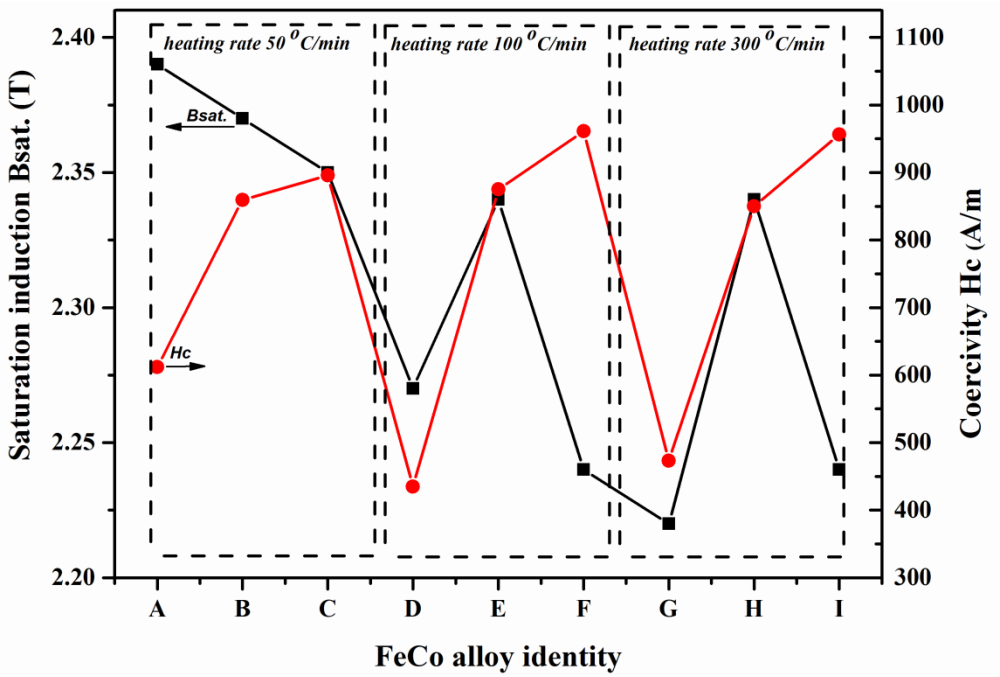

Figure 6.6. Summary of magnetic properties of FeCo alloy processed under various SPS conditions at magnetic field 25 kA/m.

Generally, most types of defects such as grain boundaries, dislocations, precipitates effect on coercivity. Order-disorder transformation has also an influence on the final value of coercivity since the coercivity of ordered state is higher than the disordered state at room temperature [1]. The ordered structure was increased in samples sintered at 800 and 850 ºC, giving a reason for increasing coercivity in comparison to samples sintered at 1100 ºC. Furthermore, it is claimed by [2] that the coercivity is inversely proportion to grain size in the micron size order. An increase in grain size was observed at the high sintering temperature. However, the fast heating rate of 300 ºC.min^{-1} was effective in reducing grain size, as shown in (Figure 6.2), therefore an increase in coercivity was observed. Conflicting behaviour is observed when the sintering temperature is increased to 1100 ºC, due to the reduction in volume fraction of the ordered state at faster heating rates (Figure 6.4), and increase the grain size. Moreover, sintering at high temperature helps in releasing

the coercivity dependent on residual stresses in the material which are introduced during mechanical pressing and also causes more purification for structure.

6.2.4. Mechanical properties and Fracture surface study

The stress-strain curves of the FeCo alloy sintered under different sintering conditions are shown in (Figures 6.7, a, b, c). A summary of the mechanical and magnetic properties is presented in Table 6.2. A high tensile strength was observed in the FeCo alloys sintered at 850 ºC and 800 ºC for 5 and 15 min, in comparison to the FeCo alloys sintered at 1100 ºC without dwelling. All samples failed before yielding; apart from samples sintered under the slowest heating rate of 50 ºC min^{-1}. In spite of the decrease in the ultimate tensile strength of the samples sintered at 1100 ºC without dwelling, an obvious yield point and improvement in elongation were achieved. The variations in the mechanical properties of the FeCo alloy with different sintering conditions are summarised in Table 6.2. The hardness of the samples also changed with variations in the sintering conditions, which is due to the variations in final density. An almost continuous increase in hardness is observed with increasing density.

In general, the ordered intermetallic alloys have a high strength even at high temperature; yet they are very brittle. Therefore, improving the ductility and toughness of intermetallic alloys like FeCo alloy is a priority for the use of such high performing magnetic alloys in industrial applications. The mechanical property of FeCo alloys, including; ultimate tensile strength, yield strength, ductility and hardness, are governed by parameters such as the grain size, density and the degree of long range ordering. Furthermore, the ductility of the FeCo alloy is very sensitive to impurities in the microstructure, since a partial disordering at the grain boundaries can relieve the inherent brittleness of the FeCo alloy [22].

Increasing the dwelling time of the sintering process from 5 min to 15 min at sintering temperatures of 850 ºC and 800 ºC led to an improvement in densification; and therefore the tensile strength of the FeCo alloy was slightly increased. The ultimate tensile strength decreased in the FeCo alloys sintered at 1100 ºC without dwelling, however, the samples sintered at this temperature show an improvement in yield strength; with a remarkable increase in ductility.

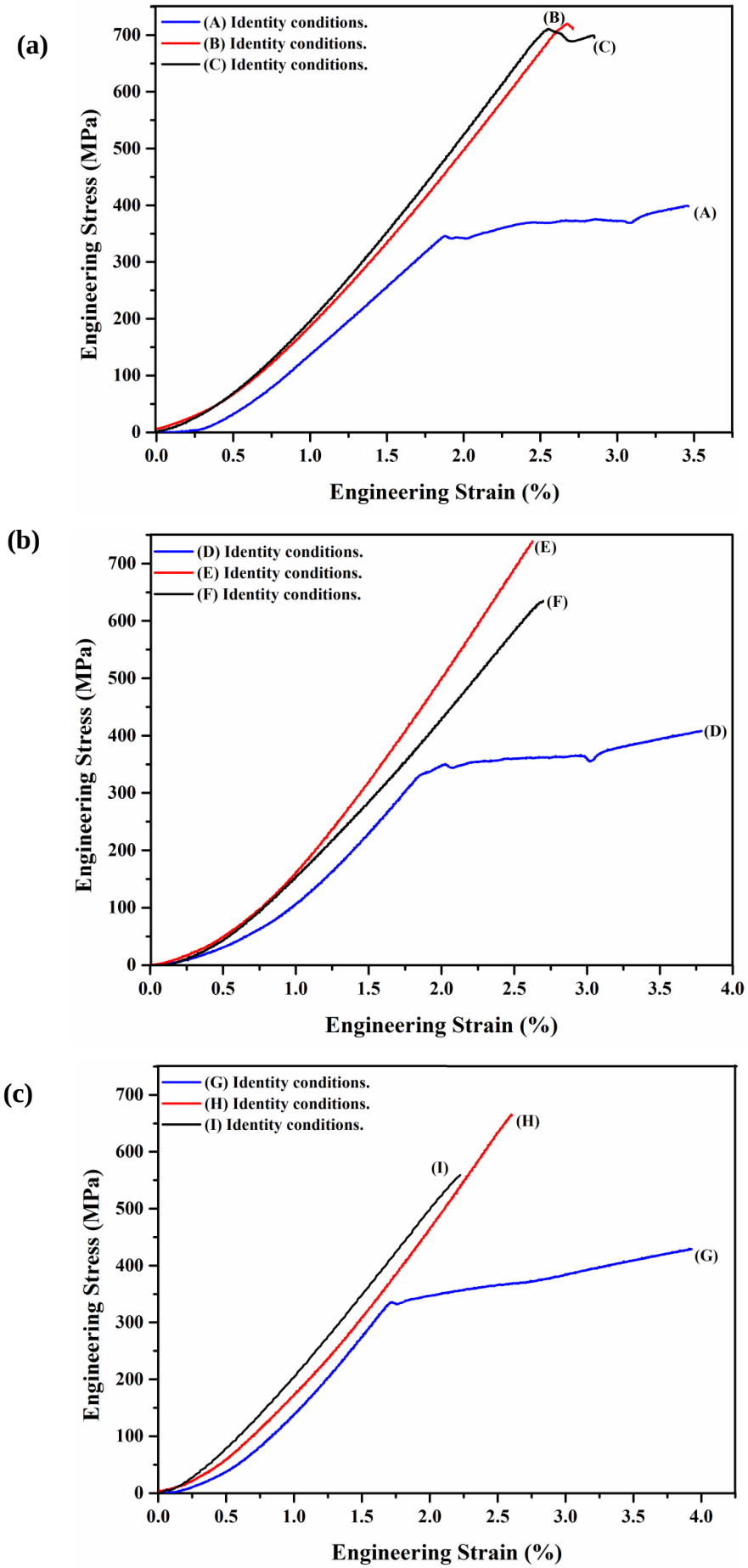

Figure 6.7. Tensile stress-strain curves of FeCo alloys sintered at indicated conditions for heating rates;(a) 50 C.min^{-1}:(b) 100 C.min^{-1}and (c)300 C.min^{-1}.

Table 6.2. Mechanical and magnetic properties of FeCo alloy at different sintering conditions.

FeCo alloy identity	Ultimate tensile strength (MPa)	Yield strength (MPa)	Elongation (%)	Hardness STDEV (VHN)		Saturation induction Bsat.(T)	Coercivity Hc (A/m)
A	400	340	3.47	237.8	3.7	2.39	612
B	Fail at yield stress	710	2.71	310.2	5.3	2.37	859
C	Fail at yield stress	687.5	2.86	313.5	4.9	2.35	896
D	409	341.6	3.79	248.0	5.8	2.27	435
E	751	Fail before yield stress	2.62	311.1	5.1	2.34	875
F	634	Fail before yield stress	2.71	298.0	5.9	2.24	961
G	431	330	3.95	244.0	5.8	2.22	473
H	667	Fail before yield stress	2.61	316.3	8.9	2.34	850
I	561	Fail before yield stress	2.23	274.2	7.6	2.24	956

The high sintering temperature of 1100 ºC promotes grain growth, as shown in Figure 6.2. This factor has a significant influence on the yield strength and the elongation of the equiatomic FeCo alloy. The yield strength and the elongation are higher in the disordered state than in the ordered state; and both states follow the Hall-Petch relationship in which the yield strength increases with reducing grain size [20, 226]. An agreement with the Hall-Petch relationship is observed in the decrease yield strength of larger grained samples (sintered at 1100 ºC with a heating rate of 50 ºC min^{-1}). Schulson and Baker [227] reported that the ductility of the NiAl alloy can be improved by reducing the grain size to a critical value of 20 μm, when the stress required to nucleate cracking is less than the stress required to propagate a crack, leading to additional plastic follow during deformation. There are no similar studies on the behaviour of FeCo alloy regarding such critical grain sizes; thus, it is suggested that the grain size may be at or near to the critical grain size in samples sintered at 1100 ºC, leading to an improvement in ductility.

The peak of the superlattice line (100) decreased in samples sintered at 1100 ºC, as the volume fraction of the ordered structure was reduced. The fully disordered structure can exhibit a 4 % elongation in comparison to zero elongation in the completely ordered equiatomic FeCo alloy. The yield strength is also higher in the disordered structure as compared to the ordered structure. Unfortunately, the kinetics of long range ordering are very fast, which can only be suppressed by the very fast quenching (~ 4000 ºC s^{-1}) of a thin

sample annealed in the disordered region [2, 20, 28, 29]. All sintered samples produced in this study were cooled inside the SPS furnace, with cooling rates far from that required to achieve a completely disordered structure. As a consequence, the microstructure is in a partially disordered state. Therefore, the contribution from the disordered structure to the observed ductility in the FeCo alloys sintered at 1100 ºC, which show around 4 % elongation, can only be small. Hence, another parameter must be considered to evaluate the final ductility. Approximately full density has been achieved in the sintered sample; and this factor also has a considerable positive effect on the ductility.

Rapid solidification showed that the ductility of the intermetallic alloys can be significantly improved in comparison to conventional processing methods. This was attributed to a refinement of the microstructure, elimination of the segregation of harmful elements and a reduction in the volume fraction of the ordered structure [228]. The grain boundary bonding in the ordered FeCo alloy is very weak, leading to an inherently brittle material. There are two reasons for this weakness; the first is the inherent weakness in the bonding itself, and the second is the segregation of harmful elements such as C, O & S [228]. SPS is often reported to produce a 'cleaning' effect of the grain boundaries. The increase in the sintering temperature to 1100 ºC also leads to greater plasticity in the powder particles during sintering than when sintered at lower temperatures. Thus, a breakdown of the oxide film may have occurred more easily during sintering, promoting any cleaning processes at high temperature and more direct bonding between grains. The role of SPS in removing the oxides for samples sintered at 1100 ºC can be observed in (Figure 6.3), and is also demonstrated by [229]. No evidence from X-ray for carbon contamination from the sintering die. Therefore, high purification during sintering has a significant contribution to the improved ductility.

The fracture surfaces of samples sintered under different SPS conditions are shown in (Figure 6.8). Revealing a change from mostly intergranular fracture along the grain boundaries for samples sintered at lower sintering temperatures, to transgranular type fracture with some plastic deformation for samples sintered at 1100 ºC. This indicates that the grain boundary bonding has been improved in the high sintering temperature samples; since the intrinsic weakness of grain boundaries is the main reason for a dominant intergranular fracture mode in the equiatomic FeCo and Fe-rich alloys, in both the ordered and disordered states [21]. Using a high sintering temperature of 1100 ºC causes an increase in vacancy concentration, which would aid in mass transport. The path of mass flow mainly occurs along the grain boundaries towards the bond between the particles [6,

230], which leads to an improvement in granular bonding. From a close look at the fracture surface of the samples sintered at 1100 ºC, 850 ºC and 800 ºC for different heating rates, more short cracks were observed in samples sintered at lower sintering temperatures in comparison to samples sintered at 1100 ºC. The nucleation of cracks is higher in the lower sintering temperature samples, which can be attributed to the refinement in grain size. With an increase in the heating rate, more cracks and porosity were introduced to the microstructure, suggesting that the lower sintering heating rate is more suitable for obtaining a less defective microstructure. Spherical powder morphology with a high level of porosity was observed on the fracture surface of samples sintered for a 5 min dwell time. Such structures are usually caused by an insufficient dwell time for the realisation of a uniform sintering temperature across the sample under the fast heating rates. The fracture mode may not reflect the improvement in ductility; the fracture surface of the previously mentioned work on a tensile-tested NiAl alloy exhibited a mixture of intergranular and transgranular fracture; even when the grain size was refined from 145 µm, giving an elongation of 3 %, to 8 µm, giving an elongation of 41 % [227]. Therefore, it appears that a significant improvement in granular bonding has occurred by sintering at 1100 ºC; which can be rationalised to be due to the cleaning of grain boundaries, and the removal of residual gases. The ductility and fracture modes of the FeCo alloy are very sensitive to interstitial impurities [228], and the residual gases can easily convert to pores in the bulk compact, leading to a decrease in ductility [229].

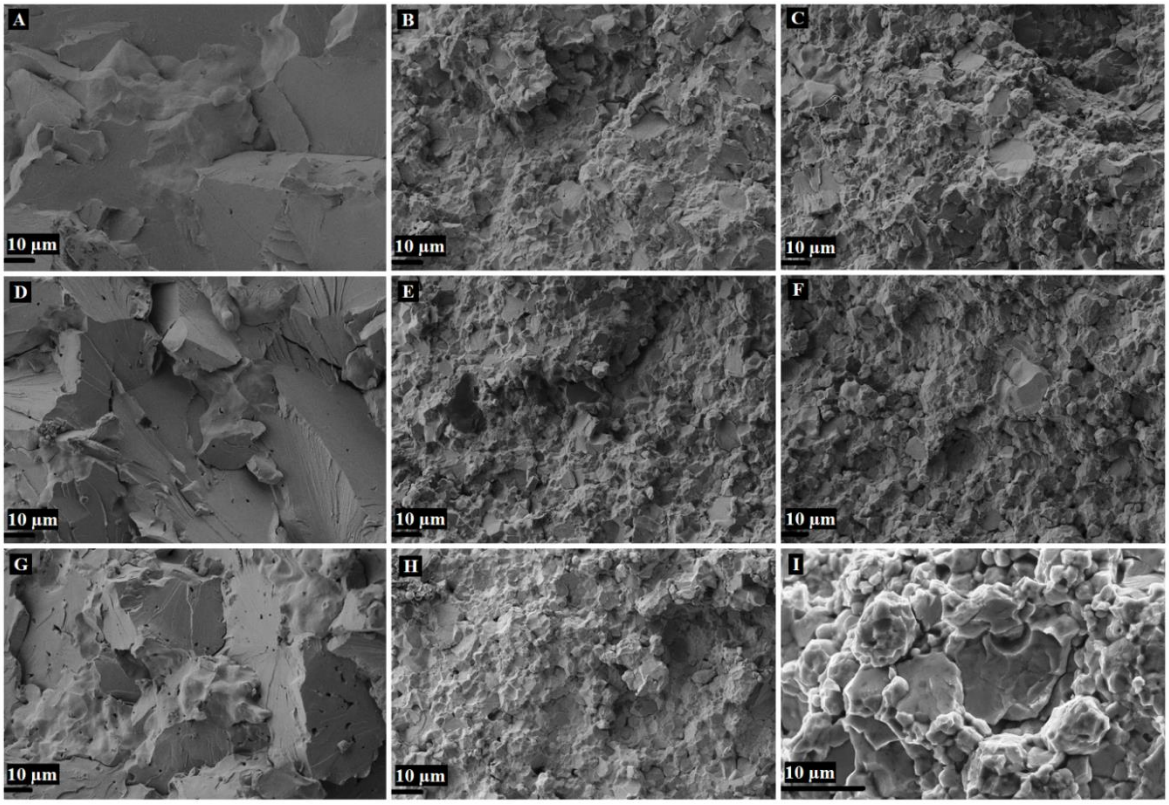

Figure 6.8. Fracture surfaces of FeCo alloys consolidated sintered at indicated symbols.

Summary

Near full densification was achieved by sintering at 50 MPa through control on sintering time and temperature, which helps in increasing the span life of graphite die. Fast heating rates were not suitable to obtain full densification, however, significant refinement in microstructure was observed at fast heating rate due to avoiding the non-densifying mechanism at the low sintering temperature. An improvement in elongation, yield strength and magnetic properties can be achieved by sintering at 1100 °C, 50 ºC/min, 50 MPa without dwelling time, due to more purification at a high sintering temperature in SPS. The inherent intergranular fracture due to the weakness in grain boundary bonding can be suppressed to show transgranular fracture for all heating rates at sintering temperature of 1100 ºC. Therefore, sintering conditions of 1100 ºC, 50 ºC/min, 50 MPa without dwelling time were used for all subsequent works.

Chapter 7: Results and discussions of dispersion GNPs in flake FeCo alloy powder

7.1. Introduction

The previous strategies for dispersion carbonaceous nanomaterials did not enable to obtain a uniform dispersion. Therefore, in order to obtain uniform dispersion for GNPs in FeCo alloy the morphology of the powder was changed to flaked shape, which has good compatibility with GNPs. The sintering temperature of 1100 ºC, 50 ºC/min, 50 MPa without dwelling were used to densify the composites because these parameters were effective in improving the properties of the alloy.

7.2. Characteristics of powders

7.2.1. As received GNPs

TEM image of as received GNPs (Figure 7.1) exhibits wrinkled graphene for dimensions 216 × 104 × 42 nm. Fragments of GNPs are observed, sticking to the larger plate which may result from synthesis procedure for graphene or subsequent functionalization.

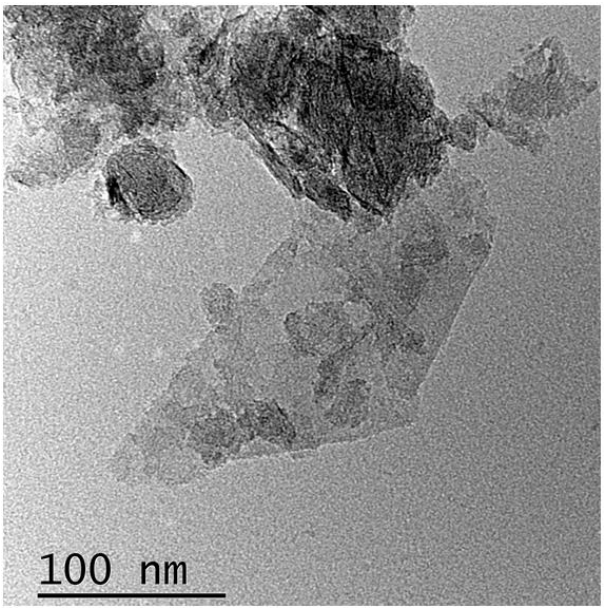

Figure 7.1.Transmission Electron Microscope (TEM) of as received GNPs.

7.2.2. As received FeCo powders

As received powder shows the spherical morphology of wide variety in size as confirmed in (Figure 7.2a) one of the disadvantages here of gas atomised powder is that small particles growth on large particles. This provides an inherent pocket for agglomeration

carbon nanostructure. After 6 h ball milling flaky shape was obtained for FeCo alloy powder (Figure 7.2b) for dimension ranged from 8.58 µm to 52.8 µm. An increase in particles size was occurred due to predominating welding processes compared to fracture processes during ball milling. Advantages such as improving shear force by flaky powder during dispersion, removing such surface pocket in as-received powder and better particles size distribution can be utilised to promote dispersion GNPs in FeCo alloy powder.

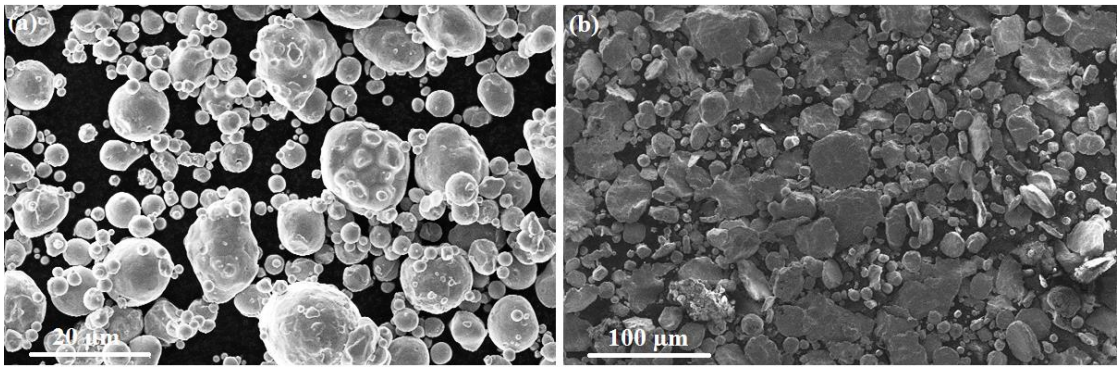

Figure 7.2. SEM images for; (a) spherical as received FeCo powder, (b) Flake FeCo powder after ball milling alloy.

7.3. Effect ball milling on densification of FeCo alloy powders

The profiles for changing average piston speed, temperature, and pressure with the time of FeCo alloy sintered at different SPS conditions are shown in Figure 7.3. No more densification occurs in both procedures after 600 sec as confirmed by level off the average piston speed. An improvement in densification is observed in sample sintered by procedure B, showing an earlier decrease and level off in average piston speed with time than procedure A. This can be attributed to introducing more stresses during changing the powder morphology to flake, application of pressure at room temperature and higher sintering temperature. However, higher expansion is observed in FeCo alloy sintered by procedure B, due to high sintering temperature.

The relative density of the sintered materials is seen in Figure 7.4. The lowest values for relative density were 97.5 % and 98 % in 4 vol. % GNPs composites produced by procedure A and B respectively. While the highest values of relative density were 99.5 % for 3 vol. % GNPs procedure B and 98.7 % for 1 vol. % GNPs procedure A. Obtaining the highest value of density in procedure B even at higher loading vol. % GNPs confirms the high-quality dispersion in procedure B. Ball milling in air atmosphere promotes the formation of maghemite as previously proved. In the alternative procedure using inert atmosphere helps in reducing oxidation during ball milling, leading to high density.

Further, it seems, factors such improve compaction between GNPs and flaky shape of FeCo alloy powder and consolidation at high temperature (densification mechanism) are more suitable to obtain high density in GNP/FeCo alloy composite.

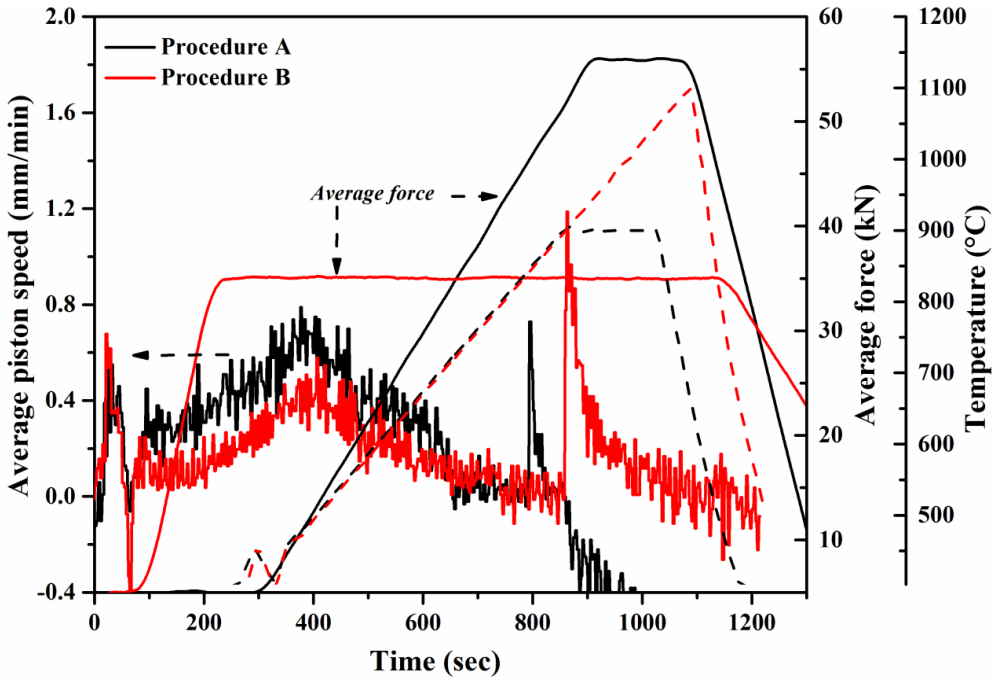

Figure 7.3. Variation of Average piston speed, Temperature, and Average force against Time for as received FeCo alloy consolidated using different procedures during SPS.

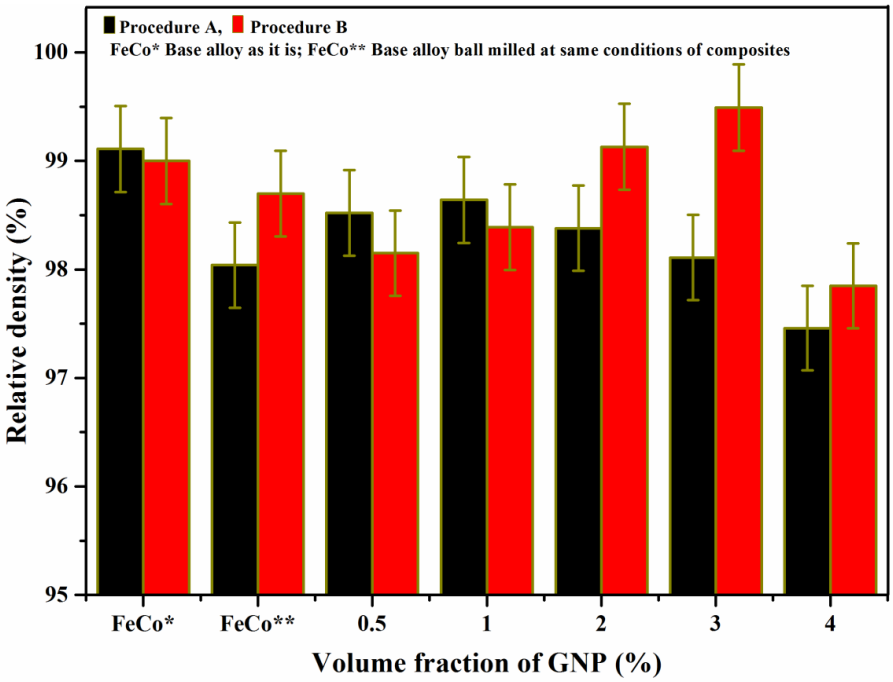

Figure 7.4. Relative density versus volume fraction for consolidated material.

7.3. Microstructure studies

The optical microstructure of sintered materials is exhibited in Figure 7.5. Significant changes were observed in the microstructure. As received FeCo alloy shows grain growth

for sintering at elevated temperature (Figure 7.5b) in comparison to sintering at lower temperature Figure 7.5a. From shrinkage curve, the densification is completed at a temperature far lower than 1100 ºC, so the elapsed time after that promotes grain growth, leading to coarse microstructure.

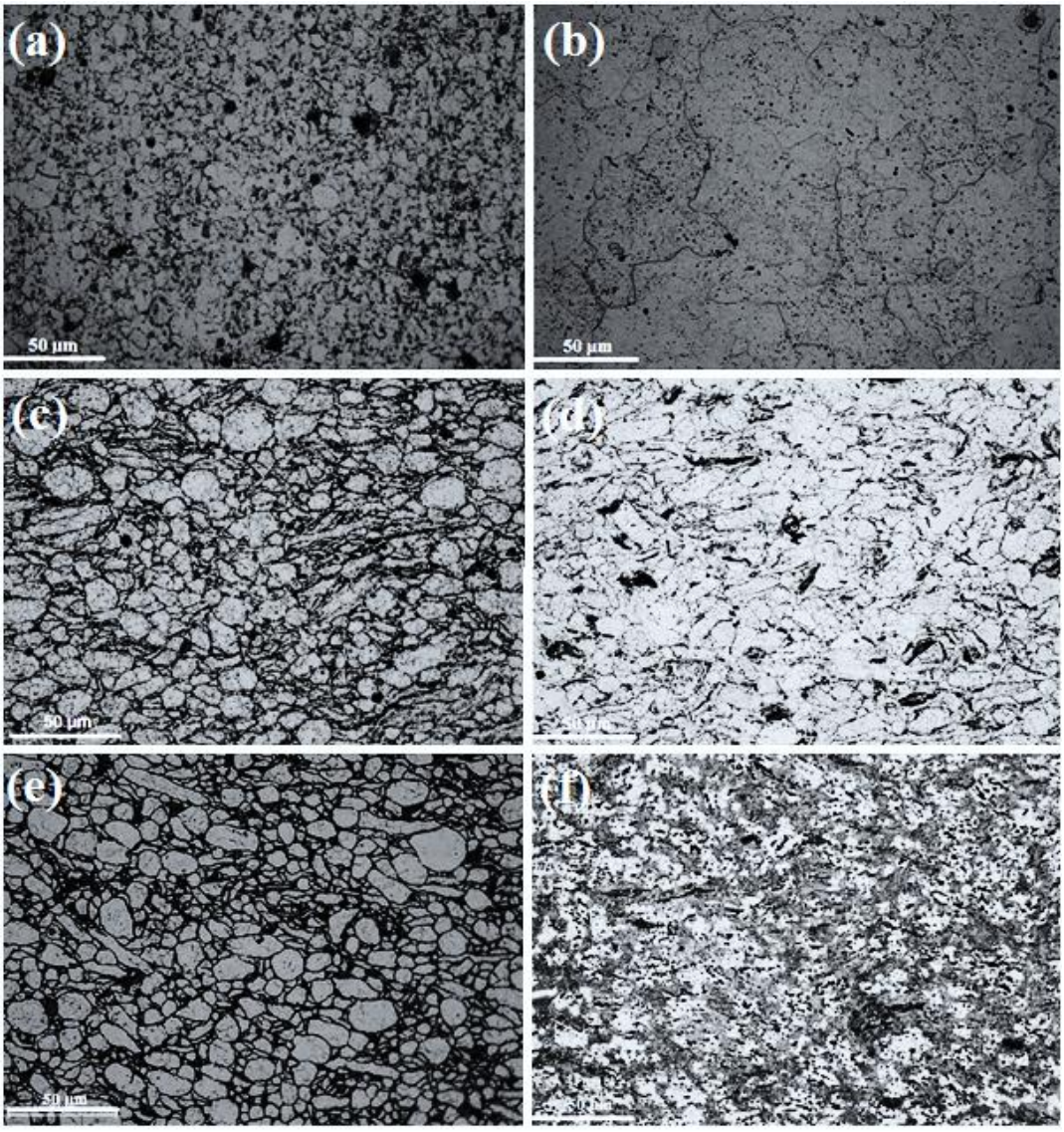

Figure 7.5. Optical microstructure of; (a) and (b) as received FeCo alloy, (c) and (d) for ball milled alloy at same conditions of composites and finally, (e) and (f) 4 vol.% GNPs composite, for procedure A and B respectively.

It has been shown in (Figure 7.2b) that ball milling has a significant effect on powder morphology the consequence of that is observed in the microstructure. The distribution for particles powder was better than as received, due to a long duration for milling in planetary ball milling under argon, which helps to weld the small particles on the larger particles. The structure in composites following procedure A shows agglomeration for GNPs at grain boundaries, which increases with high loading of vol. % GNPs. Interesting enough, this behaviour is converted to uniform dispersion in procedure B as shown in Figure 7.5f. Ball milling processes were used here for a limited time 1 h in order to dispersion GNP in FeCo

alloy powder. Changing, the morphology of powder to flake shape increase shear forces by particles during dispersion, leading to uniform distribution for GNPs on grain boundaries. Opposite to material prepared using procedure A, GNPs were embedded inside grains in the second procedure, as seen in Figure 7.5f. This can be attributed to acquiring the base powder some ductility after deformation, as ball milling processes change the order structure to disorder in FeCo alloy.

7.4. Magnetic properties

The upper halves of hysteresis curves for the consolidated materials following procedure A and B are shown in Figure 7.6, the magnetic properties of the sintered materials are summarised in Figures 7.7 and 7.8. Using magnetic field of (25 kA/m) does not enable to obtain saturation in composite materials prepared in procedure B, which shows a continuous decrease in induction with increasing the volume fraction of GNPs. However, after annealing at 600 ºC of 1 h and increasing the applied magnetic field to (140 kA/m), the saturation was achieved up to 3 vol. % GNP. The general trend for coercivity values in composite materials fabricated using procedure B are to increase as the loading of vol. % GNPs is increased even after annealing, exceeding the coercivity values of composites prepared using procedure A.

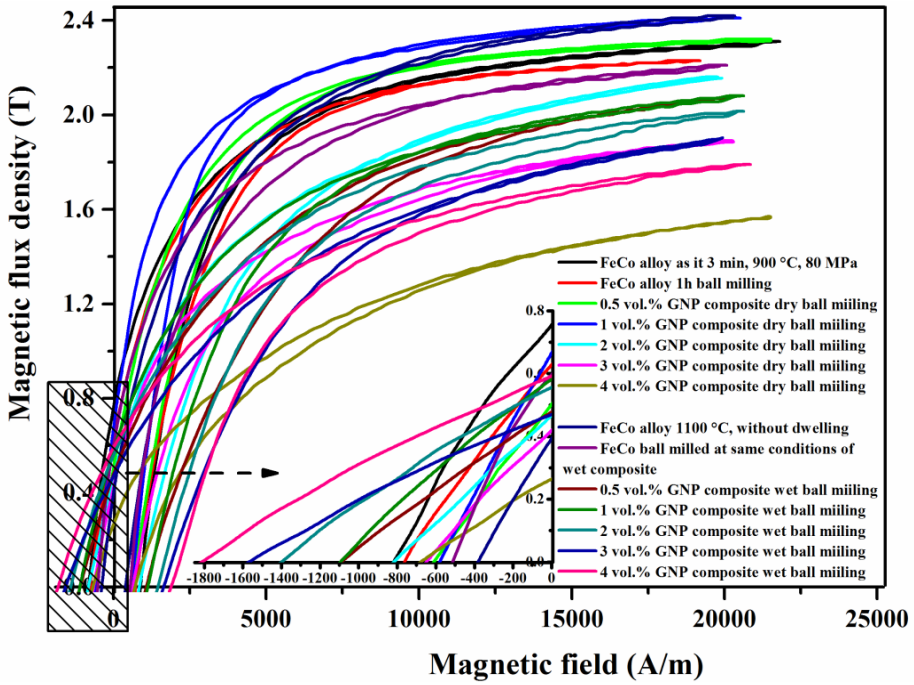

Figure 7.6. Upper halves of the hysteresis curves of the indicated materials.

The relative density was higher in the composite prepared using procedure B at higher loading of vol. % GNPs as compared to procedure A (Figure 7.4), and adding, GNPs

promotes the ordered structure (Figure 7.9b), it is reported that the saturation induction of ordered structure is higher than disordered structure [1]. These factors must improve the saturation induction in composite material prepared by procedure B. However, the formed precipitates and stresses in structure due to long ball milling time of alloy and high sintering temperature overcome on these advantages, causing a slight decrease in saturation. Various values for saturation induction with altered grain sizes have been reported by [49]. Kuhrt et al. [231] reported that grain refinement due to ball milling may cause a drop in magnetisation of material. A significant amount of domain walls is curved and lied at the intersection with grain boundaries [232]. Hug et al. [47] studied the effect of plastic deformation on magnetic properties. The researchers noticed that the intergranular stresses due to increased dislocations density may change the anisotropy constant K_1, leading to deteriorating in magnetic properties. Increased dislocations density owing to a long time of ball milling prevents achieving saturation induction at a low applied field of (25 kA/m). Finally, the precipitates are the most deteriorate factor on saturation induction, it is hard to detect formation of carbide from XRD, which might be in an amount less than the sensitivity of the instrument.

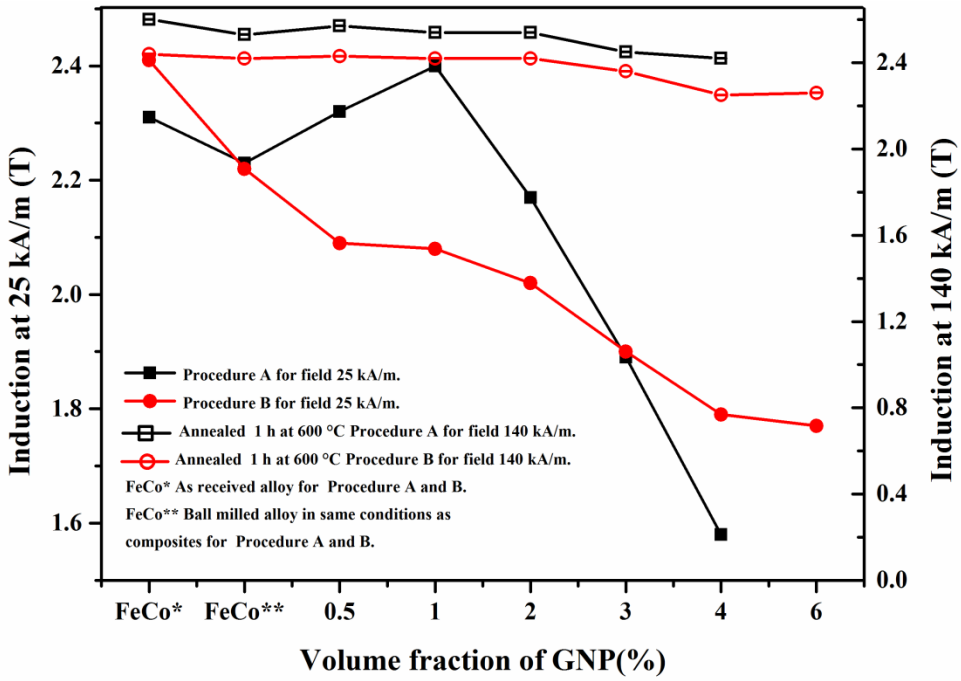

Figure 7.7. Summarize the variation in saturation induction of consolidated materials against volume fraction.

In the conventional rule, the increase in grain size of micron scale reduces the coercivity value. The microstructure was changed significantly in procedure B due to increasing sintering temperature, long ball milling time and uniform dispersion of various loading vol. % GNP as shown in Figure 7.6. The subsequence of that is a considerable change in

coercivity values. The coercivity of monolithic FeCo alloy sintered at 1100 ºC in procedure B was decreased as compared to FeCo alloy sintered at 900 ºC in producer A, this is due to the increase in grain size in samples sintered at high temperature. However, the refined microstructure from uniform dispersion for GNPs in FeCo alloy using procedure B and formation for precipitates by sintering at high temperature caused a significant increase in coercivity. Annealing processes at 600 ºC for 1 h leads to an increase in coercivity in procedure B; this could be attributed to increasing in ordered structure as the annealing was performed in ordered region. The wide range slow scan and the slower scan of a narrow range to detect ordered state of X-ray patterns of as received FeCo alloy and its composite are shown in Figures 7.9 a and b. Increasing ordered structure was observed with introducing GNPs to monolithic FeCo alloy, which is another reason for increasing the coercivity in composite materials as the coercivity of ordered structure is higher than disordered structure at room temperature [1]. However, adding carbonaceous nanomaterial to FeCo alloy combined with ball milling promotes nanocrystallite in composite [167]. In that case, the coercivity follows a direct proportion to the nanocrystallite size of the ordered structure. The effect of this structure was predominate compared to the effect of grain size on coercivity in samples of procedure A were consolidated at (900 ºC), which is significantly lower than those of procedure B of (1100 ºC).

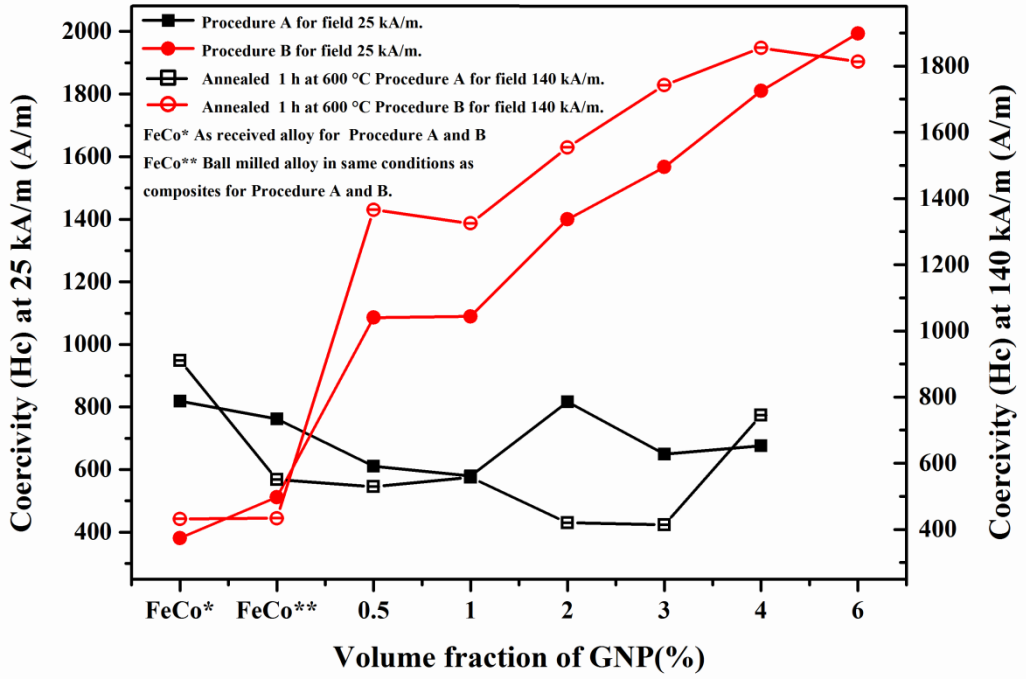

Figure 7.8. Summarize the change in coercivity against volume fraction of consolidated materials

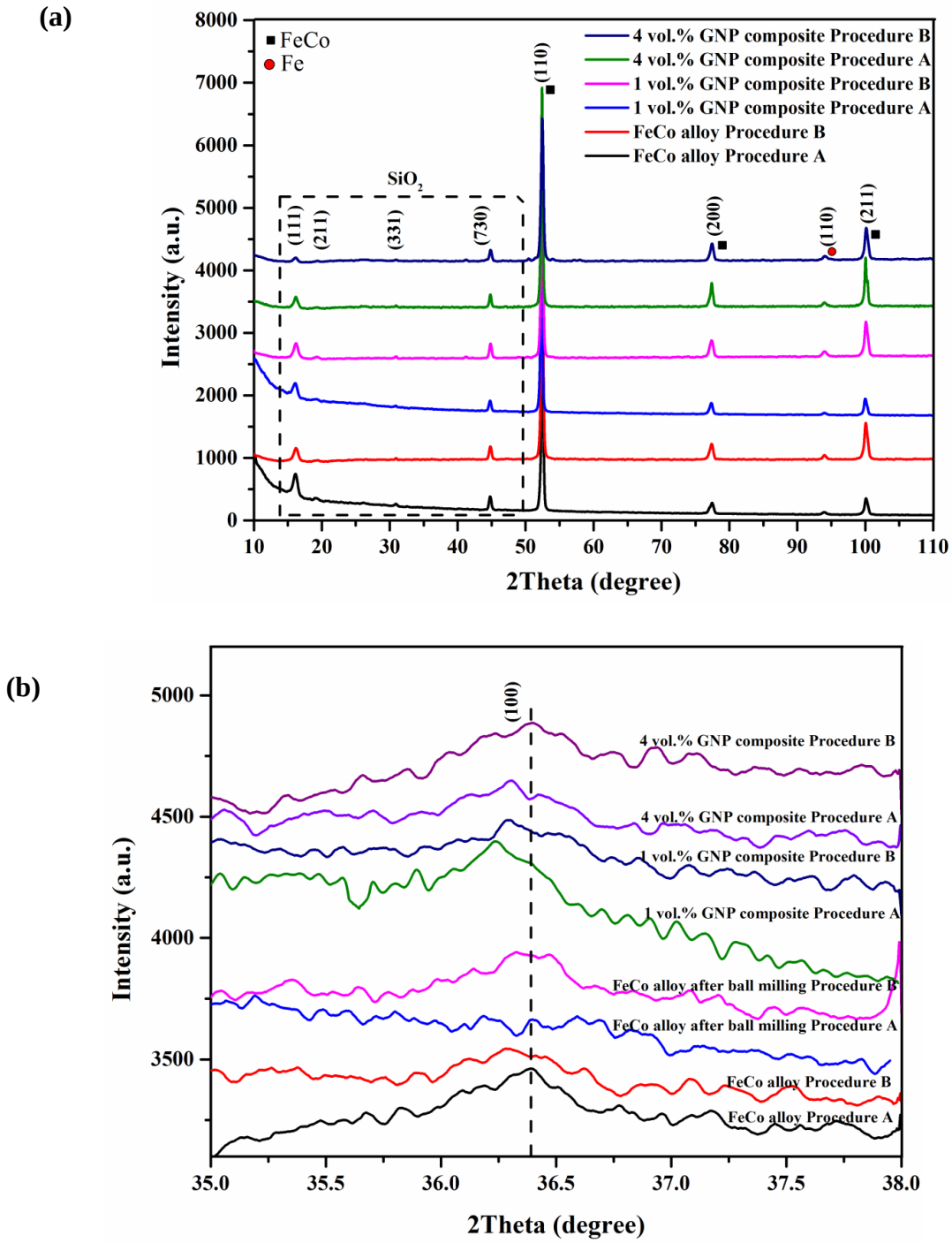

Figure 7.9. X-ray diffraction patterns of consolidated materials of indicated volume fractions, (a) wide range of scan, (b) superlattice range (100).

7.5. Mechanical properties

The stress-strain curves of as received FeCo alloy, ball milled FeCo alloy at same conditions of composite materials and the composite materials of different volume fraction sintered following procedures A and B are shown in Figures 7.10 a and b.

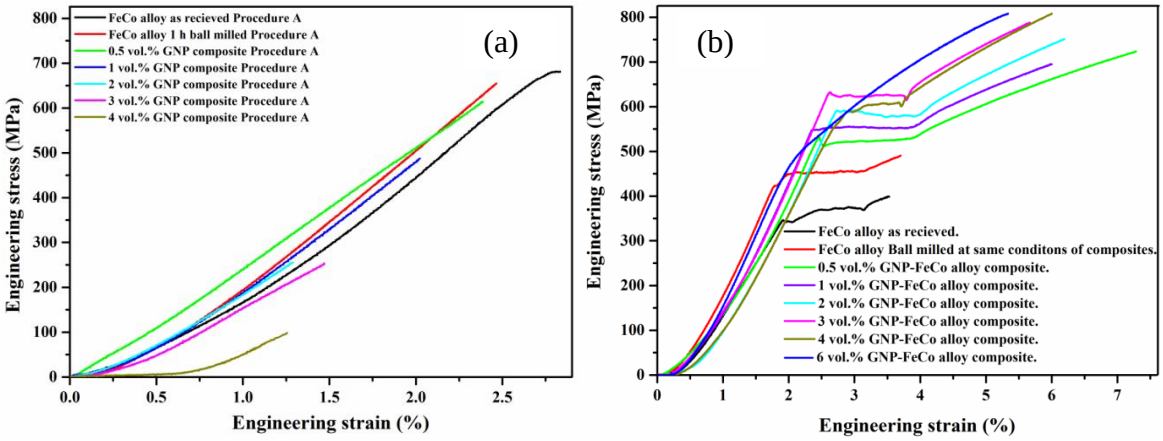

Figure 7.10. Stress-strain curves of composites prepared by: (a) procedure A; (b) procedure B.

A summary of the ultimate tensile strength, yield strength and elongation against volume fraction of reinforcement for the both procedures are shown in Figures 7.11 and 7.12. Failure before yield stress is observed for composites material prepared following procedure A, introduce more loading of GNP up to 4 vol. % deteriorates strength and failure strain to unexpected values of 97 MPa and 1.3 % respectively. However, a dramatic change happens in the mechanical properties of composites prepared by procedure B.

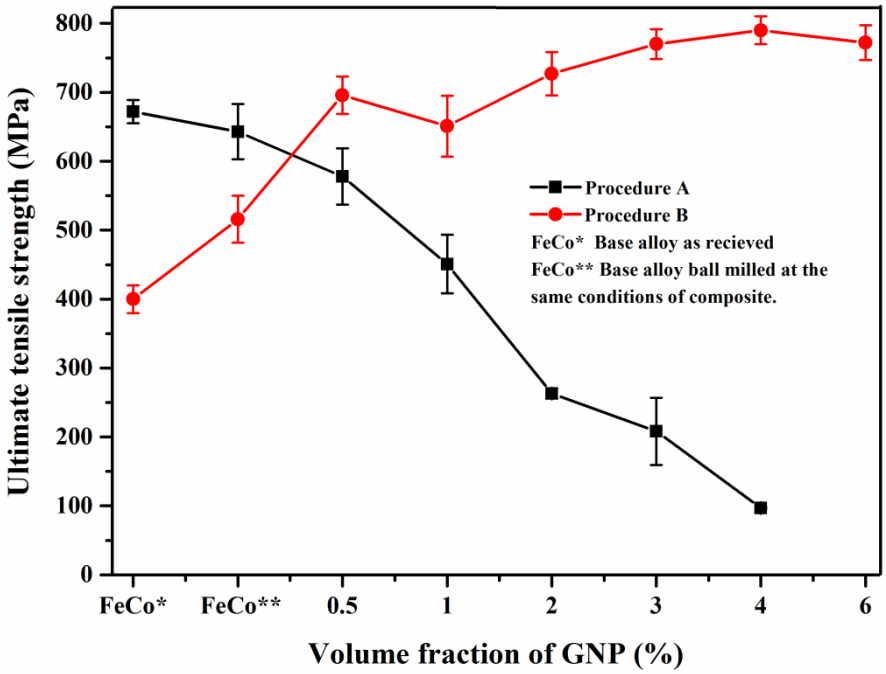

Figure 7.11. Summarise of ultimate tensile strength of sintered materials.

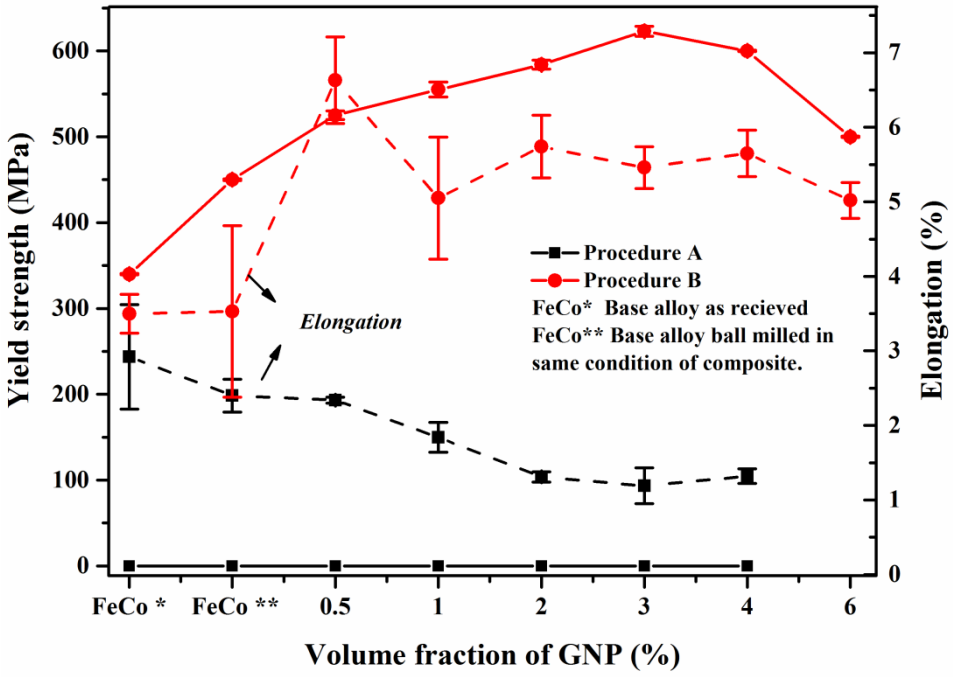

Figure 7.12. Variation of yield strength and elongation for sintered materials.

Materials sintered at conditions of this procedure were distinctly exhibited yield stress feature even without including GNPs. A considerable improvement in elongation was observed which exceeded 7 % in some sample, showing maximum average value 6.6 % at loading 0.5 vol. % GNPs. The highest value for the ultimate tensile strength of 790 MPa was observed in 4 vol. % GNP composite, exhibiting ~ 100 % increase over as received FeCo alloy. The yield strength was significantly increased in from 340 MPa to 623 MPa in 3 vol. % GNPs, showing ~ 85 % improvement. Overall, a linear increase in mechanical properties can be observed with increasing in volume fraction of GNPs in procedure B. The mechanical properties were compared with some commercial FeCo alloy in Table 7.1.

Table 7.1 Shows comparison for mechanical properties for GNP-FeCo alloy composites with some commercial alloys.

Material	Ultimate tensile strength (MPa)	Yield strength (MPa)	Elongation (%)	Reference
FeCo alloy (ordered state)	250	0	0	[21]
FeCo alloy (disordered state)	NA	400	4	
FeCo-2V alloy (disordered state)	654	380	17.7	[39]
FeCo-2V-Boron alloy (ordered state)	687	285	13.2	[39]
FeCo-Carbon or Boron (ordered state)	Fail before yield strength without improvement in elongation			[39]
FeCo-GNP composites (0.5-6 vol.% GNP)	696-790	525-600	5.65-6.63	This study

7.5.1. Tensile test

The significant decrease in mechanical properties of procedure A is due to poor dispersion. Furthermore, the restacking of GNPs due to effect of the π-π attraction force between the sheets from poor dispersion is a serious issue compared to single layer graphene, as it is easily close to graphite micro size, and the agglomerated sheets are easily slipping with respect to each other under stress, causing very poor properties in procedure A.

Three mechanisms can contribute to the improvement in mechanical properties are observed in the composite prepared using procedure B, which are: (1) Orowan strengthening. (2) Dislocation density. (3) Load bearing [233]. The microstructure observation shows that the GNPs were embedded inside grain following procedure B. Meanwhile, that the mechanism such Orowan strengthening works properly here. Further, different in thermal expansion between reinforcement and matrix increases dislocation density in composite materials [234]. Orowan [17] proposed a relationship between the change in yield strength Δσ and separation distance λ between dispersed particles, equations 7-1 and 7-2, in which relies on shear stress required to bow the dislocation between particles in this separation. This mechanism is very effective for reinforcement size < 100 nm.

$$\Delta\sigma = \frac{0.13Gb}{\lambda} \ln \frac{r}{b} \tag{7-1}$$

So, the decrease in separation between particles improves yield strength. The volume fraction for reinforcement and separation can express by [233].

$$\lambda = dp \left[\left(\frac{1}{2Vp}\right)^{\frac{1}{3}} - 1 \right] \tag{7-2}$$

Here, dp is particle diameter, Vp is the volume fraction of reinforcement, b is the Burgers vector, r is the radius of the particle, and G is the shear modulus.

Meanwhile, good dispersion at a high-volume fraction of reinforcement reduces the separation between particles, leading to high yield strength, which is explained the increased yield strength with volume fraction GNPs in composites produce using procedure B.

The interface bonding in the composite can be categorised into mechanical, physical bonding (van der Waals interactions), diffusion bonding and reaction bonding [235]. Observation of TEM for GNPs exhibited wrinkled morphology which improves the mechanical bonding with FeCo alloy powder during ball milling. Sintering at elevated

temperature 1100 ºC in procedure B has also effect on the interface, enhance wettability between reinforcement and matrix alloy due to increased sintering temperature has been reported by [236]. Improve interface bonding due to ball milling and SPS combine with the high aspect ratio for GNPs increase transformation of the stresses via the interface, leading to great improvement in mechanical properties. The conventional Shear lag model for load transfer from matrix to reinforcement in microfiber composite was also used in carbon nanostructure composite [10].

7.5.2. Lüders region

The abrupt (discontinuous) yielding stresses and lüders region are observed in materials sintered using procedure B conditions. It is deformation feature which is mostly noticed in the ordered material, relating to the mobility of dislocations in ordered structure [42]. Preventing dislocation mobility prior to yielding due to (i) the dislocations density is low, (ii) pinning by interstitial atoms, or other dislocations [216]. The great tendency to exhibit this behaviour in FeCo alloy occurs at larger grain size in order states. Zhao and Baker claimed a formula between lüders strain and grain size: $\varepsilon_{L=} (k/\theta) \times d^{-1/2}$. Here, ε_L is lüders strain, k is Hall-Petch parameter, θ represents work-hardening rate, and d is the grain size [21]. As grain size decreased the lüders strain will be increased [237]. Variation in lüders strain with volume fraction of GNPs is shown in Figure 7.13. The highest value for lüders strain is noticed at loading 1 vol. % of GNPs composite, due to the efficient pinning for dislocations motion at this fraction. The pining effect was dropped at a higher volume fraction of GNPs, owing to increasing dislocation density with increasing loading of vol. % GNPs. Moreover, the decreased density values of sintered composite at a higher fraction from GNPs also makes deformation by dislocation motion easy. Further, as reordering increase, the dislocation density will drop in addition the motion of dislocation will be easier than the partially ordered structure in which the super dislocation will move with less creation for antiphase boundaries [29]. High loading of vol. % GNPs shows an increase in the fraction of ordered state (Figure 7.9b), causing a decrease in lüders strain.

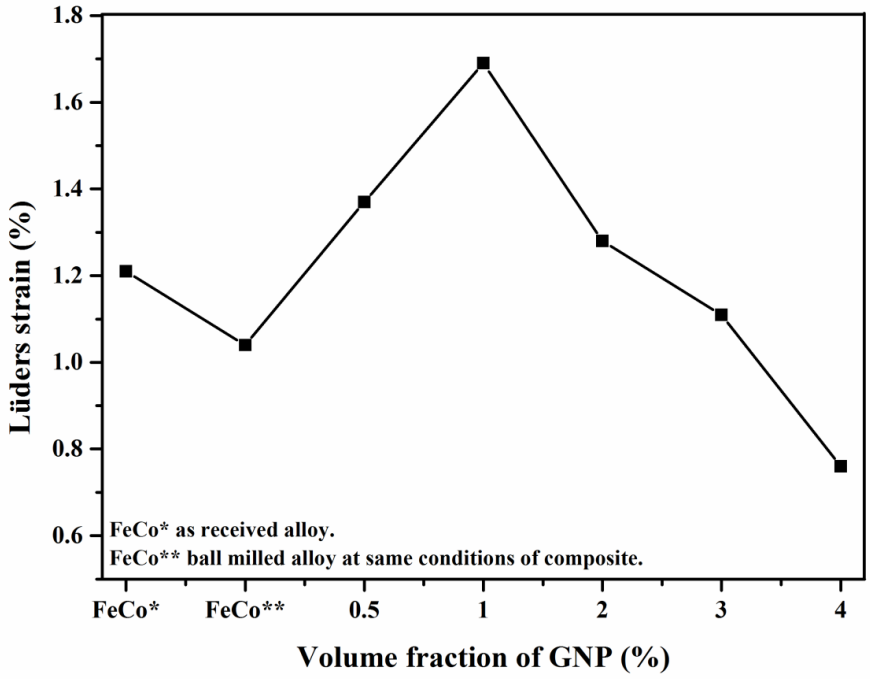

Figure 7.13. Effect volume fraction of GNPs on lüders strain.

7.5.3. Ductility

Different parameters influence on the elongation in equiatomic FeCo alloy and its composites. The reduction in ductility in procedure A can be attributed to the poor dispersion which leads to the overlapping of GNPs and forming thick nanoplatelets, which are easily slip under stress and to also to formation oxide from ball milling in air. Ball milling in the inert atmosphere not only promote uniform dispersion [238], but also helps to reduce the effect of the oxidising atmosphere on ductility and densification. At high oxygen content, the oxide creates a surface barrier prevent surface diffusion, leading to drop in densification [239]. XRD in (Figure 7.9a) shows that high sintering temperature in procedure B was effective in removing oxide (SiO_2), also the uniform dispersion in this procedure has a significant positive influence on elongation, as it reduces the porosities and improves the bonding between reinforcement and matrix. Limit number of slip reduce ductility in equiatomic FeCo alloy [22]. George et al. [39] noticed that the slip refinement by fine precipitate can improve ductility in the ternary FeCo-2V alloy. A mechanism of dispersing slip can be introduced by doping GNPs in FeCo alloy, which provides crack propagation inhibitors, a barrier for dislocation pile-up and microstructure refiner, which are favourable to improve ductility.

7.5.4. Hardness

The change in Vickers hardness with the volume fraction of GNPs is shown in Figure 7.14. Increased hardness values in procedure A up to 1 vol. % GNPs can be related to the oxidation due to ball milling in the air and to the finer microstructure from sintering at the lower sintering temperature of 900 ºC. However, different behaviour is observed at high volume fraction, the martial sintered in procedure B revealed an increase in the hardness, which is rationalised to improve densification, owing to better dispersion and to increase the amount of the precipitates with increasing the volume fraction.

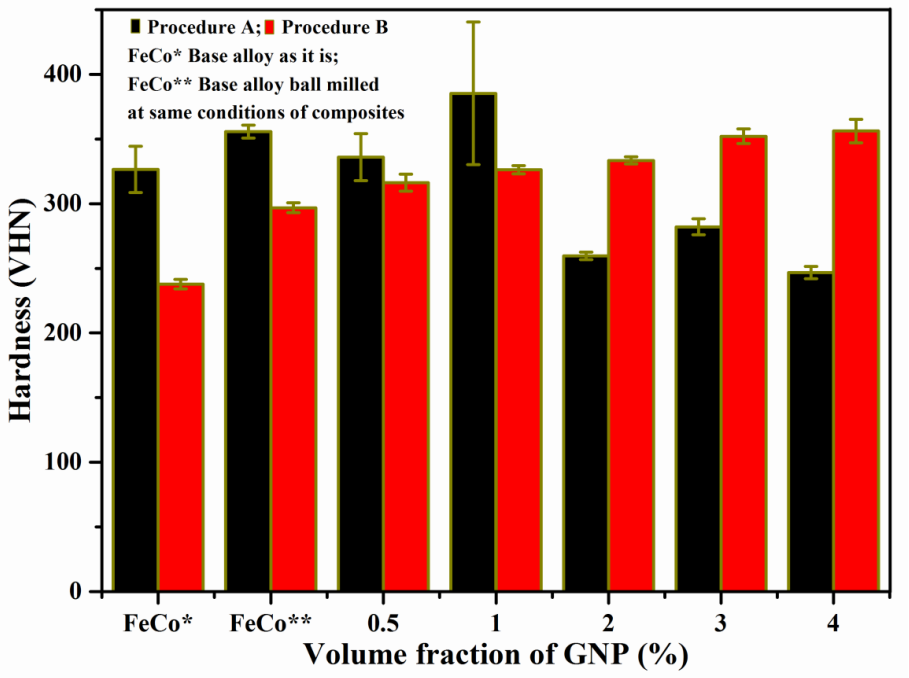

Figure 7.14. Vickers hardness of sintered materials.

7.5.5. Fracture surface

The inherent intergranular fracture in both ordered and disordered equiatomic FeCo alloy [1], which is observed in material fabricated using procedure A, is changed in samples sintered in procedure B to transgranular fracture mode, due to improving the grain boundary bonding Figure 7.15. In composites fabricated following procedure B the fracture surface reveals dimples surrounding transgranular fracture, as illustrated in Figure7.16. Unfortunately, the distribution of patched ductile area was restricted to present GNPs. GNPs were observed inside dimples and bridging grain boundaries confirming the role of GNPs in improving the grain boundaries bonding when the uniform dispersion is achieved. This also provides an evident about maintaining the integrity of GNPs after fabrication

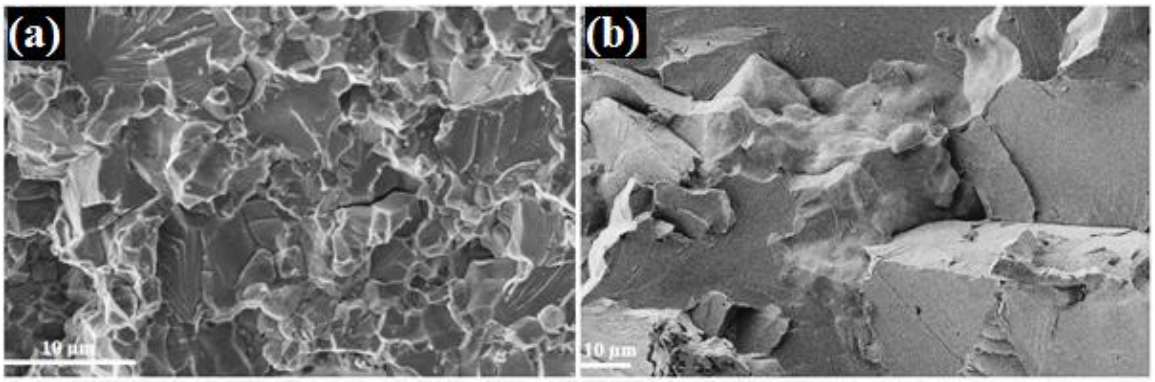

Figure 7.15. SEM images for fracture surface of; (a, b) as received FeCo alloy, for procedure A and B respectively.

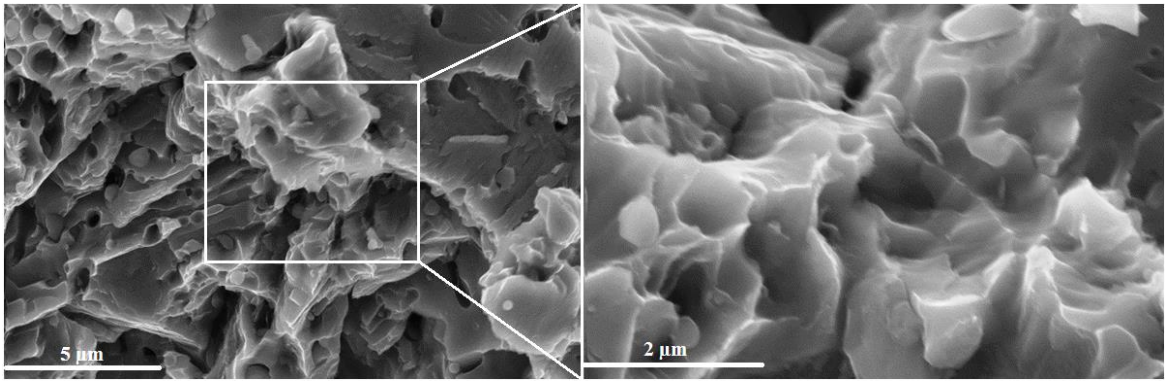

Figure 7.16. SEM images illustrate formation of dimples 4 vol. % GNPs composite procure B.

7.6. Raman spectra

The Raman spectra of as received GNP and composite consolidated following both procedures are shown in (Figure 7.17), the most characterise bands for graphene are observed, the quality of graphene is analysed by the intensity ratio (R=ID/IG) [240, 241]. The main peaks are observed in GNPs composites, indicating the integrity of GNPs were maintained during fabrication processes. The R ratio was increased from 1.00 in raw GNPs to 1.27 in a composite prepared using procedure A. Interestingly, this ratio was reduced in procedure B to 1.14 compared to the former procedure, even the sintering temperature was increased. This is the advantage of SPS over conventional sintering processes in preserving the nanostructure for sintered materials. The reduction in R ratio in procedure B can be assigned to reduce the impact effect by balls due to using the isopropanol alcohol as PCA and to release functionalization oxide at high consolidation temperature.

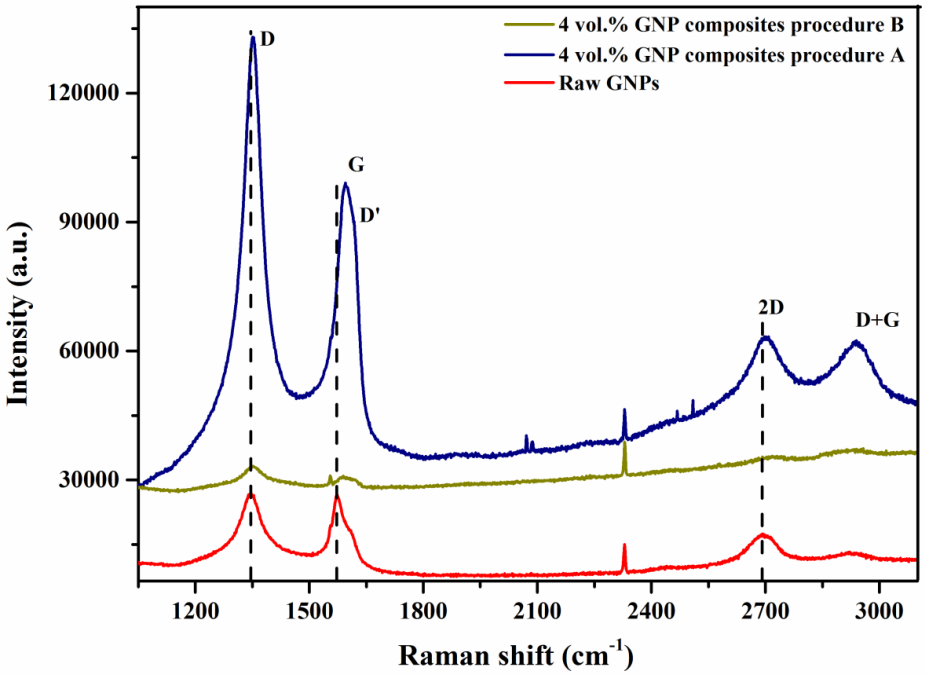

Figure 7.17. Raman spectra of GNPs and GNPS composites.

Summary

The flaked FeCo alloy powder is more compatible to dispersion GNPs, therefore a uniform dispersion of up to 6 vol. % GNP in FeCo alloy was achieved. The high SPS sintering temperature helps to improve densification in GNPs composites without damaging the GNPs. A significant increase of ~ 85 % and ~ 100 % can be achieved in the yield and ultimate strengths, respectively, compared to the as-received alloy. A notable improvement in the ductility of the extremely brittle equiatomic FeCo alloy can be achieved through a uniform dispersion of GNPs; which causes a refinement of the slip systems, prevents crack propagation and leads to a fine microstructure. The fracture mode was changed from intergranular fracture, due to the inherent intergranular weakness of grain boundaries, to transgranular fracture, showing patches of dimples comprising of GNPs in the composites. A high saturation induction of (2.4 T) was obtained in the composite of 2 vol. % GNP at an applied field of 140 kA/m, showing the best combination of the mechanical and magnetic properties. A very fine microstructure obtained due to the homogenous dispersion of the GNPs in the FeCo alloy composites leads to a significant increase in coercivity.

Chapter 8: Results and discussion of heat treatment of 4 vol. % GNP composites

8.1. Introduction

Heat treatment has a significant influence on the properties of FeCo alloy. The yield strength, elongation and coercivity are very sensitive to annealing heat treatment, due to the variation in grain size, ordered-disorder state, and phase transformation. The current work aims to maintain soft properties in GNP-FeCo alloy composites. High volume fraction composites of 4 % were selected due to the high increase in coercivity of these composites.

8.2. Microstructural changes after heat treatment

The microstructure of the sintered as received FeCo alloy, ball milled FeCo alloy, 4 vol. % GNP-FeCo alloy composite without heat treatment and after quenching from 600 ºC, 710 ºC and 900 ºC are seen in Figure 8.1. A wide difference in microstructure is observed between FeCo alloy and composite material, the large grain size in as received FeCo alloy was firstly reduced by ball milling, which was further reduced after adding GNP to the alloy. The microstructure of 4 vol. % GNP composite was very sensitive to the change in quenching temperature. High-magnification scanning electron microscopy (SEM) images with EDS analyses of 4 vol.% GNP composites quenched from 710 ºC and 900 ºC are shown in Figures 8.2, 8.3 and 8.4, which were used to check the variation in chemical composition and to monitor the precipitate and GNPs after heat treatment. The pearlitic structure was observed at low quenching temperatures up to 710 ºC, which was produced even in samples without heat treatment, due to the reaction of FeCo alloy with the excessive carbon from the soot and amorphous layer on the surface of raw GNPs at the high sintering temperature. Furthermore, the interfacial reactions of GNPs with FeCo alloy also help to increase the amount of carbides in the sintered composite materials, see Figure 8.4. The pulsed electric current helps in increasing the speed of precipitate and reducing the temperature of transformation, leading to form the precipitate at a temperature lower than normal processes [242]. The lamellar structure was disappeared at quenching temperature of 900 ºC, due to converting the laminate structure to spherical structure. The EDS analysis does not show a significant change in chemical composition in samples quenched from 710 ºC and 900 ºC, as seen in Figures 8.2 and 8.3.

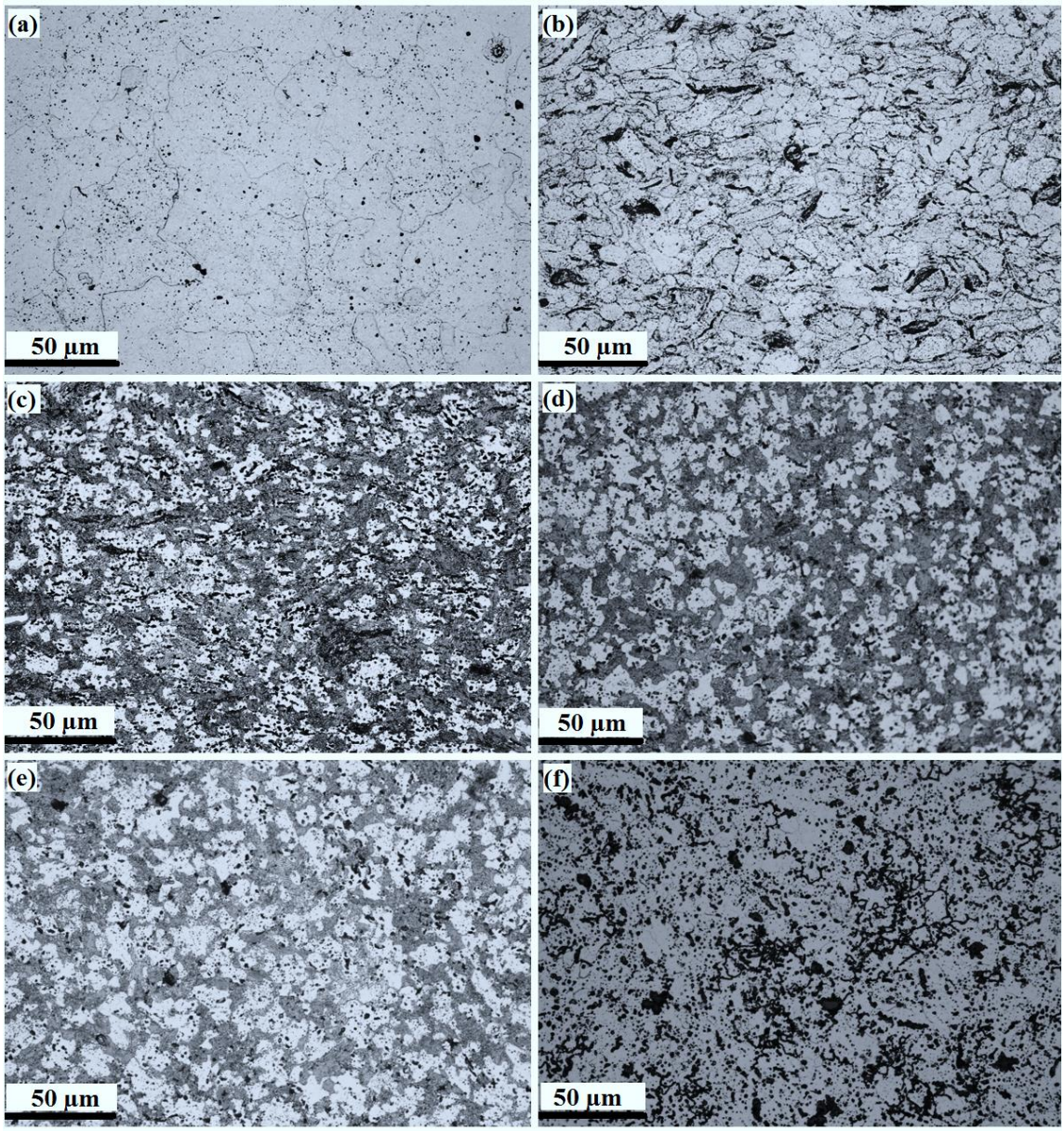

Figure 8.1. Optical microstructure of (a and b) FeCo alloy before and after ball milling without heat treatment, (c, d, e and f) are 4 vol.% GNP composite without heat treatment and with heat treatment, quenched from 600, 710 and 900 °C respectively.

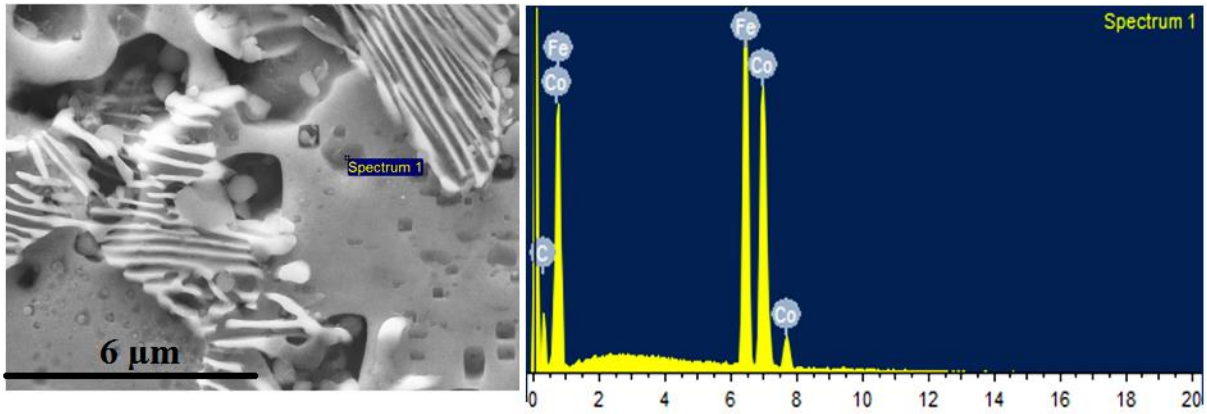

Figure 8.2. SEM microstructure and EDS analysis of 4 vol. % GNP-FeCo composite quenched from 710 °C.

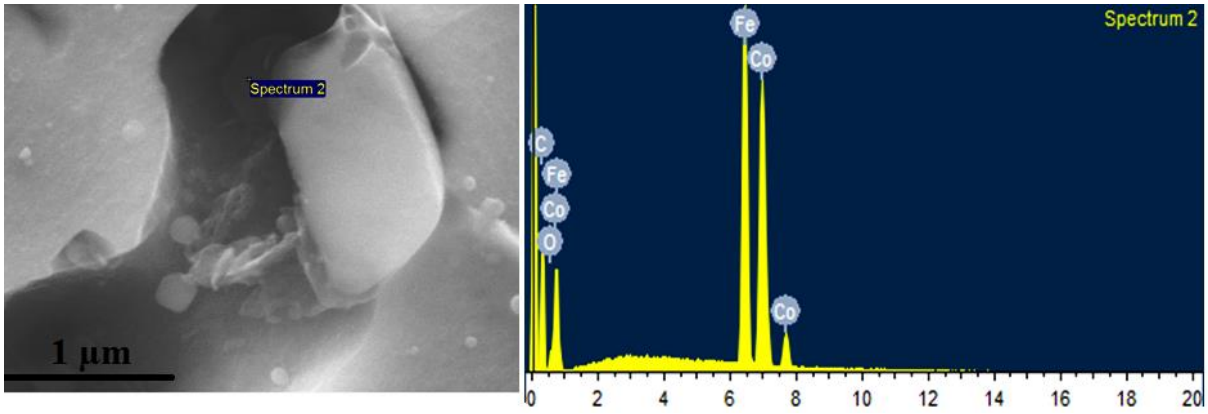

Figure 8.3. SEM microstructure and EDS analysis of 4 vol. % GNP-FeCo composite quenched from 900 °C.

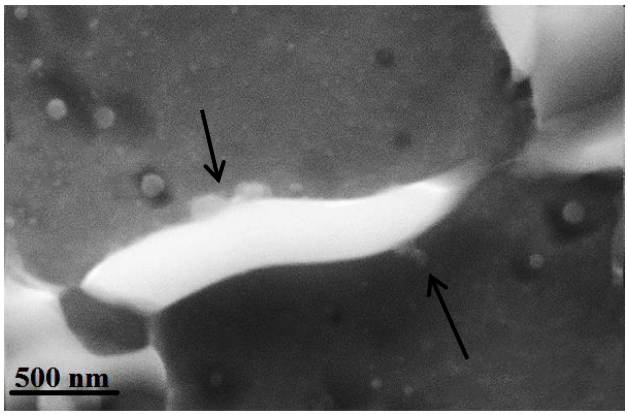

Figure 8.4. High magnification SEM for the interface in 4 vol. % GNP-FeCo composite quenched from 710 °C.

8.3. X-ray diffraction results

X-ray histograms of as received FeCo alloy, 4 vol.% GNP-FeCo alloy composite without heat treatment and after quenching from 600, 710, 900 ºC are shown in Figure 8.5, in order to observe the formed phase during heat treatment the curves were enlarged. The X-ray patterns were compared with standard data (JCPDS), giving an evidence for carbides formation. The intensity of iron carbide peaks was changed with increasing quenching temperature, which can be rationalised to spheroidizing the iron carbide at quenching

temperature of 900 ºC. It has been already explained that the GNPs were kept intact during the process as shown in Figure 8.4, which suggests that the carbides were formed from the reaction with soot and the amorphous carbon layer on the surface of GNPs. The influence of heat treatment on the ordered structure is shown in Figure 8.6, the ordering was increased after embedding GNP in FeCo alloy.

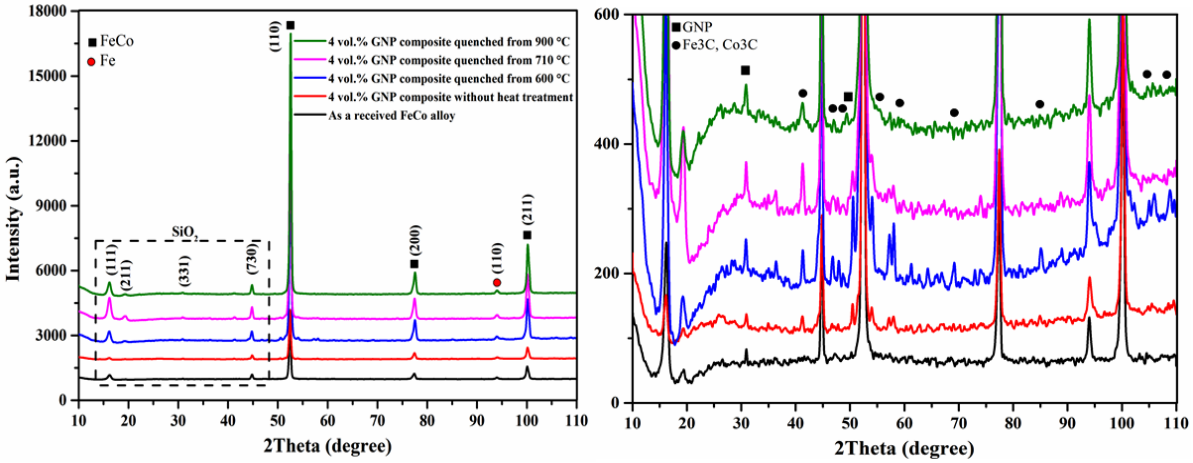

Figure 8.5. X-ray diffraction of; as received FeCo alloy, 4 vol.% GNP-FeCo alloy composite without heat treatment and after quenching from indicated temperature.

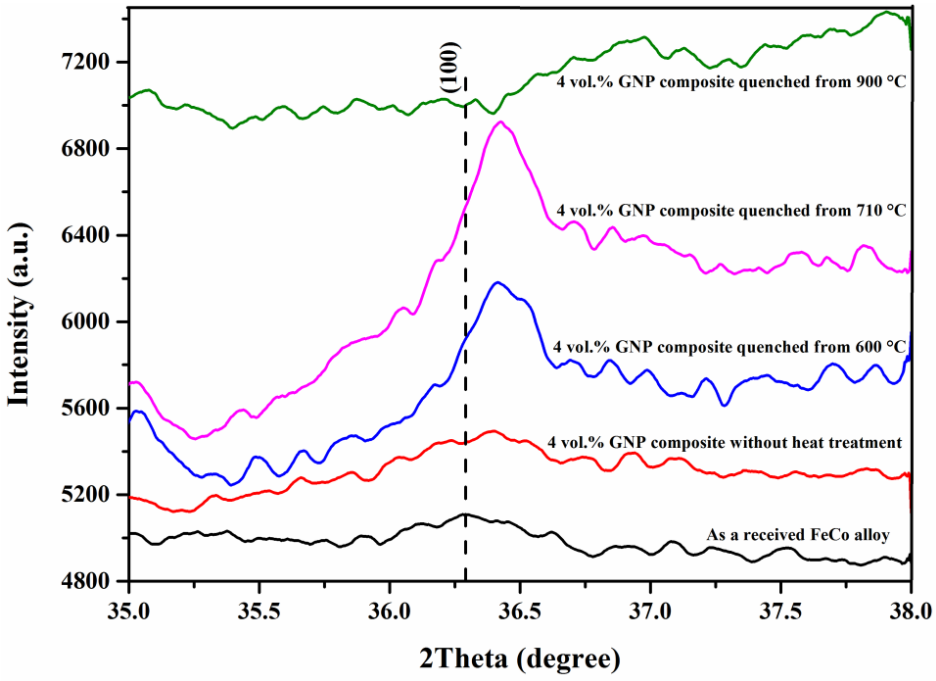

Figure 8.6. X-ray diffraction of superlattice line (100) of indicated densified materials.

Quenching from a temperature in the range of ordered structure at 600 ºC or 710 ºC leads to increases in volume fraction of the ordered structure. Upshifting and broadening in the superlattice peak were observed due to included strains from dispersion and quenching processes.

8.4. Raman spectroscopy results

Raman spectra of raw GNPs and 4 vol. % GNP-FeCo alloy composite without heat treatment and after quenching from 900 ºC are shown in Figure 8.7. GNPs were maintained intact after sintering and heat treatment processes as evidence from present the G band. However, the band was split due to the induced thermal stress from the heat treatment.

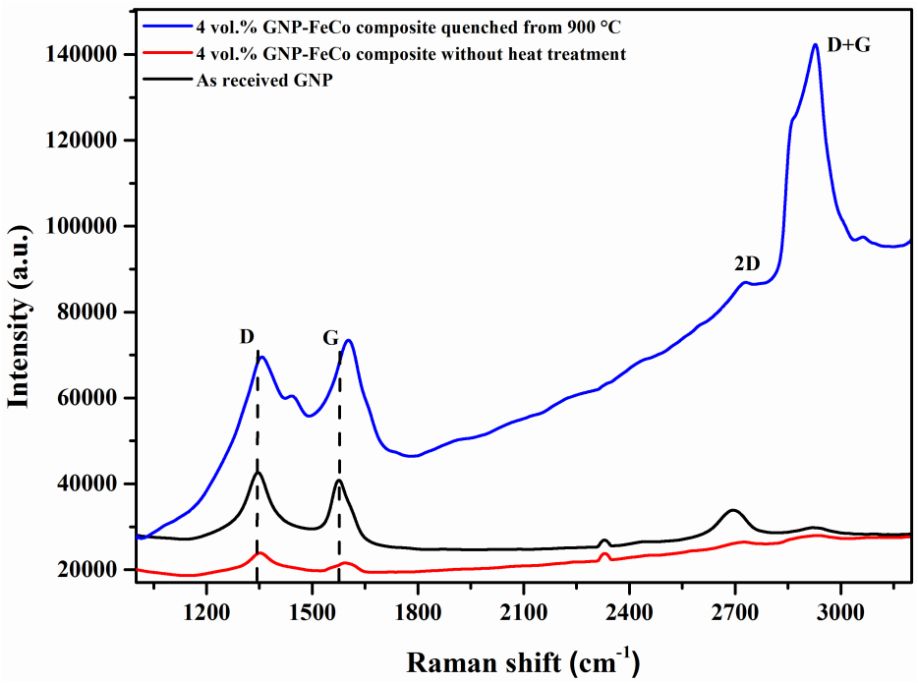

Figure 8.7. Raman spectrums of the indicated material.

The intensity ratio R (I_D/I_G) in (Table 8.1) reveals that the defects were increased after sintering. However, quenching from 900 ºC in an inert atmosphere was very effective in reducing the defects to lower value than raw GNPs, due to releasing the functionalization oxides and the amorphous carbon surface layer on GNP.

Table 8.1: Raman intensity ratio R (I_D/I_G) of sintered materials.

Materials	R(I_D/I_G)
Raw GNP	1.06
4 vol.% GNP-FeCo composite without heat treatment	1.14
4 vol.% GNP-FeCo composite quenched from 900 ºC	0.96

8.5. Magnetic properties after heat treatment

The upper halves of hysteresis curves of as a received FeCo alloy, 4 vol. % GNP-FeCo alloy composite without heat treatment and after quenching from 600, 710, 750, 800 and

900 ºC are shown in Figure 8.8. The variations in magnetic properties of the aforementioned materials with quenching temperature are seen in Figure 8.9.

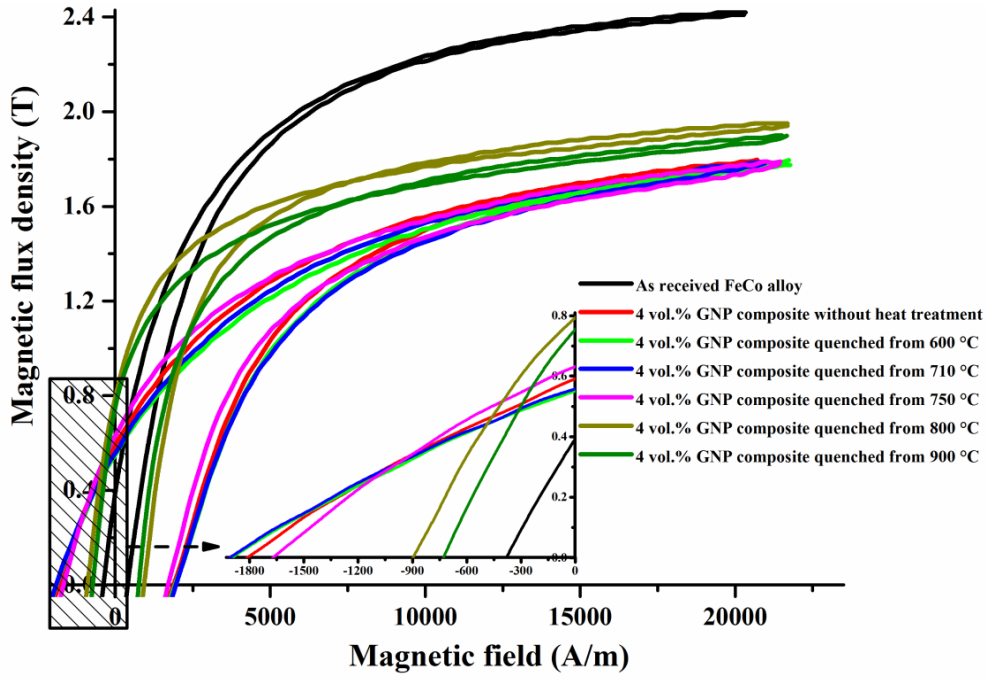

Figure 8.8. Upper halves of hysteresis curves of the indicated materials.

Adding high volume fraction of 4 % GNP to FeCo alloy caused a significant decrease in saturation induction combined with a considerable increase in coercivity. However, quenching from a temperature higher than 750 ºC led to an increase in saturation induction with a considerable decrease in coercivity. The ordered structure was significantly increased after quenching from ordered region temperatures of 600 ºC and 710 ºC (Figure 8.6), which has saturation induction higher than the disordered structure. However, a small increase in saturation induction was noticed after quenching from temperature higher than 750 ºC, this can be attributed to the change in morphology of precipitates or even dissolution of these precipitates at higher quenching temperature. The spheriodizing of carbides at high quenching temperature of 900 ºC provides less obstacle resistance to domain wall movement as compared to the laminar structure. The coercivity is a strongly related function to heat treatment process because of the variation in the microstructure. The ordered structure shows higher coercivity value than the disordered structure [46]. Therefore, quenching from a temperature higher than the critical temperature between ordered-disordered structures (T_c ~ 730 ºC) [1], led to a reduction in coercivity, due to less ordered structure, see Figure 8.6. Furthermore, the kinetic of grain growth at a temperature greater than critical temperature is very fast, so the coercivity was decreased at high quenching temperature, as it is inversely proportion to grain size [43, 49, 232]. The heat

treatment was performed without subsequent ageing treatment, therefore, the included thermal stresses during quenching can cause an increase in coercivity value, since the required magnetic force to change the direction along easy magnetisation axis is determined by the strains rather than the crystal anisotropy [27, 243]. It is also not possible to ignore the influence of; size, shape, distribution and nonmagnetic behaviour of the reinforcement on the coercivity and microstructure of the composite.

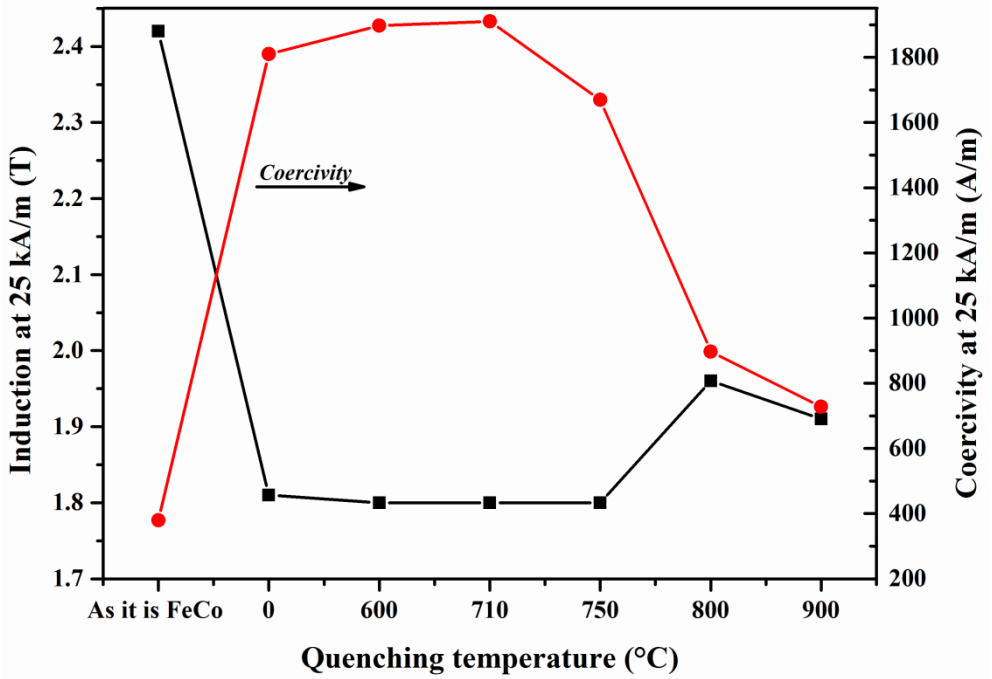

Figure 8.9. Change in saturation induction and coercivity of; as received FeCo alloy without heat treatment, 4 vol. % GNP composite without heat treatment which is indicated by (0 °C) and after quenching from 600, 710, 750, 800 and 900 °C respectively.

8.6. Mechanical properties after heat treatment

Tensile stress-strain curves of as a received FeCo alloy, 4 vol. % GNP-FeCo alloy composites without heat treatment and after quenching from 600, 710, 750, 800 and 900 ºC are shown in Figure 8.10. The interesting change in stress-strain curves to notice is the behaviour of lüders strain, which was observed in samples without heat treatment and those were quenched from temperature up to 710 ºC, while it was completely disappeared after quenching from a temperature higher than 750 ºC. This strain is normally produced when the motion of dislocations is inhibited, and it is almost observed in the ordered structure due to the difficulty in dislocations motion [42]. X-ray diffraction shows a significant increase in the volume fraction of the ordered structure at low quenching temperatures of 600 and 710 ºC (Figure 8.6), therefore, the value of lüders strain was high in samples quenched from these temperatures. In comparison to the commercial FeCo-2V alloys, which show a peak in lüder strain at ~ 720 ºC [30], this peak is at 600 ºC in 4 vol.%

GNP-FeCo alloy composite, due to more precipitate and the intensive plastic deformation in the structure of commercial alloys.

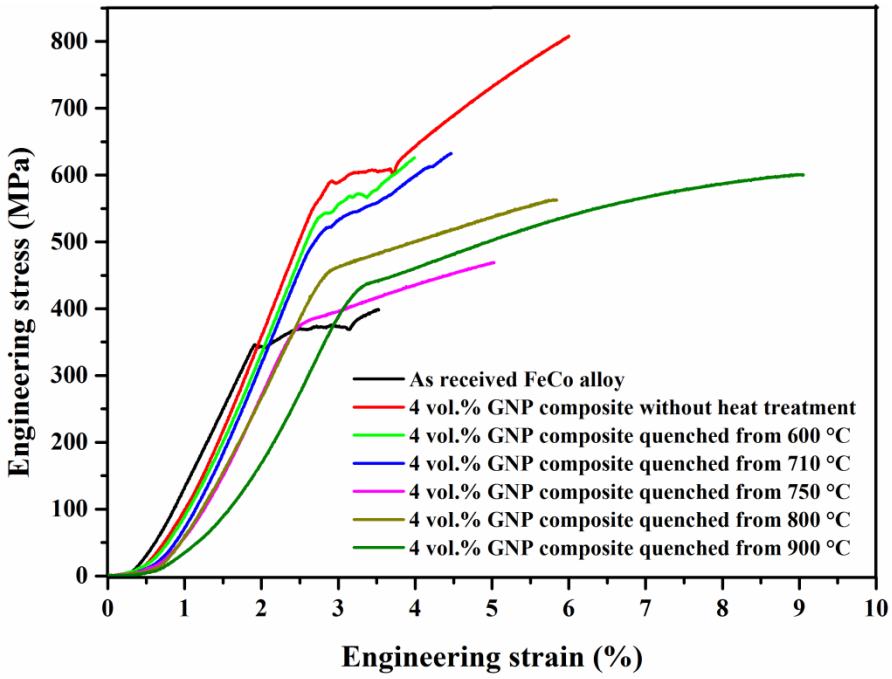

Figure 8.10. Tensile stress-strain curves of the indicated materials.

A summary of ultimate strength, yield strength, and elongation against quenching temperature for the aforementioned materials is shown in Figures 8.11 and 8.12. The ultimate tensile strength and yield strength were significantly increased in 4 vol. % GNP-FeCo alloy composites without heat treatment as compared to the base FeCo alloy, however, ultimate strength and yield strength were decreased after heat treatment. The increase in the ordered structure at quenching temperatures up to 750 ºC (Figure 8.6) leads to high ultimate strength in the composite material because the ultimate strength of the ordered structure is higher than disordered structure [244]. An increase in yield strength can be achieved by refining grain size or precipitate and by increasing dislocation density, while a loss in strength occurs after grain growth and recrystallization, change in texture and dissolute the precipitate. As the quenching temperature was increased, the grain size was increased (Figure 8.1), therefore the strengthening by grain boundaries was consequently diminished. A comparison has been made to notice the variation in microstructure after quenching from 710 ºC and 900 ºC in (Figures 8.2 and 8.3), showing a change in the amount and morphology of the precipitates. The strengthening influence of precipitate is reduced as the annealing temperature is increased, due to coarsening or even dissolving the precipitates [245]. Thus, the effect of precipitate on strength was reduced further with increasing quenching temperature to 900 ºC.

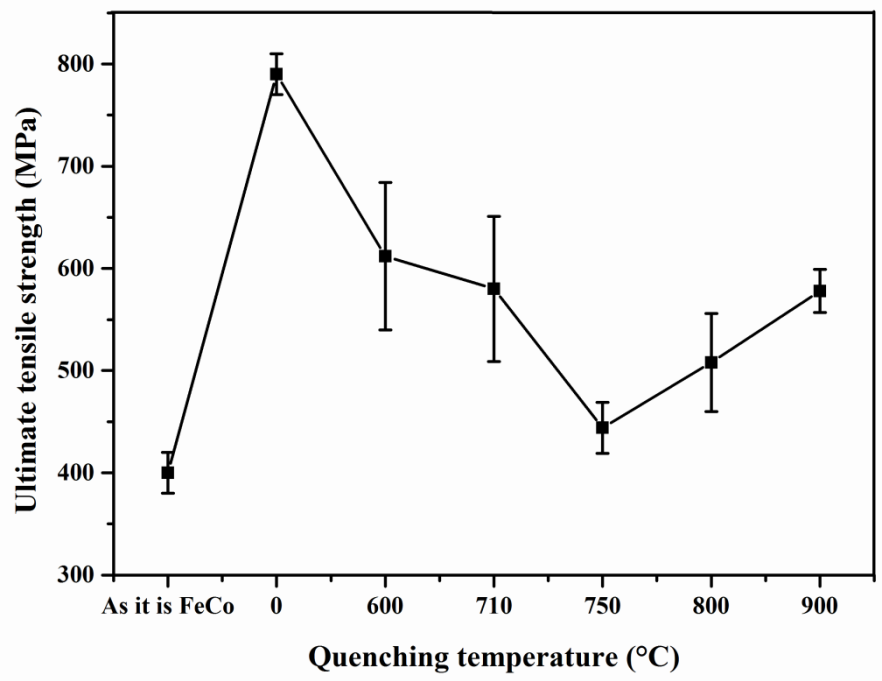

Figure 8.11. Variation of ultimate strength of 4 vol. % GNP composite without heat treatment (0 °C) and after quenching temperatures of; 600, 710, 750, 800 and 900 °C respectively.

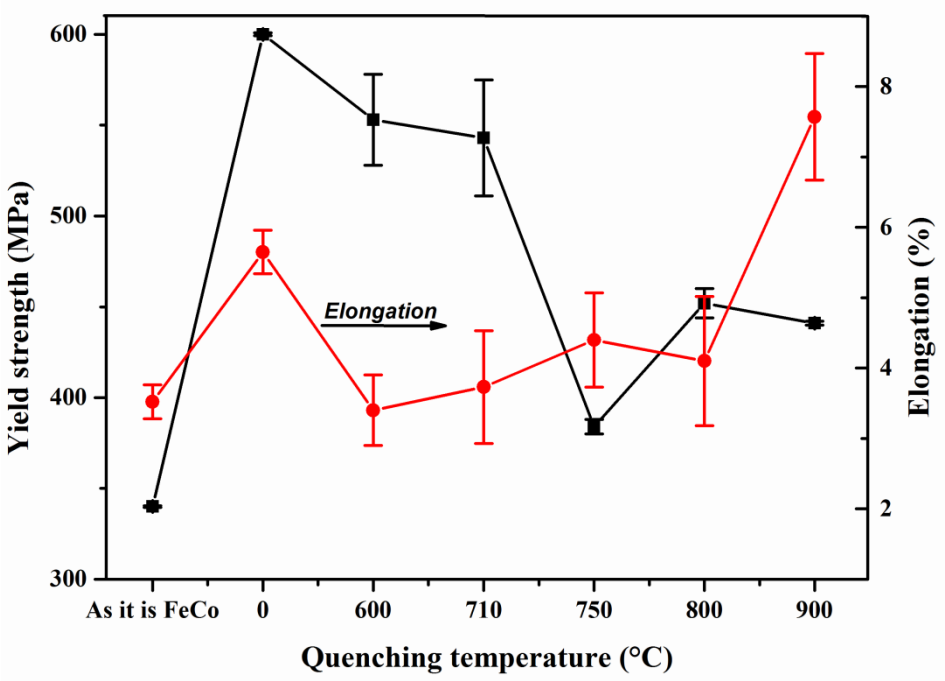

Figure 8.12. Variation of yield strength and elongation of 4 vol. % GNP composite without heat treatment (0 °C) and after quenching temperatures of; 600, 710, 750, 800 and 900 °C respectively.

The elongation was significantly increased at the highest quenching temperature of 900 °C in comparison to the lower quenching temperatures. The behaviour of ductility in the composite was compared with commercial alloy of low and high vanadium content [41, 226], showing more consistent with high vanadium content alloy, where the peak in elongation is obtained by annealing in disordered region rather than ordered region temperature of (T~710 °C) [29, 41]. Enhancement in ductility can be attributed to an

increase in disordered structure and to spheriodizing of carbides. The brittleness in FeCo alloy was also related to impurity content [228]. Adding GNPs to FeCo alloy not only improve densification, as carbonaceous nanoplatelets promote the rearrangement between the powder particles in the early stage due to their self-lubricant feature, but also help to remove the oxide layer on the particle of base alloy through interfacial reaction [246]. Moreover, the enhanced quality of GNPs at high quenching temperature (Table 8.1) and formation disordered structure led to better interface bonding, and better bridging for the cracks by GNPs, which are necessary to obtain high ductility. GNPs can maintain integrity during spark plasma sintering process even at a high sintering temperature of 1900 ºC, however, the GNPs used here were not high quality, showing an amorphous layer of carbon, which can easily diffuse and react with metals to produce carbides [38, 245]. Adding carbon to equiatomic FeCo alloy can improve the ductility of the alloy only after intensive cold rolling [38]. Therefore, the role of precipitates in strengthening and ductility is very low in comparison to the GNPs and disordered structure. As a cast FeCo2V shows zero elongation at room temperature and only by quenching from 850 ºC the alloy can acquire good ductility irrespective to grain size, due to the disordered structure [25, 247]. The recrystallisation and recovery processes, which have a significant influence on the ductility, are different according to annealing temperatures [248]. Again, the samples were only quenched without further heat treatment, therefore these parameters are ignored.

The variation of Vickers hardness values of as received FeCo alloy, 4 vol. % GNP-FeCo alloy composite without heat treatment and after quenching from 600, 710, 750, 800 and 900 ºC are seen in Figure 8.13. The peak value in hardness was obtained in 4 vol. % GNP-FeCo alloy composite without heat treatment, while the lowest value achieved after quenching from 900 ºC. This can be attributed to decrease the ordered structure in samples quenched from temperatures higher than 710 ºC, which is normally harder than the disordered structure. The spheroidization of lameraller structure may also have an effect on the hardness value.

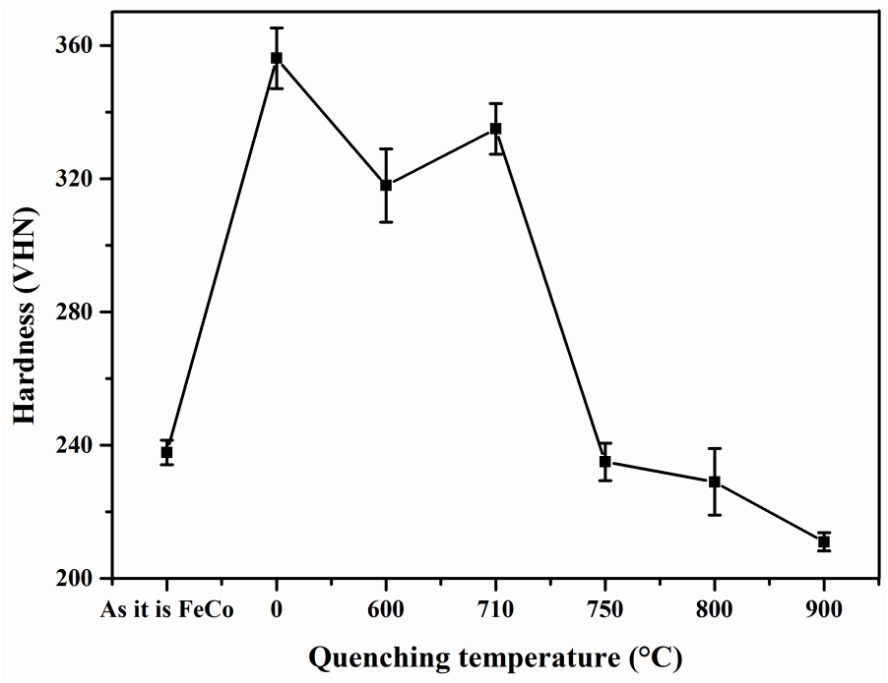

Figure 8.13. Variation in hardness of 4 vol. % GNP composite without heat treatment (0 ºC) and after quenching from temperatures of; 600, 710, 750, 800 and 900 ºC respectively.

8.7. Fracture surface analysis

The fracture surface of as received FeCo alloy before and after ball milling without heat treatment, 4 vol.% GNP-FeCo alloy composite without heat treatment and after quenching from 600, 710 and 900 ºC are shown in Figure 8.14. Significant variations were observed after processing FeCo alloy, the transgranular fracture mode of as received FeCo alloy was refined after ball milling due to a reduction in grain size after ball milling. Adding GNPs to FeCo alloy caused more refinement in grain size, and showing more cleavage areas which were combined with dimples close to grain boundaries in composite without heat treatment. When 4 vol. % GNP composite was quenched from 900 ºC the surface of fracture exhibited a ductile fracture with very fine dimples. EDS analysis and SEM observations (Figures 8.3 and 8.14) reveal that spherical carbides, which is increased with temperature due to the increase in carbon diffusivity [249], and GNPs were included in the pits, which cause the fine dimples in fracture surface. Long cracks were observed on the fracture surfaces of all quenched samples, which might be formed by including hydrogen during heat treatment. GNPs were observed to work as bridging of the formed cracks and as a barrier to stop the propagation of cracks as indicated by arrows in Figure 8.14.

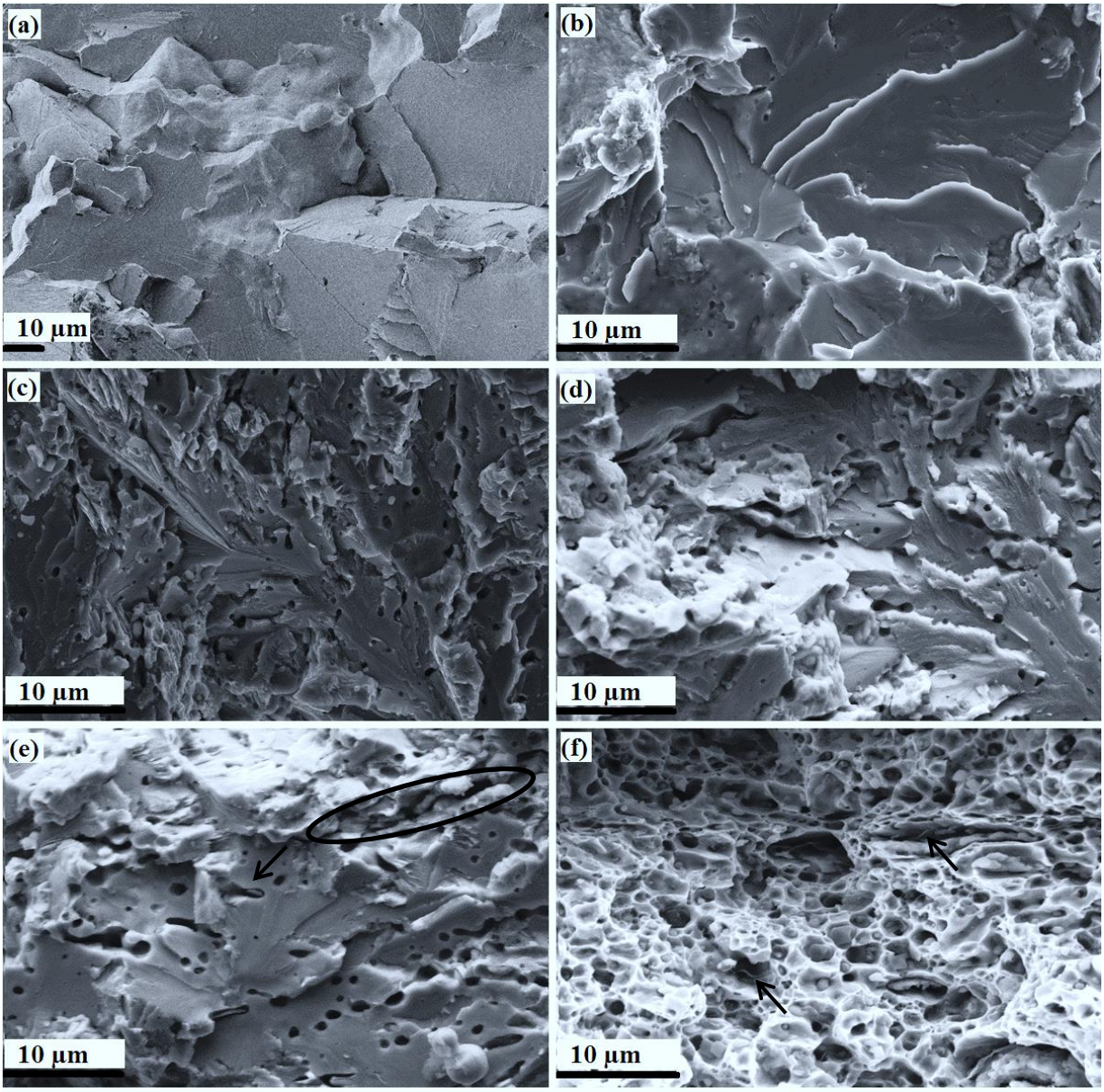

Figure 8.14. SEM fracture surface of (a and b) FeCo alloy before and after ball milling without heat treatment, (c, d, e and f) are 4 vol.% GNP composite without heat treatment, quenched from 600, 710 and 900 ºC respectively, arrow indicate to GNPs, ellipse to cracks.

Summary

Heat treatment caused significant changes in microstructure. Despite the Raman spectrum revealed that the structure of GNPs was intact during the process, the carbon precipitate was formed due to the reaction the amorphous carbon layer on the GNPs with FeCo alloy. The elongation in 4 vol. % GNP composite can be increased by disordering the structure by quenching from 900 °C, which changed the laminar shape of precipitates to spherical. Therefore, the fracture surface showed very fine dimpled structure including GNPs. The spherical morphology for precipitate led to a significant decrease in coercivity value.

Chapter 9: Results and discussion of high energy ball-milling of 1.5 vol. % CNT composite

9.1. Introduction

High energy ball milling is one of the adopted methods to improve the dispersion and interface bonding in composite materials. In the current work, a limited volume fraction of 1.5 % CNTs was used to reinforce FeCo alloy in order to achieve better combination between the mechanical and magnetic properties. To avoid undesired excessive ball milling time to keep high quality for reinforcement with uniform dispersion and good interface bonding, the ball milling time was optimised.

9.2. Characterisation of raw material and consolidated materials

9.2.1. Raw material

The morphologies of the raw FeCo and CNT materials are shown in Figure 9.1. A spherical morphology with a wide particle size distribution is observed in the as received FeCo alloy. The entangled CNT clusters exhibit a variation in the tube diameters and in the number of layers. Damage has been observed on the surface of some these tubes, as shown by the arrows.

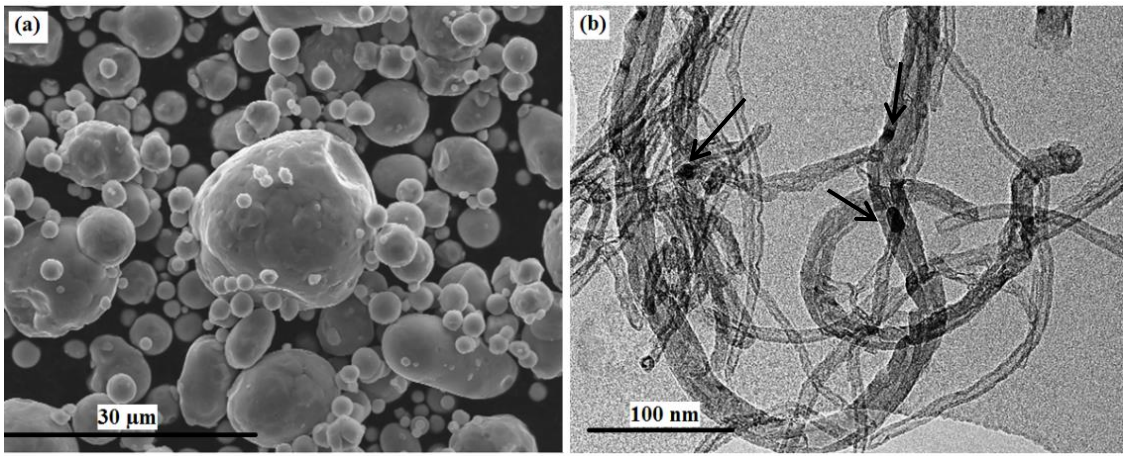

Figure 9.1. Morphology of as-received (a) SEM of FeCo alloy powder and (b) TEM of CNTs.

9.2.2. Effect ball milling time on the morphology of FeCo alloy and CNTs dispersion

The SEM morphology of the ball milled FeCo alloy and composite powders are presented in Figure 9.2. The morphology of FeCo powder was altered during the ball milling process. The spherical shape of the as received FeCo powder was deformed into plate-like particles after 0.5 h milling while the variation in particle size was broad, with little particle welding occurring during this time. Increasing the ball-milling time to 1 h led to broader particles size due to increased degree of plastic deformation and more welding between powder particles. The welding processes increased as the time increased and became significant after 4 and 6 h of ball-milling. In the composite powder, ball-milling up to 0.5 h was not effective in dispersing the CNTs; bundles of carbon nanotubes were observed between and on the surface of particles. Extending the time to 1 h increased the size of the FeCo particles with improved CNT dispersion on the particle surface and some evidence for the embedding CNTs into the particles. FeCo particles welding began after 2 h ball-milling, in which small particles were welded onto larger ones. As a result, almost all the carbon nanotubes were embedded into the FeCo alloy particles at this milling time. After 6 h the surface of the particles became very smooth and no free carbon nanotubes can be seen. Adding CNTs to the monolithic FeCo alloy powder altered the powder behaviour during the ball-milling process; leading to a reduction in particle size, as seen in Figure 9.2. This can be attributed to the increase in the fracture rates due to the embedded CNTs, which increase the hardness of the particles. The fractured particles were observed after 4 h ball-milling time in the composite material, while the welding process was observed in the monolithic FeCo alloy at this time. The CNT clusters acted as a lubrication barrier against welding between the powder particles during the initial stage of dispersion, after shortening of the CNTs by ball milling [250]. This barrier was gradually removed, leading to embedded CNTs inside the particles during cold welding increasing the strain hardening rate in the deformed particles [162].

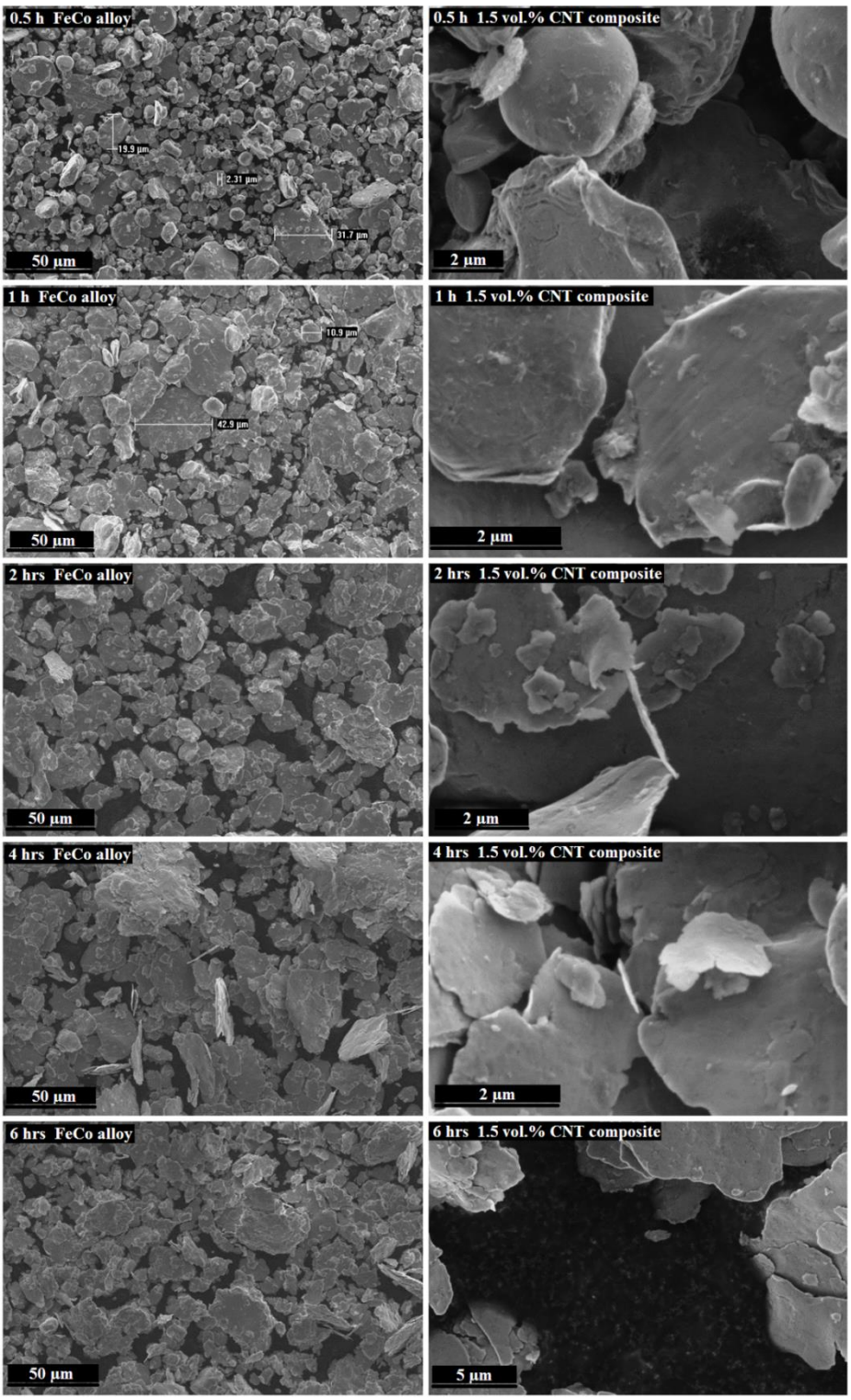

Figure 9.2. Surface morphology of the monolithic FeCo alloy and composite powders ball milled for the indicated ball-milling time.

9.2.3. Densification and density of consolidated materials

SPS shrinkage curves of the as received FeCo alloy, ball-milled monolithic FeCo alloy and 1.5 vol.% CNTs composite are presented in Figure 9.3.

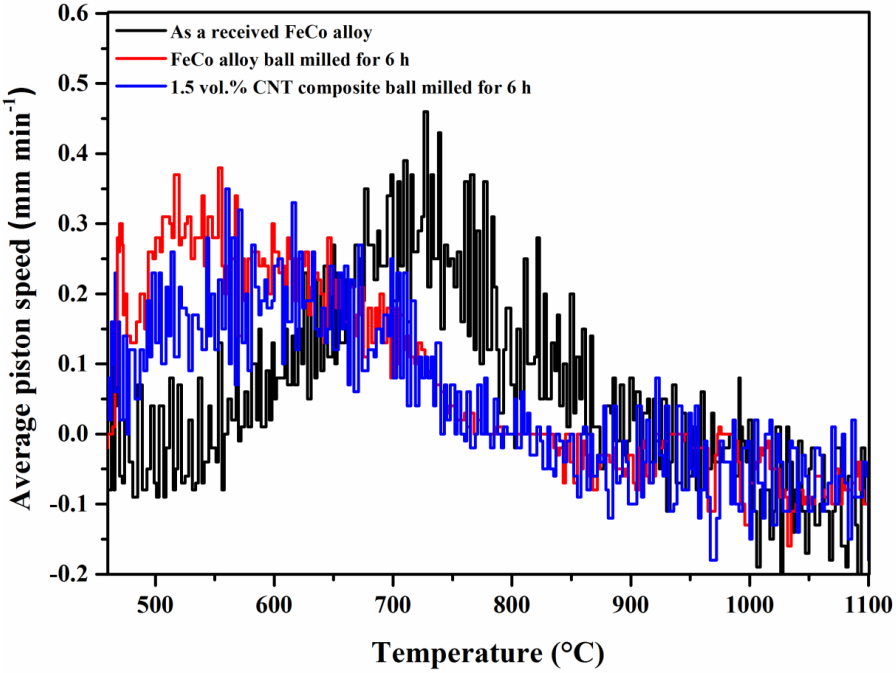

Figure 9.3. Change in average piston speed against temperature for the indicated materials.

A different in sintering behaviour is observed in curves between the three materials. This can be attributed to the difference in powder composition and morphology; due to the different levels of plastic deformation experienced during the ball-milling process. There is a shift in the sintering curve to lower temperatures for the ball-milled FeCo and composite powders, as compared to the as received FeCo alloy. This can be attributed to the effect of ball-milling, which introduced a higher dislocation density to the material and therefore a higher strain energy compared to the as received FeCo alloy; lowering the activation energy for sintering. Densification occurred over a broader temperature range for the ball milled monolithic FeCo alloy and 1.5 vol.% CNT composite compared to as-received FeCo alloy as confirmed from broadening in shrinkage curves. Increasing ball milling time to 6 h increased the degree of agglomerations in the monolithic FeCo alloy and 1.5 vol.% CNT composite powders (Figure 9.2). These agglomerations made sintering of ball-milled powder rather difficult than as-received powder [212]. Extended milling time to 6 h leads to decrease in density of both consolidated monolithic FeCo alloy and 1.5 vol.% CNT composite as shown in Figure 9.4. However, the relative density of composite material was higher than monolithic FeCo alloy. This can be rationalised to the role of CNT in decreasing agglomeration in powder after milling, as seen in Figure 9.2. The highest value

of the relative density of 100 % was achieved after milling time of 1 h in 1.5 vol.% CNT composite, suggesting that the morphology of powder at this time is more suitable for consolidating under the sintering pressure of 50 MPa.

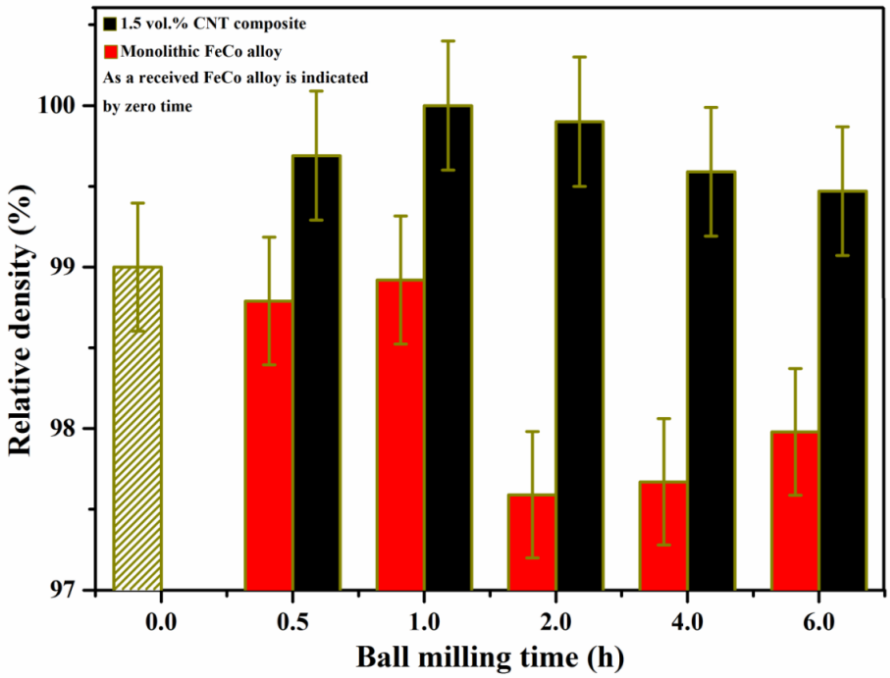

Figure 9.4. Variation of relative density of SPS sintered 1.5 vol. % CNT composite with ball milling time.

9.2.4. Microstructure of consolidated materials

SEM microstructure images of the consolidated materials are shown in Figures 9.5 and 9.6. It can be seen that CNT agglomeration was reduced with increasing ball-milling time. A uniform dispersion of CNTs is observed after 6 h ball-milling time in which the CNTs were embedded into the grains. The elongated structure in monolithic FeCo alloy was refined with increasing ball-milling time as shown in samples ball-milled for 6 h compared to 0.5 h of monolithic FeCo alloy, as shown in Figure 9.5. Unfortunately, the consolidated materials exhibit porosity, which can be attributed to the agglomeration occurring in the composite and monolithic FeCo alloy powders during ball milling. Employing a 50 MPa sintering pressure was not sufficient to breakdown this agglomeration during sintering. However, the agglomeration was reduced in composites and hence density was improved. Adding CNTs to the FeCo alloy reduces the grain size due to the increased strain hardening, and subsequently, fracturing rates occurring as the CNTs become embedded within the particles of the base powder. Furthermore, grain growth was inhibited by the presence of CNTs during the sintering process. Both factors cause a refinement in the microstructure of composite materials.

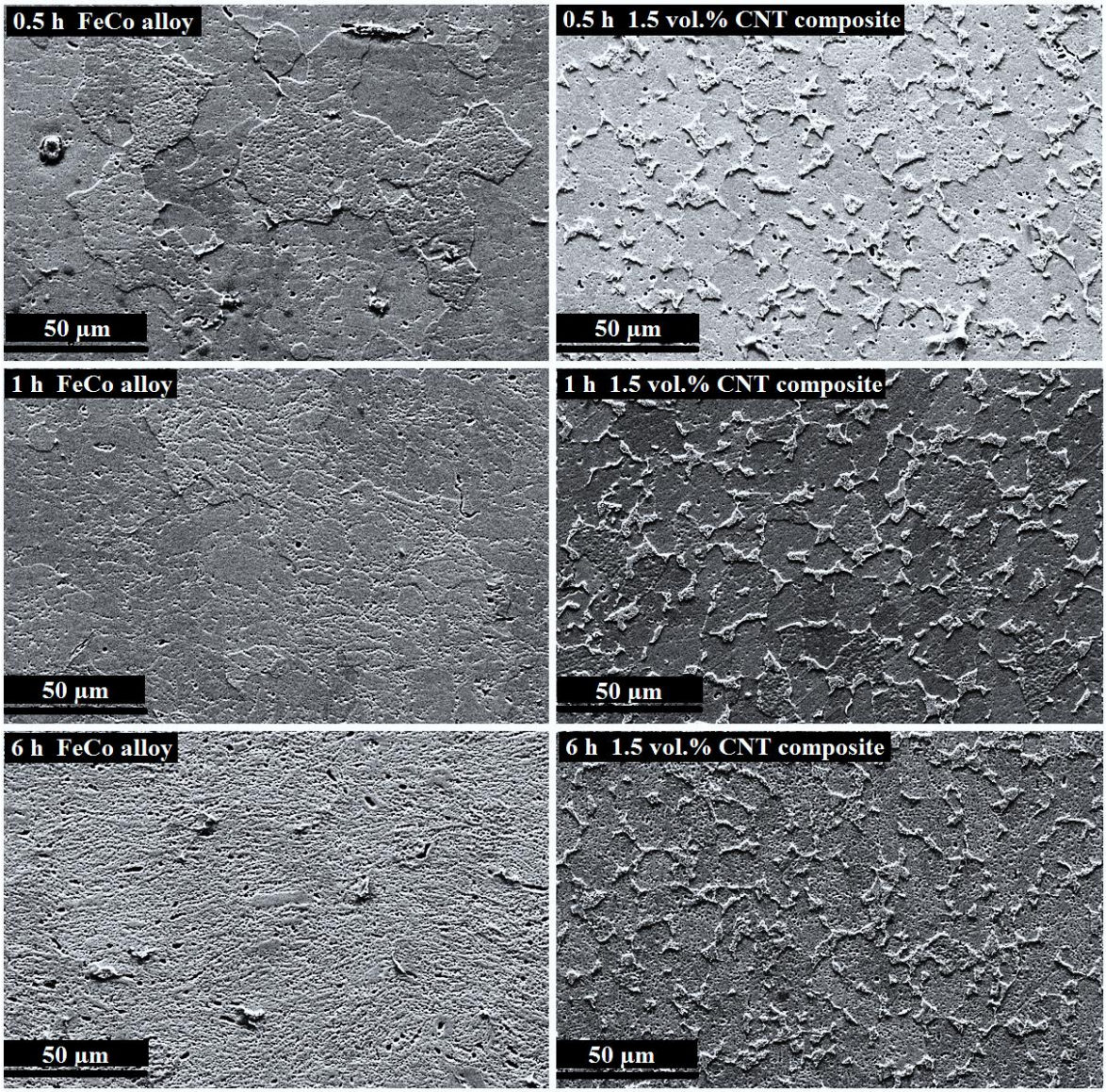

Figure 9.5. SEM microstructure of monolithic FeCo alloy and 1.5 vol. % CNT composite of indicated ball-milling time.

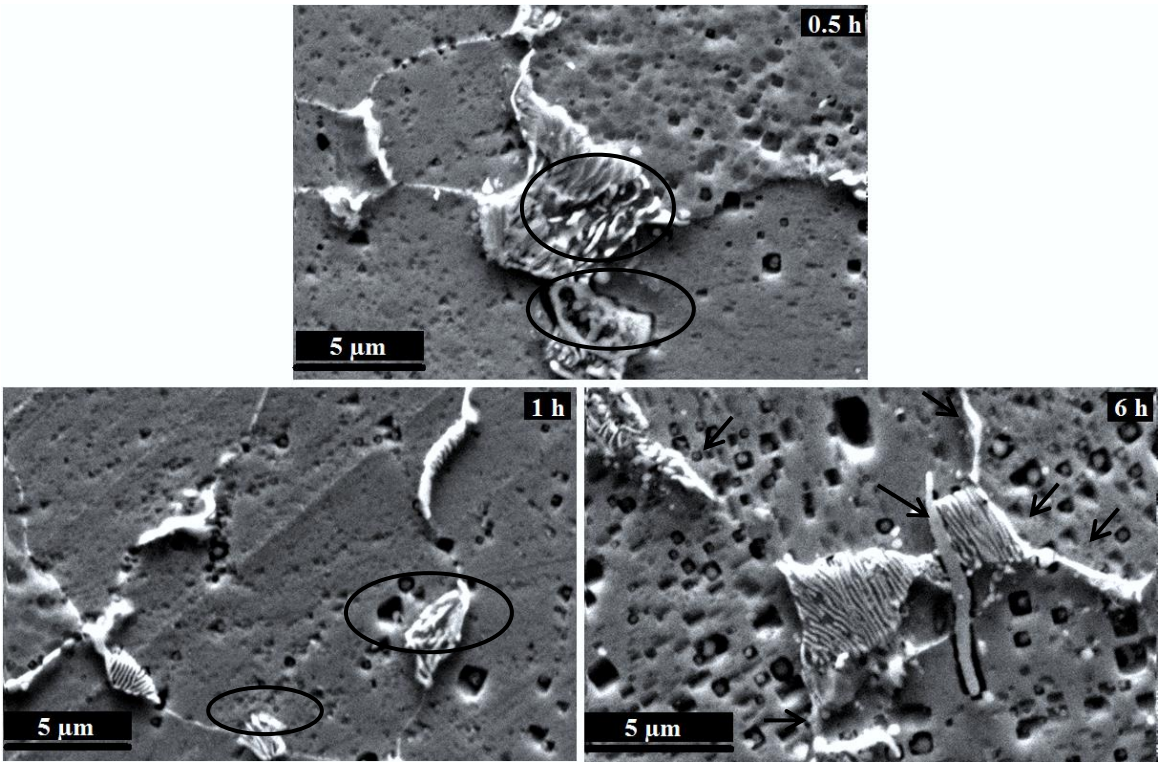

Figure 9.6. High-magnification SEM microstructure of 1.5 vol. % CNT composite of signified ball-milling time, the arrows indicate to single CNT, and the ellipses to agglomerated CNT.

9.2.5. X-ray diffraction (XRD) analysis

XRD analysis of the as received FeCo alloy, ball-milled monolithic FeCo alloy and 1.5 vol. % CNT composites processed at different ball-milling times of 1, 4, and 6 h are presented in Figure 9.7. The as-received powder contained oxidises due to exposure to air; as confirmed from the silicon oxide peaks which were present prior to milling. Carbon was already present in the as received FeCo alloy as a result of the fabrication processes used. In order to check the interaction between the FeCo alloy and the CNTs during ball milling, the XRD profile was enlarged as shown in the inset in Figure 9.7. The intensity of the carbon peak was increased in the 1.5 vol. % CNT composite, as would be expected. Very low-intensity peaks of iron carbide were observed, which were also formed in the monolithic FeCo alloy. However, the slight increase in the intensity of the carbide peaks in the composite materials can be attributed to the reaction with the amorphous carbon in the CNTs. The TEM work shows that amorphous carbon is present on the surface of the as-received CNTs (Figure 9.1), hence may not be an artefact of the milling process. It has been reported by [100] that the CNTs are stable and do not react with the metal matrix alloy as long as their quality is high and the level of defect tubes is low.

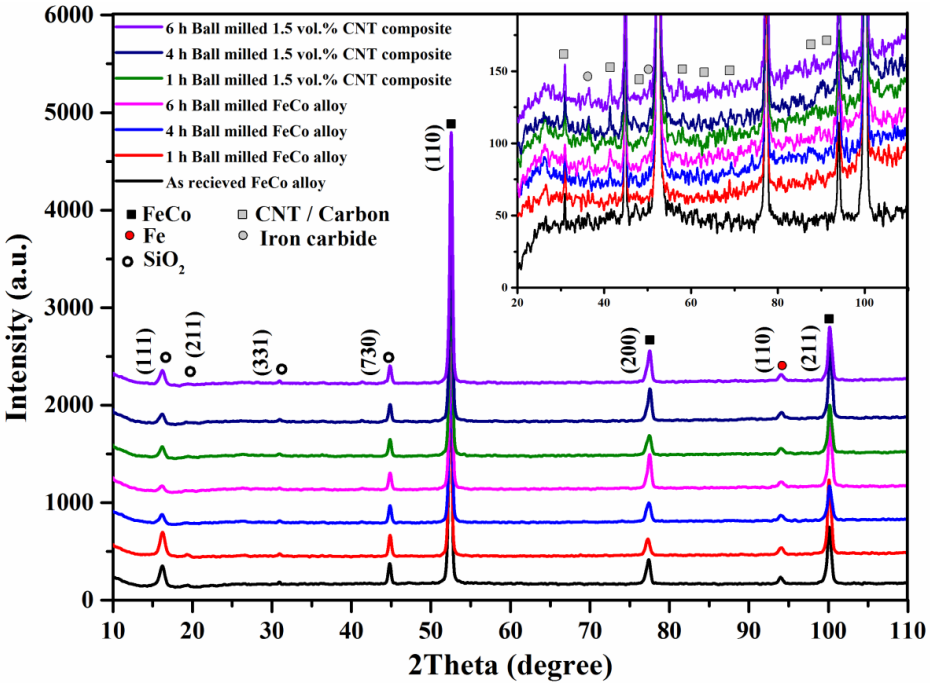

Figure 9.7. X-ray diffraction patterns of consolidated materials for indicated milling time.

The crystallite size and lattice strain due to dislocation concentration can be evaluated from the peak broadening in the XRD profile [251]. The effect of strain on the *d*-spacing may be classified as uniform and nonuniform. Peak position is very sensitive to uniform strain while peak broadening and intensity are affected by nonuniform strain [252]. The shift in the diffraction lines of the XRD corresponds to strains induced in the materials. A nanocrystalline structure was formed during ball milling, as confirmed by TEM observation Figure 9.8.

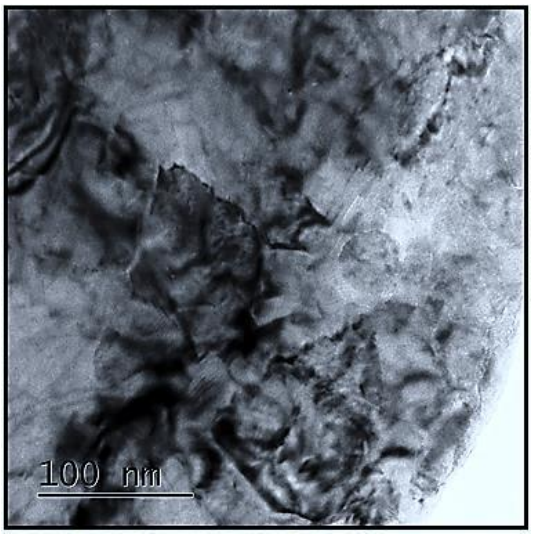

Figure 9.8. TEM image shows formation of a nanocrystalline structure in the powder of the monolithic FeCo alloy after ball-milling for 6 h.

As well as TEM imagining, the crystallite size can be estimated using the Scherrer method, which relies on X-ray profile analysis. XRD diffraction patterns of a slow scan analysis in the range of the expected superlattice lines for the consolidated materials are shown in Figure 9.9. The anti-phase domain size was measured using this method for the superlattice line (100). The APDS was decreased with extended ball-milling time in the monolithic FeCo alloy, becoming 22.48 nm after 6 h ball-milling. In the 1.5 vol. % CNT composite, a maximum APDS of 34.27 nm was observed after 6 h ball-milling time. This might be due to the lubricating role played by the CNTs during ball milling, which reduces the intensity of the impact of ball-milling on the crystallite structure. The highest intensity value of the superlattice line (100) was observed after an extended milling time of 6 h for both the monolithic FeCo alloy and the 1.5 vol. % CNT composite. Introducing CNTs to the FeCo alloy increases the volume fraction of the ordered structure in the composite compared to the monolithic FeCo alloy [167]. Up-shifting was observed for both the monolithic FeCo alloy and the 1.5 vol. % CNT composites, as confirmed from the increasing diffraction angle with ball-milling time. A slight increase in peak shifting is seen in the composites as compared to the monolithic alloy; corresponding to the increased value of strain hardening in composites from embedded CNTs into the FeCo particles.

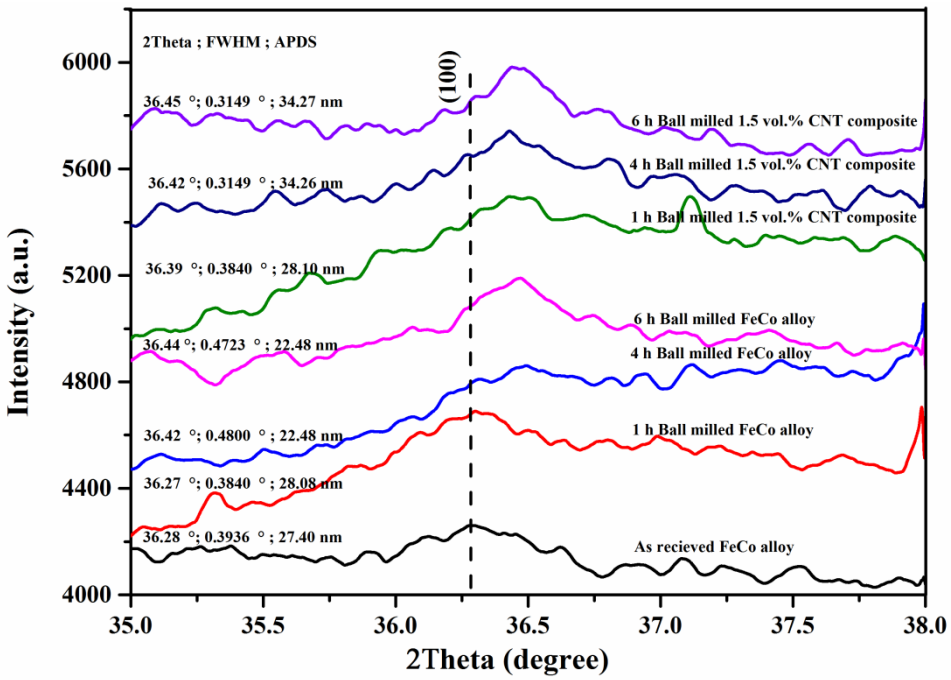

Figure 9.9. Slow scan XRD patterns, illustrating (100) superlattice reflections for the indicated materials, the diffraction angle (2Theta), the full width half maximum (FWHM) and the anti-phase domain size (APDS) are also displayed.

9.2.6 Structural integrity of CNTs

Raman spectroscopy is a popular tool for the characterization of the structure and properties of carbon nanostructures [253]. The CNTs as raw and after embedding in the 1.5 vol. % CNT composites were evaluated using Raman spectroscopy, as shown in Figure 9.10.

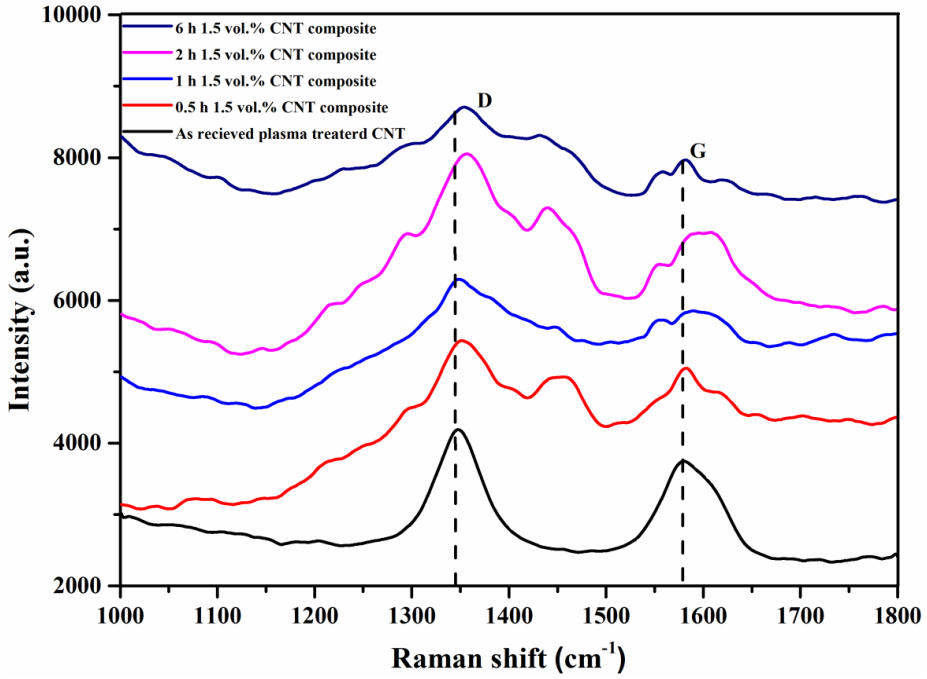

Figure 9.10. Raman spectra of as received CNT and 1.5 vol. % CNT composite at different ball-milling time.

One characteristic feature of single-walled carbon nanotube (SWNT) observed by Raman spectroscopy is the splitting of the G band. The raw CNTs employed were a multiwall carbon tube (MWCNT). The absence of any splitting in the G band in MWCNTs compared to the large splitting in the G band to G^{+}-G^{-} for small diameter SWNT tubes is due to the large diameter of the outer tubes and variation in diameter distribution within the individual MWNTs; which are considered to be an assembly of diameters ranging from small to very large [254]. The reason behind the splitting in G band is the difference in the sources of vibration observed during the Raman spectroscopy test. G^{+} is associated with vibration frequencies occurring along the tube axis while the frequencies that result from vibration along the circumference of tube lead to G^{-} [255]. However, it is possible to observe a clear splitting in the G band in multiwall CNTs of a small innermost diameter and prepared by hydrogen arc discharge [256]. This was attributed to the effect of environment, which becomes relatively small for innermost nanotube compared interactions between SWNTs which occurred in different environments [254]. The splitting decreased as the outer diameter of the carbon nanotubes increased. The wall layers in the

CNTs were decreased after ball milling, as shown from splitting in the G band of the Raman spectra. Slippage between shells and thinning of the CNTs occur during ball milling, leading to a reduced diameter in the CNTs at extended milling time; leading, eventually to the observation of splitting in G-band.

The nature of the interface bonding between the carbon nanotubes and the matrix material can influence on the lattice vibrations of the CNTs, causing a shift in the Raman spectra. A detailed study on the correlation between transferred tensile stresses and G peak position has been reported by [257]. Downshift was observed in the split G bands and this shifting was higher in the sample ball-milled for the full 6 h. This could be due to the fact that the interfacial bonding between the CNTs and the matrix alloy has improved, allowing more stresses to be transferred from the FeCo matrix to the CNTs, or due to the increased heat and stresses encountered during the longer ball-milling times. It is not possible here to ignore the effect of stresses from ball-milling in the observed shifting.

The intensity ratio R (I_D / I_G) is usually used to characterise the damage in the CNTs. The calculated ratios of the consolidated materials are presented in Table 9.1. The intensity ratio (R) decreased in the consolidated materials for all ball-milling times in comparison to the as-received CNTs. There are two possible reasons for this improvement in CNTs quality after fabrication. The first is attributed to releasing the functional oxide group during the sintering processes, and the second is the purification of CNTs due to slippage of the outer shells during the ball-milling process. It can be seen that the R ratio increases with increasing ball-milling time reflecting the increased damage done to the CNTs during ball milling. However, the highest value of the R ratio for the ball milled samples is still significantly lower than the as-received CNTs (Table 9.1). Therefore, while some damage has been induced by ball milling, this is minimal and far outweighed by the positive effects of the corresponding improvement in CNT dispersion.

Table 9.1. Raman spectra characteristics of the as received and 1.5 vol. % CNT composites at various ball milling time.

Milling time (h)	**0**	**0.5**	**1**	**2**	**6**
R= (I_D/I_G) ratio	**1.11**	**1.03**	**1.04**	**1.09**	**1.09**

9.2.7. Magnetic properties

The upper hysteresis curves of the consolidated FeCo alloy and 1.5 vol. % composites which are ball milled at different time are presented in Figure 9.11. A summary of the magnetic properties measured for the consolidated materials is shown in Figure 9.12.

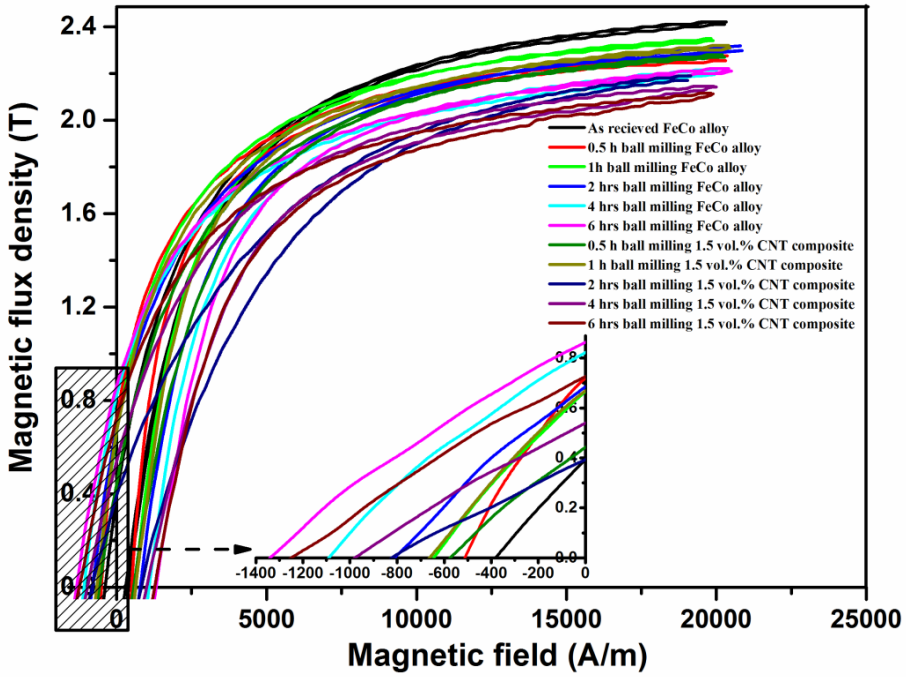

Figure 9.11. Upper halves of hysteresis curves of the indicated materials.

The saturation induction decreased after ball milling the monolithic FeCo alloy and 1.5 vol. % CNT composite materials in comparison to the as-received FeCo alloy; showing peak saturation values of 2.35 T and 2.33 T after a milling time of 1 h for the monolithic FeCo alloy and 1.5 vol. % CNT composite materials respectively. The lowest values of coercivity were observed after 0.5 h of ball milling, giving values of 511 A/m and 573.5 A/m for the monolithic FeCo alloy and 1.5 vol. % CNT composite respectively. The coercivity values increased as the ball-milling time increased; giving the highest values, at the longest ball milling times, of 1335 A/m and 1248 A/m for the monolithic FeCo alloy and 1.5 vol.% CNT composite, respectively. The composite materials exhibited lower coercivity values in comparison to the monolithic FeCo alloy at ball-milling times of 4 and 6 h as shown in Figure 9.12.

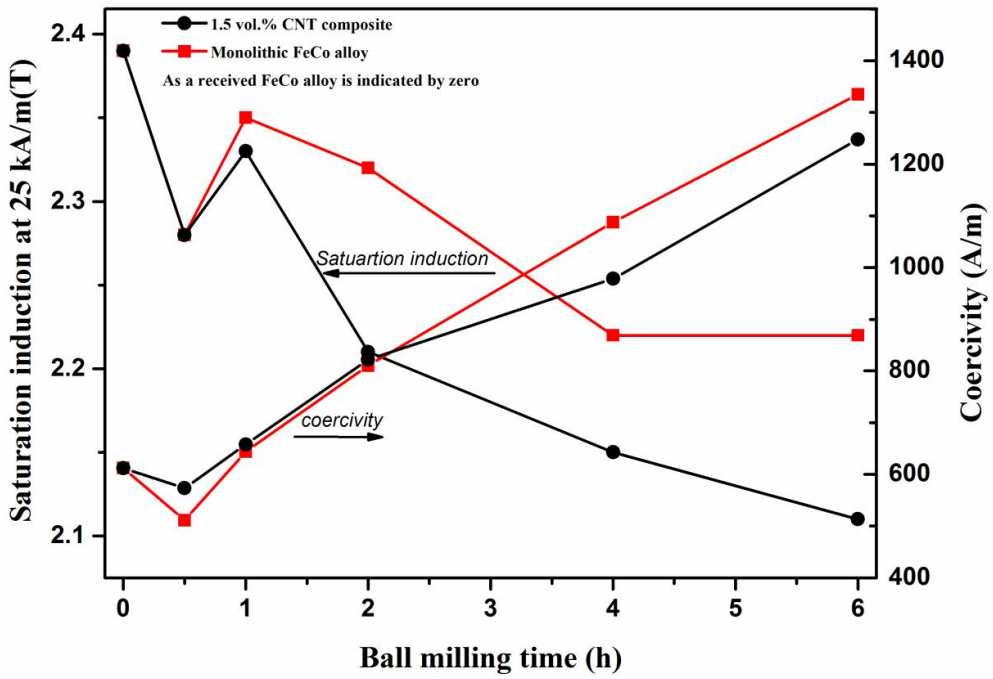

Figure 9.12. Summary of the magnetic properties of monolithic FeCo alloy and 1.5 vol. % CNT composite at different ball milling time.

The magnetic properties are affected by changes in microstructure, strains and presence of impurities. The permeability and coercivity of magnetic materials are particularly sensitive to these parameters. Almost all plastic deformation of magnetic materials reduces the permeability of materials [27]. In spite of the increases in volume fraction of the ordered state and in the density of the 1.5 vol. % CNT composite materials (Figures 9.4 and 9.9) ball milled for longer times, the saturation induction was decreased in composite materials. Since density is clearly not the main source of this decrease in saturation induction, other factors must be considered. XRD results in (Figures 9.7 and 9.9) showed more broadening and shifting in the composite materials in comparison to the monolithic FeCo alloy. This can be attributed to the increased strain hardening occurring in the composite materials owing to the embedding CNTs in FeCo particles. Having another source of strain in the composite decreases the permeability of the 1.5 vol. % CNT composite materials in comparison to the monolithic FeCo alloy; making full saturation at an applied field of 25 kA/m very difficult. Another reason for the decreasing saturation induction in the 1.5 vol. % CNT composite is the reaction of the CNTs with the base alloy in both cases of intact and damaged CNTs. TEM images of the plasma treated CNTs show imperfections and some dark areas which are probably metal inclusions, occurring from the reaction with the metallic catalyst used during their fabrication [211]. These sites become preferred areas for chemical reaction with FeCo alloy, leading to a dilution of the saturation induction. X-ray diffraction (Figure 9.7) shows that the CNTs were damaged with increasing ball milling time. The resulting disordered carbon reacts with the alloy,

forming carbides, and leading to deterioration in the magnetic properties. The relative density was decreased in the materials after extending the ball-milling time, resulting in a decrease in saturation induction for both the monolithic FeCo alloy and the composite materials.

The increased coercivity values observed with further ball-milling time can be attributed to increased strain, which was not completely annealed during sintering due to the zero dwell time employed during sintering. XRD results did not show any evidence of contamination from the milling balls or jar during the milling processes. However, it is possible that the volume fraction of impurities might be beyond the sensitivity of the XRD technique. XRD does show that carbide was formed from the reaction of iron with the amorphous carbon of the CNTs. The coercivity value of the composite was not affected significantly by this carbide as confirmed from the lower value in the coercivity of composite materials compared to monolithic FeCo alloy (Figure 9.12), due to the very low volume fraction of this carbide. The microstructure observations (Figure 9.5) showed that the structure was refined as ball milling time increased. It is well known that the coercivity is inversely proportional to the grain size, indicating that the fine microstructure is behind the high increase in coercivity for both the monolithic FeCo alloy and the 1.5 vol. % CNT composite. An increased porosity level generated due to agglomeration of the monolithic FeCo alloy and composite powder at an extended ball-milling time can also have a contribution to the increase in coercivity value at a further ball milling time.

9.2.8. Mechanical properties

The stress-strain curves for the sintered as received FeCo alloy, ball milled FeCo alloy and 1.5 vol.% CNT composite at different ball milling time, are shown in Figure 9.13. The variations in ultimate tensile strength and yield strength as a function of ball-milling time for the monolithic FeCo alloy and the 1.5 vol. % CNT composites are summarised in Figure 9.14. Since the CNTs altered the milling behaviour of the FeCo alloy powder, the tensile strength, yield strength, elongation, and hardness of the consolidated FeCo alloy composites were affected accordingly. The highest improvement in ultimate strength due to the addition of CNTs was achieved after 1 h ball-milling time; increasing by almost 50 %. The highest value of ultimate tensile strength of 611.33 MPa was obtained in the 1.5 vol. % CNT composite after 6 h of milling combined with the highest yield tensile strength of 536.33 MPa.

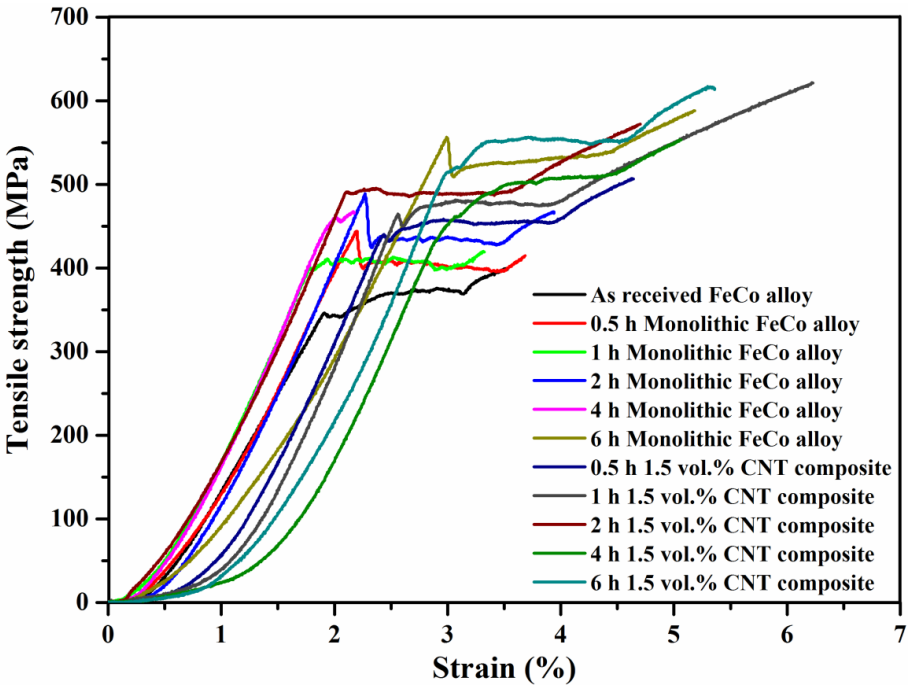

Figure 9.13. Tensile stress-strain curves of monolithic FeCo alloy and 1.5 vol. % CNT composite for different ball-milling time.

The monolithic FeCo alloy exhibited increased in ultimate tensile strength and yield strength with increasing ball-milling time. The improved ultimate tensile strength and yield strength in the monolithic FeCo alloy after ball-milling will be due to the observed refinement in grain size (Figure 9.5), and to the increased strain hardening effects as a result of the stresses introduced during ball-milling, which increase with extended ball-milling time. In the CNT composites, the reinforcement improves the mechanical properties through several different physical mechanisms, including; thermal mismatch, Orowan looping and shear lag. Detailed explanations of these mechanisms are reported in [258]. These mechanisms are generally related to dislocation density, inhibiting dislocation movement and transferring the load from the matrix to the reinforcement via the interface. Therefore, the quality of the reinforcement, its dispersion, and the interface bonding are the key parameters for achieving the highest improvement in properties. The trend of ultimate strength with ball-milling time shows a maximum improvement after only 1 h ball-milling time. The quality of the CNTs is directly related to the ball-milling time (Table 9.1), therefore, the reduced ball-milling time led to less damage in the CNTs.

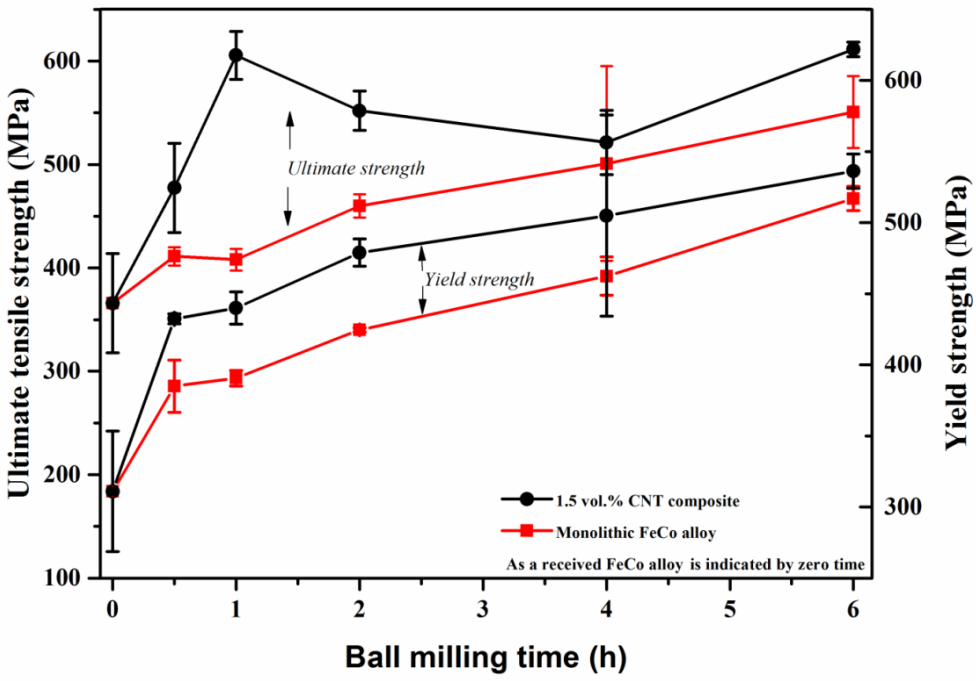

Figure 9.14. Ultimate tensile strength and yield strength of monolithic FeCo alloy and 1.5 vol. % CNT composite with different ball-milling time.

A greatly reduced degree of carbide formation in comparison to the longer ball milling times may also be playing a part; since the lower concentration of carbide and functionalization groups would provide better sites for improved interface bonding. Under controlled conditions, the formation of carbides can have a beneficial effect on the interface bonding and on the overall properties [259]. Regarding the effect of density on properties; the density was shown to be reduced with further ball-milling time (Figure 9.4), which has been attributed to alterations in the densification processes occurring due to the changes in morphology and consistency of the powder ball milled for extended periods of time. As the ball-milling time was reduced to 1 h, 100 % relative density was achieved (Figure 9.4). Grain size refinement was higher in the composites as compared to the monolithic FeCo alloy; due to the role of CNTs in inhibiting grain growth (Figure 9.5). Microstructural refinement is one of the most important strategies for the improvement of the properties of FeCo alloys. The phase transformation occurring between the ordered and disordered structures has a significant effect on the mechanical and physical properties. Irrespective of grain size, the yield strength and elongation are increased in the disordered Fe50Co as compared to the ordered structure [21]. Further ball-milling time increased the volume fraction of the ordered phase, which was increased further as the CNTs become embedded into the FeCo alloy; as shown in Figure 9.9. Therefore, improvements in mechanical properties brought about due to the embedding of CNTs in monolithic FeCo alloy at extended ball milling times have been offset by the increase in volume fraction of the ordered phase

The hardness value of the consolidated as-received FeCo alloy was much lower than that of the ball-milled monolithic FeCo alloy and 1.5 vol. % CNT composites, an increase in hardness values was observed with increasing ball-milling time in the monolithic FeCo alloy Figure 9.15.

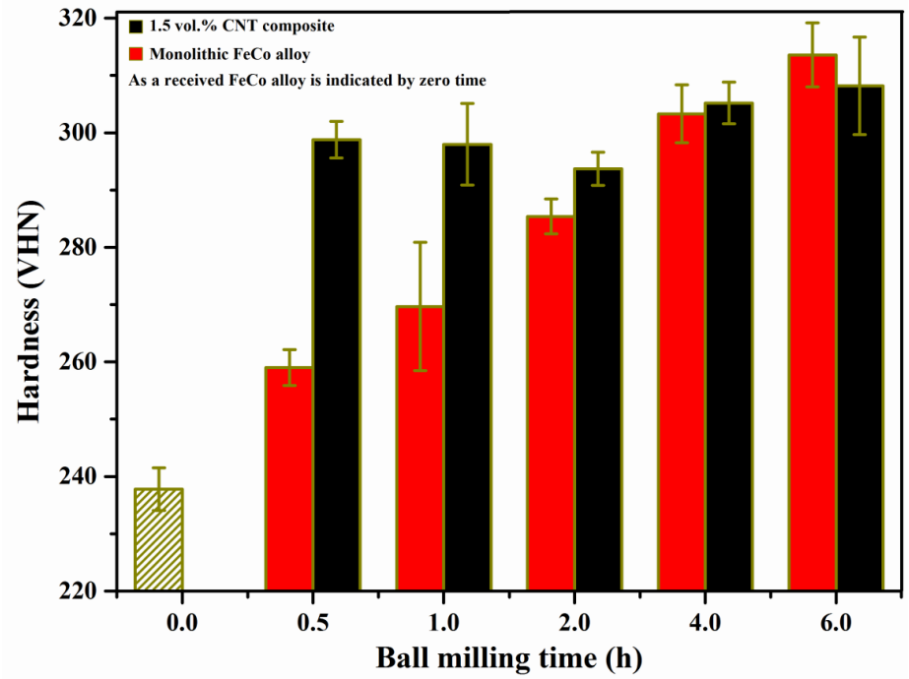

Figure 9.15. Changes of hardness with ball milling time of monolithic FeCo alloy and 1.5 vol. % CNT composite.

This difference in hardness after ball-milling is possibly attributed to the high dislocation density introduced to the material and to structural refinement observed in the ball-milled samples. The measurements of crystalline size demonstrate refinement in the monolithic FeCo alloy with further ball-milling time as shown in (Figure 9.9), accounting for the increased hardness. The behaviour in hardness of the 1.5 vol. % CNT composites cannot be scaled linearly with ball milling time. The increase in hardness was significant up to 1 h ball-milling time and then was decreased after 2 and 4 h. After 6 h ball milling the hardness was decreased in the composite as compared to the monolithic FeCo alloy. Adding CNTs to the FeCo alloy causes further refinement in the microstructure (Figure 9.5), and a finer microstructure leads to increases in hardness value. Moreover, the relative density was higher in the 1.5 vol. % CNT composite compared to the monolithic FeCo alloy (Figure 9.4), which will have a significant effect on the hardness. XRD shows an increase in the degree of the ordered structure as the ball-milling time was increased and with the introduction of CNTs, as shown in Figure 9.9. Hardness values are significantly high in the ordered structure compared to the disordered structure. Ordering in the FeCo alloy significantly raises the work hardening rate and reduces elongation [260]. Therefore,

the amount of strain hardening was increased as the stresses and the ordered phase were increased with further ball-milling time; leading to the highest value of hardness of 308.2 ±8.49 VHN and 313.6 ±5.59 VHN for the 1.5 vol. % CNTs composite and the monolithic FeCo alloy, respectively, after 6 h ball-milling; in spite of the decrease in relative density, as seen in Figure 9.4.

The elongation was significantly increased from 2.82 % in the monolithic FeCo alloy to 6.09 % in 1.5 vol. % CNT composite when the materials were prepared at the same history of 1 h ball-milling Figure 9.16.

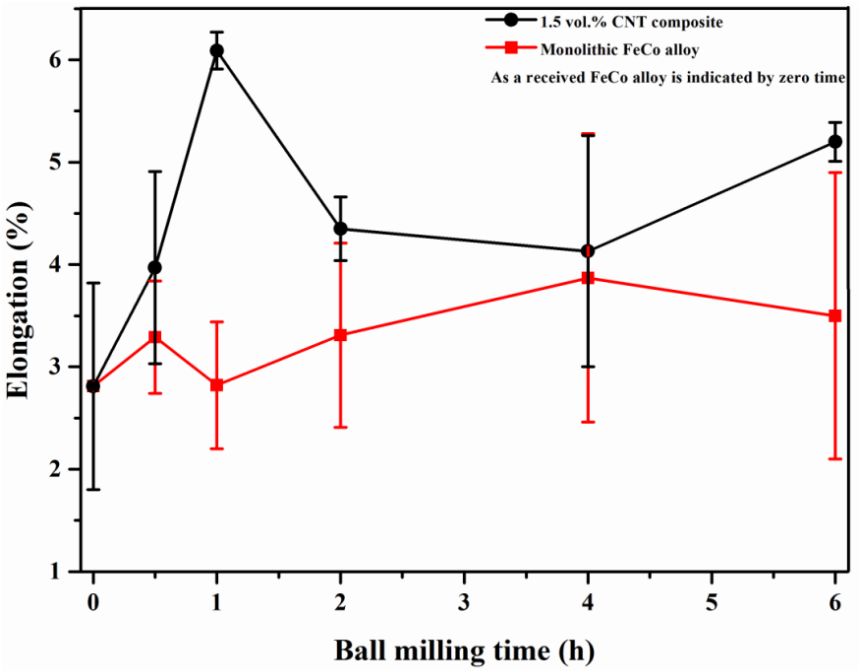

Figure 9.16. Elongation of monolithic FeCo alloy and 1.5 vol. % CNT composite with different ball-milling time.

Elongation then was decreased after 6 h ball-milling for both the FeCo alloy and the 1.5 vol. % CNT composite; but was still higher in the latter than in the former. The elongation of the FeCo alloy composite is generally affected by; the ductility of the base alloy, the quality of the reinforcement and its dispersion, the reinforcement-matrix interfacial bonding and the volume fraction of ordered phase. Optimisation of the ball-milling time is very important to achieve the best dispersion with high interfacial bonding and minimised damage to the CNTs. Ball-milling for 6 h has been reported as the best time for embedding the CNTs inside the Al matrix particle without the formation of a carbide and with minimum damage to the CNTs; leading to the highest improvement in tensile strength and mechanical properties [250]. However, the quality of the CNTs, ball-milling conditions, and matrix material must be considered in the optimisation of the ball-milling time.

The results show that the highest value of elongation was achieved after 1 h ball-milling time. Different factors contributed to the improved elongation after a limited ball-milling time of 1 h. Firstly, the damage of the CNTs was very low as confirmed in Table 1, thereby the formed carbide from reaction with CNTs was also low at this milling time. The second factor is the powder morphology; this was not significantly affected after 1 h ball milling time, hence agglomeration was not present and sintering processes were not retarded as in samples milled for longer. The final density of the compact was therefore improved. Thirdly, since the ball milling time was short the introduction of impurities by the milling media was minimised. Therefore, the negative effect of impurities on the elongation behaviour was reduced in this composite. Finally, since the elongation of the ordered structure in Fe50Co at room temperature is zero [21], the decrease in the elongation value for both the monolithic FeCo alloy and the 1.5 vol. % CNT composite after 6 h ball-milling was most due to the increased volume fraction of ordered structure.

9.2.9. Fractography studies

The fracture surface images for both monolithic FeCo alloy and 1.5 vol. % CNT composite, are seen in Figure 9.17. The dominant fracture mode in the FeCo alloy in both the ordered and disordered states is intergranular fracture, due to the inherent weakness in grain boundaries bonding [1]. Transgranular fracture was observed for both the monolithic FeCo alloy and the 1.5 vol. % CNT as shown in Figure 9.17. This is an indication that an improvement in granular bonding has been achieved in the FeCo alloy using this procedure. However, porosity was noted on the fracture facets; especially for the extended ball-milling time of 6 h, which can be attributed to the effect of agglomeration of the powder on the densification processes. Pull out of single CNTs is observed; with the FeCo alloy being tightly adhered to the surface of CNT as shown by the arrow in (Figure 9.18). This indicates that a strong interfacial bonding and uniform dispersion has been achieved. The observed patches of dimples on the fracture surface can be attributed to the improvement in bonding between the FeCo grains and the CNTs, which has significantly improved the elongation in the 1.5 vol. % CNT composite.

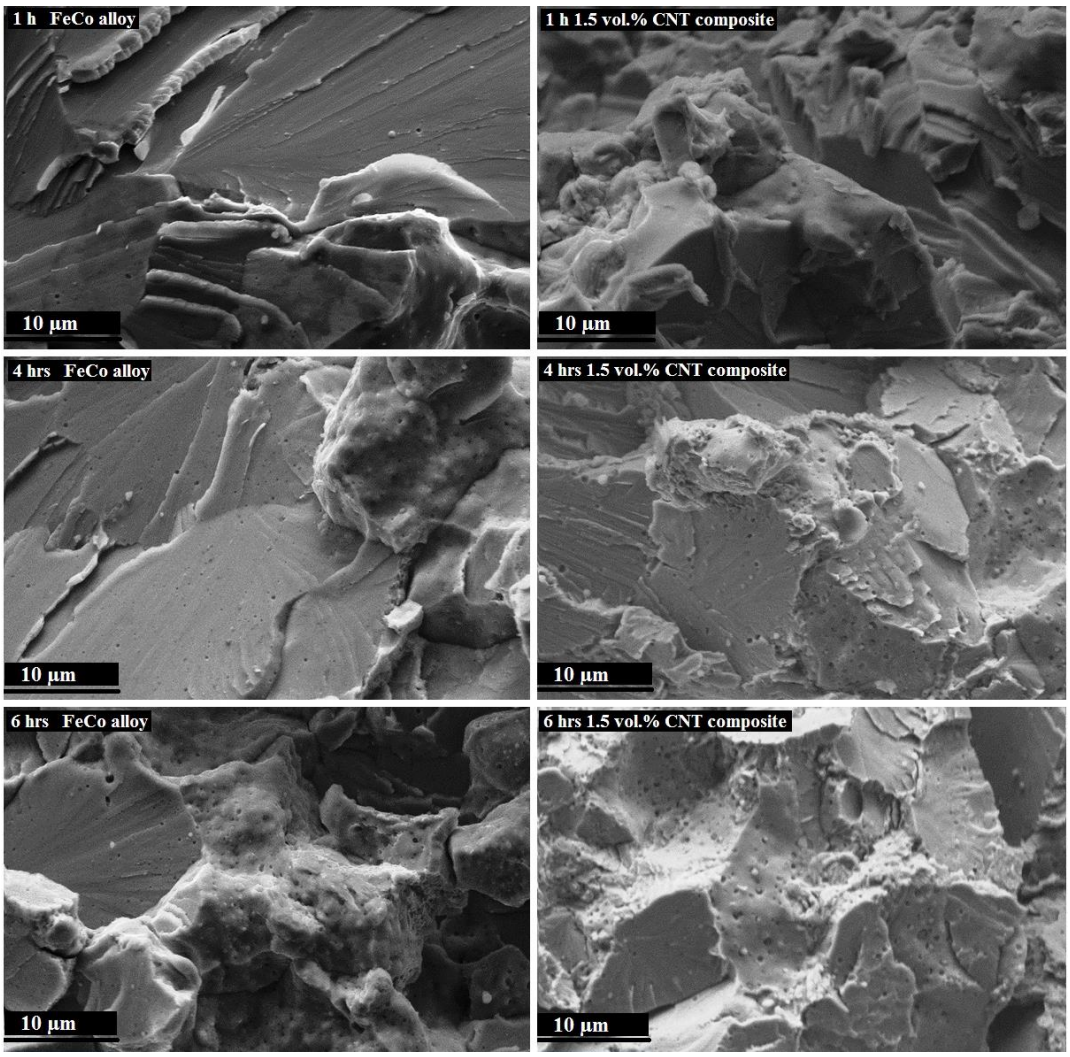

Figure 9.17. Fractographs of monolithic FeCo alloy and 1.5 vol. % CNT composites for indicated ball-milling times.

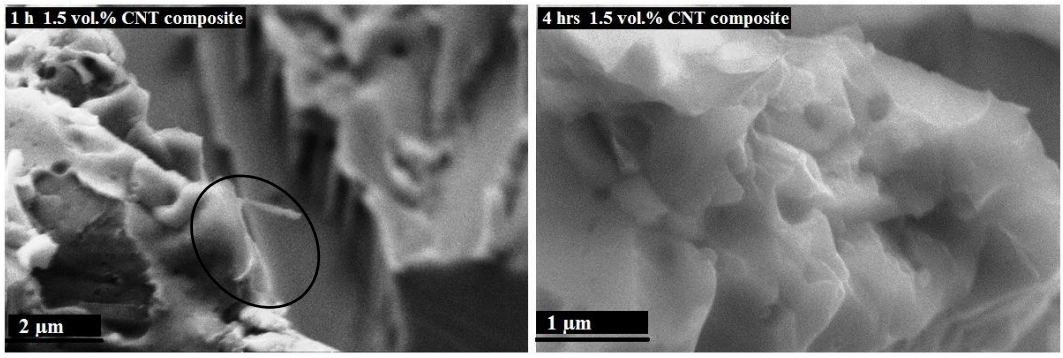

Figure 9.18. High magnification SEM of fracture surface of 1.5 vol. % CNT composites for indicated ball-milling times.

Summary

CNTs worked as a lubricant during ball-milling, leading to improve densification and to reduce agglomeration in composite powder, however, the completely embedded CNTs and drought the lubricant after 6 h ball-milling caused agglomeration in composite powder. Dual influenced roles on the quality of reinforcement were played by ball-milling, the first being to cause thinning of the CNTs and the second being to convert the unstable CNT into amorphous carbon. The tensile and yield strength were increased with increasing ball-milling time to 6 h; the highest value for strengthening was achieved after 1 ball-milling time for 50 %, showing a significant increase in elongation as well. The fracture surface showed evidence for strong interfacial bonding by ball-milling. Patches of dimples were observed which are attributed to improved grain boundary bonding by CNTs. The highest values of saturation induction of 2.35 T and 2.33 T in the monolithic FeCo alloy and 1.5 vol. % CNT composite, respectively were achieved after 1 h ball-milling, due to improved density and less amount of formed carbides. However, the coercivity was significantly increased with ball-milling time, owing to grain size refinement and more carbide formation.

Chapter 10: Results and discussion of high energy ball-milling of 1 vol. % GNP composite

10.1. Introduction

The interface bonding has significant effect on mechanical and magnetic properties, poor bonding causes determination in both properties due to including porosities and undesired precipitates. High energy ball milling was used to obtain better interface bonding for dispersion a limit 1 vol. % GNP in FeCo alloy, in order to achieve better combination between mechanical and magnetic properties through improving the dispersion and interface bonding.

10.2. Characterisation of raw material and consolidated materials

10.2.1. Raw material

The spherical morphology of FeCo alloy powder is shown in (Figure 10.1a), while the raw graphene nanoplate (GNP) can be seen in Figure 10.1b.

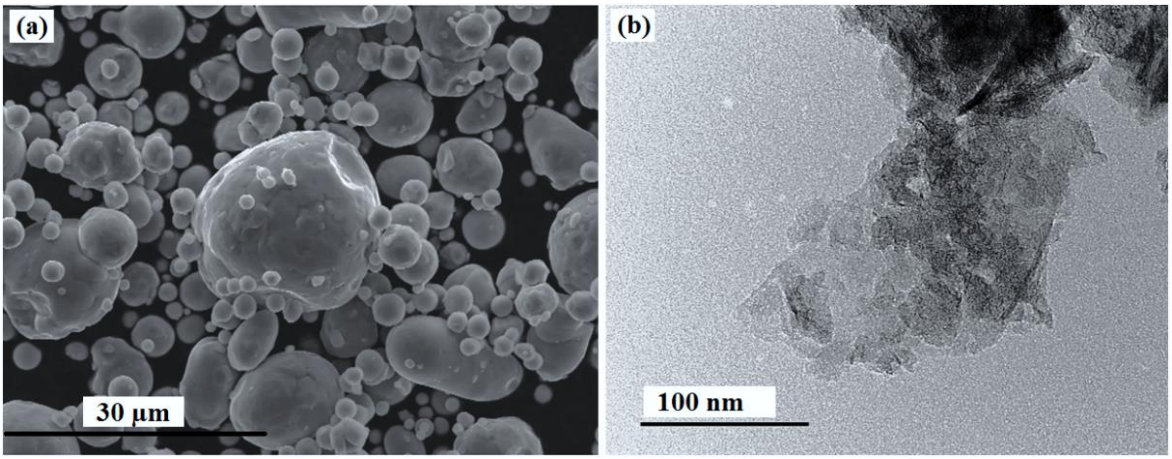

Figure 10.1. Morphology of as-received (a) SEM of FeCo alloy powder and (b) TEM of GNP.

10.2.2. Effect ball milling time on the morphology of FeCo powder and GNPs dispersion

The change in morphology of FeCo alloy powder without and with the addition of GNP for different ball-milling time is shown in Figure 10.2. Several changes occur during mechanical alloying of composite powders, which can be classified to morphological and microstructural. Intensive plastic deformation of particles can produce refinement in grains

size, change in crystallite size and for a considerable amount of internal stress a variation in lattice parameter can occur [261].

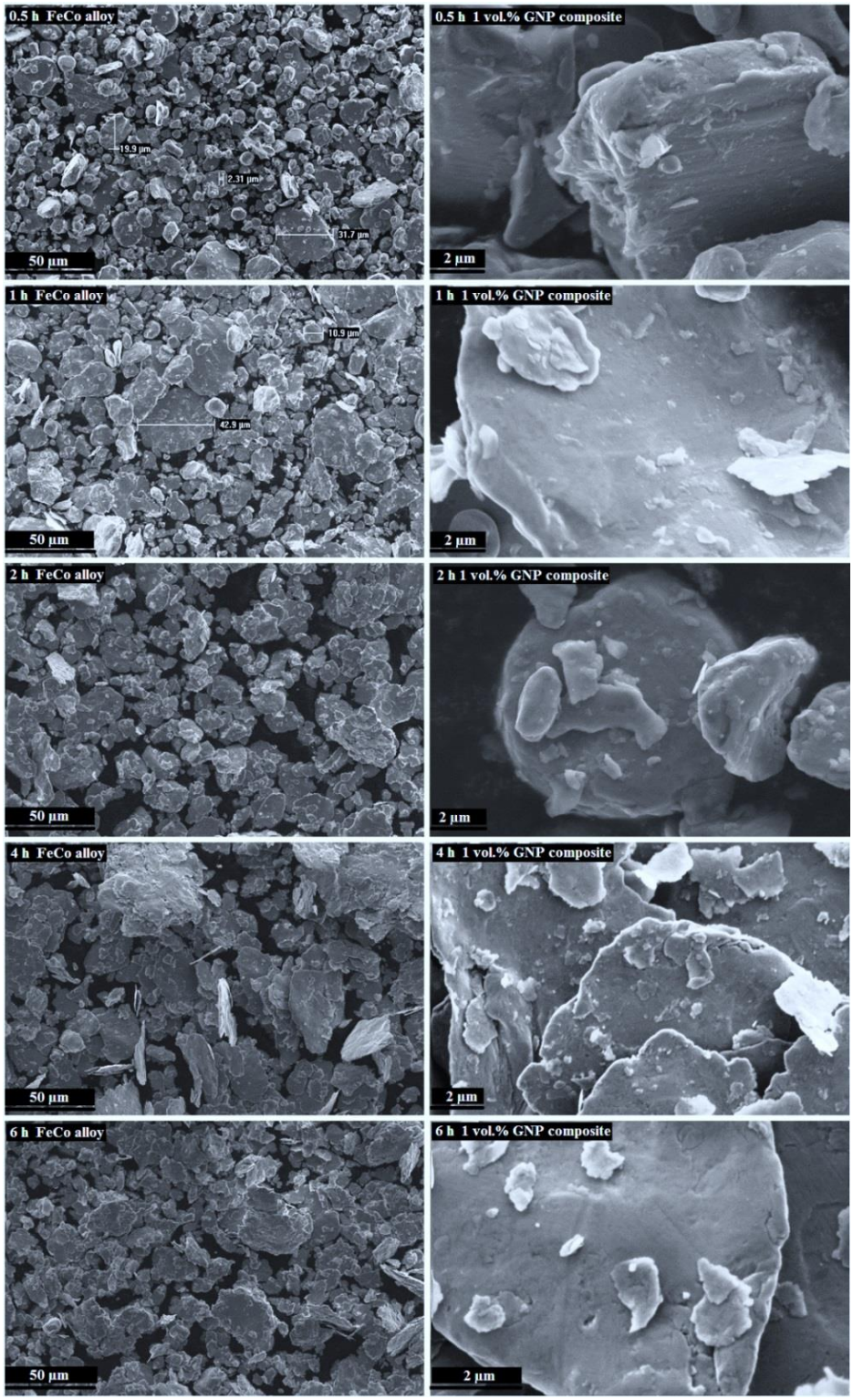

Figure 10.2. Surface morphology of the indicated materials and ball-milling time.

Generally, the sequence of milling stages is, the deformation of particles to flattened shape, cold welding of flaked particles and then fragmentation the flake. The spherical shape of as received FeCo alloy powder was changed to thick plate shape

particles after 0.5 h milling, and only minimal welding between the particles is observed at this time due to the effect of PCA in reducing temperature and lubrication the powder during ball milling. Extending ball-milling time to 1 h causes more plastic deformation in powder particles, thus the diameter of the flattened particles was considerably increased, however, the welding processes between the particles of the powder after 1 h ball-milling was not significant. Collision medium temperature was increased as the time of ball milling was extended to 4 h and 6 h, therefore evaporation in the liquid lubricant occurred and eventually an intensive welding happened especially in monolithic FeCo alloy powder. As a result, thick and wide plates were favourably formed in monolithic FeCo alloy powder as compared to thin and smaller flakes were formed in the composite powder, due to the higher ductility in monolithic FeCo alloy powder.

In composite powder, the GNPs were dispersed on the surface of FeCo alloy particles at 0.5 h ball-milling time, and then the strongly adhered GNPs on the surface of particles were gradually embedded into the FeCo alloy particles with increasing the time, through fracture and welding mechanisms which occurred constantly during the mechanical alloying. It has been reported by [262] that there is no change in dimension of carbon nanotubes after 1 h ball milling, as they are embedded into the particles and are protected from damage of balling medium. Thus, the GNPs were exposed to shortening before they were embedded into the particles of FeCo alloy powder. It is claimed that the small fragments of GNPs which are produced during mechanical alloying are uniformly dispersed into a metal matrix through fracture and welding process [263]. The 2D morphology and wide surface area in GNPs which were tightly adhered to the surface of FeCo alloy particles made the doping of sheets into base particles extremely difficult even after 2 h ball milling time. There is no evidence for GNPs on the surface of FeCo alloy particles after 6 h ball milling time, suggesting that the most of the GNPs were completely embedded into the powder particles. The particle size was reduced after adding GNPs to the FeCo alloy powder due to the dual role for carbon nanostructure during dispersion, firstly GNPs work as a barrier and lubricant to reduce the welding between the particles, and secondly GNPs cause a considerable increase in fracture rate in the composite particles owing to increase strain hardening after embedding GNPs into the base powder. It is reported in [264] that the embedded GNPs accelerate the milling process in the metal matrix through increasing the work hardening. EDS mapping of 1 vol. % GNP composite after 6 h ball milling time shows a homogenous dispersion of GNPs into FeCo alloy powder Figure 10.3. The uniform dispersed carbonaceous nanomaterial can only be

embedded into base particles powder during the mechanical alloying, as the agglomerated carbonaceous nanomaterial prevents the bonding between the particles of matrix powder [264]. Therefore, it is expected that the interface bonding is significantly improved between GNPs and FeCo alloy.

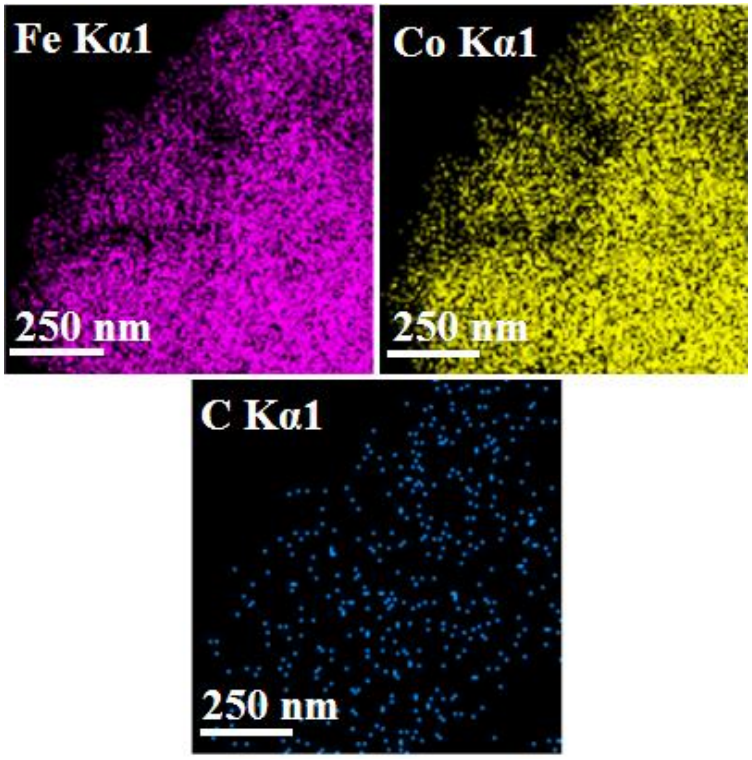

Figure 10.3. EDS mapping of 1 vol. % GNP composite after 6 h ball milling.

10.2.3. Shrinkages curve and density of the sintered materials

Shrinkage curves of as received FeCo alloy and after 1 h ball milling FeCo alloy with and without addition GNPs are shown in Figure 10.4. The first peak was accordingly changed with the rearrangement of powder particles whilst applying a high sintering pressure of 50 MPa instantly at room temperature. Therefore, a broad difference is observed in this peak between as received FeCo alloy compared to ball milled monolithic FeCo alloy and 1 vol. % GNP composite. The morphology of FeCo alloy powder was changed due to plastic deformation during the ball milling process, the included GNPs in FeCo alloy powder works as lubricant which improves the powder compact.

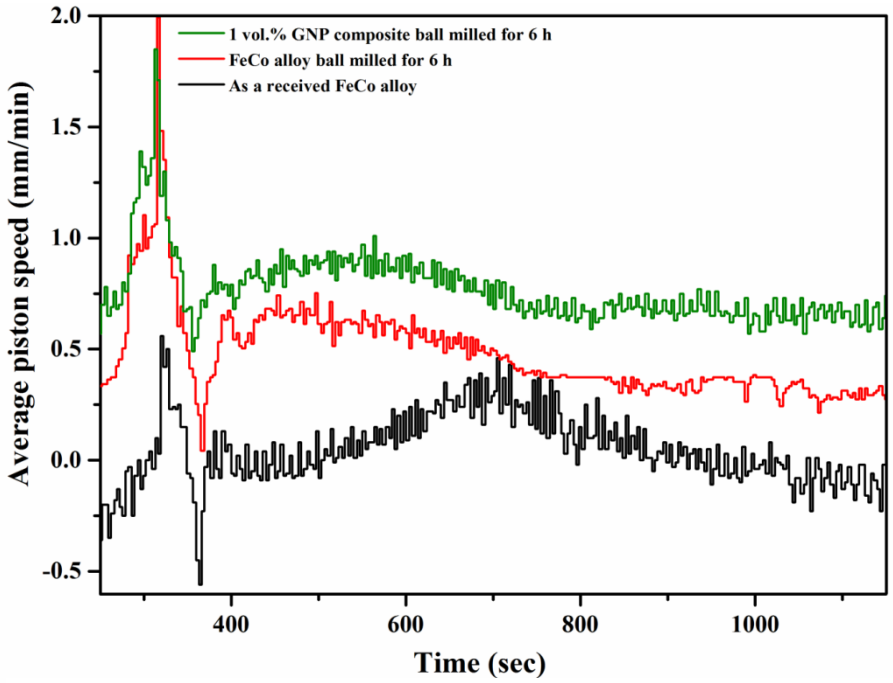

Figure 10.4. Change in average piston speed against time for the indicated materials.

Spherical morphology of as received FeCo alloy powder allows excellent mobility as compared to flaked particles powder due to the high friction area and bridge forming during packing in the latter powder. As a result, the reduced average piston speed is observed in the as received FeCo alloy as a compared to the rest. While the second peak is associated with shrinkage in powder during sintering. Average piston speed was earlier decreased in materials sintered after 6 h ball milling time compared to as-received FeCo alloy. This can be attributed to the effect of both ball-milling and GNPs addition on densification processes. The stresses were introduced in the powder during ball milling processes, therefore the dislocation density was increased either from the ball milling or from the difference in thermal expansion between the base alloy and the reinforcement. The densification of as received FeCo alloy happend in a narrow range of time as compared to a longer duration of time in ball milled monolithic FeCo alloy and 1 vol. % GNP composite, as shown in Figure 10.4. This can be attributed to the formation of agglomerations in powder after a ball milling time of 6 h. Despite the addition of GNPs making a slight change in shrinkage curve of composite compared to FeCo alloy, at the same regime of ball milling, the density was increased significantly after adding GNPs to FeCo alloy. The intensive welding processes and high level of agglomeration in monolithic FeCo alloy powder made sintering of powder very difficult [212]. Difficulty in the sintering process from agglomerations in powder has an effect on the relative density of the produced materials, which are shown in Figure10.5. Generally, the relative density of monolithic FeCo after ball milling was reduced with extending the time of milling.

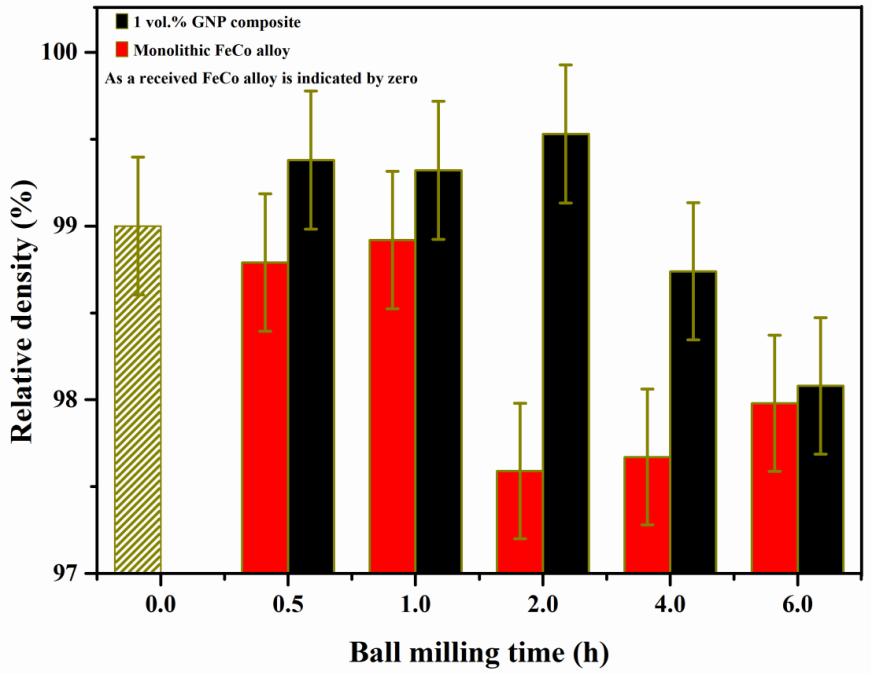

Figure 10.5. Variation of relative density of SPS sintered 1 vol. % GNP composite with ball milling time.

On the other hand, the relative density was increased in 1 vol.% GNP composite as a compared to as-received FeCo alloy as the ball milling time was increased, showing the maximum value of (99.53 ±0.39)% after 2 h milling time. After that, the relative density was decreased for both monolithic FeCo alloy and 1 vol.% GNP, showing the lowest value of (98.08 ±0.39)% in 1 vol.% GNP composite after 6 h ball-milling time, however the relative density of composite was maintained at the higher values than the monolithic FeCo alloy for the same regime of ball milling. This can be attributed to the role of GNPs in improving densification processes, adding GNPs to FeCo alloy powder reduces the agglomeration in milled powder due to the lubrication effect and causing an increase in fracturing processes than welding in composite powder owing to a raised strain hardening rate, as seen in Figure 10.2. Further, the slight difference in the electrical conductivity between the monolithic FeCo alloy and 1 vol.% GNPs for the same regime of ball milling might have also effect on densification of the composite, see Table 2.6.

10.2.4 Microstructure of consolidated materials

The variation in the microstructure of FeCo alloy and 1 vol. % GNP-FeCo alloy composites at a different time of ball milling is shown in Figure 10.6. Elongated grains were observed in monolithic FeCo alloy for all ball milling times, the deformation in powder particles during ball-milling processes leads to this structure. As the time was extended the structure was refined, however, the included porosities were noticeably increased, as seen in Figure 10.6. After adding GNP to FeCo alloy, the grain size was

reduced, owing to the effect the GNPs in reducing the particle size of powder during ball milling and pinning grain growth during sintering. In the composite material, the agglomerated GNPs were gradually dissociated with ball milling time, therefore the uniform dispersion of GNPs is observed in 6 h ball-milled composite. Furthermore, the densification was also improved, therefore, the porosities in microstructure were reduced in the composite material in comparison to the monolithic FeCo alloy.

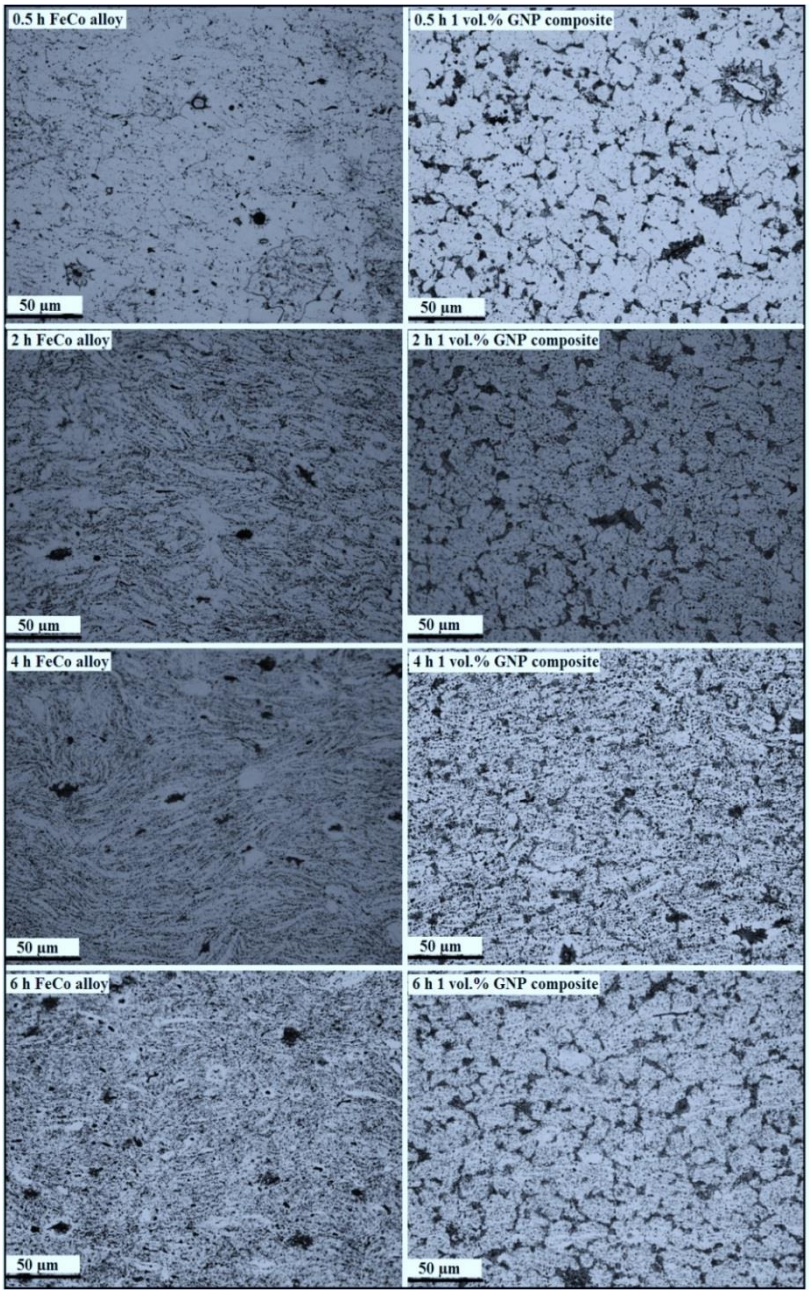

Figure 10.6. Optical microscope microstructure of monolithic FeCo alloy and 1 vol. % GNP composite of indicated ball-milling time.

10.2.5. X-ray diffraction (XRD) analysis

The XRD histograms of the as received FeCo alloy, ball milled monolithic FeCo alloy and 1 vol. % GNP composites at different time are compared in Figure 10.7.

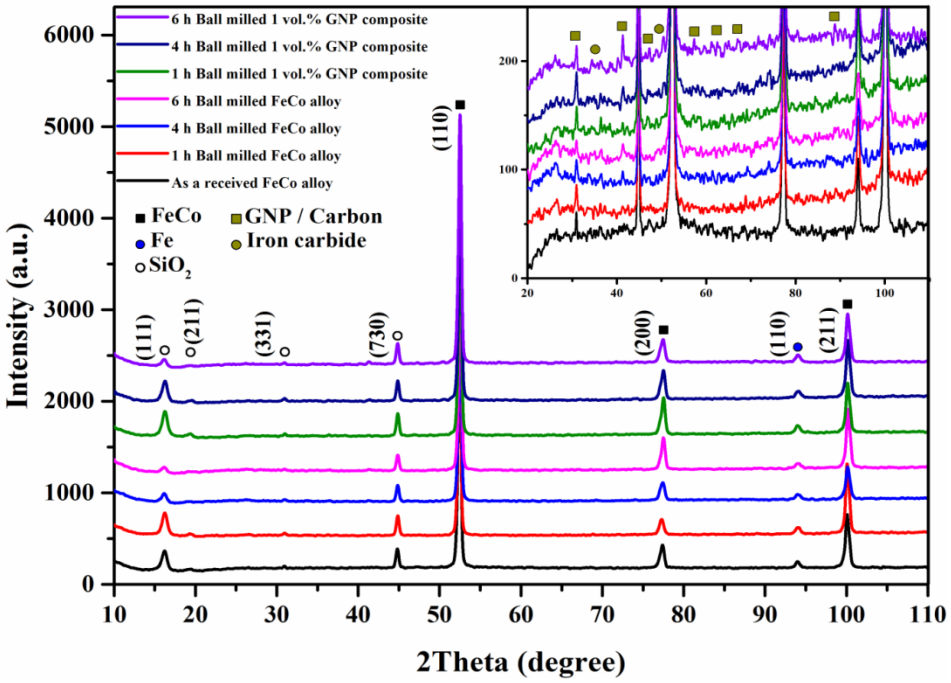

Figure 10.7. X-ray diffraction patterns of consolidated materials for indicated milling time.

The silicon oxide was included in as a received FeCo alloy, which could be a contamination in the powder from the supplier or due to exposure the FeCo powder to air as it contains a trace of silicon. In spite of there is no evidence from XRD results for contamination after ball milling, it is believed that it might be at percentage below the sensitivity of X-ray instrument, and almost the contamination is from the steel ball rather than the tungsten carbide coated jar as the hardness in latter is higher than the former. It is reported by [156] that the powder welded onto the ball surfaces which creates a barrier against excessive wear of grinding medium and does not contaminate the powder, so very low contamination can be expected in the sintered materials. A very weak peak of iron carbide was noticed in composite after 6 h ball milling. However, carbon was observed in as a received FeCo alloy, the damaging of GNPs structure from ball milling caused an increase in the amount of carbon, which was eventually reacted with iron to form the carbide.

The XRD histograms for the ordered phase are shown in Figure 10.8. The decrease in peaks intensity with appreciable widening and shifting was observed after ball milling. This can be rationalised to the effect of ball milling, and to embedding GNP which is believed to cause a change in the orientation of crystals in metal matrix [265]. Two reasons

can be interpreted the line broadening: the residual stresses and small crystal size of less than (1000 Å). The mechanical alloying of matrix powder leads to include strains in powder due to cold work which causes upshifting for peaks [266, 267]. Introducing GNPs to FeCo alloy by ball milling causes an increase in the ordered structure Figure 10.8. However, the intensity of the superlattice line (100) was decreased in 1 vol. % GNP composite after 6 h ball-milling time compared to other time of milling. This might be due to intensive damage in GNP structure after a long time of ball milling, which reduces the efficiency of GNP to make a change in the structure. However, extending ball milling time reduced the crystallite size, especially in 1 vol. % GNPs composite.

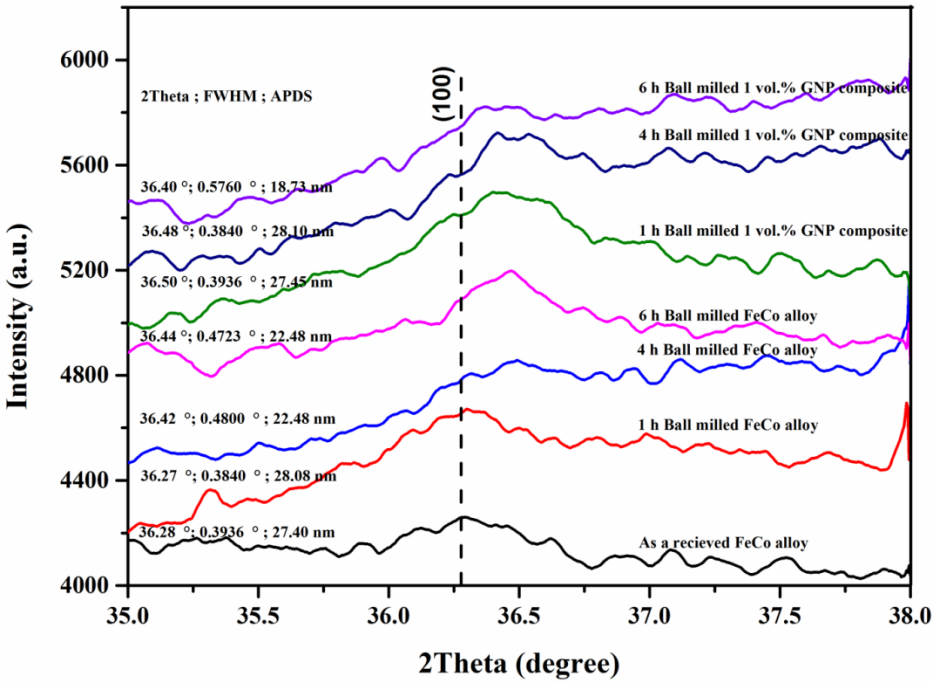

Figure 10.8. Slow scan XRD patterns, illustrating (100) superlattice reflections for the indicated materials, the diffraction angle (2Theta), the full width half maximum (FWHM) and the anti-phase domain size (APDS) are also displayed.

10.2.6. Raman spectra study

Raman spectroscopy is routinely used for characterisation of graphene structure. The quality of as received GNP was low as confirmed from the presence of D′ and the high intensity of R in spectra of raw GNPs [268], indeed high-quality graphene shows G and 2D peaks without showing D peak. Raman spectra results show a splitting in G band but not in a 2D band, as seen in Figure 10.9.

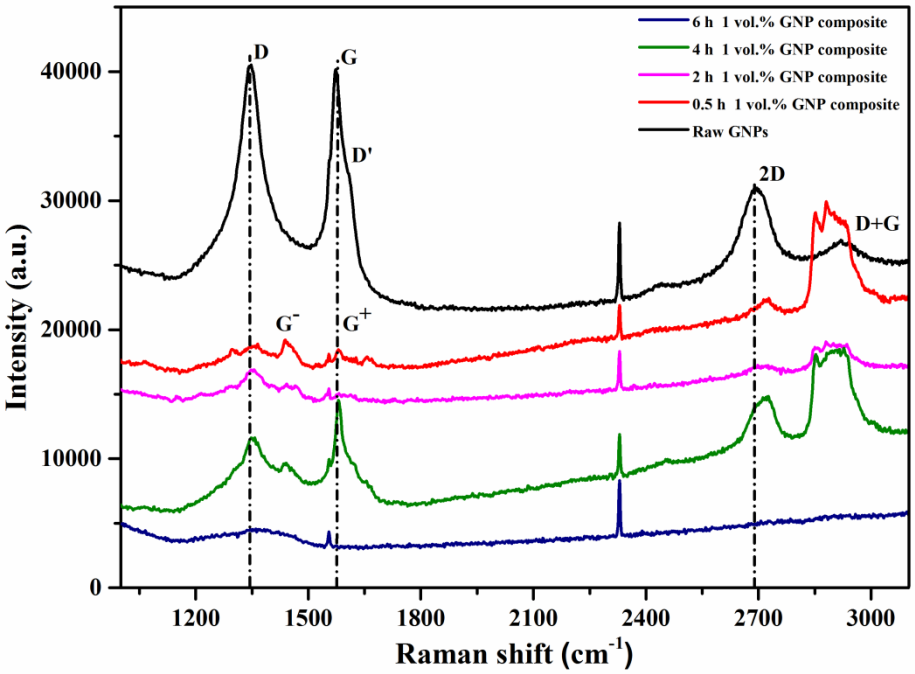

Figure 10.9. Raman spectra of the indicated materials at different ball-milling time.

Under the effect of strain, the G and 2D bands are split and shifted. The shifting is strongly related to direction and magnitude of strain [268, 269]. Redshift which is related to phonon softening is observed under tensile load while blue shifting is related to phonon hardening under compressive loading or hydrostatic pressure, the shift is increased with increasing the strain [270, 271]. Raman spectra show an absence of splitting in the 2D band, this can be attributed to the lower value of strains and insufficiency of these strains to create splitting in the 2D band, while splitting and shifting in G band was observed, which can be attributed to the effect of tensile strain on GNPs [268]. Raman spectra frequency of carbon fibre is very sensitive to the applied strains for either tension or compression case, thus the relationship between Raman shift and strain can be used as a mechanical sensor for qualify of the interface bonding and the efficient of stress transformation in nanocomposites [271, 272]. Raman spectra show a red shift and splitting in G band of the composite materials, therefore it is expected that the ball milling and spark plasma sintering processes led to an increase in interfacial bonding between GNPs and the matrix FeCo alloy. The stresses at the interface of composite comprise a combination of stresses which are included by the differences in thermal expansion between the reinforcement and matrix material, and the stresses from load transformation. Thus more stress transferred via high interface bonding in GNPs composite cause an increase in G band splitting and an increase in redshift under tensile load. However, the splitting and shifting in G band cannot be only related to the interface bonding, since ball-milling up to 0.5 h composite shows high intensity in G^- band in spite of that the GNPs are

rarely to be embedded and are only to be dispersed on the surface of particles of FeCo alloy powder at this time. The directly applied stresses by balls of the collision medium play a significant role also on the splitting and the shifting of Raman spectra peaks.

It is a fact that the extensive ball-milling processes cause a serious damage in carbon nanostructure. During ball-milling process, the crystalline size of graphite is reduced with time to achieve an ultimate crystalline reduction, after a limited value of reduction the graphite is unstable with ball milling time and conversion to the amorphous state is started. The fraction of the amorphous carbon formed from carbon nanostructure increases with extending ball milling time, a complete amorphization can occur only after ~ 500 h milling time at BPR ~ 1:100 under stainless balls [273, 274]. The intensity ratios *R* for the damage in GNPs are shown in Table 10.1. Before the GNPs get embedded within the particles of FeCo alloy powder the damage was increased with time up to 2 h ball-milling time, then the *R* was reduced considerably after 4 h ball-milling when the GNPs were doped in particles. This suggests that the best ball-milling time is 4 h which shows an improvement in the quality of GNPs and dispersion as confirmed in Figure 10.2. Enhancing the quality of GNPs can be rationalised to the role of ball-milling processes in exfoliation of GNPs to a thinner sheet with surfaces free from functionalization groups and less defects especially when GNPs are just started to be embedded into FeCo particles. The serious damage in GNPs after this time can also attribute to the low quality of raw GNPs, the accumulative damage from ball milling even after relatively short milling time of 6 h leads to a high fraction of amorphization in GNPs. Furthermore, however, the GNPs were completely doped within particles of FeCo alloy powder after 6 h ball milling time, which reduced the influence of collision media on the structure of GNPs. The high sensitivity of GNPs to Fe contamination accelerates the amorphization depending on the quality of GNPs, this raises another issue for dispersion GNPs in iron base alloy as compared to other alloys, high-quality GNP was milled in aluminium matrix alloy to 24 h at BPR 20:1 without losing the crystalline structure [274, 275].

Table 10.1 $R = (I_D/I_G)$ ratio of as received and 1 vol. % GNPs consolidated composites at different ball-milling

Milling time (h)	**0**	**0.5**	**1**	**2**	**4**	**6**
$R = (I_D/I_G)$ **ratio**	**1.00**	**1.01**	**1.04**	**1.12**	**0.80**	**(damaged)**

10.2.7. Magnetic properties

Figure 10.10 shows the upper halves of hysteresis curves of monolithic FeCo alloy and 1 vol. % GNP composite for a different ball milling time. Magnetic properties are summarised in Figure10.11.

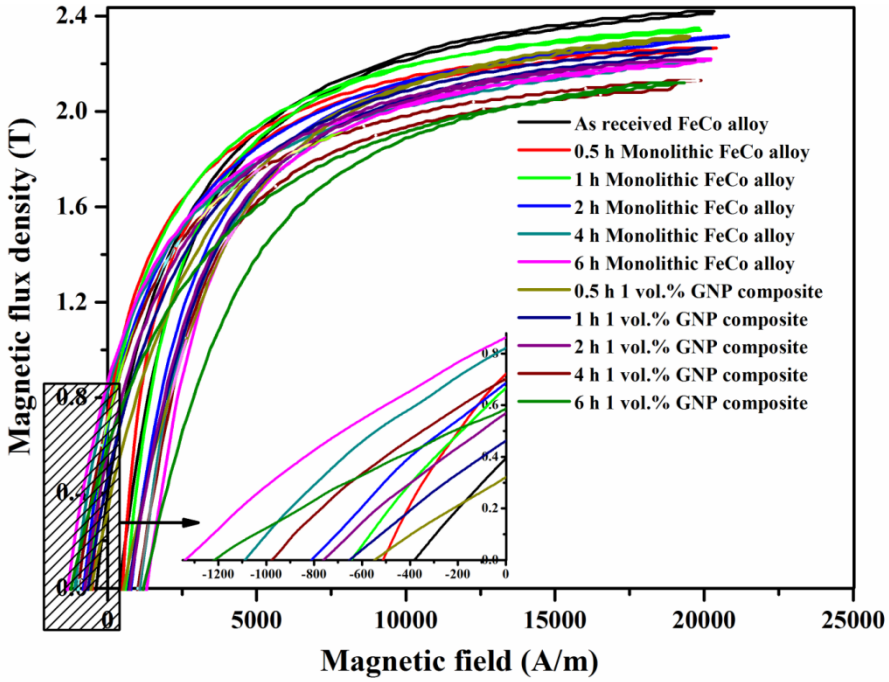

Figure 10.10. Upper halves of hysteresis curves of sintered materials at different ball-milling time.

The saturation induction at 25 kA/m was decreased after ball milling the monolithic FeCo alloy and 1 vol. % GNP composite materials as compared to as-received FeCo alloy. In comparison the samples after ball milling, the peak values in saturation induction of 2.35 T in monolithic FeCo alloy was obtained after 1 h ball milling time, while for 1 vol. % GNP composite materials after 0.5 h ball milling time. Up to 4 h ball milling the saturation induction was sharply decreased, and then a slight change in saturation induction with time was noticed in the sintered materials, showing lower value in composite with respect to base alloy. The lowest values of coercivity were observed after 0.5 h ball-milling time of values 511 A/m and 547 A/m for monolithic FeCo alloy and 1 vol. % GNP composite respectively. Then the coercivity value was significantly increased as the ball milling time was increased, giving the highest values of 1335 A/m and 1211 A/m in monolithic FeCo alloy and 1 vol.% GNP composite respectively after 6 h ball milling time. Interestingly the coercivity was lower in composite materials than the monolithic FeCo alloy when the time of ball milling was extended after 1 h, as seen in Figure 10.11.

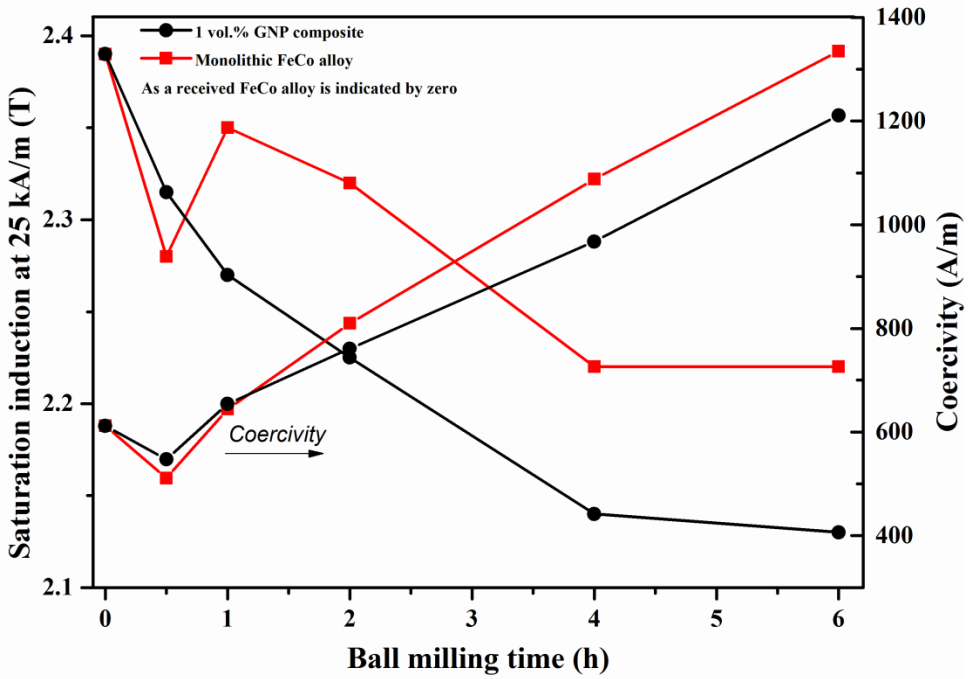

Figure 10.11. Summarize of magnetic properties of monolithic FeCo alloy and 1 vol. % GNP composite.

Increasing the saturation induction for FeCo alloy after extending the time from 0.5 h to 1 h is due to the improvement in the relative density of the consolidated material after 1 h ball milling time, as seen in Figure 10.5. The relative density was mainly reduced with extending the time of ball milling; therefore, the saturation induction was accordingly reduced. The reduced value for relative density after extending ball milling time was rationalised to difficulty in the densification of the agglomerated powder. XRD results show carbide formation after 6 h ball milling (Figure 10.7), from the other side Raman spectra exhibit a serious damage in GNPs structure at that time, as seen in Figure 10.9. Therefore, the formed carbide and more contamination with extending ball milling time are worked together as deteriorating factors for magnetic properties, which are further deteriorated due to more stresses introduced during ball milling processes [27].

It is well known that the coercivity is very sensitive to microstructure, inclusion, and density. The microstructure is refined with extending the time and more porosities are included in structure at ball milling time of 6 h, as shown in Figure 10.6. These parameters combine with increasing contamination either from collision medium or the damage in GNPs during ball milling lead to the significant increase in coercivity. On the other hand, the composite materials show a slightly decrease in coercivity as compared to the monolithic FeCo alloy with extending ball milling time. It seems that the impact force of balls during the process was firstly consumed in spreading GNPs on the surface of particles of FeCo alloy, so the introduced stresses to matrix FeCo alloy was lower than the

monolithic FeCo alloy at the same conditions. Then, the GNPs were effectively worked as the lubricant during ball milling process. These advantages reduce the deteriorating effect of powder agglomeration and stresses in the composite, leading to a slight decrease in coercivity of composite material. It has been also reported that the coercivity in the ordered structure is higher than the disordered structure [46]. Therefore, as the fraction of the ordered structure is increased, the coercivity value is increased as well. After 6 h ball milling the GNP was ineffective in formation ordered structure because of the excessive damage of its structure from ball milling process, this is another factor to the decrease in coercivity of composite in comparison to monolithic FeCo alloy after further ball milling time.

10.2.8. Mechanical properties

The stress-strain curves and the variation in ultimate tensile strength and yield strength with ball milling time of the sintered as received FeCo alloy, ball milled monolithic FeCo alloy and 1 vol. % GNP composites are shown in Figures 10.12 and 10.13 respectively.

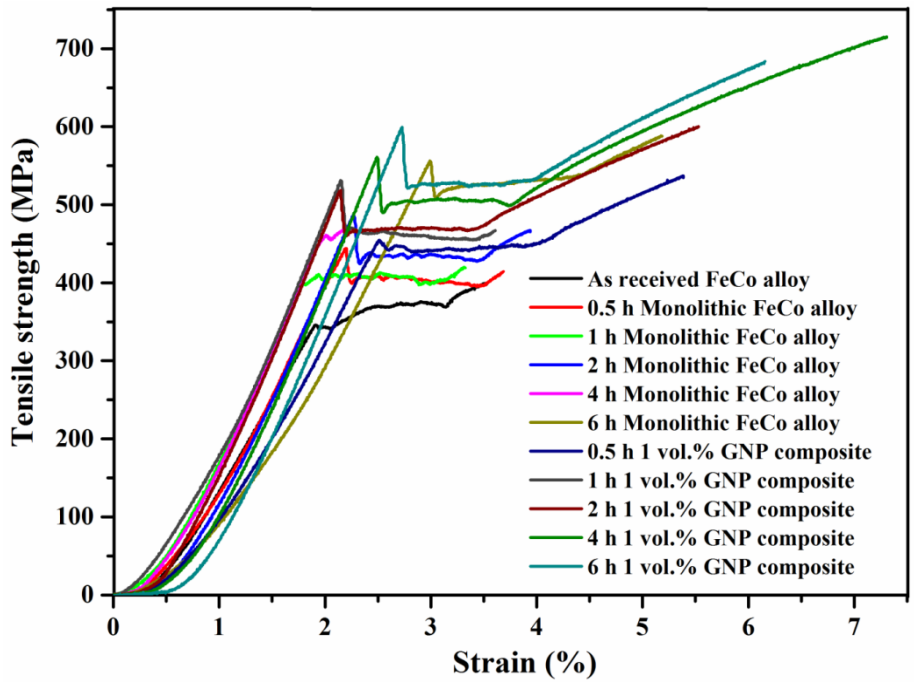

Figure 10.12. Tensile stress-strain curves for sintered materials of different ball-milling time.

Both ultimate tensile strength and yield strength were increased in monolithic FeCo alloy and 1 vol. % GNP composite with the time of ball milling, however, the increase in strength was higher in composite than the base alloy. Despite increasing yield strength with further ball milling time, the improvement in yield strength was not significant in composite as compared to the base alloy after longer ball milling time. The highest

improvement in ultimate tensile strength was achieved after 4 h ball milling time for value 695 ±30.19 MPa in 1 vol.% GNP composite.

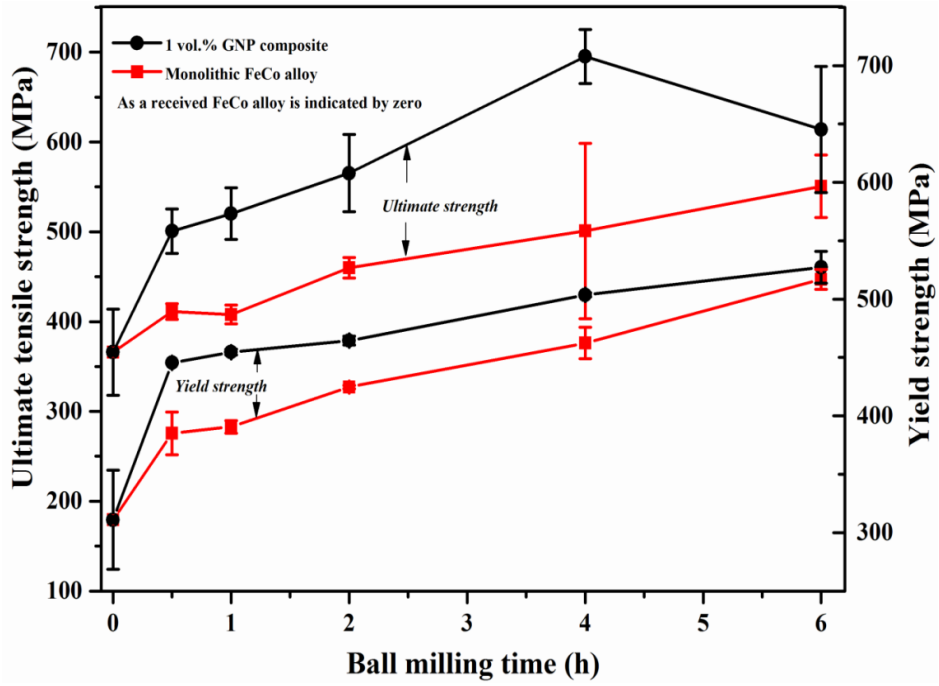

Figure 10.13. Ultimate tensile strength and yield strength of monolithic FeCo alloy and 1 vol. % GNP composite with different ball-milling time.

The improvement in the mechanical properties with extending ball milling time can be attributed to the gradual enhancement in dispersion GNPs as the time increased, as seen in Figure 10.2. Despite the significant reduction in GNPs defects after 4 h ball milling time, as seen in (Figure 10.9), the uniform dispersed for GNPs after 6 h ball milling time was combined with a serious damage in GNPs structure. The ineffectiveness for PCA after extending the time leads to lower strengthening effect, because of its influence on dispersion [156]. As a result of that, the amount of load which must be carried by reinforcement was significantly reduced, showing a decrease in the overall strength of the composite. Moreover, more stresses and contamination were introduced to the powder with extending ball milling time.

The variation in elongation for both monolithic FeCo alloy and 1 vol. % GNP composite with ball milling time is shown in Figure 10.14. The elongation was significantly increased from (3.87 ±1.41) in monolithic FeCo alloy to (7.14 ±0.24) in composite materials of the same condition for ball milling time 4 h. Then, the ductility was decreased for both monolithic FeCo alloy and composite material with increasing ball milling time. Optical microstructure observations (Figure 10.6) reveal an increase in porosity fraction of samples ball milled to 6 h, which is attributed to the difficulty in sintering due to the agglomeration in ball milled powder. After 4 h the GNPs were fully

embedded into the particles of FeCo alloy powder (Figure 10.2), giving not the only advantage of uniform dispersion for GNPs in FeCo alloy but also high interface bonding between the sheets and the base alloy. As a result of that, the ductility was considerably improved at this milling time in composite. It is well known that ball milling refines the structure, which is favourable to improve the elongation, calculations of nanocrystallite structure (Figure 10.8) exhibit a reduction in crystallite size. The slight improvement in elongation of monolithic FeCo alloy with ball milling time can be attributed to the refinement in structure.

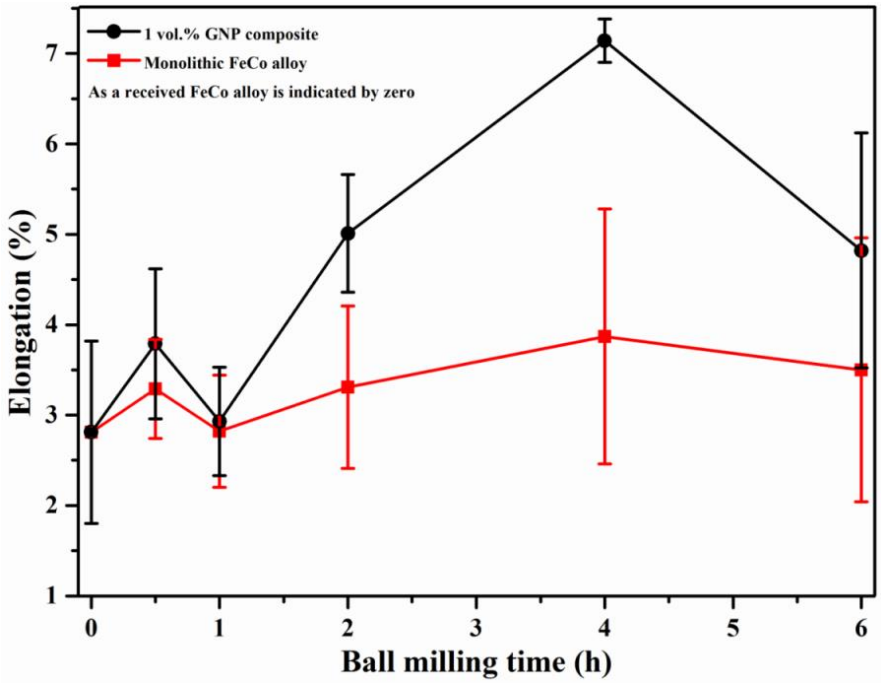

Figure 10.14. Elongation of monolithic FeCo alloy and 1 vol. % GNP composite with different ball-milling time.

Hardness measurements showed a significant increase in hardness values of both the monolithic FeCo alloy and 1 vol. % GNP composite after ball milling processes as compared to as-received FeCo alloy, as shown in Figure 10.15. Generally, the hardness of monolithic FeCo alloy and 1 vol. % GNP composite was increased with extending ball-milling time. Up to 2 h ball milling time, the hardness value was higher in GNP composite than the monolithic FeCo alloy, then this behaviour was conflicted. The highest hardness values of 313.6 ±5.59 and 312 ±2.47 VHN was obtained after 6 h ball milling time in monolithic FeCo alloy and 1 vol. % GNP composite respectively as compared to 237.8 ±3.7 VHN in as-received FeCo alloy. The ordered structure was increased with ball milling and the addition of GNPs, however, the effect of GNPs in formation ordered structure after 6 h ball milling time was reduced due to the damage in GNPs structure. Iron carbides were formed at this time, leading to an increase in the hardness of composite materials, but not as much as the improvement in hardness from the ordered structure in monolithic FeCo

alloy. As a result, the highest value for hardness was obtained in monolithic FeCo alloy after 6 h ball milling which can be attributed to the difference in volume fraction of ordered structure. It has been reported that the hardness of the ordered structure under deformation is higher than the disordered structure [260]. The structure refinement with extending ball milling time has also positive affect on increasing the hardness value of the sintered materials.

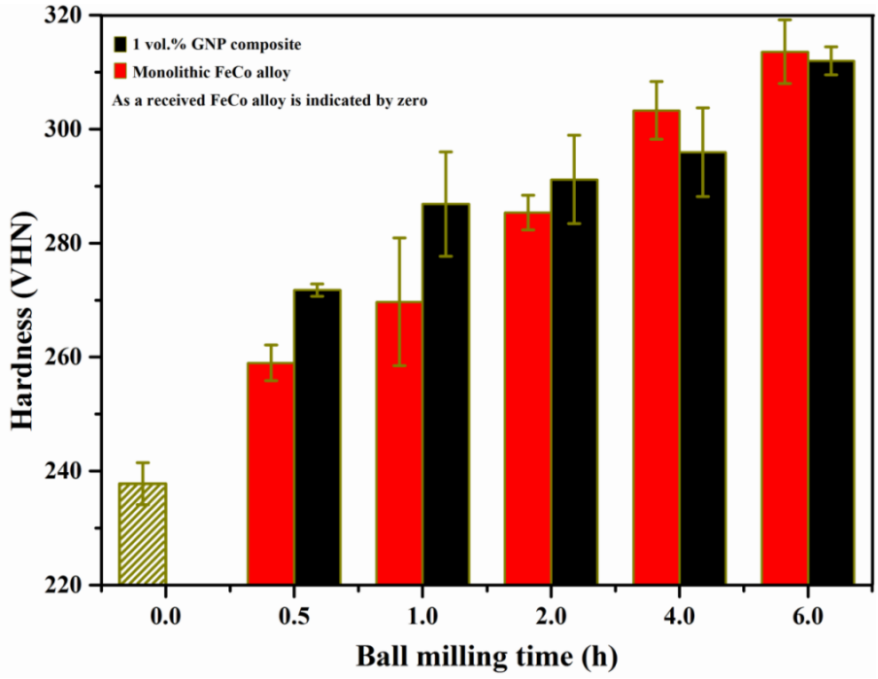

Figure 10.15. Changes of hardness with ball milling time of monolithic FeCo alloy and 1 vol. % GNP composite.

10.2.9. Fractography studies

A transgranular fracture mode was observed in the monolithic FeCo alloy and 1 vol. % GNPs composite, as seen in Figure 10.16. However, the influence of adding GNPs to FeCo alloy can be identified clearly. After 4 h ball milling time undensified particles were observed in fracture surface of the monolithic FeCo alloy and also the grain size was larger in monolithic FeCo alloy than the composite. Adding GNPs to FeCo alloy led to considerable reduction in the agglomeration in powder during the ball-milling process. The undensified area was increased with extending ball-milling time to 6 h in the monolithic FeCo alloy, while the 1 vol. % GNPs composite does not show evidence for undensified area even with increasing the time of ball milling. However, the porosities on the facets of fracture were increased with ball milling time for both the composite and the base alloy. Most GNPs are firmly embedded within the matrix FeCo alloy, as seen in Figure10.17, however, the porosities are observed around some sheets, the GNPs are not pulled out. Therefore, it is expected that the interfacial bonding between GNPs and the matrix FeCo

alloy is significantly improved. It is noticed that the size of the dispersed GNPs on fracture surface was not uniform this might be attributed to the effect of ball milling on shortening the fibres and also can be rationalised to inhomogeneity in the raw GNPs, as it is shown in (Figure 10.1)

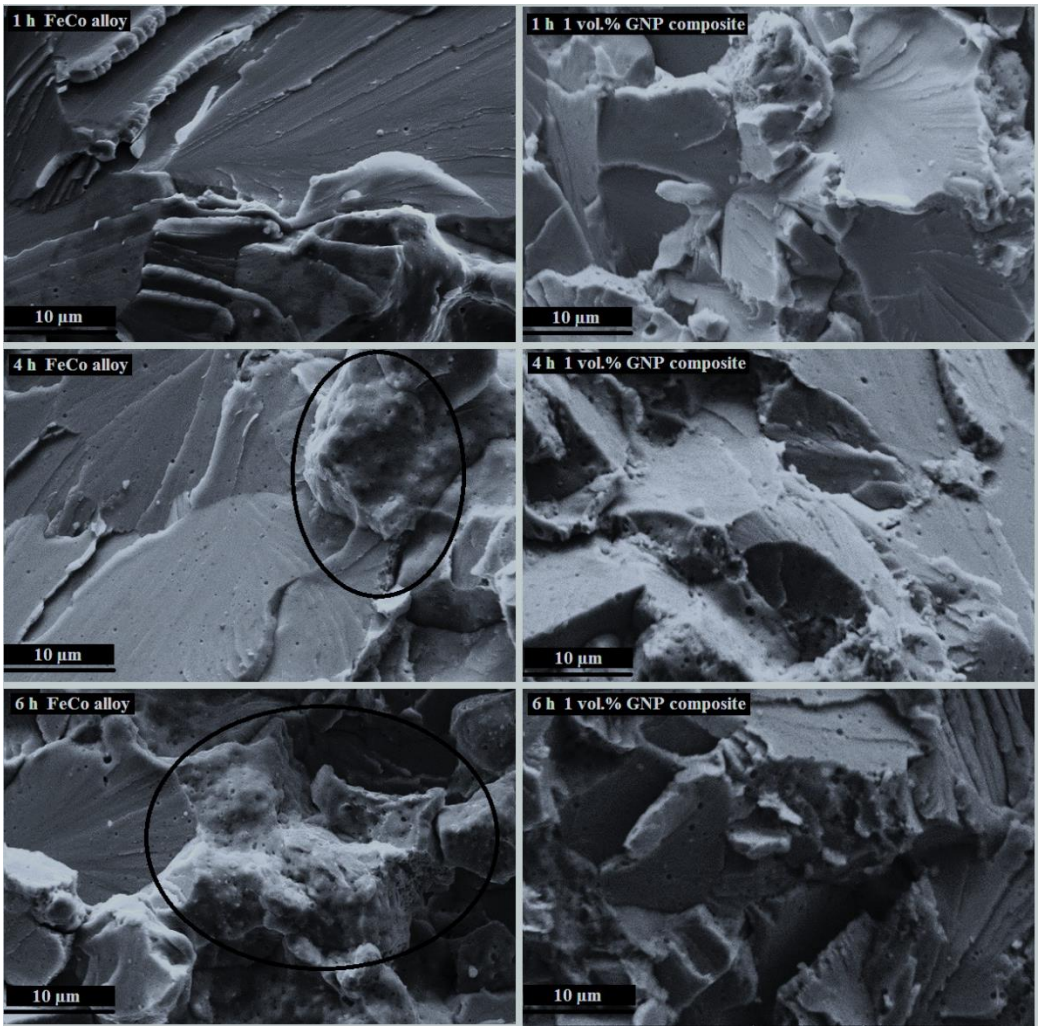

Figure 10.16. Fractographs of monolithic FeCo alloy and 1 vol. % GNP composites for indicated ball-milling times.

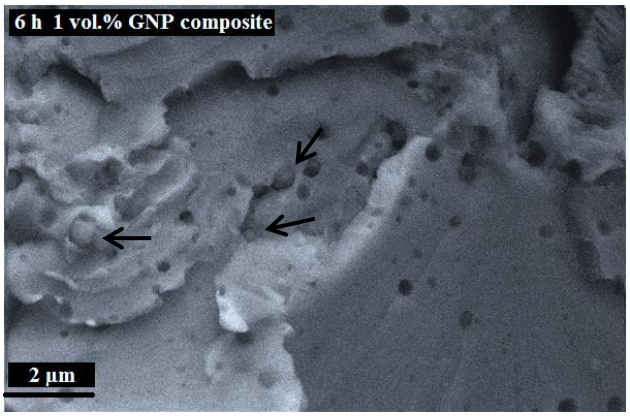

Figure 10.17. High magnification SEM of fracture surface of 1 vol. % GNP composites for indicated ball-milling times.

Summary

GNPs work as a lubricant during ball milling, therefore thin and small flakes were favourably formed in composite powder as compared to a thick and wide plate in monolithic FeCo alloy, extending ball milling time led to include porosities in microstructure due to the difficulty in sintering the agglomerated powder. The saturation induction was reduced with extending ball milling time due to the drop in density of material, while, the coercivity was increased with extending ball milling time due to poor densification, contamination, refined structure, a formation of carbide in composite, and increased ordered structure. Ball milling helps to improve the interface bonding, however, a serious damage in the structure of GNPs happens after extending the time of ball milling to 6 h. Therefore, the peak in strength and elongation are observed after 4 h ball-milling time, due to embedding GNPs within FeCo alloy powder, good interfacial bonding and refinement of the microstructure.

Chapter 11: Conclusions and recommended future works

11.1. Conclusions

In the current research novel attempts have been investigated to improve the mechanical properties of FeCo alloy with less deterioration in the magnetic properties. Due to the inherent brittleness of equiatomic FeCo alloy, it is rare to find a study on plastic deformation for the alloy under tension. The tensile test has been employed to evaluate mechanical properties of binary FeCo alloy. Effects of sintering parameters on mechanical and magnetic properties at sintering pressure of 50 MPa are considered. The influence of different methods for dispersion CNT and GNP to achieve optimum combination between mechanical and magnetic properties have been also reported. Heat treatment at different temperatures was performed to evaluate the influence of ordered structure on properties. The conclusions are drawn from the study can divide into following sections:

11.1.1. CNT composite dispersed with aid of DMF

Densification behaviour was improved by ball milling and further by embedding CNTs, this can be rationalised to the reduction in grain size produced from ball milling and CNT addition, especially at low volume fraction. Grain growth during spark plasma sintering was also inhibited by CNTs, leading to more refinement in the microstructure.

The best combination between magnetic and mechanical properties was achieved in the composite prepared by dry mixing and ball milling method, showing around 20 % enhancement in tensile strength with improved elongation at 0.5 vol. % CNT composite. However, this dispersion method was not effective at fraction exceed 1 vol. % CNTs and showed the only improvement in magnetic properties at 1 vol. % CNTs, a sharp deterioration in properties was occurred at high volume fractions due to poor dispersion and densification. Raman spectra show that the quality of CNTs was improved by pre-mixing in DMF, this can be due to more agglomeration of the powder, which prevented direct contact between the milling balls and the CNTs.

11.1.2. Using CNT to prevent overlapping between sheets in GNPs composite

The restacking between GNPs was reduced when CNTs were inserted among the nanoplatelets, which enhanced the dispersion of GNPs in FeCo alloy as compared to composites contain alone GNPs. However, inserting CNT among GNP caused more

porosity in the microstructure. Interestingly, CNT addition was very effective in refining microstructure, while the ordered nanocrystallite structure was promoted in FeCo alloy composites contain GNPs without CNTs. The highest saturation induction of (2.39 T), the lowest coercivity (583 A/m) and high hardness were achieved in 1 vol. % GNP composite. However, the tensile properties were decreased in all composite materials as compared to monolithic FeCo alloy owing to poor dispersion for the reinforcement and including porosity in the microstructure.

11.1.3. Optimise sintering parameters of monolithic FeCo alloys

The higher density of sintered FeCo alloys has been obtained by using low sintering pressure of 50 MPa as compared to samples sintered at 80 MPa by increasing sintering temperature and time, avoiding graphite die breakage at high sintering pressure. Using fast heating rate to densify FeCo alloys prompted porosities formation in the microstructure, which dropped density in consolidated materials especially at a lower sintering temperature. The tensile results of the samples sintered at 1100 ºC for all heating rates exhibited an improvement in yield strength and elongation as compared to lower sintering temperatures. Further, sintering at 1100 ºC improved grain boundary bonding as evidence from suppressing intergranular fracture in ordered binary FeCo alloy. Therefore, spark plasma sintering conditions of temperature 1100 ºC without dwelling time at a heating rate of 50 $^{o}C.min^{-1}$ were used in subsequent works to develop the properties of composite materials, in spite of a slight decline in density.

As grain growth was fast at the high sintering temperature of 1100 ºC, the coercivity was decreased accordingly regardless of heating rate. However, the highest saturation obtained at heating rate 50 $^{o}C.min^{-1}$ made these conditions the optimum to obtain good combination between mechanical and magnetic properties.

11.1.4. Effect dispersion of GNPs in flaked FeCo alloy powder

Using spherical FeCo alloy powder was ineffective in dispersion, leading to significant deterioration in the properties. However, using flaked FeCo alloy powder was more compatible to improve the dispersion, which enabled uniform dispersion up to 6 vol. % GNPs. Therefore, the mechanical properties of the composite were significantly improved in comparison to monolithic FeCo alloy, an increase to ~ 85 % and ~ 100 % were achieved in yield strength and ultimate strength respectively. Despite using high sintering temperature, the GNPs were maintained intact, leading to a considerable increase in ductility of the ordered FeCo alloy, which is normally failed with zero elongation. This can

be due to refining slip system, preventing crack propagation and fine microstructure of homogeneous dispersed GNPs composite. Fracture surface studies showed that the grain boundaries bonding was improved by GNPs, since a patch of dimples comprised GNPs were observed on the fracture surface of tensile samples.

Despite the saturation induction of (2.4 T) was achieved in flake FeCo alloy composites up to 2 vol. % GNPs at an applied field of 140 kA/m, the coercivity was significantly increased, due to change in microstructure and precipitates. Therefore, a suitable heat treatment is required for the better combination between magnetic and mechanical properties.

11.1.5. Heat treatment of 4 vol. % GNP composites

Raman spectra results showed that the quality of GNPs was improved, due to removing amorphous carbon from GNPs, the carbides were formed by the reaction the base alloy with the amorphous carbon. The coercivity was significantly high in samples heat treated in ordered temperature due to the precipitates and increased ordered structure, however, spheriodizing or even dissolve the precipitates during heat treatment in disordered temperature caused a significant decrease in coercivity with a slight increase in saturation induction.

All quenched samples showed lower ultimate strength and yield strength than composites without heat treatment, might be due to the influence of GNPs on ordering. The highest values of ultimate strength and yield strength were obtained from quenching from ordered region, however, the highest elongation was achieved by quenching from the disordered temperature of 900 ºC, due to increasing the disordered structure. The transgranular fracture can be changed to ductile fracture by quenched from 900 ºC, showing very fine dimples comprised GNPs, which bridge cracks and inhibit cracks propagation.

11.1.6. Effect of high-energy ball milling time on dispersion 1.5 vol. % CNTs in FeCo alloy

CNTs were dispersed and gradually embedded into the FeCo alloy particles with extending the time of ball milling. Intensive welding and agglomeration in the monolithic or composite powders occurred after a long time of ball milling, reducing the sintering ability for the powders and including more porosity in sintered materials.

Ball-milling plays a dual role, the first one causes thinning of CNTs and the second is to convert the unstable CNTs to amorphous carbon which reacts with FeCo alloy powder to form metal carbides. Ultimate tensile strength and yield strength were increased with extending ball milling time, however, the highest value for the strengthening of 50 % and elongation were obtained after 1 h ball milling time, due to poor densification as the time of ball milling was extended. The interfacial bonding between CNTs and FeCo alloy powder was improved, SEM of fracture surface showed less pull-out for fibres and the patches of dimples on the fracture. The magnetic properties were deteriorated owing to poor densification, powder agglomeration as the time of ball milling was increased.

11.1.7. Effect of high-energy ball milling time on dispersion 1 vol. % GNPs in FeCo alloy

The 2-D morphology for GNPs makes the dispersion of GNPs more difficult than 1-D morphology of CNTs. The density was significantly improved with including GNPs, which worked as a lubricant during ball milling, however, extending ball milling time led to include porosities in microstructure due to the difficulty in sintering the agglomerated powder. Ball milling helps to improve the interface bonding, the G-band of Raman spectra was split and red shifting was occurred due to strong interface bonding, however the improvement in interface bonding cannot increase after 6 h ball milling time due to the serious damage in the structure of GNPs.

The deteriorate in magnetic properties after extending ball milling time is due to the drop in density of the material, carbide formation and contamination, and more stresses were introduced which declined the permeability for materials. The peak in strength and elongation were observed after 4 h ball-milling time, due to embedding GNPs within FeCo alloy powder, good interfacial bonding and further refinement in the microstructure.

11.2. Recommended future works

11.2.1. Optimisation of SPS conditions

Variation in spark plasma sintering conditions showed different behaviour for mechanical and magnetic properties in the current work. However, wide sintering parameters have not covered yet such as sintering without dwelling at a temperature lower than 1100 ºC, and even in same sintering temperature with considering the influence of dwelling time on properties or sintering pressure and heating rate as slower than 50 ºC min^{-1}.

11.2.2. Effect flaked powder on properties

Dispersion of GNPs was improved when the morphology of powder was changed to flake shape by using ball milling to prepare the composites. However, there is no systematic study on the effect of thickness and size of flaked particles on the dispersion and on the final properties.

11.2.3. Improve densification of high energy ball milling composite

High energy ball milling showed significant improvement in dispersion and interface bonding, however, the full potential of CNTs or GNPs was not achieved due to the agglomeration in composite powder and poor densification after extending ball milling time. The densification can improve by optimising the suitable sintering pressure to break down the agglomeration, or by selecting the suitable amount or even the type of process control agent (PCA) to achieve the appropriate ball milled powder size, which enables approximate full densification.

11.2.4. Extended the work to other alloys

The effect of sintering conditions and the strategy of flaked powder, which proved homogeneous dispersion of GNPs, can be used to test the properties of another alloy such Fe-Si alloy. Or to improve the stability of FeCo-2V alloys at elevated temperatures, since the creep, fatigue and corrosion resistance properties, which are crucial in modern more electric applications, can improve significantly in composite materials.

11.2.5. Deformation of FeCo alloy composite

Deformation by rolling has been used to improve the dispersion of reinforcement in different ductile matrix composite, also cold and hot rolling were used to improve the properties of FeCo alloy through refining the structure and homogenising precipitates dispersion. The current study exhibits improvement in the ductility of FeCo alloy after embedding GNPs, however, the workability of those composites has not evaluated yet. Therefore, rolling the composites could be used for further improvement in interface bonding, dispersion, and density of FeCo composite, which all have a significant influence on the final properties.

11.2.6. Using different carbonaceous reinforcement

Recently, graphene oxide (GO) is widely used for prepare in-suite graphene composites. Due to the high hydrophilic affinity of the GO which enables very well dispersed in the

aqueous solvent during pre-mixing or ball milling as a compared to graphene, the dispersion of GO is much easier than dispersion graphene with less overlapping between the sheets. This method also enables to obtain thin and wide area reduced graphene, which can improve the properties significantly.

11.2.7. Coating for reinforcement

One of the ways, which is used to improve the interface bonding, is by coating the reinforcement, electroless plating was used for coating CNT to prepare FeCo composite with agglomeration during coating processes. However, a comparison between the influences of different coating methods is still missing, which might help to figure out the best coating procedure to reduce the agglomeration and improve dispersion, interface bonding and eventually the final properties.

11.2.8. Scaling Spark plasma sintering

Spark plasma sintering process has unique advantages over classical sintering process, sample with dimension approaching half meter size have been produced by SPS, which can be rolled to desired thickness lamination. Therefore, and due to the improvement achieved in this work in properties of FeCo alloy by SPS alone or with addition of the reinforcement, commercialisation of the process for producing the initial bulk raw magnetic material may be feasible for producing laminations for electrical machines for high value, high performance applications. However, a systematic study is required starting from modifying SPS machine to the subsequent process for the final product.

References

[1] Sundar, R.S. and Deevi, S.C., 2005. Soft magnetic FeCo alloys: alloy development, processing, and properties. *International materials reviews*, *50*(3), pp.157-192.

[2] Sourmail, T., 2005. Near equiatomic FeCo alloys: constitution, mechanical and magnetic properties. *Progress in Materials Science*, *50*(7), pp.816-880.

[3] Mani, M.K., 2014. *Development of Fe-50Co alloy and its composites by spark plasma sintering.* PhD thesis, Cardiff University.

[4] Mamedov, V., 2002. Spark plasma sintering as advanced PM sintering method. *Powder Metallurgy*, *45*(4), pp.322-328.

[5] Munir, Z.A., Quach, D.V. and Ohyanagi, M., 2011. Electric current activation of sintering: a review of the pulsed electric current sintering process. *Journal of the American Ceramic Society*, *94*(1), pp.1-19.

[6] Munir, Z.A., Anselmi-Tamburini, U. and Ohyanagi, M., 2006. The effect of electric field and pressure on the synthesis and consolidation of materials: a review of the spark plasma sintering method. *Journal of Materials Science*, *41*(3), pp.763-777.

[7] Saheb, N., Iqbal, Z., Khalil, A., Hakeem, A.S., Al Aqeeli, N., Laoui, T., Al-Qutub, A. and Kirchner, R., 2012. Spark plasma sintering of metals and metal matrix nanocomposites: a review. *Journal of Nanomaterials*, *2012*, p.18.

[8] Rajan, T.P.D., Pillai, R.M. and Pai, B.C., 1998. Reinforcement coatings and interfaces in aluminium metal matrix composites. *Journal of Materials Science*, *33*(14), pp.3491-3503.

[9] Khakbiz, M. and Akhlaghi, F., 2009. Synthesis and structural characterization of Al-B_4C nano-composite powders by mechanical alloying. *Journal of Alloys and Compounds*, *479*(1), pp.334-341.

[10] Bakshi, S.R., Lahiri, D. and Agarwal, A., 2010. Carbon nanotube reinforced metal matrix composites-a review. *International Materials Reviews*, *55*(1), pp.41-64.

[11] Quigley, R.E.J., 1993, March. More electric aircraft. In *Applied Power Electronics Conference and Exposition, 1993. APEC'93. Conference Proceedings 1993., Eighth Annual* (pp. 906-911). IEEE.

[12] Weimer, J.A., 1993, October. Electrical power technology for the more electric aircraft. In *Digital Avionics Systems Conference, 1993. 12th DASC., AIAA/IEEE* (pp. 445-450). IEEE.

[13] Cao, W., Mecrow, B.C., Atkinson, G.J., Bennett, J.W. and Atkinson, D.J., 2012. Overview of electric motor technologies used for more electric aircraft (MEA). *IEEE Transactions on Industrial Electronics*, *59*(9), pp.3523-3531.

[14] Ren, L., Basu, S., Yu, R.H., Xiao, J.Q. and Parvizi-Majidi, A., 2001. Mechanical properties of Fe-Co soft magnets. *Journal of materials science*, *36*(6), pp.1451-1457.

[15] Nishizawa, T. Ishida, K. Massalski, T.B. ,1990. Binary alloy phase diagrams (Vol. 2). 2nd edn., ASM International, Metal Park (OH), p. 1186.

[16] Kuhn, H. and Medlin, D., 2000. *Mechanical Testing and Evaluation* (Vol.8). ASM Handbook. International, Materials Park (OH) USA.

[17] Dieter, G.E. and Bacon, D.J., 1986. *Mechanical metallurgy* (Vol. 3). New York: McGraw-Hill.

[18] Johnston, W.G. and Gilman, J.J., 1959. Dislocation velocities, dislocation densities, and plastic flow in lithium fluoride crystals. *Journal of Applied Physics*, *30*(2), pp.129-144.

[19] Hall, E.0., 1970. *Yield point phenomena in metals and alloys*. Macmillan and co ltd.

[20] Zhao, L., Baker, I. and George, E.P., 1992. Room temperature fracture of FeCo. In *MRS Proceedings* (Vol. 288, p. 501). Cambridge University Press.

[21] Zhao, L. and Baker, I., 1994. The effect of grain size and Fe: Co ratio on the room temperature yielding of FeCo. *Acta metallurgica et materialia*, *42*(6), pp.1953-1958.

[22] Baker, I. and Schulson, E.M., 1989. On grain boundary disorder and the tensile ductility of polycrystalline ordered alloys: A hypothesis. *Scripta metallurgica*, *23*(3), pp.345-348.
[23] John H. White, Y. W., 1932. Workable magnetic compositions containing binary alloy iron and cobalt: Patented.
[24] Persiano, A.I. and Rawlings, R.D., 1991. Effect of niobium additions on the structure and magnetic properties of equiatomic iron-cobalt alloys. *Journal of materials science*, *26*(15), pp.4026-4032.
[25] Kawahara, K. and Uehara, M., 1984. A possibility for developing high strength soft magnetic materials in FeCo-X alloys. *Journal of materials science*, *19*(8), pp.2575-2581.
[26] Tanaka, M.: US Patent # 05252940, 1991.
[27] Bozorth, R.M., 1978. *Ferromagnetism*. 2 nd edn New York, IEEE press.
[28] Clegg, D.W. and Buckley, R.A., 1973. The disorder→ order transformation in iron-cobalt-based alloys. *Metal Science Journal*, *7*(1), pp.48-54.
[29] Stoloff, N.S. and Davies, R.G., 1964. The plastic deformation of ordered FeCo and Fe_3Al alloys. *Acta Metallurgica*, *12*(5), pp.473-485.
[30] Pinnel, M.R., Mahajan, S. and Bennett, J.E., 1976. Influence of thermal treatments on the mechanical properties of an Fe-Co-V alloy (remendur). *Acta Metallurgica*, *24*(12), pp.1095-1106.
[31] Thornburg, D.R., 1969. High-Strength High-ductility Cobalt-Iron Alloys. *Journal of Applied Physics*, *40*(3), pp.1579-1580.
[32] Hailer, B.T., 2001. *Effect of Heat Treatment on Magnetic and Mechanical Properties of an Iron-Cobalt-Vanadium-Niobium Alloy*. Msc dissertation, Virginia Polytechnic Institute and State University.
[33] Sourmail, T., 2004. Evolution of strength and coercivity during annealing of FeCo based alloys. *Scripta materialia*, *51*(6), pp.589-591.
[34] Nabi, B., Helbert, A.L., Brisset, F., André, G., Waeckerlé, T. and Baudin, T., 2013. Effect of recrystallization and degree of order on the magnetic and mechanical properties of soft magnetic FeCo-2V alloy. *Materials Science and Engineering: A*, *578*, pp.215-221.
[35] Glezer, A.M. and Maleeva, I.V., 1988. Grain boundary fracture of ordered alloy FeCo. *Physics of Metals and Metallography(USSR)*, *66*(6), pp.174-175.
[36] Sundar, R.S. and Deevi, S.C., 2004. Isothermal oxidation behavior of FeCo–2V intermetallic alloy. *Intermetallics*, *12*(12), pp.1311-1316.
[37] Kawahara, K., 1983. Effect of additive elements on cold workability in FeCo alloys. *Journal of Materials Science*, *18*(6), pp.1709-1718.
[38] Kawahara, K., 1983. Effect of carbon on mechanical properties in Fe0.5Co0.5 alloys. *Journal of materials science*, *18*(7), pp.2047-2055.
[39] George, E.P., Gubbi, A.N., Baker, I. and Robertson, L., 2002. Mechanical properties of soft magnetic FeCo alloys. *Materials Science and Engineering: A*, *329*, pp.325-333.
[40] Jordan, K.R., Stoloff N.S., 1969. Plastic deformation and fracture in FeCo-2%V. *Trans Metal Soc AIME*;245:2027–34.
[41] Sundar, R.S. and Deevi, S.C., 2004. Effect of heat-treatment on the room temperature ductility of an ordered intermetallic Fe-Co-V alloy. *Materials Science and Engineering: A*, *369*(1), pp.164-169.
[42] Pitt, C.D. and Rawlings, R.D., 1983. Lüders strain and ductility of ordered Fe-Co-2V and Fe-Co-V-Ni alloys. *Metal science*, *17*(6), pp.261-266.
[43] Davies, R.G. and Stoloff, N.S., 1966. A study of grain growth in FeCo-V. *AIME MET SOC TRANS*, *236*(11), pp.1605-1608.
[44] Jiles, D.C., 2003. Recent advances and future directions in magnetic materials. *Acta Materialia*, *51*(19), pp.5907-5939.
[45] Herzer, G., 2013. Modern soft magnets: Amorphous and nanocrystalline materials. *Acta Materialia*, *61*(3), pp.718-734.

[46] Bogma, K.K., 1966. Temperature studies of the magnetic properties of FeCo. *Phys Metals Metallogr, 1966, 22, 2, 148-151*.
[47] Hug, E., Hubert, O. and Guillot, I., 2000. Effect of strengthening on the magnetic behaviour of ordered intermetallic 2 % V-CoFe alloys. *Journal of magnetism and magnetic materials*, *215*, pp.197-200.
[48] Hug, E., Hubert, O. and Clavel, M., 1997. Some aspects of the magnetomechanical coupling in the strengthening of nonoriented and grain-oriented 3 % SiFe alloys. *IEEE transactions on magnetics*, *33*(1), pp.763-771.
[49] Fingers, R.T. and Kozlowski, G., 1997. Microstructure and magnetic properties of Fe-Co alloys. *Journal of applied physics*, *81*(8), pp.4110-4111.
[50] Jiles, D. 1991. *Introduction to magnetism and magnetic materials*. 1st ed. Chapman & Hall London.
[51] Jiles, D. 2016. *Introduction to magnetism and magnetic materials*. 3ed ed. CRC Press.
[52] Herzer, G., 1990. Grain size dependence of coercivity and permeability in nanocrystalline ferromagnets. *IEEE Transactions on Magnetics*, *26*(5), pp.1397-1402.
[53] Zeng, Q., Baker, I., McCreary, V. and Yan, Z., 2007. Soft ferromagnetism in nanostructured mechanical alloying FeCo-based powders. *Journal of Magnetism and Magnetic Materials*, *318*(1), pp.28-38.
[54] Lee, B.H., Ahn, B.S., Kim, D.G., Oh, S.T., Jeon, H., Ahn, J. and Do Kim, Y., 2003. Microstructure and magnetic properties of nanosized Fe-Co alloy powders synthesized by mechanochemical and mechanical alloying process. *Materials Letters*, *57*(5), pp.1103-1107.
[55] Zhang, H.W., Gopalan, R., Mukai, T. and Hono, K., 2005. Fabrication of bulk nanocrystalline Fe-C alloy by spark plasma sintering of mechanically milled powder. *Scripta materialia*, *53*(7), pp.863-868.
[56] Dijkstra, L.J. and Wert, C., 1950. Effect of inclusions on coercive force of iron. *Physical Review*, *79*(6), p.979.
[57] Yu, R.H., Basu, S., Ren, L., Zhang, Y., Parvizi-Majidi, A., Unruh, K.M. and Xiao, J.Q., 2000. High temperature soft magnetic materials: FeCo alloys and composites. *IEEE transactions on magnetics*, *36*(5), pp.3388-3393.
[58] Moumeni, H., Alleg, S. and Greneche, J.M., 2005. Structural properties of Fe50Co50 nanostructured powder prepared by mechanical alloying. *Journal of Alloys and Compounds*, *386*(1), pp.12-19.
[59] Loureiro, J.M., Batista, A.C., Khomchenko, V.A., Costa, B.F.O. and Le Caër, G., 2011. Order-disorder phenomena from X-ray diffraction in FeCo alloys annealed and ground at high energy. *Powder Diffraction*, *26*(03), pp.267-272.
[60] Cullity, B.D. 1978. *Elements of X-ray diffraction*, 2nd edn. Addison-Wesley publishing company, United States of America, pp 284,288.
[61] Martin, J. 2006. *Materials for engineering*. Wood head Publishing.
[62] Hirschhorn, J.S., 1969. *Introduction to Powder Metallurgy*. American Powder Metallurgy Institute.
[63] Orru, R., Woolman, J., Cao, G. and Munir, Z.A., 2001. Synthesis of dense nanometric $MoSi_2$ through mechanical and field activation. *Journal of Materials Research*, *16*(05), pp.1439-1448.
[64] Bernard, F., Charlot, F., Gaffet, E. and Munir, Z.A., 2001. One-Step Synthesis and Consolidation of Nanophase Iron Aluminide. *Journal of the American Ceramic Society*, *84*(5), pp.910-914.
[65] Kubota, M., 2007. Properties of nano-structured pure Al produced by mechanical grinding and spark plasma sintering. *Journal of Alloys and Compounds*, *434*, pp.294-297.
[66] Kim, K.T., Cha, S.I., Hong, S.H. and Hong, S.H., 2006. Microstructures and tensile behavior of carbon nanotube reinforced Cu matrix nanocomposites. *Materials Science and Engineering: A*, *430*(1), pp.27-33.

[67] Yue, M., Zhang, J.X., Liu, W.Q. and Wang, G.P., 2004. Chemical stability and microstructure of Nd-Fe-B magnet prepared by spark plasma sintering. *Journal of Magnetism and Magnetic Materials*, *271*(2), pp.364-368.
[68] Kwon, Y.S., Dudina, D.V., Korchagin, M.A. and Lomovsky, O.I., 2004. Microstructure changes in TiB_2-Cu nanocomposite under sintering. *Journal of materials science*, *39*(16), pp.5325-5331.
[69] Chen, X.J., Khor, K.A., Chan, S.H. and Yu, L.G., 2004. Overcoming the effect of contaminant in solid oxide fuel cell (SOFC) electrolyte: spark plasma sintering (SPS) of 0.5 wt.% silica-doped yttria-stabilized zirconia (YSZ). *Materials Science and Engineering: A*, *374*(1), pp.64-71.
[70] Kwon, H., Estili, M., Takagi, K., Miyazaki, T. and Kawasaki, A., 2009. Combination of hot extrusion and spark plasma sintering for producing carbon nanotube reinforced aluminum matrix composites. *Carbon*, *47*(3), pp.570-577.
[71] Cha, H.R., Yun, C.H., Son, H.T. and Cho, J.I., 2007. The Improvement of permeability and strength in soft magnetic composites motor core using spark plasma sintering process. In *Advanced Materials Research*, 26, pp. 609-612).
[72] Zhaohui, Z., Fuchi, W., Lin, W., Shukui, L. and Osamu, S., 2008. Sintering mechanism of large-scale ultrafine-grained copper prepared by SPS method. *Materials Letters*, *62*(24), pp.3987-3990.
[73] Diouf, S. and Molinari, A., 2012. Densification mechanisms in spark plasma sintering: effect of particle size and pressure. *Powder Technology*, *221*, pp.220-227.
[74] Song, X., Liu, X. and Zhang, J., 2006. Neck Formation and Self-Adjusting Mechanism of Neck Growth of Conducting Powders in Spark Plasma Sintering. *Journal of the American Ceramic Society*, *89*(2), pp.494-500.
[75] Shen, Z., Johnsson, M., Zhao, Z. and Nygren, M., 2002. Spark plasma sintering of alumina. *Journal of the American Ceramic Society*, *85*(8), pp.1921-1927.
[76] Nygren, M. and Shen, Z., 2004. Spark plasma sintering: possibilities and limitations. In *Key Engineering Materials*, 264, pp. 719-724.
[77] Azzaza, S., Alleg, S., Moumeni, H., Nemamcha, A.R., Rehspringer, J.L. and Greneche, J.M., 2006. Magnetic properties of nanostructured ball-milled Fe and Fe50Co50 alloy. *Journal of Physics: Condensed Matter*, *18*(31), p.7257.
[78] Chermahini, M.D., Sharafi, S., Shokrollahi, H. and Zandrahimi, M., 2009. Microstructural and magnetic properties of nanostructured Fe and Fe50Co50 powders prepared by mechanical alloying. *Journal of Alloys and Compounds*, *474*(1), pp.18-22.
[79] Poudyal, N., Rong, C.B. and Liu, J.P., 2011. Morphological and magnetic characterization of Fe, Co, and FeCo nanoplates and nanoparticles prepared by surfactants-assisted ball milling. *Journal of Applied Physics*, *109*(7), p.07B526.
[80] Turgut, Z., Nuhfer, N.T., Piehler, H.R. and McHenry, M.E., 1999. Magnetic properties and microstructural observations of oxide coated FeCo nanocrystals before and after compaction. *Journal of applied physics*, *85*(8), pp.4406-4408.
[81] Turgut, Z., Fingers, R.T., Piehler, H.R. and McHenry, M.E., 2000. Microstructural and magnetic observations of compacted FeCoV nanoparticles. *IEEE transactions on magnetics*, *36*(5), pp.3024-3025.
[82] Tung, D.K., Phong, P.T., Phong, L.T.H., Dai, N.V., Nam, D.N.H. and Phuc, N.X., 2015. Structural and magnetic properties of mechanically alloyed Fe50Co50 nanoparticles. *Journal of Alloys and Compounds*, *640*, pp.34-38.
[83] Do Kim, Y., Chung, J.Y., Kim, J. and Jeon, H., 2000. Formation of nanocrystalline Fe-Co powders produced by mechanical alloying. *Materials Science and Engineering: A*, *291*(1), pp.17-21.
[84] Mani, M.K., Viola, G., Reece, M.J., Hall, J.P. and Evans, S.L., 2012. Structural and magnetic characterization of spark plasma sintered Fe-50Co alloys. *MRS Online Proceedings Library Archive*, *1516*, pp.201-207.

[85] Bakshi, S.R. and Agarwal, A., 2011. An analysis of the factors affecting strengthening in carbon nanotube reinforced aluminum composites. *Carbon*, *49*(2), pp.533-544.
[86] Doel, T.J.A. and Bowen, P., 1996. Tensile properties of particulate-reinforced metal matrix composites. *Composites Part A: Applied Science and Manufacturing*, *27*(8), pp.655-665.
[87] Ma, Z.Y., Li, Y.L., Liang, Y., Zheng, F., Bi, J. and Tjong, S.C., 1996. Nanometric Si_3N_4 particulate-reinforced aluminum composite. *Materials Science and Engineering: A*, *219*(1-2), pp.229-231.
[88] Deng, C.F., Ma, Y.X., Zhang, P., Zhang, X.X. and Wang, D.Z., 2008. Thermal expansion behaviors of aluminum composite reinforced with carbon nanotubes. *Materials Letters*, *62*(15), pp.2301-2303.
[89] Deng, C.F., Wang, D.Z., Zhang, X.X. and Ma, Y.X., 2007. Damping characteristics of carbon nanotube reinforced aluminum composite. *Materials letters*, *61*(14), pp.3229-3231.
[90] Scharf, T.W., Neira, A., Hwang, J.Y., Tiley, J. and Banerjee, R., 2009. Self-lubricating carbon nanotube reinforced nickel matrix composites. *Journal of Applied Physics*, *106*(1), p.013508.
[91] Mani, M.K., Viola, G., Reece, M.J., Hall, J.P. and Evans, S.L., 2014. Influence of coated SiC particulates on the mechanical and magnetic behaviour of Fe-Co alloy composites. *Journal of Materials Science*, *49*(6), pp.2578-2587.
[92] Neubauer, E., Kitzmantel, M., Hulman, M. and Angerer, P., 2010. Potential and challenges of metal-matrix-composites reinforced with carbon nanofibers and carbon nanotubes. *Composites Science and Technology*, *70*(16), pp.2228-2236.
[93] Esawi, A.M., Morsi, K., Sayed, A., Gawad, A.A. and Borah, P., 2009. Fabrication and properties of dispersed carbon nanotube-aluminum composites. *Materials Science and Engineering: A*, *508*(1), pp.167-173.
[94] Choi, H., Shin, J., Min, B., Park, J. and Bae, D., 2009. Reinforcing effects of carbon nanotubes in structural aluminum matrix nanocomposites. *Journal of Materials Research*, *24*(08), pp.2610-2616.
[95] He, C.N., Zhao, N.Q., Shi, C.S. and Song, S.Z., 2009. Mechanical properties and microstructures of carbon nanotube-reinforced Al matrix composite fabricated by in situ chemical vapor deposition. *Journal of Alloys and Compounds*, *487*(1), pp.258-262.
[96] Iijima, S., 1991. Helical microtubules of graphitic carbon. *nature*, 354(6348), pp.56-58.
[97] Reilly, R.M., 2007. Carbon nanotubes: potential benefits and risks of nanotechnology in nuclear medicine. *Journal of Nuclear Medicine*, *48*(7), pp.1039-1042.
[98] Martins-Júnior, P.A., Alcântara, C.E., Resende, R.R. and Ferreira, A.J., 2013. Carbon nanotubes: directions and perspectives in oral regenerative medicine. *Journal of dental research*, *92*(7), pp.575-583.
[99] Ruoff, R.S., Qian, D. and Liu, W.K., 2003. Mechanical properties of carbon nanotubes: theoretical predictions and experimental measurements. *Comptes Rendus Physique*, *4*(9), pp.993-1008.
[100] Ma, P.C., Siddiqui, N.A., Marom, G. and Kim, J.K., 2010. Dispersion and functionalization of carbon nanotubes for polymer-based nanocomposites: a review. *Composites Part A: Applied Science and Manufacturing*, *41*(10), pp.1345-1367.
[101] Kuzumaki, T., Miyazawa, K., Ichinose, H. and Ito, K., 1998. Processing of carbon nanotube reinforced aluminum composite. *Journal of Materials Research*, *13*(09), pp.2445-2449.
[102] Zhan, G.D., Kuntz, J.D., Wan, J. and Mukherjee, A.K., 2003. Single-wall carbon nanotubes as attractive toughening agents in alumina-based nanocomposites. *Nature materials*, *2*(1), pp.38-42.
[103] Song, Y.S. and Youn, J.R., 2005. Influence of dispersion states of carbon nanotubes on physical properties of epoxy nanocomposites. *Carbon*, *43*(7), pp.1378-1385.

[104] Dillon, A., Jones, K.M., Bekkedahl, T.A. and Kiang, C.H., 1997. Storage of hydrogen in single-walled carbon nanotubes. *Nature*, *386*(6623), p.377.
[105] De Heer, W.A., Chatelain, A. and Ugarte, D., 1995. A carbon nanotube field-emission electron source. *Science*, *270*(5239), pp.1179-1181.
[106] Kong, J., Franklin, N.R., Zhou, C., Chapline, M.G., Peng, S., Cho, K. and Dai, H., 2000. Nanotube molecular wires as chemical sensors. *science*, *287*(5453), pp.622-625.
[107] Hafner, J.H., Cheung, C.L. and Lieber, C.M., 1999. Direct growth of single-walled carbon nanotube scanning probe microscopy tips. *Journal of the American Chemical Society*, *121*(41), pp.9750-9751.
[108] Bianco, A., Kostarelos, K. and Prato, M., 2005. Applications of carbon nanotubes in drug delivery. *Current opinion in chemical biology*, *9*(6), pp.674-679.
[109] Mermin, N.D., 1968. Crystalline order in two dimensions. *Physical Review*, *176*(1), p.250.
[110] Novoselov, K.S., Geim, A.K., Morozov, S.V., Jiang, D., Zhang, Y., Dubonos, S.V., Grigorieva, I.V. and Firsov, A.A., 2004. Electric field effect in atomically thin carbon films. *science*, *306*(5696), pp.666-669.
[111] Kim, H., Abdala, A.A. and Macosko, C.W., 2010. Graphene/polymer nanocomposites. *Macromolecules*, *43*(16), pp.6515-6530.
[112] Potts, J.R., Dreyer, D.R., Bielawski, C.W. and Ruoff, R.S., 2011. Graphene-based polymer nanocomposites. *Polymer*, *52*(1), pp.5-25.
[113] Huang, X., Qi, X., Boey, F. and Zhang, H., 2012. Graphene-based composites. *Chemical Society Reviews*, *41*(2), pp.666-686.
[114] Wu, Z.S., Zhou, G., Yin, L.C., Ren, W., Li, F. and Cheng, H.M., 2012. Graphene/metal oxide composite electrode materials for energy storage. *Nano Energy*, *1*(1), pp.107-131.
[115] Wang, J., Li, Z., Fan, G., Pan, H., Chen, Z. and Zhang, D., 2012. Reinforcement with graphene nanosheets in aluminum matrix composites. *Scripta Materialia*, *66*(8), pp.594-597.
[116] Walker, L.S., Marotto, V.R., Rafiee, M.A., Koratkar, N. and Corral, E.L., 2011. Toughening in graphene ceramic composites. *Acs Nano*, *5*(4), pp.3182-3190.
[117] Liang, J., Wang, Y., Huang, Y., Ma, Y., Liu, Z., Cai, J., Zhang, C., Gao, H. and Chen, Y., 2009. Electromagnetic interference shielding of graphene/epoxy composites. *Carbon*, 47(3), pp.922-925.
[118] Brownson, D.A., Kampouris, D.K. and Banks, C.E., 2011. An overview of graphene in energy production and storage applications. *Journal of Power Sources*, *196*(11), pp.4873-4885.
[119] Wang, Y., Li, Z., Wang, J., Li, J. and Lin, Y., 2011. Graphene and graphene oxide: biofunctionalization and applications in biotechnology. *Trends in biotechnology*, *29*(5), pp.205-212.
[120] Sun, X., Liu, Z., Welsher, K., Robinson, J.T., Goodwin, A., Zaric, S. and Dai, H., 2008. Nano-graphene oxide for cellular imaging and drug delivery. *Nano research*, *1*(3), pp.203-212.
[121] Bae, S., Kim, H., Lee, Y., Xu, X., Park, J.S., Zheng, Y., Balakrishnan, J., Lei, T., Kim, H.R., Song, Y.I. and Kim, Y.J., 2010. Roll-to-roll production of 30-inch graphene films for transparent electrodes. *Nature nanotechnology*, *5*(8), pp.574-578.
[122] Yu, A., Roes, I., Davies, A. and Chen, Z., 2010. Ultrathin, transparent, and flexible graphene films for supercapacitor application. *Applied physics letters*, *96*(25), p.253105.
[123] Yu, M.F., Lourie, O., Dyer, M.J., Moloni, K., Kelly, T.F. and Ruoff, R.S., 2000. Strength and breaking mechanism of multiwalled carbon nanotubes under tensile load. *Science*, *287*(5453), pp.637-640.
[124] Treacy, M.J., Ebbesen, T.W. and Gibson, J.M., 1996. Exceptionally high Young's modulus observed for individual carbon nanotubes. *Nature*, *381*(6584), p.678.

[125] Park, C., Ounaies, Z., Watson, K.A., Crooks, R.E., Smith, J., Lowther, S.E., Connell, J.W., Siochi, E.J., Harrison, J.S. and St Clair, T.L., 2002. Dispersion of single wall carbon nanotubes by in situ polymerization under sonication. *Chemical physics letters*, *364*(3), pp.303-308.
[126] Lee, C., Wei, X., Kysar, J.W. and Hone, J., 2008. Measurement of the elastic properties and intrinsic strength of monolayer graphene. *science*, *321*(5887), pp.385-388.
[127] Balandin, A.A., Ghosh, S., Bao, W., Calizo, I., Teweldebrhan, D., Miao, F. and Lau, C.N., 2008. Superior thermal conductivity of single-layer graphene. *Nano letters*, *8*(3), pp.902-907.
[128] Du, X., Skachko, I., Barker, A. and Andrei, E.Y., 2008. Approaching ballistic transport in suspended graphene. *Nature nanotechnology*, *3*(8), pp.491-495.
[129] Esumi, K., Ishigami, M., Nakajima, A., Sawada, K. and Honda, H., 1996. Chemical treatment of carbon nanotubes. *Carbon*, *34*(2), pp.279-281.
[130] Yu, R., Chen, L., Liu, Q., Lin, J., Tan, K.L., Ng, S.C., Chan, H.S., Xu, G.Q. and Hor, T.A., 1998. Platinum deposition on carbon nanotubes via chemical modification. *Chemistry of Materials*, *10*(3), pp.718-722.
[131] Wang, S.C., Chang, K.S. and Yuan, C.J., 2009. Enhancement of electrochemical properties of screen-printed carbon electrodes by oxygen plasma treatment. *Electrochimica Acta*, *54*(21), pp.4937-4943.
[132] Knupfer, M., 2001. Electronic properties of carbon nanostructures. *Surface science reports*, *42*(1), pp.1-74.
[133] Vaisman, L., Wagner, H.D. and Marom, G., 2006. The role of surfactants in dispersion of carbon nanotubes. *Advances in colloid and interface science*, *128*, pp.37-46.
[134] McCarthy, B., Coleman, J.N., Czerw, R., Dalton, A.B., Carroll, D.L. and Blau, W.J., 2001. Microscopy studies of nanotube-conjugated polymer interactions. *Synthetic Metals*, *121*(1-3), pp.1225-1226.
[135] Strano, M.S., Moore, V.C., Miller, M.K., Allen, M.J., Haroz, E.H., Kittrell, C., Hauge, R.H. and Smalley, R.E., 2003. The role of surfactant adsorption during ultrasonication in the dispersion of single-walled carbon nanotubes. *Journal of Nanoscience and Nanotechnology*, *3*(1-1), pp.81-86.
[136] Islam, M.F., Rojas, E., Bergey, D.M., Johnson, A.T. and Yodh, A.G., 2003. High weight fraction surfactant solubilization of single-wall carbon nanotubes in water. *Nano letters*, *3*(2), pp.269-273.
[137] Lu, K.L., Lago, R.M., Chen, Y.K., Green, M.L.H., Harris, P.J.F. and Tsang, S.C., 1996. Mechanical damage of carbon nanotubes by ultrasound. *Carbon*, *34*(6), pp.814-816.
[138] Kim, Y.A., Hayashi, T., Fukai, Y., Endo, M., Yanagisawa, T. and Dresselhaus, M.S., 2002. Effect of ball milling on morphology of cup-stacked carbon nanotubes. *Chemical physics letters*, *355*(3), pp.279-284.
[139] Kim, K.T., Cha, S.I., Gemming, T., Eckert, J. and Hong, S.H., 2008. The Role of Interfacial Oxygen Atoms in the Enhanced Mechanical Properties of Carbon-Nanotube-Reinforced Metal Matrix Nanocomposites. *Small*, *4*(11), pp.1936-1940.
[140] Kondoh, K., Threrujirapapong, T., Imai, H., Umeda, J. and Fugetsu, B., 2008. CNTs/TiC reinforced titanium matrix nanocomposites via powder metallurgy and its microstructural and mechanical properties. *Journal of Nanomaterials*, *2008*, p.76.
[141] Sun, S.J. and Zhang, M.D., 1991. Interface characteristics and mechanical properties of carbon fibre reinforced copper composites. *Journal of materials science*, *26*(21), pp.5762-5766.
[142] Tham, L.M., Gupta, M. and Cheng, L., 2001. Effect of limited matrix-reinforcement interfacial reaction on enhancing the mechanical properties of aluminium-silicon carbide composites. *Acta Materialia*, *49*(16), pp.3243-3253.

[143] Tang, Y., Liu, L., Li, W., Shen, B. and Hu, W., 2009. Interface characteristics and mechanical properties of short carbon fibers/Al composites with different coatings. *Applied Surface Science*, *255*(8), pp.4393-4400.
[144] Tjong, S.C., 2007. Novel nanoparticle-reinforced metal matrix composites with enhanced mechanical properties. *Advanced engineering materials*, *9*(8), pp.639-652.
[145] Ma, Z.Y., Tjong, S.C., Li, Y.L. and Liang, Y., 1997. High temperature creep behavior of nanometric Si_3N_4 particulate reinforced aluminium composite. *Materials Science and Engineering: A*, *225*(1-2), pp.125-134.
[146] Thostenson, E.T. and Chou, T.W., 2003. On the elastic properties of carbon nanotube-based composites: modelling and characterization. *Journal of Physics D: Applied Physics*, *36*(5), p.573.
[147] Laha, T., Agarwal, A., McKechnie, T. and Seal, S., 2004. Synthesis and characterization of plasma spray formed carbon nanotube reinforced aluminum composite. *Materials Science and Engineering: A*, *381*(1), pp.249-258.
[148] Noguchi, T., Magario, A., Fukazawa, S., Shimizu, S., Beppu, J. and Seki, M., 2004. Carbon nanotube/aluminium composites with uniform dispersion. *Materials Transactions*, *45*(2), pp.602-604.
[149] Jiang, L., Fan, G., Li, Z., Kai, X., Zhang, D., Chen, Z., Humphries, S., Heness, G. and Yeung, W.Y., 2011. An approach to the uniform dispersion of a high volume fraction of carbon nanotubes in aluminum powder. *Carbon*, *49*(6), pp.1965-1971.
[150] He, C., Zhao, N., Shi, C., Du, X., Li, J., Li, H. and Cui, Q., 2007. An Approach to Obtaining Homogeneously Dispersed Carbon Nanotubes in Al Powders for Preparing Reinforced Al-Matrix Composites. *Advanced Materials*, *19*(8), pp.1128-1132.
[151] Cha, S.I., Kim, K.T., Arshad, S.N., Mo, C.B. and Hong, S.H., 2005. Extraordinary strengthening effect of carbon nanotubes in metal-matrix nanocomposites processed by molecular-level mixing. *Advanced Materials*, *17*(11), pp.1377-1381.
[152] Kim, K.T., Eckert, J., Liu, G., Park, J.M., Lim, B.K. and Hong, S.H., 2011. Influence of embedded-carbon nanotubes on the thermal properties of copper matrix nanocomposites processed by molecular-level mixing. *Scripta Materialia*, *64*(2), pp.181-184.
[153] Rashad, M., Pan, F., Tang, A. and Asif, M., 2014. Effect of graphene nanoplatelets addition on mechanical properties of pure aluminum using a semi-powder method. *Progress in Natural Science: Materials International*, *24*(2), pp.101-108.
[154] Sridhar, I. and Narayanan, K.R., 2009. Processing and characterization of MWCNT reinforced aluminum matrix composites. *Journal of Materials Science*, *44*(7), pp.1750-1756.
[155] Suryanarayana, C., Ivanov, E. and Boldyrev, V.V., 2001. The science and technology of mechanical alloying. *Materials Science and Engineering: A*, *304*, pp.151-158.
[156] Suryanarayana, C., 2001. Mechanical alloying and milling. *Progress in materials science*, *46*(1), pp.1-184.
[157] Suryanarayana, C. and Al-Aqeeli, N., 2013. Mechanically alloyed nanocomposites. *Progress in Materials Science*, *58*(4), pp.383-502.
[158] Tjong, S.C., 2013. Recent progress in the development and properties of novel metal matrix nanocomposites reinforced with carbon nanotubes and graphene nanosheets. *Materials Science and Engineering: R: Reports*, *74*(10), pp.281-350.
[159] Shukla, A.K., Nayan, N., Murty, S.V.S.N., Sharma, S.C., Chandran, P., Bakshi, S.R. and George, K.M., 2013. Processing of copper-carbon nanotube composites by vacuum hot pressing technique. *Materials Science and Engineering: A*, *560*, pp.365-371.
[160] Munkhbayar, B., Nine, M.J., Jeoun, J., Bat-Erdene, M., Chung, H. and Jeong, H., 2013. Influence of dry and wet ball milling on dispersion characteristics of the multi-walled carbon nanotubes in aqueous solution with and without surfactant. *Powder technology*, *234*, pp.132-140.

[161] Yuan, J.M., Chen, X.H., Chen, X.H., Fan, Z.F., Yang, X.G. and Chen, Z.H., 2008. An easy method for purifying multi-walled carbon nanotubes by chlorine oxidation. *Carbon*, *46*(9), pp.1266-1269.
[162] Esawi, A. and Morsi, K., 2007. Dispersion of carbon nanotubes (CNTs) in aluminum powder. *Composites Part A: Applied Science and Manufacturing*, *38*(2), pp.646-650.
[163] Singhal, S.K., Pasricha, R., Teotia, S., Kumar, G. and Mathur, R.B., 2011. Fabrication and characterization of Al-matrix composites reinforced with amino-functionalized carbon nanotubes. *Composites Science and Technology*, *72*(1), pp.103-111.
[164] Liao, J. and Tan, M.J., 2011. Mixing of carbon nanotubes (CNTs) and aluminum powder for powder metallurgy use. *Powder technology*, *208*(1), pp.42-48.
[165] Azadehranjbar, S., Karimzadeh, F. and Enayati, M.H., 2012. Development of NiFe-CNT and Ni_3Fe-CNT nanocomposites by mechanical alloying. *Advanced Powder Technology*, *23*(3), pp.338-342.
[166] Pang, L.X., Sun, K.N., Ren, S., Sun, C., Fan, R.H. and Lu, Z.H., 2007. Fabrication and microstructure of Fe_3Al matrix composite reinforced by carbon nanotube. *Materials Science and Engineering: A*, *447*(1), pp.146-149.
[167] Mani, M.K., Viola, G., Reece, M.J., Hall, J.P. and Evans, S.L., 2014. Fabrication of carbon nanotube reinforced iron based magnetic alloy composites by spark plasma sintering. *Journal of Alloys and Compounds*, *601*, pp.146-153.
[168] Mani, M.K., Viola, G., Reece, M.J., Hall, J.P. and Evans, S.L., 2014. Improvement of interfacial bonding in carbon nanotube reinforced Fe-50Co composites by Ni-P coating: Effect on magnetic and mechanical properties. *Materials Science and Engineering: B*, *188*, pp.94-101.
[169] Mani, M.K., Viola, G., Reece, M.J., Hall, J.P. and Evans, S.L., 2014. Mechanical and magnetic characterisation of SiC whisker reinforced Fe-Co alloy composites. *Materials Science and Engineering: A*, *592*, pp.19-27.
[170] Rafiee, M.A., Rafiee, J., Srivastava, I., Wang, Z., Song, H., Yu, Z.Z. and Koratkar, N., 2010. Fracture and fatigue in graphene nanocomposites. *small*, *6*(2), pp.179-183.
[171] Bartolucci, S.F., Paras, J., Rafiee, M.A., Rafiee, J., Lee, S., Kapoor, D. and Koratkar, N., 2011. Graphene-aluminum nanocomposites. *Materials Science and Engineering: A*, *528*(27), pp.7933-7937.
[172] Chu, K. and Jia, C., 2014. Enhanced strength in bulk graphene-copper composites. *physica status solidi (a)*, *211*(1), pp.184-190.
[173] Rafiee, M.A., Rafiee, J., Wang, Z., Song, H., Yu, Z.Z. and Koratkar, N., 2009. Enhanced mechanical properties of nanocomposites at low graphene content. *ACS nano*, *3*(12), pp.3884-3890.
[174] Kumar, H.P. and Xavior, M.A., 2014. Graphene reinforced metal matrix composite (GRMMC): a review. *Procedia Engineering*, *97*, pp.1033-1040.
[175] Kim, J., Cote, L.J., Kim, F., Yuan, W., Shull, K.R. and Huang, J., 2010. Graphene oxide sheets at interfaces. *Journal of the American Chemical Society*, *132*(23), pp.8180-8186.
[176] Boostani, A.F., Tahamtan, S., Jiang, Z.Y., Wei, D., Yazdani, S., Khosroshahi, R.A., Mousavian, R.T., Xu, J., Zhang, X. and Gong, D., 2015. Enhanced tensile properties of aluminium matrix composites reinforced with graphene encapsulated SiC nanoparticles. *Composites Part A: Applied Science and Manufacturing*, *68*, pp.155-163.
[177] Wimalasiri, Y. and Zou, L., 2013. Carbon nanotube/graphene composite for enhanced capacitive deionization performance. *Carbon*, *59*, pp.464-471.
[178] Yen, M.Y., Hsiao, M.C., Liao, S.H., Liu, P.I., Tsai, H.M., Ma, C.C.M., Pu, N.W. and Ger, M.D., 2011. Preparation of graphene/multi-walled carbon nanotube hybrid and its use as photoanodes of dye-sensitized solar cells. *Carbon*, *49*(11), pp.3597-3606.

[179] Wang, P.N., Hsieh, T.H., Chiang, C.L. and Shen, M.Y., 2015. Synergetic effects of mechanical properties on graphene nanoplatelet and multiwalled carbon nanotube hybrids reinforced epoxy/carbon fiber composites. *Journal of Nanomaterials*, *2015*, p.7.
[180] Yazdani, B., Xia, Y., Ahmad, I. and Zhu, Y., 2015. Graphene and carbon nanotube (GNT)-reinforced alumina nanocomposites. *Journal of the European Ceramic Society*, *35*(1), pp.179-186.
[181] Yazdani, B., Porwal, H., Xia, Y., Yan, H., Reece, M.J. and Zhu, Y., 2015. Role of synthesis method on microstructure and mechanical properties of graphene/carbon nanotube toughened Al_2O_3 nanocomposites. *Ceramics International*, *41*(8), pp.9813-9822.
[182] Rashad, M., Pan, F., Tang, A., Asif, M. and Aamir, M., 2014. Synergetic effect of graphene nanoplatelets (GNPs) and multi-walled carbon nanotube (MW-CNTs) on mechanical properties of pure magnesium. *Journal of Alloys and Compounds*, *603*, pp.111-118.
[183] Li, Z., Fan, G., Tan, Z., Guo, Q., Xiong, D., Su, Y., Li, Z. and Zhang, D., 2014. Uniform dispersion of graphene oxide in aluminum powder by direct electrostatic adsorption for fabrication of graphene/aluminum composites. *Nanotechnology*, *25*(32), p.325601.
[184] Liu, J., Khan, U., Coleman, J., Fernandez, B., Rodriguez, P., Naher, S. and Brabazon, D., 2016. Graphene oxide and graphene nanosheet reinforced aluminium matrix composites: powder synthesis and prepared composite characteristics. *Materials & Design*, *94*, pp.87-94.
[185] Hwang, J., Yoon, T., Jin, S.H., Lee, J., Kim, T.S., Hong, S.H. and Jeon, S., 2013. Enhanced mechanical properties of graphene/copper nanocomposites using a molecular-level mixing process. *Advanced Materials*, *25*(46), pp.6724-6729.
[186] Nieto, A., Lahiri, D. and Agarwal, A., 2012. Synthesis and properties of bulk graphene nanoplatelets consolidated by spark plasma sintering. *Carbon*, *50*(11), pp.4068-4077.
[187] Fan, Y., Wang, L., Li, J., Li, J., Sun, S., Chen, F., Chen, L. and Jiang, W., 2010. Preparation and electrical properties of graphene nanosheet/Al_2O_3 composites. *Carbon*, *48*(6), pp.1743-1749.
[188] Janot, R. and Guérard, D., 2002. Ball-milling: the behavior of graphite as a function of the dispersal media. *Carbon*, *40*(15), pp.2887-2896.
[189] Rashad, M., Pan, F., Zhang, J. and Asif, M., 2015. Use of high energy ball milling to study the role of graphene nanoplatelets and carbon nanotubes reinforced magnesium alloy. *Journal of Alloys and Compounds*, *646*, pp.223-232.
[190] Yan, S.J., Dai, S.L., Zhang, X.Y., Yang, C., Hong, Q.H., Chen, J.Z. and Lin, Z.M., 2014. Investigating aluminum alloy reinforced by graphene nanoflakes. *Materials Science and Engineering: A*, *612*, pp.440-444.
[191] Shin, S.E., Choi, H.J., Shin, J.H. and Bae, D.H., 2015. Strengthening behavior of few-layered graphene/aluminum composites. *Carbon*, *82*, pp.143-151.
[192] Antunes, E.F., Lobo, A.O., Corat, E.J., Trava-Airoldi, V.J., Martin, A.A. and Veríssimo, C., 2006. Comparative study of first-and second-order Raman spectra of MWCNT at visible and infrared laser excitation. *Carbon*, *44*(11), pp.2202-2211.
[193] Rao, C.E.E., Sood, A.E., Subrahmanyam, K.E. and Govindaraj, A., 2009. Graphene: the new two-dimensional nanomaterial. *Angewandte Chemie International Edition*, *48*(42), pp.7752-7777.
[194] Thomson, K.E., Jiang, D., Ritchie, R.O. and Mukherjee, A.K., 2007. A preservation study of carbon nanotubes in alumina-based nanocomposites via Raman spectroscopy and nuclear magnetic resonance. *Applied Physics A*, *89*(3), pp.651-654.
[195] Saito, R., Hofmann, M., Dresselhaus, G., Jorio, A. and Dresselhaus, M.S., 2011. Raman spectroscopy of graphene and carbon nanotubes. *Advances in Physics*, *60*(3), pp.413-550.

[196] Bastwros, M., Kim, G.Y., Zhu, C., Zhang, K., Wang, S., Tang, X. and Wang, X., 2014. Effect of ball milling on graphene reinforced Al6061 composite fabricated by semi-solid sintering. *Composites Part B: Engineering*, *60*, pp.111-118.
[197] Mohiuddin, T.M.G., Lombardo, A., Nair, R.R., Bonetti, A., Savini, G., Jalil, R., Bonini, N., Basko, D.M., Galiotis, C., Marzari, N. and Novoselov, K.S., 2009. Uniaxial strain in graphene by Raman spectroscopy: G peak splitting, Grüneisen parameters, and sample orientation. *Physical Review B*, *79*(20), p.205433.
[198] Ferrari, A.C., Meyer, J.C., Scardaci, V., Casiraghi, C., Lazzeri, M., Mauri, F., Piscanec, S., Jiang, D., Novoselov, K.S., Roth, S. and Geim, A.K., 2006. Raman spectrum of graphene and graphene layers. *Physical review letters*, *97*(18), p.187401.
[199] Inam, F., Yan, H., Reece, M.J. and Peijs, T., 2010. Structural and chemical stability of multiwall carbon nanotubes in sintered ceramic nanocomposite. *Advances in Applied Ceramics*, *109*(4), pp.240-247.
[200] Cooper, C.A., Young, R.J. and Halsall, M., 2001. Investigation into the deformation of carbon nanotubes and their composites through the use of Raman spectroscopy. *Composites Part A: Applied Science and Manufacturing*, *32*(3), pp.401-411.
[201] Liu, J., Tang, J. and Gooding, J.J., 2012. Strategies for chemical modification of graphene and applications of chemically modified graphene. *Journal of Materials Chemistry*, *22*(25), pp.12435-12452.
[202] Bahr, J.L., Yang, J., Kosynkin, D.V., Bronikowski, M.J., Smalley, R.E. and Tour, J.M., 2001. Functionalization of carbon nanotubes by electrochemical reduction of aryl diazonium salts: a bucky paper electrode. *Journal of the American Chemical Society*, *123*(27), pp.6536-6542.
[203] Ham, H.T., Choi, Y.S. and Chung, I.J., 2005. An explanation of dispersion states of single-walled carbon nanotubes in solvents and aqueous surfactant solutions using solubility parameters. *Journal of Colloid and Interface Science*, *286*(1), pp.216-223.
[204] Ramirez, C., Garzón, L., Miranzo, P., Osendi, M.I. and Ocal, C., 2011. Electrical conductivity maps in graphene nanoplatelet/silicon nitride composites using conducting scanning force microscopy. *Carbon*, *49*(12), pp.3873-3880.
[205] Ramirez, C., Figueiredo, F.M., Miranzo, P., Poza, P. and Osendi, M.I., 2012. Graphene nanoplatelet/ composites with high electrical conductivity. *Carbon*, *50*(10), pp.3607-3615.
[206] Anderson, P., 2008. A universal DC characterisation system for hard and soft magnetic materials. *Journal of Magnetism and Magnetic Materials*, *320*(20), pp.e589-e593.
[207] M3003, The Expression of Uncertainty and Confidence in Measurement, Edition 3, 2012. https://www.ukas.com/download/publications/publications-relating-to-laboratory-accreditation/M3003_Ed3_final.pdf
[208] Bell, S., 1999. A Beginner's Guide to Uncertainty. *NPL Measurement Good Practice Guide*, (11).https://www.wmo.int/pages/prog/gcos/documents/gruanmanuals/UK_NPL/mgpg11.pdf
[209] Somkun, S., 2010. *Magnetostriction and magnetic anisotropy in non-oriented electrical steels and stator core laminations.* PhD thesis, Cardiff University.
[210] Manual of weighing applications part 1 density. https://www.sartorius.co.uk/fileadmin.
[211] Hirsch, A. and Vostrowsky, O., 2005. Functionalization of carbon nanotubes. In *Functional molecular nanostructures* (pp. 193-237). Springer Berlin Heidelberg.
[212] Locci, A.M., Orru, R., Cao, G. and Munir, Z.A., 2006. Effect of ball milling on simultaneous spark plasma synthesis and densification of TiC-TiB_2 composites. *Materials Science and Engineering: A*, *434*(1), pp.23-29.
[213] Alben, R., Becker, J.J. and Chi, M.C., 1978. Random anisotropy in amorphous ferromagnets. *Journal of applied physics*, *49*(3), pp.1653-1658.
[214] G. Couderchon, and J.F. Tiers: Some aspects of magnetic properties of Ni-Fe and Co-Fe alloys. Journal of Magnetism and Magnetic Materials. 26, 1(1982).

[215] Pfeifer, F. and Radeloff, C., 1980. Soft magnetic Ni-Fe and Co-Fe alloys-some physical and metallurgical aspects. *Journal of Magnetism and Magnetic Materials*, *19*(1-3), pp.190-207.
[216] Duckham, A., Zhang, D.Z., Liang, D., Luzin, V., Cammarata, R.C., Leheny, R.L., Chien, C.L. and Weihs, T.P., 2003. Temperature dependent mechanical properties of ultra-fine grained FeCo-2V. *Acta materialia*, *51*(14), pp.4083-4093.
[217] Osswald, S., Havel, M. and Gogotsi, Y., 2007. Monitoring oxidation of multiwalled carbon nanotubes by Raman spectroscopy. *Journal of Raman Spectroscopy*, *38*(6), pp.728-736.
[218] Sahoo, P.K., Panigrahy, B., Li, D. and Bahadur, D., 2013. Magnetic behavior of reduced graphene oxide/metal nanocomposites. *Journal of Applied Physics*, *113*(17), p.17B525.
[219] Yuan, B., Yu, L., Sheng, L., An, K. and Zhao, X., 2012. Comparison of electromagnetic interference shielding properties between single-wall carbon nanotube and graphene sheet/polyaniline composites. *Journal of Physics D: Applied Physics*, *45*(23), p.235108.
[220] Enoki, T. and Kobayashi, Y., 2005. Magnetic nanographite: an approach to molecular magnetism. *Journal of Materials Chemistry*, *15*(37), pp.3999-4002.
[221] Wu, H.Q., Xu, D.M., Wang, Q., Yao, Y.Z., Wang, Q.Y. and Su, G.Q., 2008. Effect of heat treatment on structure and magnetic properties of FeCoNi/CNTs nanocomposites. *Bulletin of Materials Science*, *31*(5), pp.801-806.
[222] Roura, P., Costa, J. and Farjas, J., 2002. Is sintering enhanced under non-isothermal conditions?. *Materials Science and Engineering: A*, *337*(1), pp.248-253.
[223] Hungría, T., Galy, J. and Castro, A., 2009. Spark Plasma Sintering as a Useful Technique to the Nanostructuration of Piezo-Ferroelectric Materials. *Advanced Engineering Materials*, *11*(8), pp.615-631.
[224] Hu, K., Li, X., Qu, S. and Li, Y., 2013. Effect of Heating Rate on Densification and Grain Growth During Spark Plasma Sintering of 93W-5.6Ni-1.4Fe Heavy Alloys. *Metallurgical and Materials Transactions A*, *44*(9), pp.4323-4336.
[225] Rutz, H.G. and Hanejko, F.G., 1994. High density processing of high performance ferrous materials. *International Conference on Powder Metallurgy and Particulate Materials*. Toronto, Canada.
[226] Sundar, R.S., Deevi, S.C. and Reddy, B.V., 2005. High strength FeCo-V intermetallic alloy: electrical and magnetic properties. *Journal of materials research*, *20*(06), pp.1515-1522.
[227] Schulson, E.M. and Barker, D.R., 1983. A brittle to ductile transition in NiAl of a critical grain size. *Scripta metallurgica*, 17(4), pp.519-522.
[228] Liu, C.T. and Stiegler, J.O., 1984. Ductile ordered intermetallic alloys. *Science*, 226, pp.636-643.
[229] Xie, G., Ohashi, O., Yoshioka, T., Song, M., Mitsuishi, K., Yasuda, H., Furuya, K. and Noda, T., 2001. Effect of interface behavior between particles on properties of pure Al powder compacts by spark plasma sintering. *Materials transactions*, *42*(9), pp.1846-1849.
[230] Randall M. German 1996. *Sintering theory and practice*. John Wiley and Sons, Inc.
[231] Kuhrt, C. and Schultz, L., 1992. Formation and magnetic properties of nanocrystalline mechanically alloyed Fe-Co. *Journal of applied physics*, *71*(4), pp.1896-1900.
[232] Yu, R.H., Basu, S., Zhang, Y., Parvizi-Majidi, A. and Xiao, J.Q., 1999. Pinning effect of the grain boundaries on magnetic domain wall in FeCo-based magnetic alloys. *Journal of applied physics*, *85*(9), pp.6655-6659.

[233] Zhang, Z. and Chen, D.L., 2006. Consideration of Orowan strengthening effect in particulate-reinforced metal matrix nanocomposites: a model for predicting their yield strength. *Scripta Materialia*, *54*(7), pp.1321-1326.
[234] Rashad, M., Pan, F., Asif, M. and Tang, A., 2014. Powder metallurgy of Mg-1% Al-1% Sn alloy reinforced with low content of graphene nanoplatelets (GNPs). *Journal of Industrial and Engineering Chemistry*, *20*(6), pp.4250-4255.
[235] Chu, K., Liu, Z., Jia, C., Chen, H., Liang, X., Gao, W., Tian, W. and Guo, H., 2010. Thermal conductivity of SPS consolidated Cu/diamond composites with Cr-coated diamond particles. *Journal of Alloys and Compounds*, *490*(1), pp.453-458.
[236] Li, B., Liu, Y., Li, J., Cao, H. and He, L., 2010. Effect of sintering process on the microstructures and properties of in situ TiB_2-TiC reinforced steel matrix composites produced by spark plasma sintering. *Journal of Materials Processing Technology*, *210*(1), pp.91-95.
[237] Baker, I., Nagpal, P., Liu, F. and Munroe, P.R., 1991. The effect of grain size on the yield strength of FeAl and NiAl. *Acta metallurgica et materialia*, *39*(7), pp.1637-1644.
[238] Ong, T.S. and Yang, H., 2000. Effect of atmosphere on the mechanical milling of natural graphite. *Carbon*, *38*(15), pp.2077-2085.
[239] Sule, R., Olubambi, P.A., Sigalas, I., Asante, J.K.O. and Garrett, J.C., 2014. Effect of SPS consolidation parameters on submicron Cu and Cu-CNT composites for thermal management. *Powder Technology*, *258*, pp.198-205.
[240] Dresselhaus, M.S., Jorio, A., Hofmann, M., Dresselhaus, G. and Saito, R., 2010. Perspectives on carbon nanotubes and graphene Raman spectroscopy. *Nano letters*, *10*(3), pp.751-758.
[241] Soldano, C., Mahmood, A. and Dujardin, E., 2010. Production, properties and potential of graphene. *Carbon*, *48*(8), pp.2127-2150.
[242] Rahnama, A. and Qin, R.S., 2015. The effect of electropulsing on the interlamellar spacing and mechanical properties of a hot-rolled 0.14% carbon steel. *Materials Science and Engineering: A*, *627*, pp.145-152.
[243] Pinnel, M.R. and Bennett, J.E., 1974. Correlation of magnetic and mechanical properties with microstructure in Fe/Co/2-3 % V alloys. *Metallurgical Transactions*, *5*(6), pp.1273-1283.
[244] Fong, S.T., Sadananda, K. and Marcinkowski, M.J., 1974. Effect of strain, temperature, and atomic order on slip deformation in FeCo. *Metallurgical Transactions*, *5*(5), pp.1239-1247.
[245] Rajasekhara, S., Ferreira, P.J., Karjalainen, L.P. and Kyröläinen, A., 2007. Hall-Petch behavior in ultra-fine-grained AISI 301LN stainless steel. *Metallurgical and Materials Transactions A*, *38*(6), pp.1202-1210.
[246] Yadhukulakrishnan, G.B., Karumuri, S., Rahman, A., Singh, R.P., Kalkan, A.K. and Harimkar, S.P., 2013. Spark plasma sintering of graphene reinforced zirconium diboride ultra-high temperature ceramic composites. *Ceramics International*, *39*(6), pp.6637-6646.
[247] Kawahara, K., 1983. Structures and mechanical properties of an FeCo-2V alloy. *Journal of Materials Science*, *18*(11), pp.3427-3436.
[248] Buckley, R.A., 1979. Ordering and recrystallization in Fe-50Co-0.4% Cr. *Metal Science*, *13*(2), pp.67-72.
[249] Lu, W.J., Zhang, X.F. and Qin, R.S., 2015. Structure and properties of κ-carbides in duplex lightweight steels. *Ironmaking & Steelmaking*, *42*(8), pp.626-631.
[250] Smart, S.K., Ren, W.C., Cheng, H.M., Lu, G.Q. and Martin, D.J., 2007. Shortened double-walled carbon nanotubes by high-energy ball milling. *International Journal of Nanotechnology*, *4*(5), pp.618-633.
[251] Yogamalar, R., Srinivasan, R., Vinu, A., Ariga, K. and Bose, A.C., 2009. X-ray peak broadening analysis in ZnO nanoparticles. *Solid State Communications*, *149*(43), pp.1919-1923.

[252] Zak, A.K., Majid, W.A., Abrishami, M.E. and Yousefi, R., 2011. X-ray analysis of ZnO nanoparticles by Williamson-Hall and size-strain plot methods. *Solid State Sciences*, *13*(1), pp.251-256.
[253] Osswald, S., Flahaut, E. and Gogotsi, Y., 2006. In situ Raman spectroscopy study of oxidation of double-and single-wall carbon nanotubes. *Chemistry of materials*, *18*(6), pp.1525-1533.
[254] Dresselhaus, M.S., Dresselhaus, G., Saito, R. and Jorio, A., 2005. Raman spectroscopy of carbon nanotubes. *Physics reports*, *409*(2), pp.47-99.
[255] Jorio, A., Souza Filho, A.G., Dresselhaus, G., Dresselhaus, M.S., Swan, A.K., Ünlü, M.S., Goldberg, B.B., Pimenta, M.A., Hafner, J.H., Lieber, C.M. and Saito, R., 2002. G-band resonant Raman study of 62 isolated single-wall carbon nanotubes. *Physical Review B*, *65*(15), p.155412.
[256] Zhao, X., Ando, Y., Qin, L.C., Kataura, H., Maniwa, Y. and Saito, R., 2002. Multiple splitting of G-band modes from individual multiwalled carbon nanotubes. *Applied physics letters*, *81*(14), pp.2550-2552.
[257] Mu, M., Osswald, S., Gogotsi, Y. and Winey, K.I., 2009. An in situ Raman spectroscopy study of stress transfer between carbon nanotubes and polymer. *Nanotechnology*, *20*(33), p.335703.
[258] George, R., Kashyap, K.T., Rahul, R. and Yamdagni, S., 2005. Strengthening in carbon nanotube/aluminium (CNT/Al) composites. *Scripta Materialia*, *53*(10), pp.1159-1163.
[259] Woo, D.J., Sneed, B., Peerally, F., Heer, F.C., Brewer, L.N., Hooper, J.P. and Osswald, S., 2013. Synthesis of nanodiamond-reinforced aluminum metal composite powders and coatings using high-energy ball milling and cold spray. *Carbon*, *63*, pp.404-415.
[260] Hosoda, H., Miyazaki, S., Inoue, K., Fukui, T., Mizuuchi, K., Mishima, Y. and Suzuki, T., 2000. Cold rolling of B2 intermetallics. *Journal of alloys and compounds*, *302*(1), pp.266-273.
[261] Estrada-Guel, I., Carreño-Gallardo, C., Mendoza-Ruiz, D.C., Miki-Yoshida, M., Rocha-Rangel, E. and Martínez-Sánchez, R., 2009. Graphite nanoparticle dispersion in 7075 aluminum alloy by means of mechanical alloying. *Journal of Alloys and Compounds*, *483*(1), pp.173-177.
[262] Liu, Z.Y., Xu, S.J., Xiao, B.L., Xue, P., Wang, W.G. and Ma, Z.Y., 2012. Effect of ball-milling time on mechanical properties of carbon nanotubes reinforced aluminum matrix composites. *Composites Part A: Applied Science and Manufacturing*, *43*(12), pp.2161-2168.
[263] Kim, W.J., Lee, T.J. and Han, S.H., 2014. Multi-layer graphene/copper composites: Preparation using high-ratio differential speed rolling, microstructure and mechanical properties. *Carbon*, *69*, pp.55-65.
[264] Wu, Y., Kim, G.Y. and Russell, A.M., 2012. Mechanical alloying of carbon nanotube and Al6061 powder for metal matrix composites. *Materials Science and Engineering: A*, *532*, pp.558-566.
[265] Rashad, M., Pan, F. and Asif, M., 2016. Exploring mechanical behaviour of Mg-6Zn alloy reinforced with graphene nanoplatelets. *Materials Science and Engineering: A*, *649*, pp.263-269.
[266] Cullity, B.D. and Graham, C.D. 2011. *Introduction to magnetic materials*. John Wiley & Sons.
[267] Zhao, N., Nash, P. and Yang, X., 2005. The effect of mechanical alloying on SiC distribution and the properties of 6061 aluminum composite. *Journal of Materials Processing Technology*, *170*(3), pp.586-592.
[268] Mohiuddin, T.M.G., Lombardo, A., Nair, R.R., Bonetti, A., Savini, G., Jalil, R., Bonini, N., Basko, D.M., Galiotis, C., Marzari, N. and Novoselov, K.S., 2009. Uniaxial

strain in graphene by Raman spectroscopy: G peak splitting, Grüneisen parameters, and sample orientation. *Physical Review B*, *79*(20), p.205433.
[269] Yoon, D., Son, Y.W. and Cheong, H., 2011. Strain-dependent splitting of the double-resonance Raman scattering band in graphene. *Physical review letters*, *106*(15), p.155502.
[270] Frank, O., Tsoukleri, G., Parthenios, J., Papagelis, K., Riaz, I., Jalil, R., Novoselov, K.S. and Galiotis, C., 2010. Compression behavior of single-layer graphenes. *ACS nano*, *4*(6), pp.3131-3138.
[271] Tsoukleri, G., Parthenios, J., Papagelis, K., Jalil, R., Ferrari, A.C., Geim, A.K., Novoselov, K.S. and Galiotis, C., 2009. Subjecting a graphene monolayer to tension and compression. *small*, *5*(21), pp.2397-2402.
[272] Melanitis, N. and Galiotis, C., 1993, February. Interfacial micromechanics in model composites using laser Raman spectroscopy. In *Proceedings of the Royal Society of London A: Mathematical, Physical and Engineering Sciences* (Vol. 440, No. 1909, pp. 379-398). The Royal Society.
[273] Pérez-Bustamante, R., Bolaños-Morales, D., Bonilla-Martínez, J., Estrada-Guel, I. and Martínez-Sánchez, R., 2014. Microstructural and hardness behavior of graphene-nanoplatelets/aluminum composites synthesized by mechanical alloying. *Journal of Alloys and Compounds*, *615*, pp.S578-S582.
[274] Niwase, K., Tanaka, T., Kakimoto, Y., Ishihara, K.N. and Shingu, P.H., 1995. Raman spectra of graphite and diamond mechanically milled with agate or stainless steel ball-mill. *Materials Transactions, JIM*, *36*(2), pp.282-288.
[275] Zhang, H., Xu, C., Xiao, W., Ameyama, K. and Ma, C., 2016. Enhanced mechanical properties of Al5083 alloy with graphene nanoplates prepared by ball milling and hot extrusion. *Materials Science and Engineering: A*, *658*, pp.8-15.

Appendix

Uncertainty in measurement :

The uncertainty in density, saturation induction, and coercivity measurement was estimated according to the UKAS M3003 [207] and [208]. The sources for uncertainty from voltage measurement calibration, flux meter, resistors and in density measurement from the instrument, temperature etc. are available in [209, 210].

Table 1. Uncertainty evaluation of Bsat of the SPS consolidated material measured under DC conditions using a permeameter.

Source of uncertainty	Value ±%	Probability distribution	Divisor	C_i	u_i ±%	v_i or v_{eff}
Flux meter cal.,	0.200	Normal	2.0000	1	0.10000	∞
Sample width	0.400	Normal	2.0000	1	0.20000	∞
Sample thickness	0.700	Normal	2.0000	1	0.35000	∞
Repeatability	0.014	Rectangular	1.7321	1	0.00800	2
Combined uncertainty					0.41500	
Expanded uncertainty					0.83000	
Declare uncertainty at confident level 95%					0.85000	

Table 2. Uncertainty evaluation of Hc of the SPS sintered materials measured under DC.

Source of uncertainty	Value ±%	Probability distribution	Divisor	C_i	u_i ±%	v_i or v_{eff}
Voltmeter calibration	0.050	Normal	2.0000	1	0.02500	∞
Resistor 0.1 Ohm	0.100	Normal	2.0000	1	0.05000	∞
Path length	0.025	Rectangular	1.7321	1	0.0144	∞
Repeatability	0.200	Rectangular	1.7321	1	0.11540	2
Combined uncertainty					0.12900	
Expanded uncertainty					0.25800	
Declare uncertainty at confident level 95%					0.30000	

Table 3. Uncertainty of Archimedes' density measurement of the SPS sintered materials.

Source of uncertainty	Value ±%	Probability distribution	Divisor	C_i	u_i ±%	v_i or v_{eff}
Manufacture uncertainty	0.4000	Normal	2.0000	1	0.20000	∞
Uncertainty for air density	0.0005	Normal	2.0000	1	0.00025	∞
Sample cleaning from graphite layer (0.001g.cm^{-3})	0.0120	Rectangle	1.7321	1	0.06000	∞
Uptake water into porosity (0.0012 g.cm^{-3})	0.0150	Rectangle	1.7321	1	0.00750	∞
Uncertainty due to effect temperature	0.0030	Normal	1.0000	1	0.00300	
Combined uncertainty					0.20800	
Expanded uncertainty					0.41700	
Declare uncertainty at confident level 95%					0.50000	

List of publications based on this project

1- Albaaji, Amar J., Elinor G. Castle, Mike J. Reece, Jeremy P. Hall, and Sam L. Evans. "Mechanical and magnetic properties of spark plasma sintered soft magnetic FeCo alloy reinforced by carbon nanotubes." Journal of Materials Research 31, no. 21 (2016): 3448-3458**. DOI: https://doi.org/10.1557/jmr.2016.372**

2-Albaaji, Amar J., Elinor G. Castle, Mike J. Reece, Jeremy P. Hall, and Sam L. Evans. "Synthesis and properties of graphene and graphene/carbon nanotube-reinforced soft magnetic FeCo alloy composites by spark plasma sintering." *Journal of Materials Science* 51, no. 16 (2016): 7624-7635. **DOI: 10.1007/s10853-016-0041-2**

3- Albaaji, Amar J., Elinor G. Castle, Mike J. Reece, Jeremy P. Hall, and Sam L. Evans. "Effect of ball-milling time on mechanical and magnetic properties of carbon nanotube reinforced FeCo alloy composites." Materials & Design 122 (2017): 296-306. **DOI: 10.1007/s10853-016-0041-2**

4- Albaaji, Amar J., Elinor G. Castle, Mike J. Reece, Jeremy P. Hall, and Sam L. Evans. "Enhancement in the elongation, yield strength and magnetic properties of intermetallic FeCo alloy using spark plasma sintering." *Journal of Materials Science* 52: 13284 (2017). **https://doi.org/10.1007/s10853-017-1435-5**

5- Albaaji, Amar J., Elinor G. Castle, Mike J. Reece, Jeremy P. Hall, and Sam L. Evans. "Influence of Spark Plasma Sintering parameters on Magnetic and Structural properties of FeCo alloy". Acceptance letter from AIP Advances journal.